

Multiphase flows in Microfluidic Reactors

Présentée le 29 octobre 2020

à la Faculté des sciences et techniques de l'ingénieur
Laboratoire d'optique
Programme doctoral en mécanique

pour l'obtention du grade de Docteur ès Sciences

par

Pooria HADIKHANI

Acceptée sur proposition du jury

Prof. F. Gallaire, président du jury
Prof. D. Psaltis, directeur de thèse
Prof. A. J. deMello, rapporteur
Prof. D. Erickson, rapporteur
Prof. Ph. Renaud, rapporteur

یکی قطره باران ز ابری چکید
که جایی که دریاست من کیستم؟
چو خود را بچشم حقارت بدید
سپهرش بجایی رسانید کار
خجل شد چو پهناى دریا بدید
گر او هست حقا که من نیستم
صدف در کنارش بجان پرورید
که شد نامور لؤلؤ شاهوار
در نیستی کوفت تا هست شد
نهد شاخ پر میوه بر زمین
تواضع کند هوشمند گزین

سعدی (۶۷۰ - ۵۸۹ ه.ش)

A raindrop trickled from a cloud
And was discomfited to see the ocean's width:
'Where there's the ocean, who am I?
If it exists, then truly I do not!'
But while with disparagement's eye it saw itself,
An oyster-shell within its bosom dearly cherished it;
And heaven at length so far advanced its cause
That it became an imperial pearl, renowned:
Elevation it discovered by first becoming lowly,
Nothingness' door it pounded until existence came to be!

Saadi Shirazi (1210 – 1292)

تقدیم به مادرم، مامان شهناز

To my mother, Maman Shahnaz

Acknowledgment

I would like to thank my grandmother Maman Leila, My mother Maman Shahnaz, my father Parviz, and my brothers Parham and Babak for their love and encouragement. I would not have completed any of this without the support of them. I am and will always be grateful for their support and encouragement.

I would like to acknowledge Professor Demetri Psaltis for giving me the opportunity to work in his laboratory. I would like to thank him for his support, encouragement, advice, time, and ideas.

I would like to thank Dr. S. Mohammad H. Hashemi for enlightening conversations we had. He was always ready to talk about my project and I could find solutions for the challenges of the project by talking to him. I would like to thank Professor Miguel A. Modestino for the guidance and fruitful discussions we had. Our discussions helped me to understand the basics of electrochemistry.

I thank Professor Asghar Afshari for his help and support. I was always enjoying the meeting we had while I was doing my bachelor and master thesis with Professor Afshari where I started to understand the physics of fluid mechanics. I would like to thank Professor Sahand Majidi for discussions we had and his helps at the time I was studying at University of Tehran.

I am fortunate to have collaborated with Professor François Gallaire, Dr. Gioele Balestra, and Dr. Lailai Zhu in the inertial microfluidics project. I am also grateful to Professor Petros Koumoutsakos, Dr. Sergey Litvinov, and Petr Karnakov for the rewarding collaboration that helped me to better understand the bubble dynamics.

It has been a sincere pleasure working at LO and I am grateful to all members of the lab. I would like to thank Dr. Nicolino Stasio and Dr. Morteza Hasani Shoreh for their help with creating a holography setup. I had the privilege of working with Dr. Navid Borhani on the droplet learning project where I learned a lot from him. I am thankful to Dr. Jieping Wang for helping me with the chemical synthesis and the great discussions we had. I thank Paul Kramer whom I worked with on microfabrication processes. I wish to acknowledge Steven Alexandre Schenk for his suggestions and discussions we had.

Abstract

Hydrogen production through water electrolysis is a clean option for storing energy from renewable sources. Low-cost hydrogen production requires efficient water electrolyzers that can produce pure hydrogen at high production throughputs. Membrane-less electrolyzers are promising technologies for hydrogen production due to their simple design, low ionic resistance, and adaptability to various working conditions. The fluidic flow keeps hydrogen and oxygen bubbles from each other in these electrolyzers. Bubbles' motion in these electrolyzers affects product purity and electrochemical performance. Therefore, a thorough understanding of the two-phase flow is needed to improve the performance of membrane-less electrolyzers.

In this thesis, we explore the effects of different parameters on the bubbles' trajectory and present methods to enhance the performance of the membrane-less electrolyzers. In the first step, we study the bubble motion in rectangular microchannels. The results indicate that the Reynolds number, Capillary number, Bubble diameter, and channel aspect ratio determine the bubble lateral equilibrium position in the channel. These four parameters together can be modified to control the final equilibrium position of a bubble in a rectangular channel.

In the next step, we study the effect of bubble nucleation and interaction on the bubble cross over in membrane-less electrolyzers. We find that the large bubble detachment from the surface of the electrode and the bubble coalescence are two phenomena that lead to the bubble cross over. This problem can be resolved by increasing the flow velocity in order to detach bubbles at a smaller diameter and remove them faster from the channel. However, the energy loss due to the fluidic flow increases with the flow velocity. We showed that the bubbles become smaller without increasing the flow velocity by adding a surfactant to the electrolyte. A surfactant reduces the bubble detachment size and prevents the bubble coalescence. Furthermore, a surfactant can decrease overpotentials by reducing the residence time of bubbles on the surface of the electrode.

We use the results of the two-phase flow studies to design the porous wall electrolyzer as a new design for membrane-less electrolyzers. This design is optimized for high throughput production of hydrogen with low cross over. The porous wall electrolyzer has a significantly smaller cross over compared to membrane-less electrolyzers with parallel electrodes. The porous wall electrolyzer operates at the current density of 300 mA/cm^2 with $0.11 \pm 0.05\%$ hydrogen cross over to the oxygen side.

Finally, we develop a method for the measurement of fluidic properties. This method uses neural networks and images of two-phase flows to measure flow conditions such as flow rate and fluidic properties such as concentration. This measurement technique can be used for controlling two-phase flows in the membrane-less electrolyzers in order to prevent bubble cross over.

Keywords: Membrane-less electrolyzers, Inertial microfluidics, Surfactant, Bubble nucleation and coalescence, Two-phase flow

Résumé

La production d'hydrogène par électrolyse de l'eau est une option propre pour stocker de l'énergie de sources renouvelables. La production à bas prix d'hydrogène requiert des électrolyseurs efficaces qui peuvent produire de l'hydrogène pur avec un rendement élevé. Les électrolyseurs sans membrane constituent une technologie prometteuse car elles possèdent un design simple, une faible résistance ionique et peuvent s'adapter à différentes conditions de fonctionnement. Le flux fluïdique permet de garder les bulles d'hydrogène et d'oxygène les unes à l'écart des autres dans l'électrolyseur. Le mouvement des bulles dans ce dernier affecte la pureté de l'hydrogène produit et la performance électrochimique. Ainsi, il est indispensable de bien comprendre la mécanique d'un flux composé de deux phases pour améliorer la performance de ces électrolyseurs sans membrane.

Dans cette thèse, nous nous attacherons à explorer les différents paramètres influençant la trajectoire des bulles, puis nous présenterons des méthodes pour améliorer la performance d'un électrolyseur sans membrane. Premièrement, nous étudions le mouvement des bulles dans des micro-canaux rectangulaires. Les résultats montrent que le nombre de Reynolds, le coefficient de Capillarité, le diamètre des bulles et le ratio de la section rectangulaire du canal influencent la position d'équilibre dans le canal. Nous pouvons contrôler ces quatre paramètres pour choisir la position d'équilibre des bulles dans le canal rectangulaire.

Nous étudions ensuite la création des bulles et l'effet de croisement entre les bulles au sein d'un électrolyseur sans membrane. Nos recherches permettent de montrer que le détachement des bulles de la surface de l'électrode et la fusion de bulles sont deux phénomènes entraînant le croisement des bulles d'hydrogène et d'oxygène dans le canal. Nous pouvons résoudre ce problème en augmentant la vitesse du flux dans le but de créer des bulles de plus faible diamètre et de les évacuer plus vite du canal. Cependant, la perte d'énergie augmente avec la vitesse à cause des frottements du fluïde. Nous avons donc montré qu'il est possible de diminuer le diamètre des bulles en ajoutant un surfactant à l'électrolyte. Ce dernier permet de réduire la taille des bulles et évite leur fusion. L'usage d'un surfactant diminue enfin les sur-potentiels en réduisant le temps durant lequel les bulles sont à la surface de l'électrode.

L'analyse des flux biphasés a permis de concevoir la paroi poreuse de ce nouveau type d'électrolyseur sans membrane. Ce design est optimisé pour permettre une production à un rythme élevé d'hydrogène, avec un faible taux de croisement entre les bulles. La paroi poreuse de l'électrolyseur permet de diminuer les collisions entre les bulles de manière significative par rapport à un électrolyseur sans membrane avec des électrodes parallèles. La paroi poreuse de l'électrolyseur délivre une densité de courant de 300 mA/cm^2 , ce qui permet d'avoir seulement $0.11 \pm 0.05\%$ des bulles d'hydrogène qui passent du côté de l'électrode de l'oxygène.

Finalement, nous avons développé une méthode de mesure des propriétés des fluïdes. Cette méthode utilise des réseaux de neurones et des images de flux biphasés afin de mesurer les propriétés du flux, telles que la concentration. Cette technique de mesure peut être utilisée pour contrôler les flux biphasés dans l'électrolyseur sans membrane dans le but d'éviter que les bulles ne se mélangent.

Mots-clés : électrolyseur sans membrane, micro fluidique inertielle, Surfactant, formation et fusion de bulles, flux biphasé

Contents

Acknowledgment	VII
Abstract	IX
Résumé.....	XI
Contents	XIII
Table of figures	XVII
Table of tables.....	XXVII
Chapter 1	1
Introduction	1
Chapter 2.....	7
Inertial manipulation of bubbles in rectangular microfluidic channels.....	7
2.1 Introduction	8
2.2 Experimental set-up.....	10
2.3 Numerical simulation	12
2.4 Validation of simulations.....	14
2.5 Results	15
2.6 Conclusion.....	24
Chapter 3.....	25
The impact of surfactants on the inertial separation of bubbles in microfluidic electrolyzers	25
3.1 Introduction	25
3.2 Methods	26
3.3 Forces acting on the bubble	29
3.4 Results and discussion	31
3.5 Conclusion.....	42
Chapter 4.....	45
Membrane-less electrolyzer with porous walls for high throughput and pure hydrogen production.....	45
4.1 Introduction	45
4.2 Procedures	48
4.3 Results and discussion	49
4.4 Conclusion	60
Chapter 5.....	61

Learning from droplet flows in microfluidic channels using deep neural networks.....	61
5.1 Introduction	61
5.2 Methods	63
5.3 Results	64
5.4 Conclusion.....	67
Chapter 6.....	69
Conclusion.....	69
Appendix A.....	73
Inertial manipulation of bubbles in rectangular microfluidic channels.....	73
A.1 Microfabrication	73
A.2 Numerical simulations for different grid sizes	74
A.3 Equilibrium position of the bubble in the rectangular channel.....	75
A.4 Equilibrium position of the bubble in the rectangular channel.....	76
A.5 Experimental results for the effect of Reynolds number on the bubble position	77
A.6 Shear rate at the channel cross section	78
A.7 Effect of the surfactant.....	79
Appendix B	81
The impact of surfactants on the inertial separation of bubbles in microfluidic electrolyzers	81
B.1 Microfabrication	81
B.2 Image processing and bubble detection	82
B.3 Forces acting on the bubble at the detachment	86
B.4 Electrolyte properties and the flow rates	90
B.5 Power loss due to fluidic resistance	91
B.6 Hydrogen and oxygen bubbles radius at different Reynolds numbers	93
B.7 The origin of crossed bubbles	95
Appendix C	97
Membrane-less electrolyzer with porous walls for high throughput and pure hydrogen production.....	97
C1. Effect of wall pores angle and size	97
C2. Membrane-less electrolyzers	98
C3. Microfabrication	99
Appendix D.....	101
Learning from droplet flows in microfluidic channels using deep neural networks.....	101
D.1 Image preparation for the neural network	101

D.2 Neural Network Structure.....	102
D.3 Flow pattern.....	103
D.4 Concentration prediction using six networks and one image input.....	104
D.5 Concentration prediction using six networks and one image input.....	105
D.6 Results of the repeated experiment for the concentration measurement.....	106
D.7 Comparison between a clustering algorithm (nearest neighbor) classification and neural network classification.....	107
References.....	109

List of figures

Figure 1. The energy from renewable sources can replace the energy from fossil fuels. Furthermore, the excess energy from renewables can be stored in the form of hydrogen. Hydrogen can be used in industries, transportation, and energy production for domestic usage. 1

Figure 2. Hydrogen production technologies: 96 % of hydrogen is being produced by using fossil fuels. These processes produce CO₂. 4 % of hydrogen comes from water electrolysis which does not produce any pollutants. 2

Figure 3. Different types of water electrolyzers: a. Alkaline electrolyzer, b. Proton exchange membrane electrolyzer, and c. Membrane-less electrolyzer. 3

Figure 4. At low production rates, the electrode's surface coverage by bubbles is small and the bubbles do not interact. Therefore, the flow can separate the streams of bubbles effectively. The bubbles start to interact at high production rates which leads to gas cross-contamination. Furthermore, the nucleating bubbles cover the surface of the electrodes and induces overpotentials. 5

Figure 5. Forces acting on the bubble: a wall-induced lift directing towards the centerline which diminishes as the bubble moves away from the wall, a shear gradient lift that pushes the bubble towards the wall, a deformation-induced lift pointing towards the centerline which gets stronger as the bubble deformation increases. 9

Figure 6. Microfluidic device showing (a) a schematic representation of the channel geometry, (b) a photograph of the fabricated device, (b) an image of the bubble formation at the T-junction, and (d) a cross-sectional representation depicting how the radius of the bubble, r , and the bubble distance from the wall, dY , are measured at 6 mm downstream of the T-junction. (e) Experimental setup: the liquid is injected with a syringe pump and a constant pressure pump is used to introduce the gas phase into the device. Motion of bubbles is recorded with a high speed camera in the reflection mode. 11

Figure 7. Computational setup: (a) The computational mesh used in the numerical simulation. (b) In the streamwise direction, the reference frame is put on the bubble. Hence a velocity shift of U_{bubble} in the $-ex$ direction is applied on both the walls and the inlet boundary. (c) The streamwise velocity at different cross sections of the duct when the bubble reaches to its equilibrium position. (d) The time evolution of bubble velocity indicates that the bubble reaches its equilibrium position. (e) The volume of the bubble is monitored to guarantee its time invariance. The bubble's lateral position (f) and velocity profile around the bubble (g) are extracted from the equilibrium solution. 14

Figure 8. Effect of Re on the lateral position of the bubble: Experimental results and the corresponding numerical simulations are for the channel with 50 μm width and 50 μm . The bubble diameter is normalized by the channel width. By increasing the Re , the bubble moves gradually towards the wall. 16

Figure 9. Simulation results of Reynolds number's effect on the lateral position of a bubble in a square channel. The blue points and the red points show the equilibrium position of the bubble in the horizontal and vertical direction, respectively. All the simulations are carried out for $D = 0.4$ and $Ca = 0.1$. The initial bubble position is at $(Y,Z) = (0.7667,0.6)$ 17

Figure 10. Effect of the Ca on the bubble position for the square channel: The carrier fluid in the first row is isopropanol and in the second row is ethanol. Ca has a smaller value when the carrier fluid is ethanol and as a result, the bubble is closer to the wall. As the Ca increases, the bubble moves further away from the wall. The channel's cross sectional dimensions in the experiments is $50 \mu m$ by $50 \mu m$. Numerical simulations, corresponding to the same parameter, support the experimental results. The color bar shows the velocity in the flow direction which is normalized with the centerline velocity. 18

Figure 11. Simulation results for the square channel at different Ca , while the Re and D are constant. The initial position of the bubble is $Y, Z = (0.7667,0.6)$. The blue points and the red points show the equilibrium position of the bubble in the horizontal and vertical direction, respectively. As the Ca number increases the bubble gets closer to the center and at $Ca > 0.9$ the bubble moves exactly to the center. 18

Figure 12. Effect of bubble's radius on the equilibrium position: experimental results for a channel with $50 \mu m$ width and $50 \mu m$ depth are compared with the corresponding simulations in color. The color map shows the normalized velocity of the flow in x-direction. The results show that the equilibrium position of larger bubbles is closer to the centerline than smaller bubbles. 19

Figure 13. Numerical simulations of different bubble diameters for the square channel at constant $Re = 10$ and $Ca = 0.1$. The initial position of the bubble is at $(Y, Z) = (0.7667,0.6)$. The equilibrium position of a bubble that is smaller than half of the channel is close to the wall. A bubble larger than half of the channel moves along the diagonal of the channel and by increasing the diameter of the bubble, it eventually moves to the center of the channel. 20

Figure 14. Effect of the channel geometry on the lateral position of the bubble while the Re and Ca are constant. Experimental and numerical results show that in the wider channels, the bubble equilibrium position is close to the smaller edge while in the channel with aspect ratio of one the bubble equilibrium position is in the center..... 21

Figure 15. Experimental results for three different channel aspect ratios when the carrier fluid is isopropanol. The vertical axis and horizontal axis show the bubble position and Reynolds number, respectively and the color map indicates the radius of the bubble in μm . In these diagrams, $Y = 1$ corresponds to the bubble position at the centerline and $Y = 0$ to the bubble position close to the wall. In the square channel, the bubbles are in the center of the channel or the wall based on their diameters, but in the rectangular channels, the equilibrium positions of the bubbles are closer to the smaller sidewall..... 22

Figure 16. Experimental results that show different equilibrium position of bubbles and particles: addition of a small amount of surfactant forces the bubble to behave like a particle. At the same flow rate, the equilibrium position of contaminated bubbles and solid particles are at the center of the wider channel while clean bubbles stay close to the shallower wall. 23

Figure 17. Schematic of the equilibrium position of a bubble in a clean carrier fluid (left), a bubble in a carrier fluid with surfactant (middle), and a solid particle (right). Different circles show the position of circles at different times (\times marks the initial position). The clean bubble goes to the center in the Z direction and moves towards the shallower wall. The solid particle and contaminated bubble move towards the center of the wider channel and stay centered in the Y direction..... 23

Figure 18. Simulation results for the equilibrium position of a bubble with $D = 0.4$ and initial position of $Y, Z = (0.7667, 0.6)$ in the channel at different Re and Ca..... 24

Figure 19. a. Schematic representation of the microfluidic device with two sets of small electrodes, b. a picture of the fabricated device, c. instances of bubble generation at the first and the second set of electrodes and the bubble motion at the end of the channel. There are three finger electrodes at each set of electrodes in order to consider the bubble coalescence and interaction during the bubble growth. The bubbles detached from the first set of electrodes interact and coalesce with the bubbles of the second set. This coalescence and interaction affect the bubble detachment size at the second set of electrodes. 29

Figure 20. The important forces acting on the bubble: a. before the bubble detachment and b. after the bubble detachment. a. The forces that contribute to the bubble detachment are the shear lift force (F_{SL}), the contact pressure force (F_{CP}), and the drag force (FD). The surface tension force ($F\sigma$) prohibits the bubble detachment. b. The balance of forces acting on a moving bubble in a channel determines the bubble equilibrium position. The deformation induced lift force (F_{DI}) and the wall lift force (F_w) push the bubble towards the centerline. The shear gradient lift force (F_{SG}) pushes the bubble towards the wall. 30

Figure 21. Images of bubbles at the end of the channel at different Re and two different currents using 0.5M sulfuric acid as the electrolyte. The small bubbles move to the sidewalls by increasing the Re. However, the high Re of 42 cannot keep large bubbles at the sidewalls. At the Re of 62, the bubbles are at the sidewalls because the flow detaches the bubbles at smaller sizes. The large bubble at Re=10 does not have a spherical shape because it has a larger diameter than the depth of the channel and its boundaries are in contact with the channel walls. Furthermore, a non-spherical shape can happen when bubbles coalesce where the interface of the bubble deviates from the spherical shape for a short period of time. The scale bar is $100\mu m$ 32

Figure 22. a. The bubble detachment radius at different Re. The blue and red curves show the experimental bubble detachment radius at two different currents. The black line is the detachment bubble radius predicted by solving Eq. 1. The bubble radius shows the average radius of hydrogen and oxygen bubbles together. b. The bubble detachment radius at the second set of electrodes at Re=42 and different currents. The bubble detachment size at the second set of electrodes is larger when the first set of electrodes is active. This is due to the coalescence of the bubbles at the second set of electrodes with the bubbles coming from the first set of electrodes. 33

Figure 23. The histograms of bubbles volume distribution across the width of the channel width at Re from 10 to 62 and at two different currents of $5\mu A$ and $10\mu A$: The purple bars show the volume of the bubbles that their boundaries crossed the channel centerline, the orange bars

show the volume of hydrogen bubbles, and the green bars show the volume of the oxygen bubbles. The liquid flow pushes the bubbles to the sidewalls and the distance between the stream of bubbles increases by the Re. At Re=62 the two streams are separated since the radii of the bubbles are small and no large bubbles are formed. The position of bubbles is normalized to half of the channel width. Zero on the x-axis represents the channel centerline. V_{max} and r represent the volume used to normalize the volume and the average bubble radius, respectively. 34

Figure 24. Bubbles generation and flow in 0.5 M sulfuric acid at Re=62 and currents from 80 μA to 120 μA . Top images show instances of bubble motion at the end of the channel and bottom histograms show the corresponding volume distribution of bubbles. The cross contamination starts at the current equal to 100 μA . The scale bar is 100 μm 35

Figure 25. Images of bubbles motion at the end of microchannel using 0.5 M sulfuric acid at three different concentrations of Triton X-100. At $C^* = 6$, most bubbles are flowing in the center of the channel and increasing the Re to 62 cannot push the bubbles to the sidewalls. At higher concentrations of surfactant, the bubbles become smaller and move close to the wall. At $C^* = 50$, the two bubbles streams are completely separated from each other. The applied current is 5 μA . The scale bar is 100 μm 36

Figure 26. Bubbles volume distribution at the end of the channel at three different concentration of surfactant in 0.5 M sulfuric acid. At $C^* = 6$, the bubbles detach at large radii. The equilibrium position of these bubbles is at the center of the channel which is not desired. The histograms of $C^* = 25$ and $C^* = 50$ show that increasing the surfactant concentration leads to the flow of smaller bubbles in the channel. The flow can efficiently separate these small oxygen and hydrogen bubbles. 37

Figure 27. The diagram shows the change in the bubble radius in the clean electrolyte and the electrolyte with three different concentrations of surfactant. The applied current is 5 μA 38

Figure 28. a. The radius of bubbles is plotted against the position in the channel (x) for an electrolyte with and without the surfactant. The bubble radius stays constant in an electrolyte with the surfactant since the bubble coalescence is inhibited in the presence of surfactants. b. The diagrams show the volume distribution of bubbles at different positions of the channel in an electrolyte with and without surfactant. x determines the position in the channel where $x = 3.5 mm$ is the position of the first set of electrodes, $x = 7.5 mm$ is the position of the second set of electrodes, and $x = 16 mm$ is the end of the channel. The Re is 62 and the applied current is 10 μA 39

Figure 29. Bubbles generation and motion in the microchannel in 0.5 M sulfuric acid with triton X-100 at $C^* = 50$. Part a. shows the complete product separation in an electrolyte with surfactant that is achieved at smaller Re compared to the surfactant-free electrolyte. Part b. shows that the production rate can be increased with effective product separation using the electrolyte with the surfactant. There are more bubbles at a higher production rate and they spread in a wider area in the channel. Therefore, the distribution of hydrogen and oxygen bubbles is wider in the right histograms. The scale bar is 100 μm 40

Figure 30. The diagrams show the cross over percentage in the 0.5 M sulfuric acid and the 0.5 M sulfuric acid with Triton X-100 at $C^* = 50$ at different Re and currents. In the 0.5 M sulfuric

acid, the cross over is small only at high Re and small currents. In the 0.5 M sulfuric acid with Triton X-100 at $C^* = 50$, the cross over is small (below 4%) over the range of Re and currents shown in the diagram. This diagram indicates the importance of adding surfactant to the electrolyte for effective product separation. 40

Figure 31. The images of the bubble nucleation at the current of 800 nA in the 0.5 M sulfuric acid without and with surfactant. The Re is 62. In the clean electrolyte, initially, the bubble grows and then reaches an equilibrium where the amount of gas that is being produced and introduced to the bubble becomes equal to the amount of the gas that is being dissolved in the electrolyte. In this case, the bubble covers the surface of the electrode which increases the ohmic resistance between the electrodes. In the electrolyte with the surfactant, bubbles detach faster and at small sizes. Therefore, the electrode surface remains free for the reaction. 41

Figure 32. a. The current-potential curve of the water electrolysis in a 0.5 M sulfuric acid with and without the surfactant in the microchannel at Re=62. b. PEIS measurement of 0.5 M sulfuric acid and 0.5 M sulfuric acid with surfactant using platinum wires placed at a constant distance from each other. In the PEIS measurement, the applied potential and the sinus amplitude are 2.0 V and 20 mV, respectively. The water splitting starts at the same voltage in both electrolytes and both electrolytes have the same solution resistance. Initially, the current is higher in the surfactant-free electrolyte than the electrolyte with surfactant due to the adsorption of Triton X-100 on the electrode surface. However, by increasing the production rate, the surfactant-free electrolyte diagram becomes noisy due to the long residence time of the bubbles on the electrode. This issue is not present in the electrolyte with the surfactant since the bubbles are detaching fast and their residence time on the electrode is short. 42

Figure 33. Schematics of membrane-less electrolyzers geometries: a. Parallel electrodes electrolyzer: This electrolyzer has two solid parallel catalysts. The bubbles evolve and flow between the parallel electrodes. b. Mesh electrodes electrolyzer: The electrolyte enters the space between two mesh catalysts. The electrolyte flows through the meshes and removes the generated bubbles in the meshes. c. Porous walls electrolyzer: Bubbles are being generated at the electrodes in the outer channels. The porous wall and the liquid flow prevent the bubble cross over. The bubbles are not flowing between the electrodes in this design. Therefore, it has a smaller overpotential due to the movement of bubbles compared to mesh electrodes and parallel electrodes electrolyzers. 47

Figure 34. Bubbles generation and flow at different locations in the PE electrolyzer working with 1 M H₂SO₄: a. The image shows the fabricated PE electrolyzer. Solid lines indicate the walls of the PE electrolyzer. This image is constructed by placing images of three different positions of the device next to each other. b. The applied current density is 300 mA/cm². The large bubbles are the primary cause of gas cross over since they are moving to the channel centerline. The bubbles become smaller by increasing the Re as the flow removes the bubbles faster from the channel. c. The bubbles are smaller at a lower current density of $j = 75 \text{ mA/cm}^2$. Thus, the gas cross-over is smaller at lower current densities. 50

Figure 35. Pictures of different regions of the PE electrolyzer working with 1 M H₂SO₄ + 10 – 4 M PFOS surfactant: The bubbles detach at smaller sizes at higher Re. The surfactant reduces the bubble detachment size by reducing the surface tension. Moreover, the surfactant inhibits the bubble coalescence. For this reason, the flowing bubbles are smaller in the electrolyte with

the surfactant compared to the surfactant-free electrolyte. Thus, product separation is more effective by using a surfactant. The applied current density is 300 mA/cm^2 51

Figure 36. a. Polarization curve of the PE electrolyzer working with $1 \text{ M H}_2\text{SO}_4$ with and without the PFOS surfactant: The surfactant reduces the electrode surface coverage by bubbles. Besides, the hydrogen evolution reaction has lower overpotential due to the decrease in the hydrogen solubility in the electrolyte with PFOS. Thus, the PFOS surfactant improves the electrochemical performance of the PE electrolyzer. b. Hydrogen cross over to the oxygen side at different Re : The flammability limit is shown by a dashed line. The cross over is inversely proportional to the Re . The cross over is less than the flammability limit in the surfactant-free electrolyte at $Re=109$ and $j = 75 \text{ mA/cm}^2$. However, the cross over of the PE electrolyzer is not safe by increasing the current density to 300 mA/cm^2 in the surfactant-free electrolyte. The PE electrolyzer can operate with a secure cross over by adding the PFOS surfactant to the electrolyte. 52

Figure 37. Geometry optimization of the PW electrolyzer: a. The design and boundary conditions are shown at four steps of geometry optimization. The length of wall pores is $100 \mu\text{m}$ in geometry 1. The length of wall pores is increased to $200 \mu\text{m}$ in geometry 2 to reduce the gas cross over. Afterwards, the porous walls are rotated by 0.75° in geometry 3 to have equal velocities in the wall pores. The wall pores angle with the horizontal line is 45° in geometry 4 to suppress the gas cross over completely. The contours are the water volume fraction at $t = 0.2 \text{ s}$. Hydrogen and oxygen bubbles enter the left and right channels, respectively. b. The velocity distribution at wall pores: The velocity distribution is uniform in geometries 3 and 4 thanks to the inclined porous walls. c. Average water volume fraction at porous walls and channel centerline: Water volume fraction below one at the centerline indicates gas cross over. 54

Figure 38. a. Picture of the fabricated PW electrolyzer: This picture is constructed by capturing images from different parts of the device. b. Pictures of the bubble generation and flow in the PW electrolyzer at $j = 300 \text{ mA/cm}^2$ and various Re : The porous walls keep the hydrogen and oxygen bubbles separated. This device is less vulnerable to the large bubble formation since these bubbles cannot go through the wall pores. Some small bubbles move to the middle channel and coalesce. They form a large bubble in the middle channel that cannot go through the pores. This bubble grows until the device reaches the steady-state. The final size of this bubble decreases by increasing the Re . There is no bubble in the middle channel at $Re=109$ since the flow does not allow bubbles migration to the middle channel. 56

Figure 39. Effect of PFOS surfactant on the bubble generation and flow in the PW electrolyzer working with $1 \text{ M H}_2\text{SO}_4 + 10^{-4} \text{ M PFOS}$. a. Images show the bubble generation and flow at different Re and $j = 300 \text{ mA/cm}^2$. The addition of PFOS to the electrolyte reduces the size of bubbles. There is no bubble in the middle channel in the electrolyte with surfactant at low Re . Moreover, energy losses are smaller since the wall pores as ion-conducting pathways are free from the bubbles. b. Current density of 450 mA/cm^2 is achieved without cross over using PFOS surfactant and the PW electrolyzer design. 57

Figure 40. a. Polarization curve of the PW electrolyzer: The electrode surface coverage by bubbles is smaller and the wall pores are not blocked by the bubbles in the presence of PFOS. As a result, the electrochemical performance improves by adding PFOS to the electrolyte. b.

The gas cross over is less than the flammability limit in the surfactant-free electrolyte at $Re \geq 54$. The cross over decreases further by adding the PFOS surfactant to the electrolyte. A comparison of this figure with Figure 36b shows that the cross over is significantly smaller in the PW electrolyzer than the cross over in the PE electrolyzer. c. The working potential at a constant current density of 300 mA/cm^2 : The bars indicate the standard deviation of the potential. More active area is available at higher Re due to the smaller surface coverage by the bubbles. Therefore, the overpotentials and the potential oscillations decrease by increasing the Re . Furthermore, the PFOS surfactant reduces the residence time of bubbles on the electrode surface which reduces overpotential. 58

Figure 41. The cross over, Re , and current density of membrane-less electrolyzers [20, 21, 77, 88, 89, 136, 141]: The PW electrolyzer requires smaller Re to achieve hydrogen cross over as small as the other membrane-less electrolyzers. The color bar depicts the maximum current density at which the membrane-less electrolyzers are performing water electrolysis. The PW electrolyzer is represented by PWE. The data of the points are presented in Figure 68 of Appendix C. 59

Figure 42. Using neural networks to measure fluidic properties from droplet flow patterns: (a) Schematic of the microfluidic channels (depth is $30 \mu\text{m}$), (b) Image of droplet generation. Oil flows from the side channels and the water-IPA flows from the middle channel. (c) The two-phase pattern of the droplet generation in a microfluidic device contains information about the fluid and the flow properties. Neural networks are used to extract these properties while the main process stays intact. 62

Figure 43. Images of droplet generation at different flow rates of the dispersed phase. The dispersed phase is water-IPA at a concentration of 5.5% and the continuous phase is silicone oil. The flow rate of the droplets are shown in the image and the silicone oil flow rate is 2 ml/h. Scale bar is $100 \mu\text{m}$ 64

Figure 44. (a) Flow rate measurement: the measured results are compared with the true values for a water-IPA concentration of 5.5%. The red points are the flow rates for which the network is trained and the blue points are the new flow rates. Error bars show the standard deviation of the predicted values. (b) Examples of the flow regime transitions that occur at 0.45 ml/h and 1.45 ml/h flow rate of water-IPA. Silicone oil flow rate is 2 ml/h. The scale bar is $100 \mu\text{m}$. . 65

Figure 45. Images of droplet generation at different concentrations of the water-IPA solution where the concentration of the water-IPA solution is changing from 4.0% to 7.0% with 0.5% increment. The water-IPA and the oil flow rates are 0.2 ml/h and 1.0 ml/h, respectively. The scale bar is $100 \mu\text{m}$ 65

Figure 46. Predicted concentration by the DNN is compared to the true values. (a) Concentration prediction results using one DNN, and (b) concentration prediction results using six DNNs. The red points are the concentrations that the network is trained with and the blue points are the new concentrations. Bars show the standard deviation for each case. 66

Figure 47. Additive manufacturing can be used to fabricate different parts of membrane-less electrolyzers at different scales [146]. 71

Figure 48. The neural network can monitor different measurement and control the electrochemical performance and product separation. The red rectangles are the regions that the neural network can monitor: the bubble coalescence in the fluidic channel, the sudden increase in the applied potential, and detection of hydrogen in the oxygen stream in the gas chromatograph (GC) measurement. The network can prevent the gas cross over or the increase in the input power by changing the applied current and liquid flow rate. 72

Figure 49. Microfabrication process flow..... 73

Figure 50. Diagrams of the bubble position with the error bars representing the standard deviation from the average value..... 75

Figure 51. Diagrams of the bubble position with the error bars representing the standard deviation from the average value..... 76

Figure 52. Effect of the Reynolds number on the bubble position in the square channel ($50\ \mu\text{m}$ width and depth). The continuous phase is ethanol and the error bars represent the standard deviation from the average value. $Y = 1$ corresponds to the bubble position at the centerline and $Y = 0$ corresponds to the bubble position at the wall. The diameter of the bubbles D are between 0.6276 and 0.6874..... 77

Figure 53. Shear rate at the channel cross section: Center of the channel has the smallest value of the shear rate. Also, diagonals have a smaller shear rate in comparison with the center of sidewalls. The simulation is done for $Re = 10$ in a square channel. The boundary conditions at the inlet and outlet are inlet velocity and outlet pressure, respectively. 78

Figure 54. Effect of different Triton-X concentration on the bubble position in a channel with $150\ \mu\text{m}$ width and $50\ \mu\text{m}$ depth. Since the concentration of the surfactant is enough to cover the interface of the bubble and the liquid, there is no difference between the different concentrations. 79

Figure 55. Effect of surfactant on the equilibrium position of a solid particle in a rectangular channel ($150\ \mu\text{m}$ width and $50\ \mu\text{m}$ depth). The equilibrium position of the solid particle does not change by adding the surfactant to the carrier phase. Water+Triton=X liquid is 1% volumetric aqueous solution of Triton-X..... 79

Figure 56. Fabrication process of the microchannels with small nucleation sites..... 81

Figure 57. Picture of the fabricated electrodes at the bottom of the fluidic channel: the tip of the electrodes has a $6\ \mu\text{m}$ diameter..... 81

Figure 58. Schematic of the channel design: The red squares determine the regions used to capture videos of bubbles motion. The aspect ratios are not to scale. 82

Figure 59. The histograms of bubbles volume distribution at two different sampling time and same conditions in $0.5\ \text{M}\ \text{H}_2\text{SO}_4$: 20 s videos are captured at 50 fps and 1/10000 s shutter speed. 12 s videos are captured at 500 fps and 1/10000 s shutter speed..... 83

Figure 60. Bubbles detection process: initially the noises of the images are removed using fastNIMeansDenoisingColored command. Afterwards, the images are converted to gray scale

and a median blur filter is applied in order to highlight the circles. Finally, the bubbles are detected using HoughCircles command..... 84

Figure 61. a. The advancing and receding contact angles are shown in the picture. b. The contact angle of the bubbles is measured using the image of bubble generation at $Re=62$ and current= 800 nA 88

Figure 62. a. The diagram shows the bubble generation frequency against current at $Re=62$. b. and c. show the bubble generation frequency at different Re and shear rates at current= $10\text{ }\mu\text{A}$. The bubble generation frequency increases linearly by the current but it increases non-linearly by the Re and the shear rate. 89

Figure 63. The power loss due to the fluidic resistance as a function of Reynolds number: The power loss increases non-linearly as the Re increases..... 92

Figure 64. The average radius of the oxygen and hydrogen bubbles in the electrolyte with different concentration of surfactant at the applied current of $10\text{ }\mu\text{A}$. The bubbles radii decrease as the surfactant concentration increases. Furthermore, the bubbles detach at smaller sizes by increasing the Re 93

Figure 65. The radius of oxygen and hydrogen bubbles at different surfactant concentrations, currents, and Reynolds numbers. Only separated bubbles are considered in these diagrams and the bubbles that are in the channel centerline are not used in the measurements. The bubbles radii decrease as the concentration of the surfactant increases and/or the Re increases..... 94

Figure 66. The origin of crossed bubbles at different Re and currents: the percentage is calculated by dividing the volume of bubbles based on their origin by the total volume of generated bubbles. The coalesced bubbles in the $0.5\text{ M H}_2\text{SO}_4$ are the mixture of hydrogen and oxygen bubbles. These bubbles are reported with a separate percentage since it is not possible to determine accurately the exact percentage of hydrogen and oxygen. Furthermore, the bubbles that are moving at the channel center in the $0.5\text{ M H}_2\text{SO}_4$ at $C^*=50$ are reported separately as their origin cannot be determined. The summation of the three percentages at each Re and current is the value reported in Figure 29 in the main text. 95

Figure 67. a. Changing the wall pores angle from 30° to 60° does not affect the velocity distribution in the pores or the water volume fraction in the middle channel. b. The velocity distribution in the pores remains uniform across the pores and the water volume fraction in the middle channel does not decrease when the pore size increases from $80\text{ }\mu\text{m}$ to $160\text{ }\mu\text{m}$ 97

Figure 68. The current density (a), cross over (b), Re (c), and interelectrode distance (d) of membrane-less electrolyzers shown in Figure 41..... 98

Figure 69. Fabrication process of the porous walls electrolyzer 99

Figure 70. Image processing procedure: 1. cropped image from the experiment, 2. Applying denoising algorithm to remove the noise in the image, 3. Result of edge detection algorithm in detecting droplets boundaries. 101

Figure 71. The structure of the convolutional neural networks: (a) A classifier network with two convolutional layers and two fully connected layers is used to classify the images based

on their concentrations. The convolutional filters are 5×5 and there is a max pooling layer after each convolutional layer. A dropout layer is used before the last layer. (b) A regression neural network is implemented to predict the concentration of the inputs. This network consists of three convolutional layers followed by a fully connected layer. There is a max pooling layer after each convolutional layer and a dropout layer after the fully connected layer. 102

Figure 72. Flow pattern of droplet flows: (a) 4.0% water-IPA concentration. (b) 7.0% water-IPA concentration. (c) for two different concentrations: The phase transition happens by changing the flow rate or the concentration..... 103

Figure 73. Water-IPA flow rate measurement at silicone oil flow rate of 1.5ml/h. 104

Figure 74. Concentration prediction results using six DNNs and one image input. The red points are the concentrations that the network is trained with and the blue points are the new concentrations. Bars show the standard deviation for each case. 105

Figure 75. The diagram shows the results of applying the proposed method to the repeated experiment for the concentration measurement..... 106

Figure 76. Distribution of the dataset where the number and the radii of the droplets are presented for different concentrations. 107

Figure 77. Droplet images and the features detected by the DNN: 1. The images of the droplet generation from the experiment for small and big droplets at two different concentrations. 2. The results of the edge detection algorithm applied to the images from the experiment. 3. Difference of convolutional layer outputs for two different concentrations: (a) the DNN detects the width of the droplet clusters, (b) the local number density of the droplets are identified as the brighter regions indicate higher number of droplets in one image than the other, (c) the DNN extracts the leading edges of the droplets that represent the number of droplets and their periodicity, (d) the enhanced edges of the boundaries with an emphasis on the liquid jet which is detected by brighter color..... 108

Figure 78. The convergence plot and the cost diagram. The cost function is calculated using cross entropy loss..... 108

List of tables

Table 1. Properties of the liquids used as carrier phase: density and viscosity are given at room temperature and atmospheric pressure, and surface tension is measured using pendant drop method.....	12
Table 2. Bubble equilibrium positions when the carrier fluid is isopropanol.....	15
Table 3. Bubble equilibrium positions when the carrier fluid is ethanol.....	15
Table 4. Numerical simulation of the bubble equilibrium position with different initial position	15
Table 5. Surface tension between air and 0.5 M sulfuric acid at different concentrations of Triton X-100. C^* is the normalized concentration of the surfactant by the CMC.....	28
Table 6. Properties of the fluids used in the simulations	53
Table 7. Numerical simulation results for different grid sizes.....	74
Table 8. The python code for detecting bubbles	84
Table 9. The percentage of detected hydrogen and oxygen bubbles in 0.5 M H_2SO_4 : The total amount of hydrogen and oxygen is calculated by Faraday's laws of electrolysis.	84
Table 10. The volume ratio of the generated oxygen to the generated hydrogen in the 0.5 M H_2SO_4 with and without Triton X-100.....	85
Table 11. Approximate contact angle at different Re	88
Table 12. Flow rates used in this study and the corresponding Re.....	90
Table 13. The dimensions of the fluidic tubes and the microchannel	91

Chapter 1

Introduction

Energy generation from renewable energies has been increasing in recent years while the power generation from fossil fuels has been decreasing [1]. Lowering the carbon emission is the main motivation for the increased interest in renewable energies [2]. The recent decrease in the cost of solar and wind energies is predicted to continue in the future due to technological development [3, 4]. Therefore, the cost of energy from renewable sources is becoming competitive against fossil fuels [5]. However, renewable sources are intermittent. Storing the surplus of energy from renewable sources can resolve this problem. The stored energy can be used when renewable sources are not available [6] as shown in Figure 1. Energy storage in the form of hydrogen has been regarded as one of the primary storage strategies due to the high energy density of hydrogen [7].

Hydrogen energy density per unit mass is higher than any other substance [8] and its combustion does not produce any pollutants. Therefore, it can be used as a clean fuel for transportation [9]. A hydrogen car needs a tank for storing hydrogen and a fuel cell for converting chemical energy to electricity. It should be noted that the volume and weight of these parts are larger than batteries in a small-size vehicle and short-range transportations which makes batteries more cost-efficient for this type of vehicles. On the other hand, fuel cell electric vehicles are more cost efficient than battery electric vehicles for long range transportation or high utilization transport [10]. Therefore, hydrogen fuel cells show great potential to be utilized in trucks and airplanes to have long range mobility at smaller costs and weights.

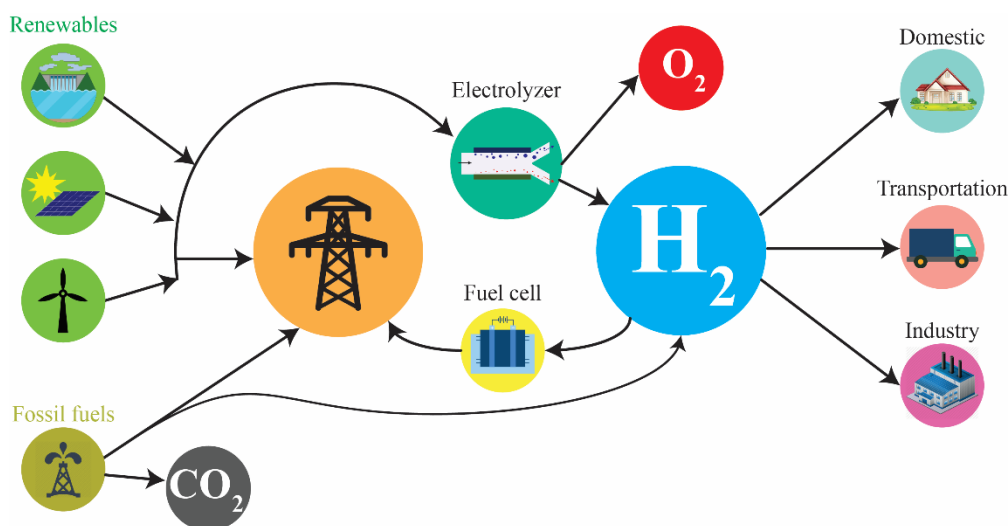


Figure 1. The energy from renewable sources can replace the energy from fossil fuels. Furthermore, the excess energy from renewables can be stored in the form of hydrogen. Hydrogen can be used in industries, transportation, and energy production for domestic usage.

Fossil fuels are the source of 96 % of hydrogen production as shown in Figure 2 [11]. Carbon dioxide is a by-product of the fossil fuel processing for the hydrogen production. The process of energy storage in the form of hydrogen should be carbon-free since lowering the carbon emission is the main goal of utilizing renewable energies. Water electrolysis is a clean hydrogen production method [12]. However, only 4 % of hydrogen is being produced by water electrolysis. The capital and operating costs of the water electrolyzers are challenges for the cost-effective hydrogen generation [13]. There is ongoing research in order to reduce the cost of hydrogen production from water electrolysis. The goal of the research is to enhance the electrolyzers efficiency, product purity, and production throughput.

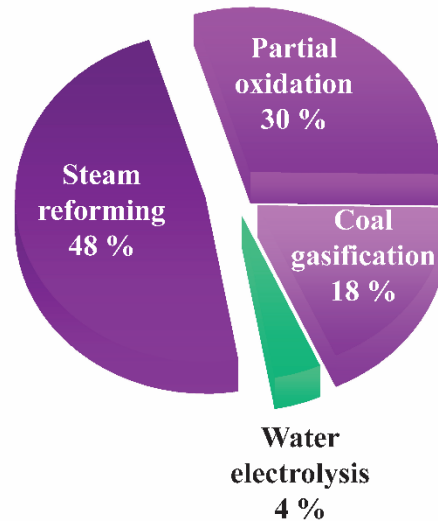
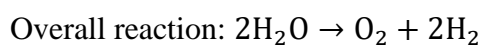
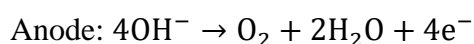


Figure 2. Hydrogen production technologies: 96 % of hydrogen is being produced by using fossil fuels. These processes produce CO₂. 4 % of hydrogen comes from water electrolysis which does not produce any pollutants.

The solubility of hydrogen and oxygen in water is extremely small. The hydrogen and oxygen products appear in the gas form in the water electrolysis reaction. Therefore, most of the electrolyzers use a membrane or a separator between the anode and cathode [14-18]. This membrane prevents the mixing of hydrogen and oxygen. This membrane should be ion conductive for the migration of protons from the anode to the cathode in acidic medium (migration of hydroxide ions from the cathode to the anode in the basic medium). The ion conductive membranes provide ionic pathways and product separation, but its integration in the water electrolyzers brings challenges such as stability, significant Ohmic losses, and increased cost.

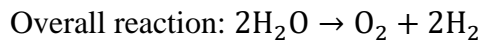
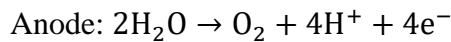
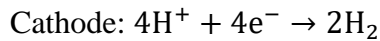
Alkaline electrolyzers [19] and proton exchange membrane (PEM) electrolyzers [14] are two types of commercially available water electrolyzers. These electrolyzers are shown in Figure 3. Alkaline electrolyzers use an alkaline electrolyte such as NaOH or KOH solutions. The water electrolysis reaction in the alkaline solution is:



Alkaline electrolyzers use a separator to prevent the mixing of hydrogen and oxygen bubbles. Furthermore, they use nickel as the catalyst for the electrolysis. These electrolyzers have long

lifetime and low manufacturing cost. However, their production rate is limited due to the ohmic resistance induced by the separator.

PEM electrolyzers utilize Nafion as a membrane which allows the migration of protons while it prevents the gas cross over. Nafion becomes acidic when it is wetted with water. In the acidic electrolyte, water molecules are oxidized at the anode to create oxygen gas and protons. The protons migrate to the cathode and are reduced to produce hydrogen gas. The reactions are:



The membrane in the PEM electrolyzer induces smaller resistance compared to the separator of alkaline electrolyzers. Moreover, PEM electrolyzers have smaller interelectrode distance and higher hydrogen purity compared to alkaline electrolyzer. On the other hand, the manufacturing cost of PEM electrolyzer is high due to the membrane and the usage of noble catalysts. Furthermore, the membrane of PEM electrolyzers need to be replaced every 3 years that reduces the lifetime and adds to the operating costs of these electrolyzers.

a. Alkaline electrolyzer b. PEM electrolyzer c. Membrane-less electrolyzer

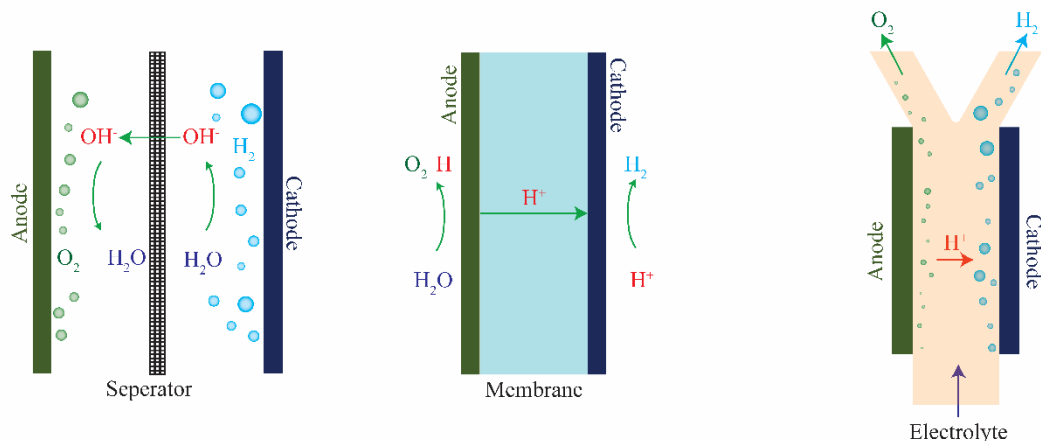


Figure 3. Different types of water electrolyzers: a. Alkaline electrolyzer, b. Proton exchange membrane electrolyzer, and c. Membrane-less electrolyzer

Membrane-less electrolyzers shown in Figure 3c have been proposed to remove the need for the membranes [20]. Eliminating the membrane in these systems reduces the losses caused by membranes, provides versatility in the range of catalysts that can be used, simplifies the design of the electrolyzer, reduces the capital costs, and increases the efficiency of the system [21, 22]. In the membrane-less electrolyzers, the fluidic flow controls the bubbles' motion and prevents the gas cross-contamination.

The liquid flow exerts forces on the bubble that determine the bubble size and lateral position in the fluidic channel [23, 24]. These forces can be tuned by the flow velocity, electrolyte physical properties, and channel geometry in order to control the bubble position and prevent the bubble cross over. Controlling the position of the bubbles leads to better product separation and more pure hydrogen production. Therefore, a thorough understanding of the bubble motion in the channel is necessary for pure hydrogen production.

The amount of hydrogen production in an electrolyzer can be determined by using Faraday's electrochemical laws. These laws can be formulated as below:

$$m = \frac{ItM}{Fz} \quad (1)$$

where I, t, M, F, z, and m are the applied current, time, molar mass of the product, Faraday constant, number of electrons needed for the half-reaction, and mass of the generated product. The amount of hydrogen production is directly proportional to the applied current based on equation 1. The throughput of the electrolyzer can be increased by increasing the current. However, the number of bubbles increases in the electrolyzer channel at higher production rates as shown in Figure 4. The bubble interaction and coalescence increase by increasing the number of flowing bubbles in the channel which leads to bubble cross over. Two-phase flow investigation helps us to control the bubbles' interaction and enhance the throughput of the membrane-less electrolyzers.

The total overpotential loss of a membrane-less electrolyzer can be determined by the following equation [25]:

$$\eta = \eta_{\text{activation}} + \eta_{\text{ohmic}} + \eta_{\text{concentration}} \quad (2)$$

where $\eta_{\text{activation}}$ is the sum of activation overpotential at the anode and cathode, η_{ohmic} is the ohmic loss due to the ions transport in the electrolyte, and $\eta_{\text{concentration}}$ is the concentration overpotential due to the concentration gradients of the reactants at the electrodes. A growing bubble decreases the active area of the electrode. The decrease in the active area increases the activation overpotentials. The residence time and diameter of the bubble increase the activation overpotentials. This overpotential can be decreased using the electrolyte flow for detaching bubbles faster from the electrode.

Bubbles flowing close to the electrode block the ionic pathways. Consequently, the flowing bubbles increase the overpotential due to the ohmic resistance between the electrodes. On the other hand, the concentration overpotential is lower since the concentration of dissolved products is lower in the vicinity of bubbles growing at the surface of the electrolyte. It is possible to detach the bubbles faster and reduce the size of the flowing bubbles by controlling the two-phase flow in the membrane-less electrolyzers. This results in lower overpotentials due to the presence of bubbles and higher efficiency of the electrolyzer.

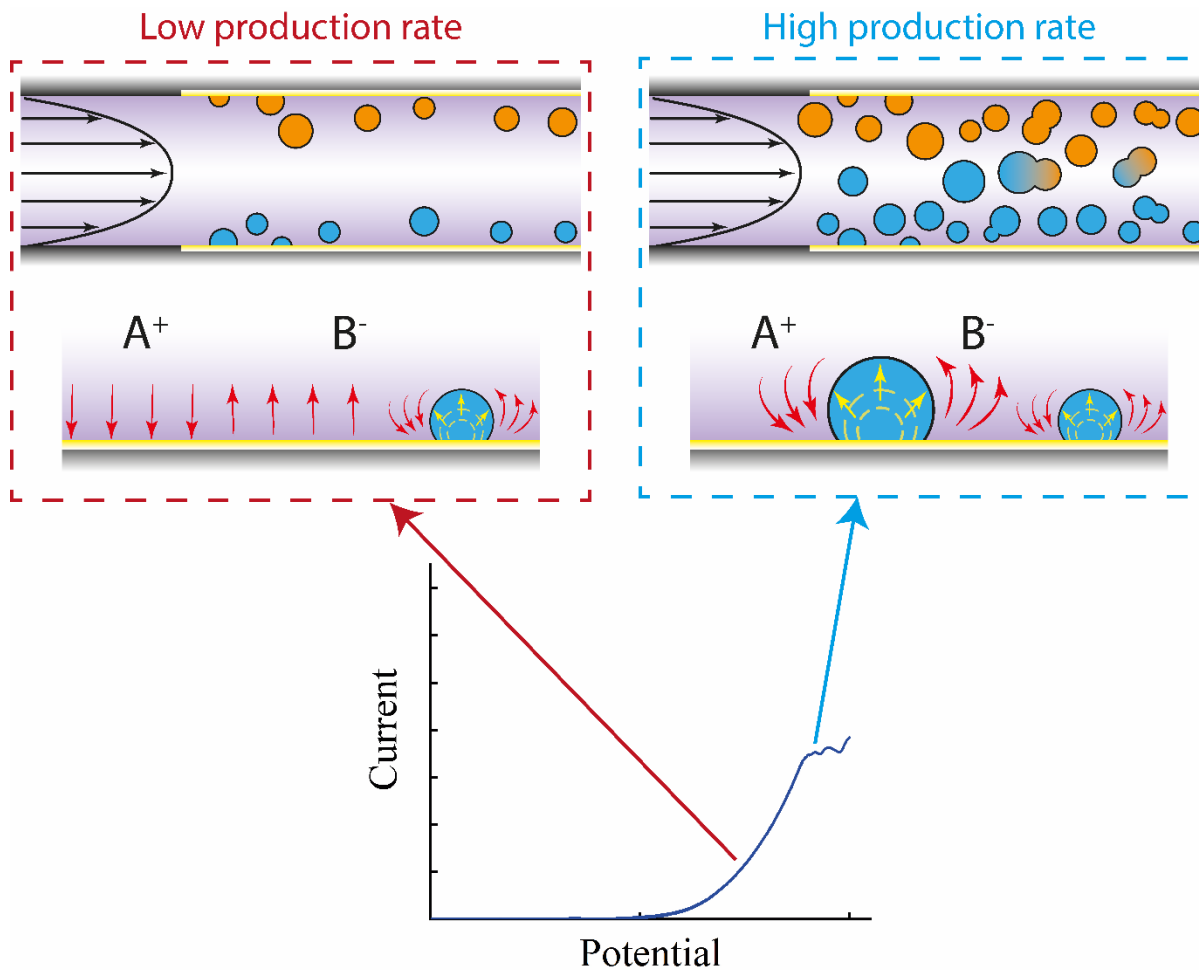


Figure 4. At low production rates, the electrode's surface coverage by bubbles is small and the bubbles do not interact. Therefore, the flow can separate the streams of bubbles effectively. The bubbles start to interact at high production rates which leads to gas cross-contamination. Furthermore, the nucleating bubbles cover the surface of the electrodes and induces overpotentials.

The main goal of this thesis is to investigate two-phase flows in membrane-less electrolyzers. This investigation helps us to improve the production throughput, purity of the products, and efficiency of the electrolyzer.

In chapter 2, we investigate experimentally and numerically the bubble motion in the rectangular microchannels. This is important for controlling the bubble position in the membrane-less electrolyzer and reducing the bubble cross over. We find the important parameters that affect the bubble lateral equilibrium position in a channel. These parameters are Reynolds number, Capillary number, bubble diameter, and the channel aspect ratio. The forces acting on a flowing bubble is proportional to these parameters. Therefore, we can control the equilibrium position of bubbles in a channel by changing the acting forces on the bubble. Furthermore, we investigate the differences of the equilibrium position between clean bubbles, contaminated bubbles, and solid particles.

We investigate bubbles nucleation at the surface of the electrode and bubble-bubble interaction as the next step in chapter 3. We build a microfluidic device with small nucleation sites in order to have control over the bubble nucleation. There are multiple nucleation sites in this device for generating bubbles at different locations of the channel. The effects of the bubble detachment size, bubble coalescence, and flow velocity on the bubble cross over are examined.

As discussed above, the cross over and the overpotentials due to the bubbles is less when bubbles are smaller in the electrolyzer. Therefore, we reduce the size of bubbles by adding a surfactant to the electrolyte.

The liquid flow is the primary mechanism for product separation in the membrane-less electrolyzers. In addition to the flow, the geometry of the membrane-less electrolyzer can be modified to decrease the gas cross over. We introduce a new design for membrane-less electrolyzers in chapter 4 that is optimized to achieve a high production rate and low cross over. The new design has three channels that are separated by two porous walls. The electrochemical reactions happen in the outer channels. The electrolyte flow through the wall pores from the middle channel towards the outer channels. The direction of flow and the wall pores prevent the bubble migration to the opposite side. We compare the electrochemical performance of the new design with a parallel electrodes electrolyzer.

We can actively control the applied current and flow velocity by monitoring the electrochemical reaction and the bubble motion in order to reduce the cross over. A monitoring method is presented in chapter 5 for the measurement of the fluidic properties. This method applies neural networks to two-phase flows for extracting information such as flow velocity and liquid concentration. This method can be used for tracking and controlling bubbles motion in the membrane-less electrolyzers.

The studies introduced in this study lead to a better understanding of two-phase flows in membrane-less electrolyzers. Therefore, we can apply this knowledge to achieve higher production rates with high product purity at higher efficiencies. Furthermore, this knowledge is beneficial in the scale-up of the membrane-less electrolyzers.

Chapter 2

Inertial manipulation of bubbles in rectangular microfluidic channels

This chapter is the postprint version of the following article published in *Lab on a chip*.

Inertial manipulation of bubbles in rectangular microfluidic channels

Pooria Hadikhani¹, S. Mohammad H. Hashemi¹, Gioele Balestra², Lailai Zhu^{3,4}, Miguel A. Modestino⁵, François Gallaire², and Demetri Psaltis¹

¹ Optics Laboratory, School of Engineering, Swiss Federal Institute of Technology Lausanne (EPFL), Lausanne, Switzerland

² Laboratory of Fluid Mechanics and Instabilities, Swiss Federal Institute of Technology Lausanne (EPFL), CH1015 Lausanne, Switzerland

³ Linné Flow Centre and Swedish e-Science Research Centre (SeRC), KTH Mechanics, SE 10044 Stockholm, Sweden

⁴ Department of Mechanical and Aerospace Engineering, Princeton University, USA

⁵ Department of Chemical and Biomolecular Engineering, Tandon School of Engineering, New York University, Brooklyn, USA

Lab on a Chip 18, no. 7 (2018): 1035-1046

<https://doi.org/10.1039/C7LC01283G>

Inertial microfluidics is an active field of research that deals with crossflow positioning of the suspended entities in microflows. Until now, the majority of the studies have focused on the behavior of rigid particles in order to provide guidelines for microfluidic applications such as sorting and filtering. Deformable entities such as bubbles and droplets are considered in fewer studies despite their importance in multiphase microflows. In this chapter, we show that the trajectory of bubbles flowing in rectangular and square microchannels can be controlled by tuning the balance of forces acting on them. A T-junction geometry is employed to introduce bubbles in a microchannel and analyze their lateral equilibrium position in a range of Reynolds ($1 < \text{Re} < 40$) and Capillary numbers ($0.1 < \text{Ca} < 1$). We find that the Reynolds number (Re), the Capillary number (Ca), the diameter of the bubble (\bar{D}), and the aspect ratio of the channel are the influential parameters in this phenomenon. For instance, at high Re , the flow pushes the bubble towards the wall while large Ca or \bar{D} moves the bubble towards the center. Also, in the shallow channels, having aspect ratios higher than one, the bubble moves towards the narrower sidewalls. One important outcome of this study is that the equilibrium position of bubbles in rectangular channels is different from solid particles. The experimental observations are in good agreement with the performed numerical simulations and provide insights into the dynamics of bubbles in laminar flows which can be utilized in the design of flow based multiphase flow reactors.

2.1 Introduction

Multiphase flows are of critical importance in systems which transcend the boundaries of a single discipline. In thermal engineering, phase change heat sinks provide higher heat transfer rates and uniform surface temperatures compared to their single phase counterparts [26]. A large number of studies have investigated the performance of these heat sinks for electronic cooling [27-30]. In the field of reactor engineering, variants of reactors including trickle-bed [31], fluidized bed [32], and bubble column reactors [33] rely on multiphase flows to enhance mass transport which requires a thorough understanding of their complex physics. Moreover, in most electrochemical systems, gaseous products evolve at the interface of the electrodes and the electrolyte, including important processes such as water electrolysis [14], chlor-alkali [34] and aluminum production [35]. Better understanding and control of the phenomena associated with multiphase flows will contribute to improving the performance of these devices. For instance, many electrochemical reactors use ion conducting membranes or porous separators between the anodic and cathodic half cells. Recently, we have shown that by tuning the flow rate of a liquid electrolyte in a microfluidic electrolyzer, it is possible to control the trajectory of the generated bubbles in a membrane-less configuration [20]. Removing the solid membrane in these systems, decreases the ohmic losses and provides flexibility in the selection of catalysts in addition to a simplified cell design [36-39]. Controlling two-phase flows by topography induced variations of the bubbles' surface energy is another way of eliminating the need for a functional membrane [40]. In this chapter, we implement experimental and numerical tools to investigate the dynamics of bubbles flowing in microfluidic channels. By doing so we are able to determine the key parameters such as the diameter of the bubble, the channel geometry, Capillary, and Reynolds numbers that influence the position of bubbles in the microchannels and provide insights into how to control bubbles' motion in the flow.

A large body of research in the field of inertial microfluidics has been dedicated to controlling the position of particles in fluidic channels since the discovery of the Segre-Silberberg effect [41, 42]. Most of the effort in this field is focused on the control of solid particles with diameters smaller than the size of the channel; typically, by one order of magnitude [43-53]. Although there are similarities between the behavior of rigid particles and bubbles, deformation of the bubbles [54-57] complicates the understanding of the physical phenomena evidenced in gas/liquid flows.

Understanding the active forces affecting bubble motion is necessary in order to explain their behavior. Important forces at moderate Re ($1 < Re < 100$), are the wall-induced lift force, the shear gradient lift force, and the deformation-induced lift force. These forces are shown schematically in Figure 5. In this range of Re number and length scale, the buoyancy lift force can be neglected since the inertia forces dominate by at least one order of magnitude. The wall-induced lift force originates from the asymmetry in the flow field around the bubble and its direction is towards the center of the channel [58]. This force decreases as the bubble moves further away from the wall since the flow asymmetry decreases. The shear gradient lift force is a result of the non-uniform velocity profile and pushes the bubble towards the wall [55, 59]. The non-uniform velocity profile induces unequal relative velocities on the two sides of the bubble and as a result, it changes the pressure distribution around the bubble. In the parabolic velocity profile, the relative velocity of the flow to the bubble is higher at the edge that is closer to the wall resulting in a smaller pressure at this side. Therefore, the bubble moves towards the

wall where the magnitude of the relative velocity is the highest [60]. Deformation of the bubble induces a force towards the centerline where the bubble can minimize its energy by reducing its deviation from the original spherical shape and gain symmetric shape [61-63]. This force is considered as a deformation-induced lift force. The balance of these forces determines the equilibrium bubble position in the crossflow direction.

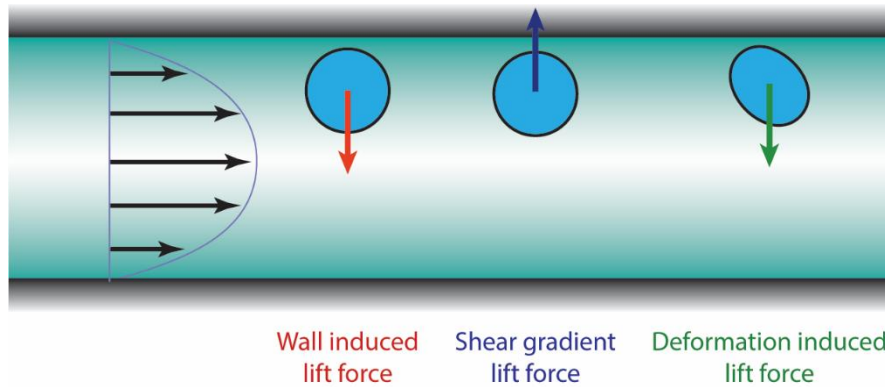


Figure 5. Forces acting on the bubble: a wall-induced lift directing towards the centerline which diminishes as the bubble moves away from the wall, a shear gradient lift that pushes the bubble towards the wall, a deformation-induced lift pointing towards the centerline which gets stronger as the bubble deformation increases.

Numerical and experimental investigations [54, 56] have confirmed the presence of the deformation-induced wall and inertial lift forces on the droplets moving in microchannels. As it will be discussed in the numerical simulation section, the non-dimensionalized governing equations depend on the Re and Ca numbers. The Re number in the channel flow is an important parameter which determines the relative importance of the lift forces. The flow of the buoyant droplets and bubbles in microfluidic channels has been investigated recently by Stan et al. [55] at low Re . Under these conditions, the forces including buoyancy, deformation-induced, wall and inertial lift forces, have comparable magnitudes [55]. In their research, the bubble position is determined by balancing the buoyant force with hydrodynamic lift forces, while at higher Re , the balance of forces acting on the bubble is different. In the study of Rivero-Rodriguez et al. [63], the motion of an unconfined bubble in circular microchannels is investigated analytically and numerically. Although their results confirm the effect of inertial and deformation-induced lift forces, the motion of the bubble in the rectangular microchannels are not included in their study.

In this chapter, we investigate the bubble motion at moderate Re ($1 < Re < 40$). We find that by moving towards larger Re , the inertial lift force starts to dominate and gradually changes the equilibrium position. The bubble position in this range of Re is determined by balancing the inertial lift forces with the wall and deformation-induced lift forces, as the effect of the buoyant force is negligible. We use experiments and numerical simulations to investigate systematically the interplay of the bubble diameter, Re , Ca , and the channel geometry in determining the steady state position of the bubbles. We demonstrate that in the channels with aspect ratios higher than one or at high Re , the bubbles stay close to the wall while increasing the Ca or the bubble diameter causes the bubble to migrate towards the centerline. We discovered that the behavior of the bubble in the rectangular channels is different from the solid particles and this behavior can be modified by using surfactants.

2.2 Experimental set-up

A T-junction geometry is fabricated to introduce nitrogen bubbles from a narrow side channel into the wide main channel as shown in Figure 6. Microfabrication of the channels starts on a double-sided silicon (Si) wafer with 1.5 μm silicon dioxide (SiO_2) layer on both sides. Two photolithography steps are performed on the topside of the wafer to enable different channel depths for the main and side channels. A second photolithography step is used on the backside to make thorough holes as fluidic access ports. Channels and ports are fabricated using Deep Reactive Ion Etching (DRIE). A 100 nm layer of silicon dioxide is grown on the silicon wafer. Finally, channels are sealed by bonding the silicon wafer to a Borofloat 33 glass wafer via anodic bonding. Figure 49 (Appendix A) describes the complete microfabrication procedure. In order to study the effect of geometry, three sets of channels are fabricated with a depth of 50 μm and widths of 50, 150, and 200 μm . The gas channel is perpendicular to the main channel and its depth and width are 5 μm . The main channel's length is 16 mm and the gas channel connects to the main channel at the midpoint along the direction of flow. There are two inlets for injecting the liquid and the gas and one as the outlet for both phases.

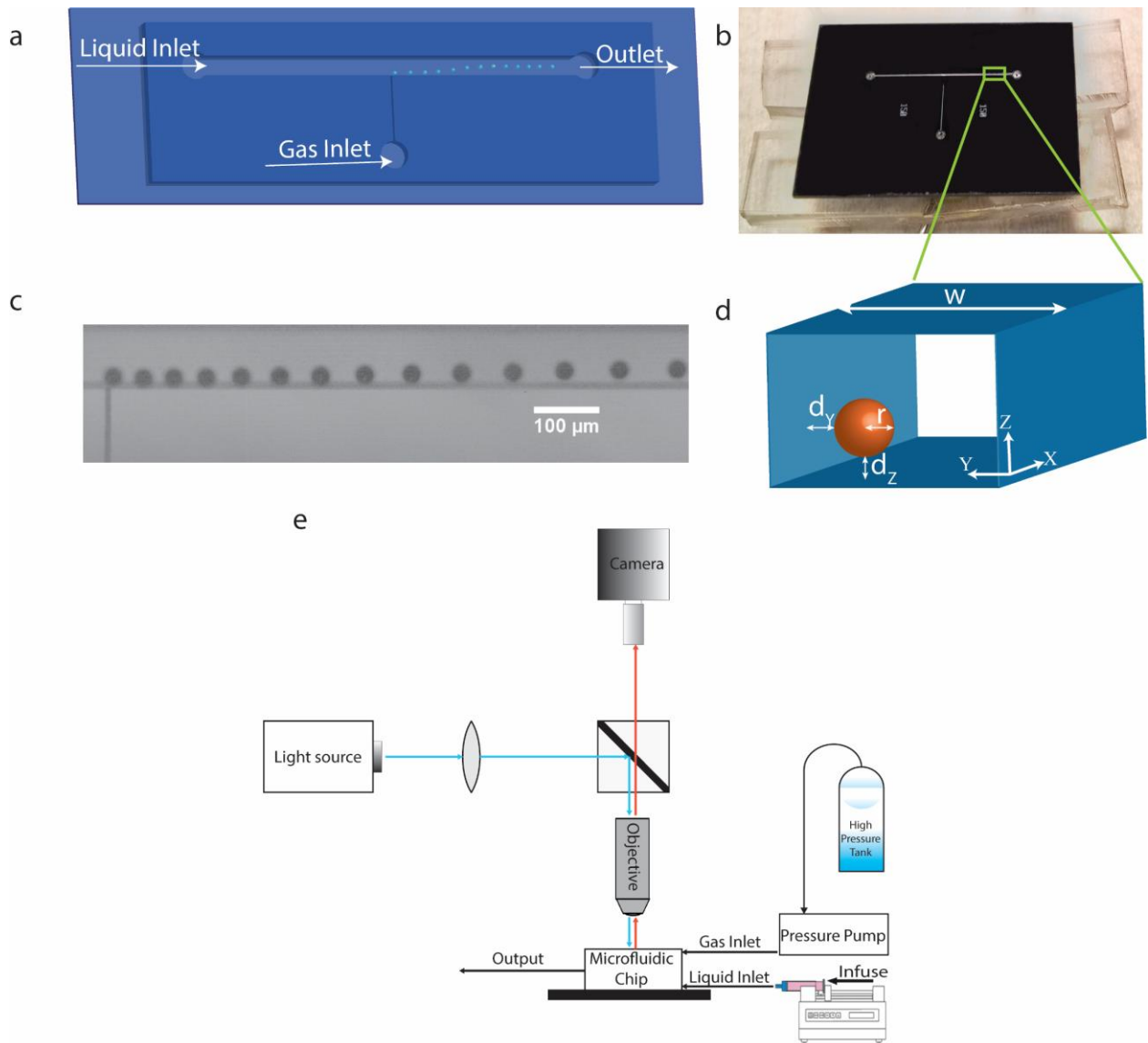


Figure 6. Microfluidic device showing (a) a schematic representation of the channel geometry, (b) a photograph of the fabricated device, (c) an image of the bubble formation at the T-junction, and (d) a cross-sectional representation depicting how the radius of the bubble, r , and the bubble distance from the wall, d_y , are measured at 6 mm downstream of the T-junction. (e) Experimental setup: the liquid is injected with a syringe pump and a constant pressure pump is used to introduce the gas phase into the device. Motion of bubbles is recorded with a high speed camera in the reflection mode.

The flow rate of the liquid and the pressure of the gas are regulated to produce different bubble radii in a wide range of Re , while Ca is changed by employing different liquids as the carrier phase. Table 1 lists the properties of water, ethanol (Thommen-Furler AG), and isopropanol (Fishner Scientific UK) which are used as a carrier phase. The surface tensions of the liquids are measured using KRUSS DSA-30 drop shape analyzer using the pendant drop method [64]. Gas bubbles are generated at the side of the channel. A syringe pump (Cronus Sigma 1000 Series) and a constant pressure pump (Elveflow OB1 MK3) are used for introducing liquid and gas phases, respectively. Bubble properties are measured at a position 6 mm downstream of the T-junction. Videos are recorded using a high-speed camera (Photron FASTCAM Mini UX100) with a frame rate of up to 10000 fps. The schematic of the experimental setup is depicted in Figure 6e. The recorded video is used to measure the bubble's distance to the side

and the bubble radius in each frame. Diagrams of the bubble position with the error bars representing the standard deviation from the average value are shown in Figure 50 (Appendix A). Based on the measured values, the following parameters are used to define the bubble position for convenience:

$$\bar{Y} = 1 - \frac{w-2r-2d_Y}{w-2r}, \quad (1)$$

$$\bar{Z} = 1 - \frac{w-2r-2d_Z}{w-2r}, \quad (2)$$

where w , r , d_Y , and d_Z are the width of the channel, the radius of the bubble, the minimum distance between the bubble's edge to the wall in the y-direction, and z-direction, respectively. According to this definition, \bar{Y} is a unit-less quantity that varies from zero to one as the bubble moves from the wall towards the center. Furthermore, it should be noted that the diameter of the bubble is normalized to the channel width:

$$\bar{D} = \frac{2r}{w}. \quad (3)$$

Table 1. Properties of the liquids used as carrier phase: density and viscosity are given at room temperature and atmospheric pressure, and surface tension is measured using pendant drop method.

	Density (kg/m^3)	Viscosity ($kg/m/s$)	Surface tension (N/m)
Water	998.2	1.01×10^{-3}	0.073
Ethanol (Thommen-Furler AG)	789.4	1.14×10^{-3}	0.022
Isopropanol (Fishner Scientific UK)	790	2.1×10^{-3}	0.021

2.3 Numerical simulation

We carry out simulations based on a commercial finite-element solver COSMOL Multiphysics. It resolves the fluid interface by the Arbitrary Lagrangian Eulerian (ALE) moving mesh technique, where the interface is represented by exact mesh lines body-fitted with the droplet/bubble.

The nondimensional incompressible Navier-Stokes equations solved by COMSOL are:

$$\begin{aligned} \nabla \cdot \mathbf{U} &= 0, \\ Re \left[\frac{\partial \mathbf{U}}{\partial t} + (\mathbf{U} \cdot \nabla) \mathbf{U} \right] &= -\nabla p + \nabla \cdot [\nabla \mathbf{U} + \nabla \mathbf{U}^T], \end{aligned} \quad (4)$$

where p is the pressure and \mathbf{U} the velocity. Re denotes the ratio of the inertial forces to the viscous forces as:

$$Re = \frac{\rho_l U_{cl} R}{\mu_l}, \quad (5)$$

where μ_l is the viscosity of the liquid, ρ_l is the density of the liquid, U_{cl} is the centerline velocity of the underlying flow, and R is the radius of the bubble at rest. The boundary condition at the interface can be written as:

$$\mathbf{n} \cdot \left[-p_l \mathbf{I} + p_g \mathbf{I} + (\nabla \mathbf{U} + (\nabla \mathbf{U})^T)_l - \frac{\mu_g}{\mu_l} (\nabla \mathbf{U} + (\nabla \mathbf{U})^T)_g \right] = \frac{1}{Ca} \mathbf{n} (\nabla \cdot \mathbf{n}). \quad (6)$$

where \mathbf{n} is the unit normal vector to the bubble interface, \mathbf{I} is the unit tensor, and l and g subscripts denote the liquid and the gas phases, respectively. The capillary number Ca compares the viscous forces against the capillary forces:

$$Ca = \frac{\mu_l U_{cl}}{\sigma}, \quad (7)$$

where σ is the surface tension on the interface. Because the viscosity ratio $\frac{\mu_g}{\mu_l} \ll 1$, we assume $\frac{\mu_g}{\mu_l} = 0$, the boundary condition Eq. (6) can be idealized to the following form:

$$\mathbf{n} \cdot \left[-p_l \mathbf{I} + p_g \mathbf{I} + (\nabla \mathbf{U} + (\nabla \mathbf{U})^T)_l \right] = \frac{1}{Ca} \mathbf{n} (\nabla \cdot \mathbf{n}). \quad (8)$$

Since the volume of the bubble is supposed to be constant, the pressure p_g can be obtained by imposing an additional constraint that the surface integral of the normal velocity on the bubble interface is zero:

$$\int_{interface} \mathbf{U} \cdot \mathbf{n} dA = 0. \quad (9)$$

We perform the simulations in the reference frame that has the same streamwise translational velocity U_{bubble} with that of the bubble. In this frame, the velocity imposed on the wall is $U_{bubble} \mathbf{e}_x$. At the inlet, the analytical velocity profile (shifted by $-U_{bubble}$) of a rectangular duct is imposed, hence the mean inlet velocity is $U_{mean} - U_{bubble} \mathbf{e}_x$, where U_{mean} is the average velocity of the underlying flow. The advantage of adopting this frame is that the droplet only translates in the spanwise direction, viz., in the plane normal to the streamwise direction and is hence not advected out of the computational domain but still allowed to freely rotate and deform. This also significantly alleviates the need for expensive remeshing and interpolation which have been the main hurdles of ALE-based simulations. Note that U_{bubble} is a time-dependent unknown obtained at every time step, and it is slaved to an additional constraint that the surface integral of the streamwise velocity on the bubble interface is zero. We launch the simulation by initially putting a spherical bubble slightly away from the center of the domain. After a transient period (see Figure 7), the bubble will reach an equilibrium state, where U_{bubble} , and the shape and lateral position of the bubble do not vary in time. We do not attempt to resolve the transient phase of the dynamics, because in this chosen reference frame, the underlying flow changes the magnitude in time, introducing an artificial acceleration term that will influence the transient dynamics. Luckily, we only focus on the equilibrium configuration of the bubble when it reaches a steady velocity U_{bubble}^{steady} and hence the artificial acceleration term vanishes without influencing the equilibrium dynamics. To confirm that the equilibrium configuration is independent of the transient dynamics, we have conducted for certain cases a new computation where the velocity of the wall and inlet is shifted by a time-invariant

magnitude, U_{bubble}^{steady} . The new equilibrium configuration is the same as the previous one, confirming that our strategy is appropriate.

We span a wide range of the three nondimensional numbers Re , Ca , and \bar{D} for a thorough computational investigation. Figure 7 shows the computational setup and results. The velocity of the bubble is monitored as a function of time to make sure the solution converges to the steady state. To verify the conservation of the bubble's volume, the temporal evolution of the bubble's volume is plotted in Figure 7d. After verifying that the equilibrium state has been reached, the bubble position and the velocity profile around the bubble are extracted and shown in Figure 7e and 4f, respectively.

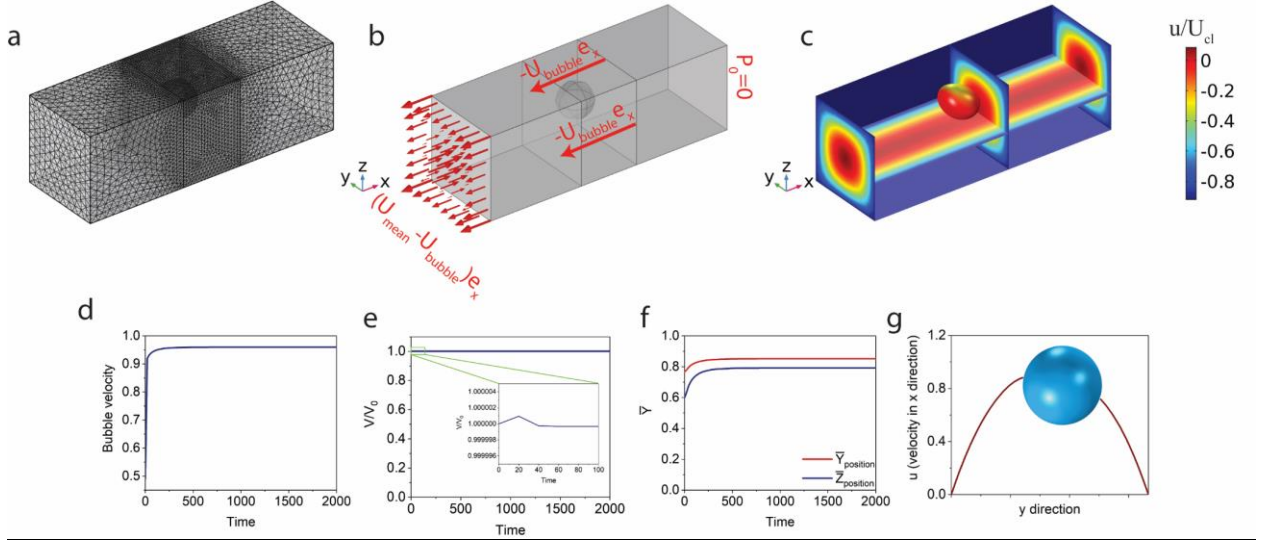


Figure 7. Computational setup: (a) The computational mesh used in the numerical simulation. (b) In the streamwise direction, the reference frame is put on the bubble. Hence a velocity shift of U_{bubble} in the $-e_x$ direction is applied on both the walls and the inlet boundary. (c) The streamwise velocity at different cross sections of the duct when the bubble reaches to its equilibrium position. (d) The time evolution of bubble velocity indicates that the bubble reaches its equilibrium position. (e) The volume of the bubble is monitored to guarantee its time invariance. The bubble's lateral position (f) and velocity profile around the bubble (g) are extracted from the equilibrium solution.

2.4 Validation of simulations

Recently, COMSOL Multiphysics has been used for simulation of droplets in circular geometries where the results are in good agreement with the asymptotic analysis and the boundary integral method that shows its capability in resolving the droplet motion [65]. Table 7 in Appendix A shows the results of the numerical simulations for different grid sizes. The grid parameter sizes of the third simulation are optimal and chosen for the numerical study. In this section, for validation of the numerical simulations with the experiments, simulations are performed over the same range of Re , \bar{D} , and Ca as in experiments. Experimental data are selected for both of the cases where bubbles go to the center or to the wall. Also, data are chosen from two different types of liquids to probe the impact of the Ca . The comparison between the two sets of results is summarized in Table 2 for isopropanol as the carrier fluid and Table 3 for ethanol as the carrier fluid. In the tables, \bar{Y} and \bar{Z} are calculated by Eq. (1) and Eq. (2). At $Re \leq 1.29$, the predicted bubble position from the simulations does not correspond to the experimental values. This discrepancy can be explained by considering the possibility that multiple equilibrium positions exist in the channel [56]. As a result, it is possible that the simulation chooses one of the equilibrium positions and the experiment the other. More

importantly, in the experiments, a row of the bubbles can be seen, while a single bubble motion is simulated numerically. At low Re , the range of influence of a bubble increases promoting inter-bubble interactions and can affect the lateral position of the bubble [66]. At higher values of Re and Ca , an excellent agreement can be seen between simulations and experiments. Table 4 shows the simulation results for the equilibrium position of the bubbles with different initial positions. The results show that the bubble, starting from different positions, reaches to the same equilibrium position. However, this result cannot be considered as a general statement since at low Re , a bubble can possibly have multiple equilibrium positions as seen for solid particles [67].

Table 2. Bubble equilibrium positions when the carrier fluid is isopropanol

Re	0.48	0.51	2.11	2.60	2.66	7.37	9.48	10.60
Ca	0.007	0.007	0.035	0.035	0.046	0.162	0.162	0.162
\bar{D}	0.74	0.78	0.64	0.78	0.60	0.48	0.61	0.69
$\bar{Y}_{experiment}$	1.00	1.00	0.52	1.01	0.52	0.36	0.48	0.77
$\bar{Y}_{simulation}$	0.80	0.95	0.53	0.96	0.48	0.36	0.50	0.80
$\bar{Z}_{simulation}$	0.88	0.86	0.56	0.96	0.50	0.36	0.50	0.83

Table 3. Bubble equilibrium positions when the carrier fluid is ethanol

Re	1.29	1.68	4.53	6.22	11.07	15.13	13.62	18.77
Ca	0.006	0.006	0.024	0.024	0.059	0.059	0.071	0.071
\bar{D}	0.64	0.84	0.56	0.78	0.55	0.75	0.57	0.78
$\bar{Y}_{experiment}$	0.13	0.99	0.09	0.32	0.17	0.34	0.14	0.36
$\bar{Y}_{simulation}$	0.69	0.86	0.19	0.44	0.19	0.38	0.19	0.54
$\bar{Z}_{simulation}$	0.81	0.88	0.24	0.45	0.20	0.38	0.19	0.54

Table 4. Numerical simulation of the bubble equilibrium position with different initial position

$Re = 2.60$ $Ca = 0.035$ $\bar{D} = 0.78$		$Re = 9.48$ $Ca = 0.162$ $\bar{D} = 0.61$	
Initial position	Equilibrium position	Initial position	Equilibrium position
$\bar{Y} = 0.71$ $\bar{Z} = 0.82$	$\bar{Y} = 0.96$ $\bar{Z} = 0.96$	$\bar{Y} = 0.87$ $\bar{Z} = 0.92$	$\bar{Y} = 0.50$ $\bar{Z} = 0.51$
$\bar{Y} = 0.60$ $\bar{Z} = 0.64$	$\bar{Y} = 0.96$ $\bar{Z} = 0.96$	$\bar{Y} = 0.67$ $\bar{Z} = 0.78$	$\bar{Y} = 0.50$ $\bar{Z} = 0.50$
$\bar{Y} = 0.42$ $\bar{Z} = 0.45$	$\bar{Y} = 0.94$ $\bar{Z} = 0.93$	$\bar{Y} = 0.46$ $\bar{Z} = 0.57$	$\bar{Y} = 0.50$ $\bar{Z} = 0.50$

2.5 Results

The influence of Re , Ca , the bubble diameter and the channel geometry on the positioning of the bubbles merits a detailed discussion. In the following subsections, each parameter's role is discussed and in the last part, the equilibrium position of the bubbles is compared to one of the solid particles.

2.5.1 Effect of the Reynolds number

The Reynolds number determines the balance of the different forces acting on the bubble. The shear gradient lift force towards the wall depends on the relative velocity at the two sides of the bubble. By increasing the Re , the difference in relative velocity at the two sides of the bubble increases and as a result, the shear gradient lift force increases. The higher relative velocity near the wall generally translates to lower pressure on the side of the bubble facing the wall, therefore, this force dominates at higher Re , pushing the bubbles towards the wall. Figure 8 shows the effect of the Re in the $50 \mu m$ wide channel. At small Re values, the bubble equilibrium position is at the centerline. Figure 9 shows the simulation results for the bubble's lateral position at different Re for $Ca = 0.1$ and $\bar{D} = 0.4$. In each simulation, the bubble's initial position is at $(\bar{Y}, \bar{Z}) = (0.7667, 0.6)$. As the Re increases, the bubble gets closer to the wall and at Re larger than 20, the bubble moves to the corner of the channel on the diagonal.

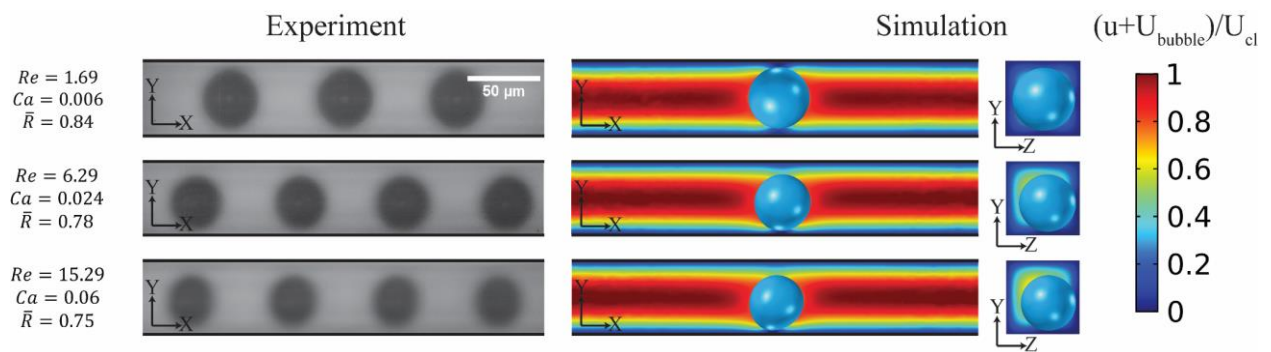


Figure 8. Effect of Re on the lateral position of the bubble: Experimental results and the corresponding numerical simulations are for the channel with $50 \mu m$ width and $50 \mu m$. The bubble diameter is normalized by the channel width. By increasing the Re , the bubble moves gradually towards the wall.

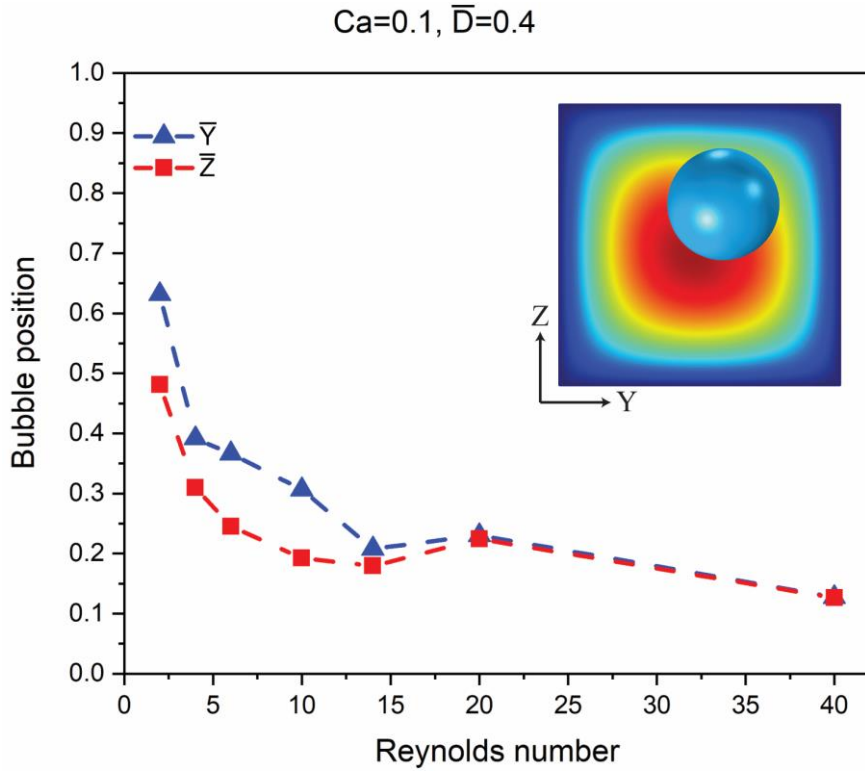


Figure 9. Simulation results of Reynolds number's effect on the lateral position of a bubble in a square channel. The blue points and the red points show the equilibrium position of the bubble in the horizontal and vertical direction, respectively. All the simulations are carried out for $\bar{D} = 0.4$ and $Ca = 0.1$. The initial bubble position is at $(\bar{Y}, \bar{Z}) = (0.7667, 0.6)$.

2.5.2 Effect of the Capillary number

The capillary number signifies the ratio of viscous forces to the surface tension forces. At large Ca , the viscous forces are stronger than the capillary forces and a bubble in this condition undergoes larger deformation. The minimum energy condition for the bubble is in the spherical shape, which is best met when it is in the middle of the channel where the velocity profile is symmetric and the velocity is the same on both sides of the bubble. As a result, the flow exerts stronger deformation-induced lift force on the bubble towards the center of the channel. Figure 10 shows the bubble position at different Ca . In this figure, the continuous phase in the first and second rows are isopropanol and ethanol, respectively. The Ca is larger in the first row and as a result, the distance between the bubble and the wall is larger in the first row. Simulation results at different Ca with $Re = 10$ and $\bar{D} = 0.4$ are shown in Figure 11. The bubble equilibrium position is closer to the centerline at larger Ca . At Ca higher than 0.9, the bubble moves to the centerline.

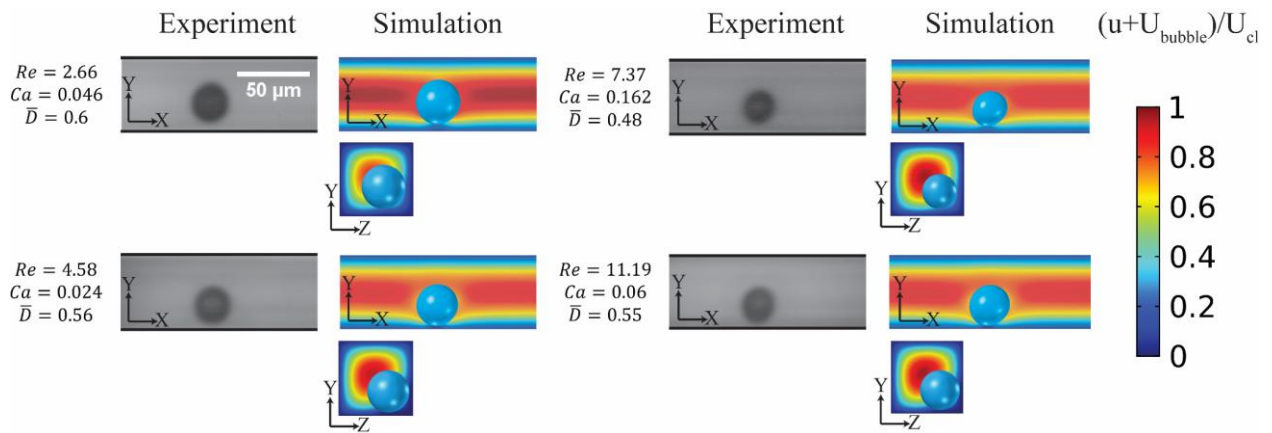


Figure 10. Effect of the Ca on the bubble position for the square channel: The carrier fluid in the first row is isopropanol and in the second row is ethanol. Ca has a smaller value when the carrier fluid is ethanol and as a result, the bubble is closer to the wall. As the Ca increases, the bubble moves further away from the wall. The channel's cross sectional dimensions in the experiments is $50 \mu m$ by $50 \mu m$. Numerical simulations, corresponding to the same parameter, support the experimental results. The color bar shows the velocity in the flow direction which is normalized with the centerline velocity.

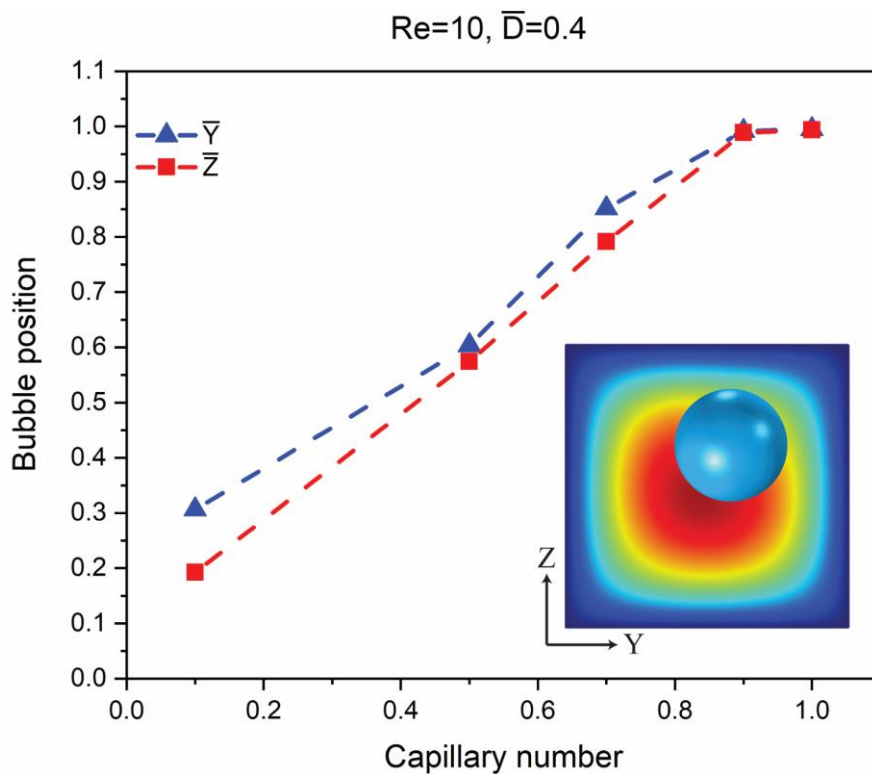


Figure 11. Simulation results for the square channel at different Ca , while the Re and \bar{D} are constant. The initial position of the bubble is $(\bar{Y}, \bar{Z}) = (0.7667, 0.6)$. The blue points and the red points show the equilibrium position of the bubble in the horizontal and vertical direction, respectively. As the Ca number increases the bubble gets closer to the center and at $Ca > 0.9$ the bubble moves exactly to the center.

2.5.3 Effect of bubble's diameter

Lateral forces acting on the bubble originate from unequal pressure and velocity around the bubble. These parameters change as the diameter of the bubble varies. Figure 12 presents the effect of bubble diameter on its equilibrium position. It can be observed that the larger bubble is closer to the channel's centerline. Figure 13 shows the results of the simulations for various bubble's diameter at constant $Re = 10$ and $Ca = 0.1$. The equilibrium position of a bubble

smaller than half of the channel is between the diagonal line and the center of the sidewall. On the one hand, such a bubble moves towards the center of the sidewall similar to a small solid particle [68]. On the other hand, the deformation-induced lift force pushes the bubble towards the diagonal line where the shear stress is smaller as shown in Figure 53 of Appendix A. Therefore, as the diameter of the bubble decreases, the deformability of the bubble decreases and equilibrium position of the bubble gets closer to the center of the sidewall. When the bubble diameter becomes larger than half of the width of the channel, the bubble moves along the diagonal and by increasing the diameter of the bubble, eventually, it moves to the centerline of the channel. Larger bubbles feel stronger wall-induced lift force towards the center and besides that, when the diameter of the bubble exceeds half of the channel, the shear gradient lift force towards the wall decreases. Therefore, as the bubble becomes larger, forces towards the center dominate and the shear gradient lift force towards the wall diminishes resulting in positioning of the bubble at the centerline.

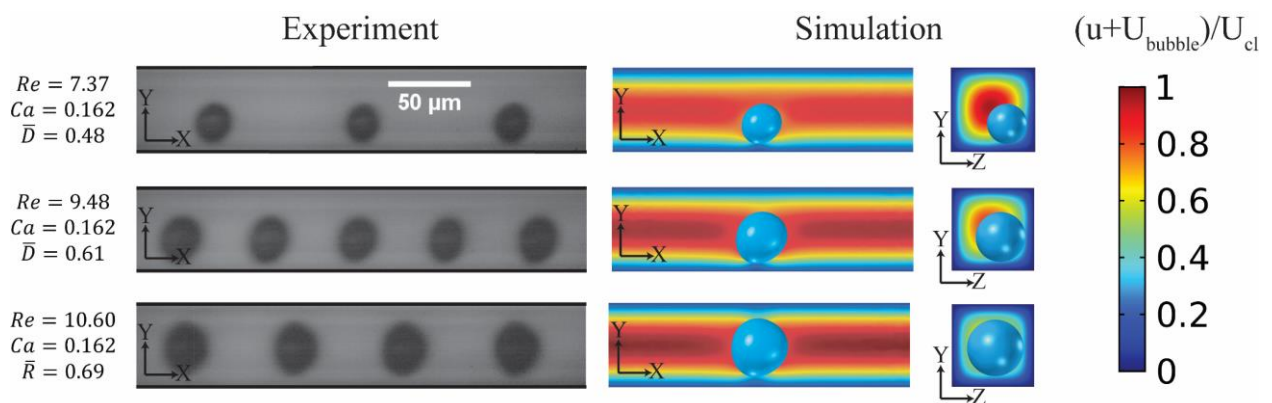


Figure 12. Effect of bubble's radius on the equilibrium position: experimental results for a channel with $50 \mu m$ width and $50 \mu m$ depth are compared with the corresponding simulations in color. The color map shows the normalized velocity of the flow in x-direction. The results show that the equilibrium position of larger bubbles is closer to the centerline than smaller bubbles.

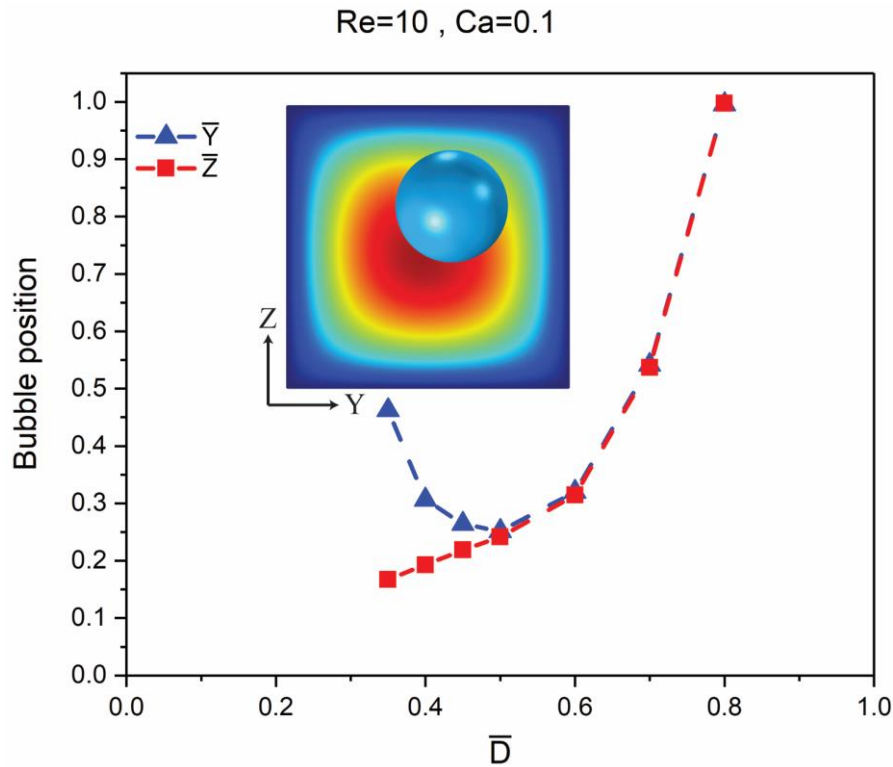


Figure 13. Numerical simulations of different bubble diameters for the square channel at constant $Re = 10$ and $Ca = 0.1$. The initial position of the bubble is at $(\bar{Y}, \bar{Z}) = (0.7667, 0.6)$. The equilibrium position of a bubble that is smaller than half of the channel is close to the wall. A bubble larger than half of the channel moves along the diagonal of the channel and by increasing the diameter of the bubble, it eventually moves to the center of the channel.

2.5.4 Effect of aspect ratio of the channel

As discussed in the previous section, bubbles with diameters larger than half of the channel with square geometry move towards the center. In the channels with aspect ratios larger than one, the bubble diameter can be larger than half of the height and smaller than half of the width of the channel. Therefore, the bubble moves towards the center in the height direction and move towards the wall in the width direction. Figure 14 shows the experimental and simulation results for channels with different aspect ratios. In the square channel, since the bubble diameter is larger than half of the channel's width, it moves to the centerline. In the channels with aspect ratios larger than one, the equilibrium position of the bubble changes from the centerline to the narrower side of the channel. Figure 15 shows the experimental results for channels with three different aspect ratios. In the square channel, bubbles can be in the center of the channel or close to the wall based on their diameters. As discussed in section 3, for bubbles with larger diameter, the forces towards the center increases and push the bubbles to the center while smaller bubbles move to the wall. On the other hand, in the rectangular channels, the equilibrium position of the bubbles with the same diameters is close to the narrow side of the channel.

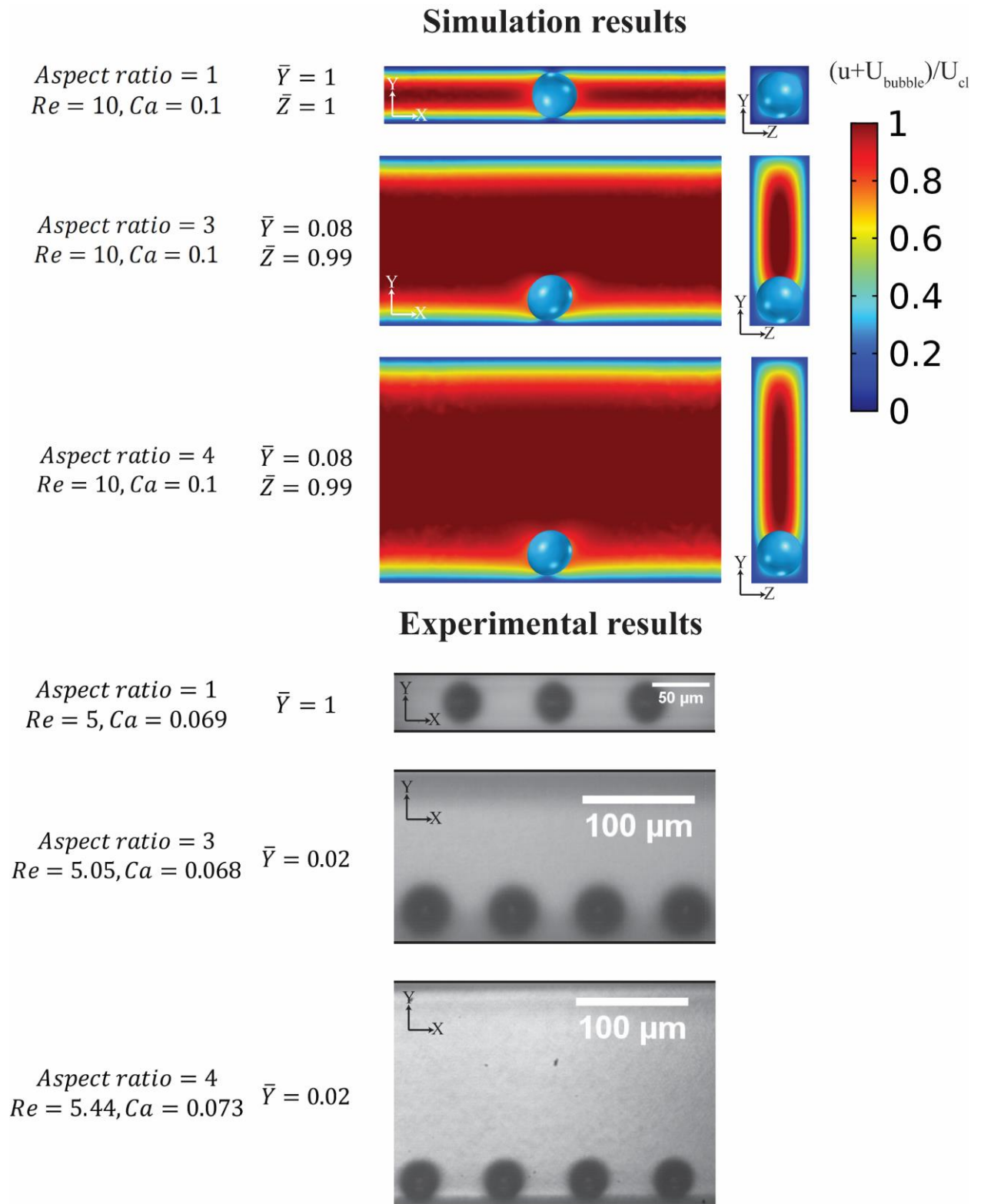


Figure 14. Effect of the channel geometry on the lateral position of the bubble while the Re and Ca are constant. Experimental and numerical results show that in the wider channels, the bubble equilibrium position is close to the smaller edge while in the channel with aspect ratio of one the bubble equilibrium position is in the center.

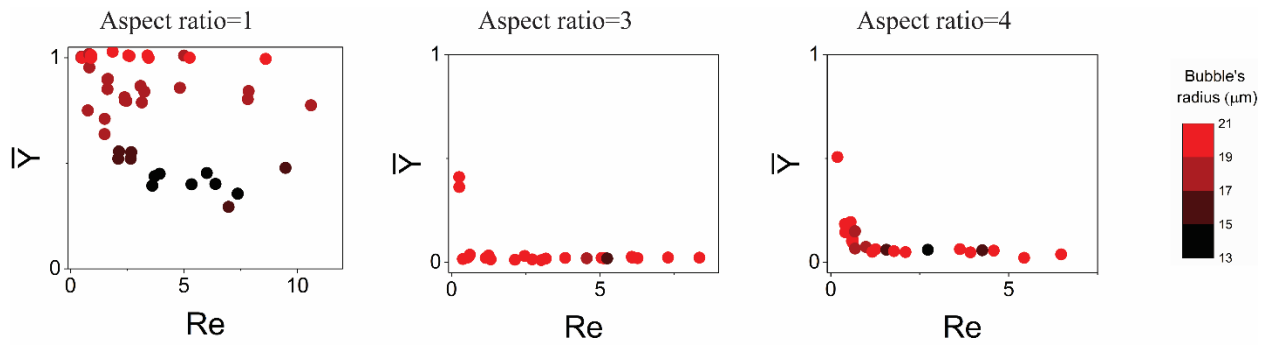


Figure 15. Experimental results for three different channel aspect ratios when the carrier fluid is isopropanol. The vertical axis and horizontal axis show the bubble position and Reynolds number, respectively and the color map indicates the radius of the bubble in μm . In these diagrams, $\bar{Y} = 1$ corresponds to the bubble position at the centerline and $\bar{Y} = 0$ to the bubble position close to the wall. In the square channel, the bubbles are in the center of the channel or the wall based on their diameters, but in the rectangular channels, the equilibrium positions of the bubbles are closer to the smaller sidewall.

2.5.5 The difference between equilibrium positions of bubbles and particles

As shown in Figure 15 for the considered parameter range, the equilibrium position of the bubble in a rectangular channel is close to the shallower edge, whereas it is known that the equilibrium position of a rigid particle in a rectangular channel is the center of the channel's longer wall [58, 68-70]. The different behavior of the bubble and the solid particle is due to the existence of rigid-fluid interface in the former and fluid-fluid interface in the latter case. To have a better comparison between rigid particles and bubbles, it is possible to add a surfactant to the carrier fluid to make bubbles behave similar to rigid particles [71, 72]. Figure 16 shows the equilibrium position of particles when the carrier fluid is water and the equilibrium position of bubbles when the continuous phase is water or a solution of water and a surfactant (a 1% volumetric aqueous solution of Triton X-100) in the channel with $150 \mu m$ width. This figure demonstrates that even with small amount of the surfactant, the bubbles move to the center of the wider channel while at the same Re , bubbles in surfactant-free water stay close to the shallower wall. By adding the surfactant to the liquid, molecules of the surfactant are adsorbed at the interface, rendering it as a no-slip surface. This phenomenon reduces the interaction of the two fluids at the interface and makes the bubbles to behave similar to the rigid particles. Figure 17 shows the schematic of the equilibrium position of clean bubbles, contaminated bubbles, and solid particles in the cross section of the channel. A clean bubble goes towards the shallower wall while a solid particle or a contaminated bubble stabilizes at the center of the wider sidewalls [68, 69].

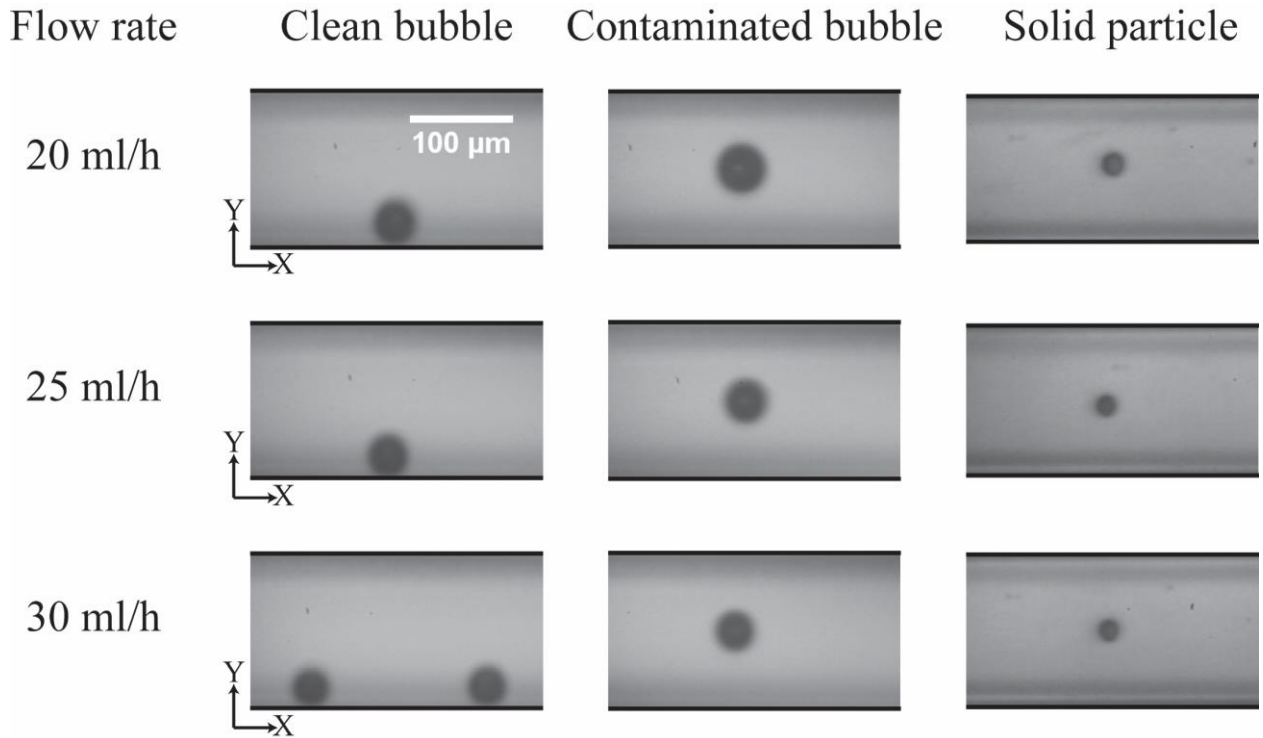


Figure 16. Experimental results that show different equilibrium position of bubbles and particles: addition of a small amount of surfactant forces the bubble to behave like a particle. At the same flow rate, the equilibrium position of contaminated bubbles and solid particles are at the center of the wider channel while clean bubbles stay close to the shallower wall.

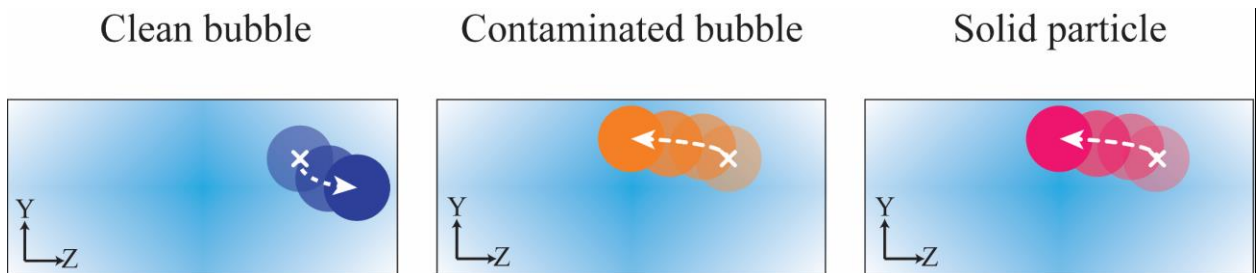


Figure 17. Schematic of the equilibrium position of a bubble in a clean carrier fluid (left), a bubble in a carrier fluid with surfactant (middle), and a solid particle (right). Different circles show the position of circles at different times (× marks the initial position). The clean bubble goes to the center in the Z direction and moves towards the shallower wall. The solid particle and contaminated bubble move towards the center of the wider channel and stay centered in the Y direction.

2.5.6 Transition of the bubble position

Given the importance of the Re , and Ca , it is of interest to elaborate more on their combined impact on the bubble behavior. Simulations are done for a bubble with the diameter of $\bar{D} = 0.4$ at different combinations of Ca and Re . In the simulations, the bubble is initially positioned at $(\bar{Y}, \bar{Z}) = (0.7667, 0.6)$ in a square channel. Color coding the equilibrium position of the bubble in Figure 18 for different Ca and Re helps to highlight the transition zone of the bubble position from the center to the wall. This figure displays that at high Re , the bubble moves to the wall (Small \bar{Y}) while at high Ca the bubble moves to the centerline (large \bar{Y}). This diagram helps in predicting the bubble position in the channel at different flow conditions. Analogous diagrams can be drawn for different bubble diameters using the proposed numerical tool.

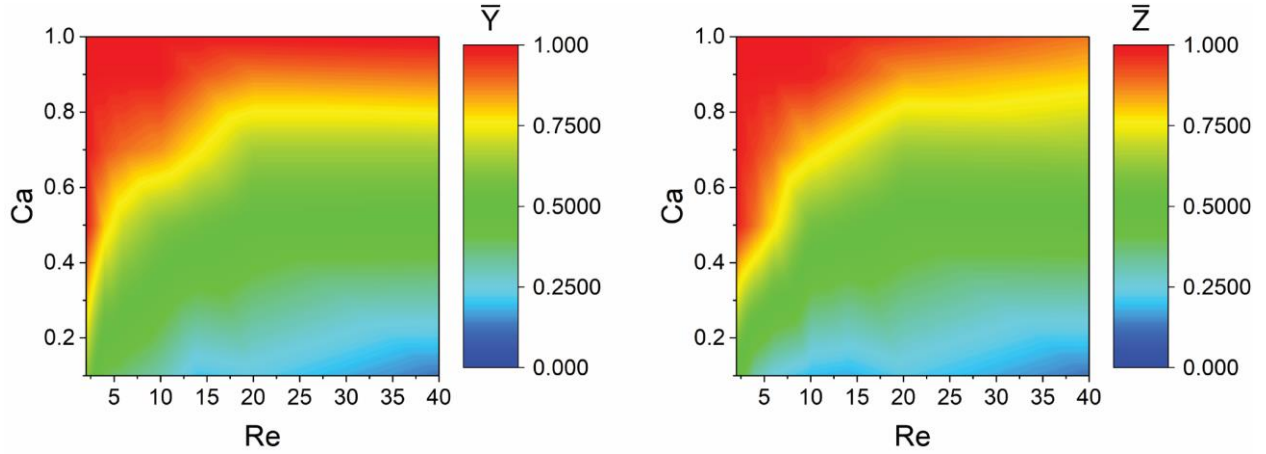


Figure 18. Simulation results for the equilibrium position of a bubble with $\bar{D} = 0.4$ and initial position of $(\bar{Y}, \bar{Z}) = (0.7667, 0.6)$ in the channel at different Re and Ca.

2.6 Conclusion

Monodisperse bubbles' motion in rectangular microchannels was investigated in order to observe their crossflow equilibrium position. The diameter of the bubble, the aspect ratio of the channel, Reynolds, and Capillary numbers are found to be the critical parameters. Analysis of the results reveals the pattern of the changes in bubbles' position. Both numerical and experimental data show that high Re flow pushes the bubbles towards the wall. Also, bubbles in the channel with aspect ratio higher than unity move to the shallower sidewall and by increasing the aspect ratio of the channel their distance from the center increases. On the other hand, by increasing the Capillary number, the bubble moves close to the center and for bubbles with $\bar{D} = 0.4$ in a square channel, at Capillary numbers higher than 0.9 their equilibrium position is at the centerline. Moreover, bubbles that have a radius smaller than half of the width of the channel move to the wall while bubbles with a radius larger than half of the channel's width move to the centerline. The comparison between the equilibrium position of a bubble and a solid particle demonstrates that the shallower wall of the rectangular channel is the equilibrium position of the bubble while the solid particle moves to the center of the wider sidewall. This study provides insights on the effective parameters in the bubble motion and the methods we presented can be employed in designing multiphase microfluidic devices. Future studies on the interactions of bubbles introduced from multiple side channels with various sizes will shed light on the complex dynamics of bubbly flows.

Chapter 3

The impact of surfactants on the inertial separation of bubbles in microfluidic electrolyzers

This chapter is the postprint version of the following article published in *Journal of the Electrochemical Society*.

The Impact of Surfactants on the Inertial Separation of Bubbles in Microfluidic Electrolyzers

Pooria Hadikhani¹, S. Mohammad H. Hashemi^{1,2}, and Demetri Psaltis¹

¹ Optics Laboratory, School of Engineering, Swiss Federal Institute of Technology Lausanne (EPFL), Lausanne, Switzerland

² Computational Science & Engineering Laboratory, ETH Zurich, Zurich, Switzerland

Journal of the Electrochemical Society 167 134504 (2020)

<https://doi.org/10.1149/1945-7111/abb6ca>

Improving the throughput of electrochemical reactions such as water electrolysis is an ongoing effort. In a membrane-less electrolyzer, product separation can be achieved via controlled two-phase flows within the electrochemical flow cells. In this case, it is important to keep the diameter of the bubbles small while ensuring that they follow an off-center trajectory in the channel. This can be accomplished by either increasing the flow, which in turn increases the power loss due to the fluidic resistance, and/or decreasing the electrical current which means a lower production rate. To avoid these drawbacks, here we show that by adding surfactants to the electrolyte, bubbles are kept smaller due to the bubble coalescence inhibition and faster bubble detachment from the electrodes. We find that by using surfactants, the required flow rate for efficient product separation and the corresponding pumping power decrease. Moreover, we show that higher throughputs can be achieved at a given flow rate by using surfactants. The surfactant used in this study introduces an undesirable increase in the overpotential. This is compensated at high production rates by a decrease of the ohmic resistance due to the surface screening of the electrodes by the generated gas bubbles.

3.1 Introduction

Hydrogen is a clean fuel for storing energy coming from renewable energy sources [73]. The key technology for clean hydrogen production is water electrolysis [74]. To use hydrogen as an energy carrier, electrolysis needs to become more economical [75]. In recent years, many studies have focused on improving the efficiency and throughput of electrolyzers to make them a low-cost alternative to the less expensive, but polluting methods such as methane steam reforming [76]. Membrane-less electrolyzers [20-22, 38, 77] relies on the fluidic flow and do not need the membranes or separators. Removing the membrane simplifies the design of the electrolyzers and can reduce the capital cost [22]. Liquid flow in the membrane-less electrolyzers prevents the gas cross over [20]. The removal of the membrane has been

investigated in other microreactors such as fuel cells [78-83] and flow batteries [84-87]. In the membrane-less electrolyzers, the liquid flow prevents the mixing of oxygen and hydrogen products. There are two types of membrane-less electrolyzers based on the electrodes configuration [22]. The first type contains two parallel electrodes and the liquid flows between them. In this case, the separation of hydrogen and oxygen bubbles is provided by inertial forces which keep the bubbles near the electrodes where they were generated [20, 21]. In the second type, the electrodes are porous and the liquid flows through mesh electrodes [38, 77, 88-90]. The hydrogen and oxygen bubbles flow through the mesh electrodes in opposite directions.

The energy conversion efficiency and product separation are two important considerations in the design of membrane-less electrolyzers. The energy conversion efficiency of a membrane-less electrolyzer is optimized by minimizing both electrical (ohmic) and fluidic resistance [39]. On the one hand, decreasing the electrodes distance reduces the electrical loss. On the other hand, the fluidic resistance increases at smaller electrodes distance as narrower channels impose larger pressure drops. The utilization of microchannels with sub 500 microns widths minimizes the overall loss and leads to a higher energy conversion efficiency [39]. However, product separation is challenging in such channels without using a membrane. The diameter of the entrained bubbles should be kept small to avoid bubbles crossing over to the opposite half-cell. The bubbles become small if they detach faster from the electrode and they do not coalesce in the interelectrode region. Increasing the flow rate decreases the diameter of bubbles by exerting larger forces on the pinned, growing bubbles [91, 92]. Furthermore, electrolyte properties such as surface tension affect the bubble detachment and coalescence. These properties can be modified by using additives that accelerate the detachment process [93, 94] or hinder the coalescence [95-97].

In this chapter, we first discuss the important forces acting on the bubble while it is growing and after its detachment. Afterwards, we study the effect of the flow rate on the bubble size and product separation. We then modify the electrolyte surface tension by adding different concentrations of a surfactant and compare the results with the surfactant-free electrolyte. A surfactant decreases the surface tension between the gas and the liquid and prevents the coalescence of bubbles. These effects lead to a reduction in bubbles size which improves product separation. Finally, we explore the effect of the surfactant on the electrode surface coverage by the bubbles as this phenomenon has a direct impact on the efficiency of the reactor.

3.2 Methods

The microfluidic electrolyzer of Figure 19 is used to study experimentally bubble motion in a rectangular microchannel. The distance between the electrodes is 123 μm since the maximum energy conversion can be achieved around 120 μm [39]. The channel width is 150 μm to be sure that the electrodes are inside the micro-channel. The channels are fabricated with a height of 100 μm because the equilibrium position of small bubbles is at the shallower sidewall in a rectangular channel [23]. Therefore, the bubbles equilibrate close to the nucleation sites.

The channel walls are fabricated in SU8 on a glass substrate. Fluidic ports are punched in a PDMS piece and a thin layer of SU8 is coated on this piece [98]. We then place the SU8 coated PDMS on top of the channels and heat it to 65°C for 15 minutes to create a temporary bond between the PDMS and the SU8 channels. The device was exposed to UV light and then it was baked at 90°C to crosslink the SU8 layer between PDMS and SU8 channels. The bonding

strength was increased by hard baking the device at 135°C for two hours in an oven. The fabrication process of the chip shown in Figure 19b is illustrated in Figure 56 of Appendix B.

There are two sets of electrodes that generate bubbles at different locations along the channel which allowed us to study the bubble interaction in the flow. The two sets of electrodes are separated by 4 mm and are placed at the bottom corners of the channel. This 4 mm distance between the two sets of electrodes allows the bubbles from the first electrodes to reach their approximate equilibrium position when they arrive at the second set of electrodes. Each set contains three finger electrodes to help us monitor bubbles interaction and coalescence while they are growing. Each nucleation site is triangular-shaped with an active area of $120 \mu\text{m}^2$ and made from a 150 nm thick platinum film deposited on top of a 50 nm thick titanium film. The tip of the electrodes should be small to generate small bubbles. However, the size of the tip is determined based on the smallest feature that can be achieved in the fabrication. The tip diameter of the fabricated electrodes is 6 μm . An image of the fabricated electrodes is shown in Figure 57 of Appendix B. The active area is $120 \mu\text{m}^2$ as a result of connecting this tip to the electrical connecting line. There is a Y-shape channel before the outlet for the product separation.

A syringe pump (Cronus Sigma 1000 Series) is used to flow 0.5 M sulfuric acid in the channel and the current is applied to the electrodes using a potentiostat (Bio-Logic SP-300). The potentiostat has two channels. Each channel is used to apply current to a set of electrodes. The current is 18 μA at an applied potential of 3V in the 0.5 M sulfuric acid. We increased the applied currents up to 200 μA in order to determine at what production rate the cross over happens. The electrolyte infiltrates into the area of the electrode beneath the channel walls. Consequently, the electrode active area is higher at this current. This infiltration happens only in the electrode areas. Thus, the position where the bubbles are being introduced to the flow remains the same at high currents. The current is reported instead of the current density in this study since the active area increases at high currents.

Triton X-100 is used as the surfactant in the 0.5 M sulfuric acid. The reason for using Triton X-100 is that it is not corrosive to the SU8 walls. This surfactant can be oxidized at the anode which leads to the degradation of the surfactant. The faradaic efficiency of the oxygen evolution reaction can decrease up to 4% in the presence of this surfactant [99]. This is discussed in more detail in section B.2 of Appendix B. But it does not participate in the hydrogen evolution reaction [99]. Furthermore, this surfactant does not affect the electrolyte conductivity [100] and we did not observe any effect on the onset potential using this surfactant. The viscosity of the electrolyte does not change significantly within the surfactant concentration range used in this study [101, 102]. Table 5 shows concentrations of the surfactant used in this study and their corresponding surface tension. The C^* is the normalized concentration of the surfactant by the critical micelle concentration (CMC). The CMC of Triton X-100 is 0.3 mM [103]. The surface tension is measured using the pendant drop method [64] where the falling droplet images are captured using KRUSS DSA-30 drop shape analyzer.

A transmission mode optical microscope with white light illumination is used for imaging. Videos of bubble motion in the microchannel are recorded using a high-speed camera (Photron FASTCAM Mini UX100) with a frame rate of up to 10000 fps. The OpenCV library [104] in Python is used to detect bubbles assuming they are spherical and determine their size and position. The image processing is explained in section B.2 of Appendix B. Table 9 in section

B.2 of Appendix B shows that the image processing method can detect more than 87% of the generated bubbles. The average volume of bubbles is calculated after image processing. Afterwards, the average bubbles' radius reported in the results section are calculated based on this average volume using the sphere volume equation. Figure 19c shows an example of bubble generation in the microchannel at different channel sections.

The liquid flow is laminar in the range of Re ($10 < \text{Re} < 62$) used. The diffusion perpendicular to the flow is the mechanism that can lead to the cross over of the dissolved gas in the liquid. Peclet number (Pe) determines the importance of diffusion in the dissolved gas cross over [79]. Pe is defined as below:

$$Pe = \frac{VL}{D_{dif}} \quad (1)$$

where V is the mean liquid velocity, L is the interelectrode distance, and D_{dif} is the diffusion coefficient. In this study, Pe is more than 2300. The transport due to the diffusion is very small compared to the liquid convection at this Pe. Thus, the cross over of dissolved gas is negligible compared to the bubbles cross over. Furthermore, the Laplace pressure of the detected bubbles is less than one bar. This pressure difference does not increase significantly the hydrogen and oxygen solubility in the electrolyte.

The cross over is mainly due to the migration of the bubbles to the opposite side. In this study, a bubble is considered a crossed bubble when its boundary crosses the channel centerline. The cross over is defined as the ratio of the total volume of crossed bubbles to the total volume of the bubbles. The cross over percentage considers hydrogen and oxygen bubbles together. The cross over can be between 0 to 100% based on this definition.

Table 5. Surface tension between air and 0.5 M sulfuric acid at different concentrations of Triton X-100. C^* is the normalized concentration of the surfactant by the CMC.

Concentration of Triton X-100 in 0.5 M sulfuric acid (mM)	Normalized concentration C^*	Surface tension σ ($\frac{\text{mN}}{\text{m}}$)
0	0	68
1.9	6	29
7.5	25	29
15.1	50	29

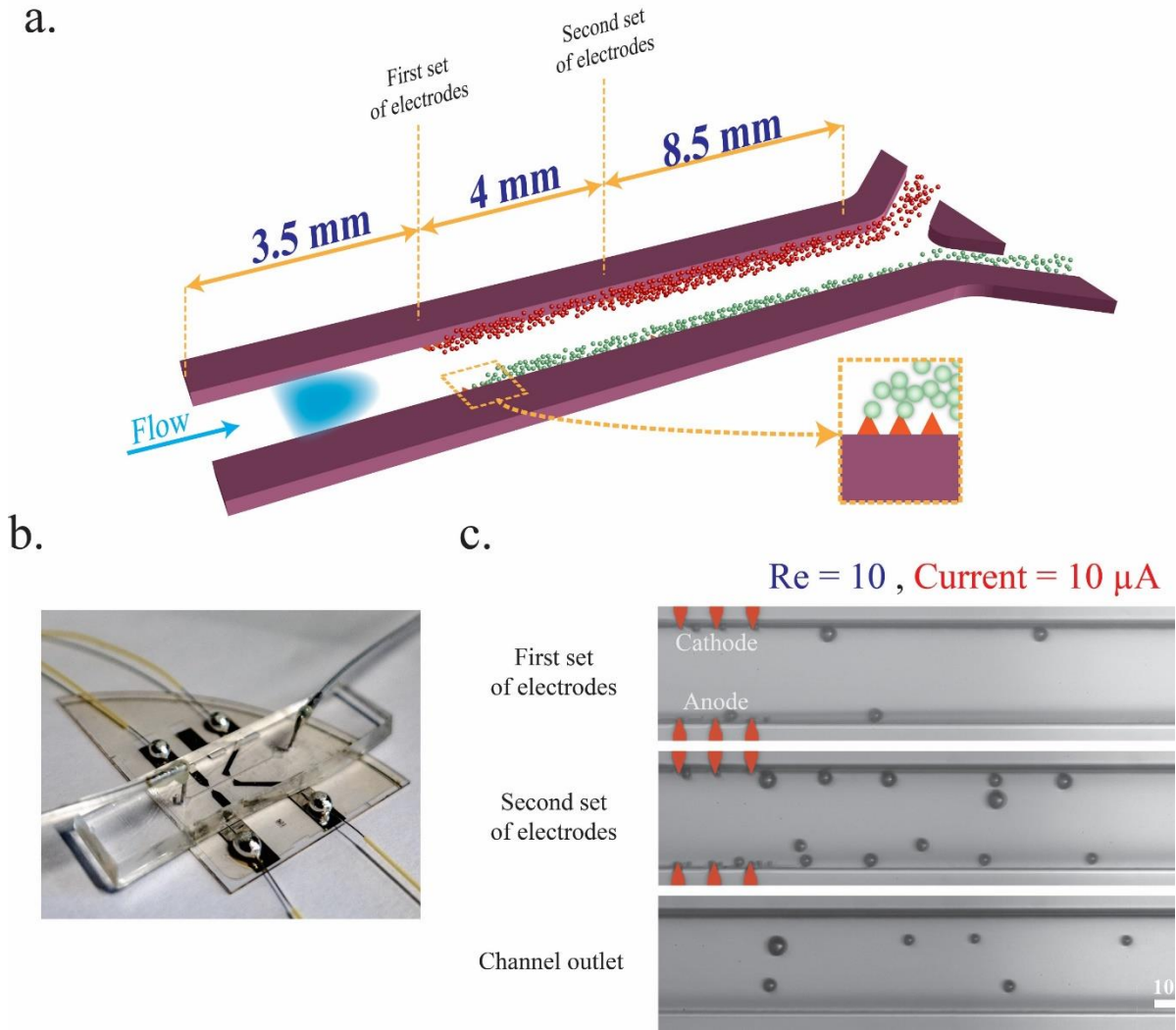


Figure 19. a. Schematic representation of the microfluidic device with two sets of small electrodes, b. a picture of the fabricated device, c. instances of bubble generation at the first and the second set of electrodes and the bubble motion at the end of the channel. There are three finger electrodes at each set of electrodes in order to consider the bubble coalescence and interaction during the bubble growth. The bubbles detached from the first set of electrodes interact and coalesce with the bubbles of the second set. This coalescence and interaction affect the bubble detachment size at the second set of electrodes.

3.3 Forces acting on the bubble

Figure 20 shows the forces acting on the bubble during the detachment process and when the bubble is moving in the channel. The effect of gravity is neglected since the ratio of the inertial forces to the gravitational forces is larger than one. The balance of forces that contribute to the bubble pinch-off are as follows [105-109]:

$$\begin{aligned} \sum F_x &= F_{\sigma,x} + F_{G,x} + F_{G,bulk} + F_D \\ \sum F_y &= F_{\sigma,y} + F_{G,y} + F_{SL} + F_{CP} \end{aligned} \quad (2)$$

F_{σ} is the surface tension force that keeps the bubble attached to the electrode surface. This force has two components and it acts parallel and perpendicular to the flow direction. The parallel component of the surface tension force is the result of the asymmetric growth of the bubble [108]. F_G is the force acting on the bubble due to the bubble growth. This force is proportional to the bubble growth rate [106, 109]. $F_{G,bulk}$ is the bubble growth force in a bulk

liquid velocity field and it contributes to the bubble detachment [109]. This force is proportional to the bulk liquid velocity and the bubble growth rate. F_{SL} is the shear lift force that helps the bubble detachment [105]. This force is the result of a non-uniform velocity profile close to the wall [106]. F_D is the drag force acting on the bubble due to the moving liquid around the bubble [105, 107]. This force is proportional to the liquid velocity and it is in the direction of the liquid flow [109]. F_{CP} is the contact pressure force [108]. This force is due to the difference between the bubble pressure and the surrounding liquid pressure at the contact line of the bubble and the wall [107, 109]. This force is proportional to the surface tension and it assists the bubble detachment [107].

The balance of these forces determines the bubble detachment size and frequency. The bubble starts to slide on the wall in the x-direction when the balance of the forces becomes zero in the x-direction. The force balance in the y-direction is zero when the bubble detaches from the wall [108]. The approximate expressions of these forces are discussed in section B.3 of Appendix B. The bubbles are generated at the corner of the channel in the experiments. These bubbles are in contact with two perpendicular walls. The force balance shown in Figure 20a describes a bubble in contact with only one wall. Although this model is not an accurate representation of the bubbles generated in the experiment, it elucidates the bubble detachment process and the effective parameters.

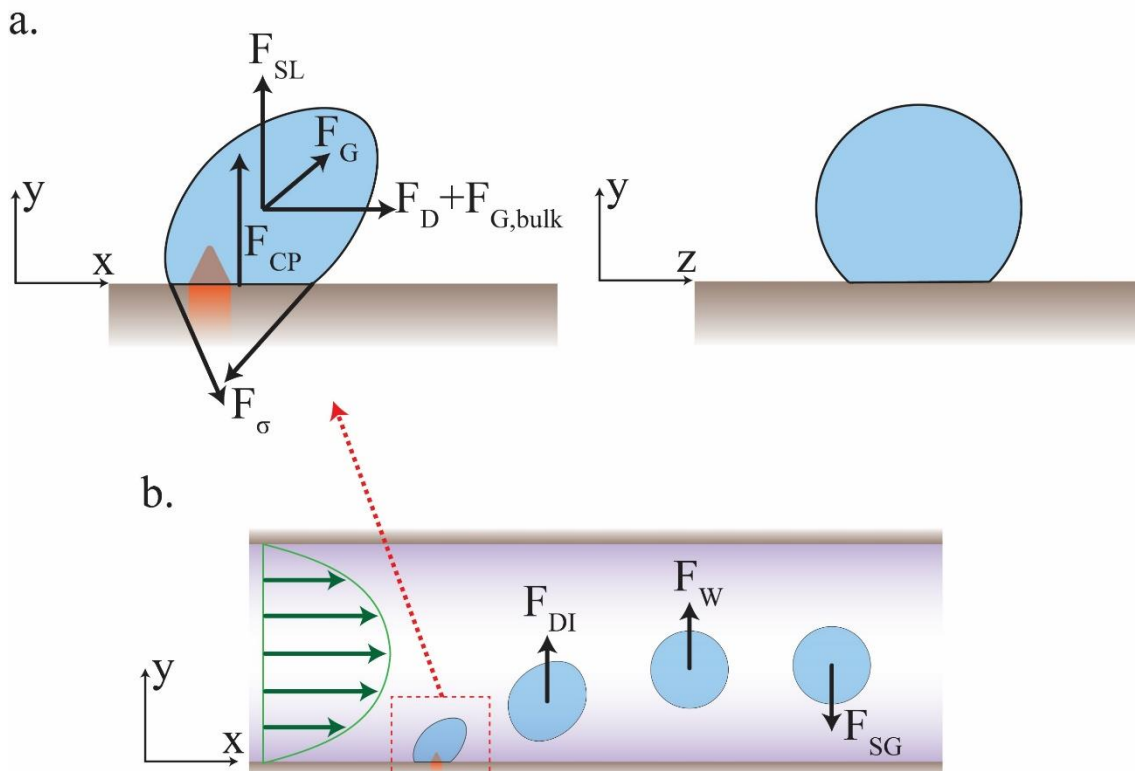


Figure 20. The important forces acting on the bubble: a. before the bubble detachment and b. after the bubble detachment. a. The forces that contribute to the bubble detachment are the shear lift force (F_{SL}), the contact pressure force (F_{CP}), and the drag force (F_D). The surface tension force (F_σ) prohibits the bubble detachment. b. The balance of forces acting on a moving bubble in a channel determines the bubble equilibrium position. The deformation induced lift force (F_{DI}) and the wall lift force (F_W) push the bubble towards the centerline. The shear gradient lift force (F_{SG}) pushes the bubble towards the wall.

The bubble moves in the flow direction due to the drag force after the detachment. The important forces that determine the lateral equilibrium position of the bubble are the shear gradient lift force, the wall induced lift force, and the deformation induced lift force [23, 110].

The velocity profile in the channel is non-uniform which creates different relative velocity and pressure distribution around the bubble [55, 111]. The shear gradient lift force is due to this difference in the relative velocity and its direction is towards the wall. The presence of the bubble close to the wall creates an asymmetry in the flow field [58]. The wall induced lift force is the result of this asymmetry in the flow field and its direction is towards the channel centerline. The surface energy of a bubble is at the minimum state when it has a spherical shape. The deformation of the bubble creates the deformation induced lift force towards the channel centerline where the bubble can have the smallest deviation from the spherical shape [58, 112]. In an electrolyte with a surfactant, the surfactant molecules move to the interface of the bubble. The bubble interface becomes immobile and the bubble starts to rotate when the surfactant molecules cover the interface completely [113, 114]. The rotation of the bubble induces the rotation induced lift force towards the centerline [58]. These forces are dependent on the flow velocity, the bubble deformation, the bubble diameter, and the geometry of the cross sectional area of the channel [23].

3.4 Results and discussion

We present the results obtained by changing the velocity and the surfactant concentration in the electrolyte and observing their influence on the product separation, the bubble diameter, and the bubble coverage of the electrodes. We use the Reynolds number (Re) as the measure of the flow rate. The Re is calculated using the following equation:

$$\text{Re} = \frac{\rho V D}{\mu} \quad (3)$$

where ρ is the density, V is the mean liquid velocity, D is the hydraulic diameter of the channel, and μ is the viscosity of the liquid. The corresponding values that are used for the Re calculation are presented in section B.4 of Appendix B.

Figure 21 shows the gaseous products at the end of the channel at different Re and currents using 0.5 M sulfuric acid. At Re=10, the bubbles are large due to the late bubble detachment and coalescence in the flow. These large bubbles move closer to the centerline compared to the smaller ones. At Re 21 and 42, the bubbles are smaller and are pushed further towards the walls as a result of stronger inertial forces. However, some large bubbles still drift very close to the centerline. These outliers are removed at Re=62, where the gaseous products are completely separated. This behavior confirms the results of our previous study [23].

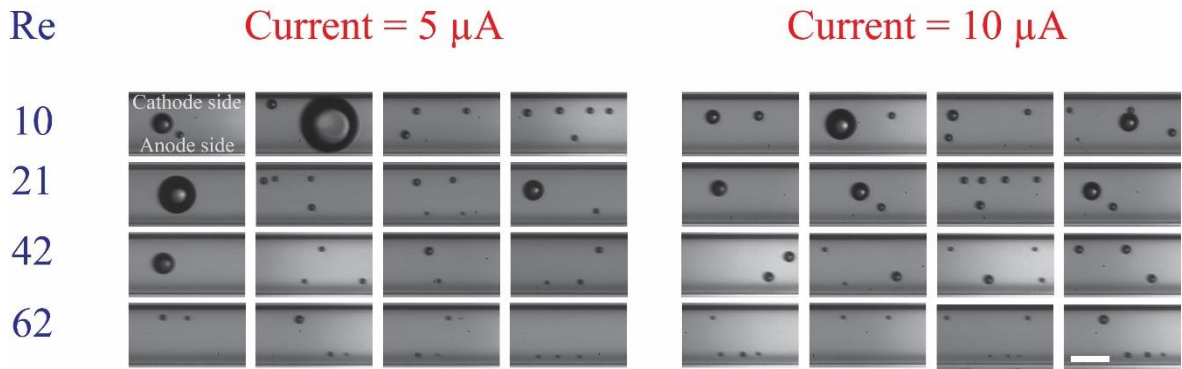
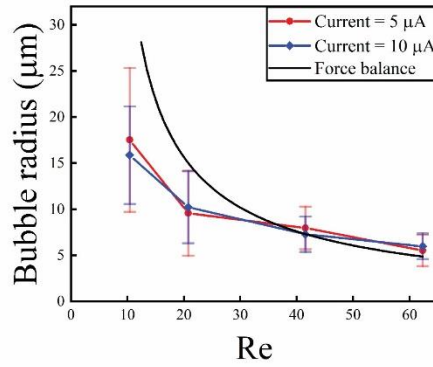


Figure 21. Images of bubbles at the end of the channel at different Re and two different currents using 0.5M sulfuric acid as the electrolyte. The small bubbles move to the sidewalls by increasing the Re. However, the high Re of 42 cannot keep large bubbles at the sidewalls. At the Re of 62, the bubbles are at the sidewalls because the flow detaches the bubbles at smaller sizes. The large bubble at Re=10 does not have a spherical shape because it has a larger diameter than the depth of the channel and its boundaries are in contact with the channel walls. Furthermore, a non-spherical shape can happen when bubbles coalesce where the interface of the bubble deviates from the spherical shape for a short period of time. The scale bar is $100\mu\text{m}$.

Figure 22a shows that the average bubble radius after detachment is inversely proportional to the Re. In this figure, both sets of electrodes are active and the radius is calculated by averaging the radius of hydrogen and oxygen bubbles. The black line is the radius predicted by solving the balance of forces acting on the detaching bubble (Eq. (1)). The predicted radius has the same trend as the experimental results. Their difference originates from the assumptions used to derive the forces such as the constant contact angle assumption, one dimensional flow assumption, and neglecting the gas dissolution and temperature variation close to the electrode that can change the surface tension. Furthermore, the force balance shows that the bubble generation frequency increases linearly by the current as shown in Figure 62 in section B.3 of Appendix B. However, the dependence of the bubble generation frequency on the Re and the shear rate is non-linear [115].

Figure 22b shows the hydrogen and oxygen bubbles radius after the detachment at Re=42 and different currents. This figure demonstrates the effect of the upstream bubble generation on the downstream bubble detachment size. The flowing bubbles from the first set of electrodes coalesce with the growing bubbles at the second set of electrodes. Therefore, the bubbles detachment size is larger at the second set of electrodes when the first set of electrodes is active.

a.



b.

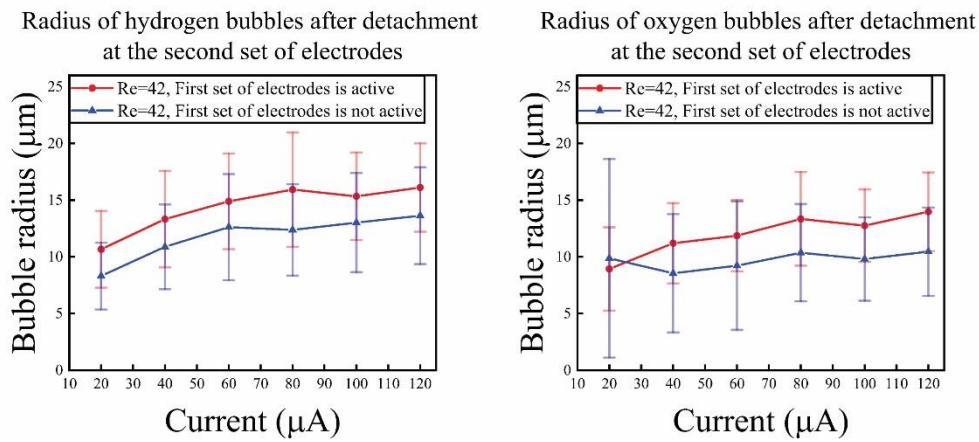


Figure 22. a. The bubble detachment radius at different Re . The blue and red curves show the experimental bubble detachment radius at two different currents. The black line is the detachment bubble radius predicted by solving Eq. 1. The bubble radius shows the average radius of hydrogen and oxygen bubbles together. b. The bubble detachment radius at the second set of electrodes at $Re=42$ and different currents. The bubble detachment size at the second set of electrodes is larger when the first set of electrodes is active. This is due to the coalescence of the bubbles at the second set of electrodes with the bubbles coming from the first set of electrodes.

To quantify the product separation in the microchannel, histograms of volume distribution of bubbles across the channel width are plotted in Figure 23. In the histograms, the purple bars represent the volume of the bubbles whose boundaries cross the channel centerline. The orange and the green color are for the hydrogen and oxygen bubbles that are kept separated. The volume distribution is normalized by the maximum volume of each case. The position of bubbles is normalized to half of the channel width which is $75 \mu m$. The zero on the horizontal axis indicates the channel centerline. The histograms confirm that the distance between the two streams of the bubbles increases as we move towards higher Re . The flow at $Re=62$ achieves complete product separation at currents of $5 \mu A$ and $10 \mu A$. It is possible to increase the current at this Re with an effective product separation. The product separation is effective up to currents below $100 \mu A$ at $Re=62$. At this current level the bubbles start to cross over as shown in Figure 24 and the Re should be increased further for higher production rates.

Re

Current (μA)

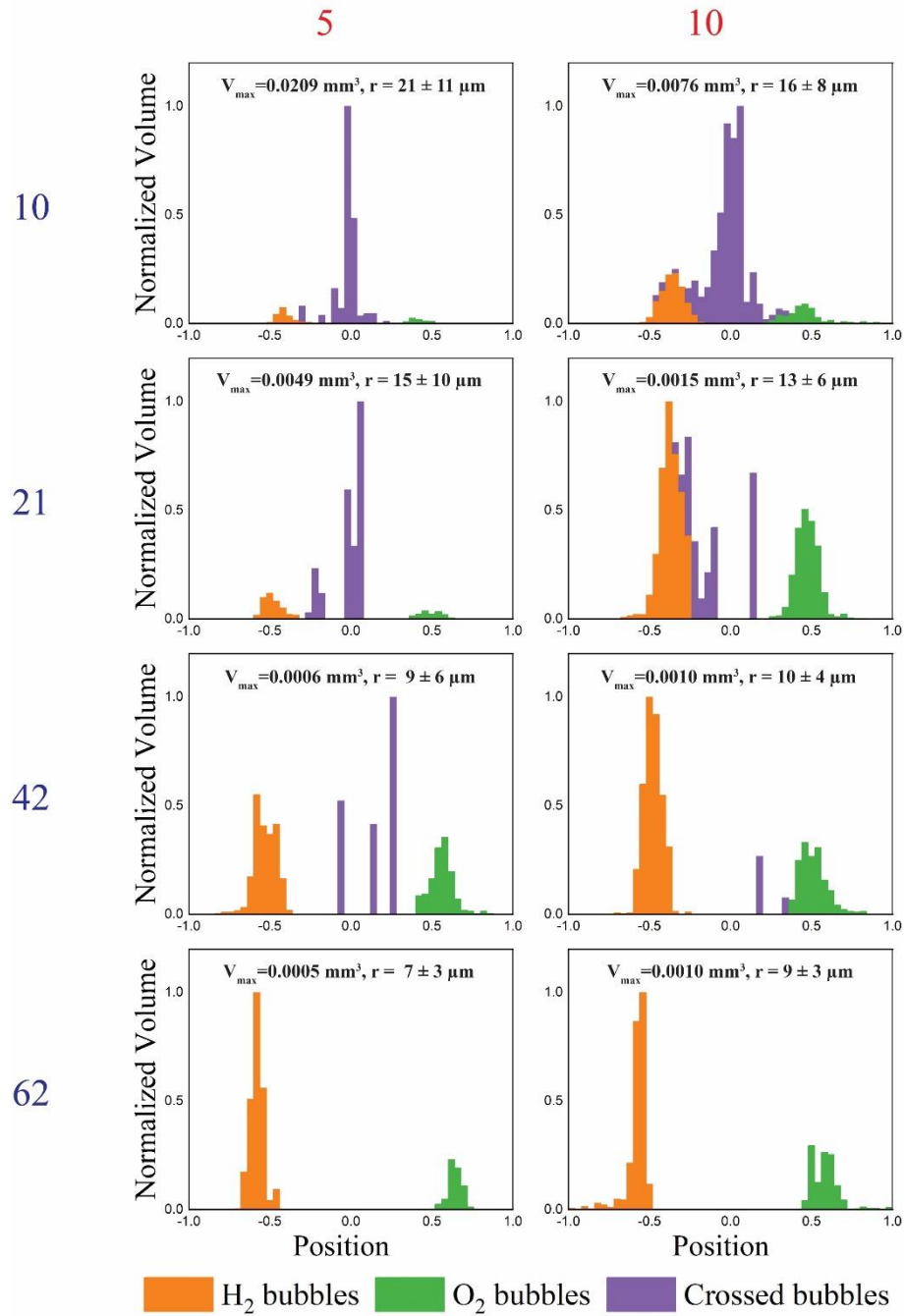


Figure 23. The histograms of bubbles volume distribution across the width of the channel width at Re from 10 to 62 and at two different currents of $5 \mu\text{A}$ and $10 \mu\text{A}$: The purple bars show the volume of the bubbles that their boundaries crossed the channel centerline, the orange bars show the volume of hydrogen bubbles, and the green bars show the volume of the oxygen bubbles. The liquid flow pushes the bubbles to the sidewalls and the distance between the stream of bubbles increases by the Re. At Re=62 the two streams are separated since the radii of the bubbles are small and no large bubbles are formed. The position of bubbles is normalized to half of the channel width. Zero on the x-axis represents the channel centerline. V_{\max} and r represent the volume used to normalize the volume and the average bubble radius, respectively.

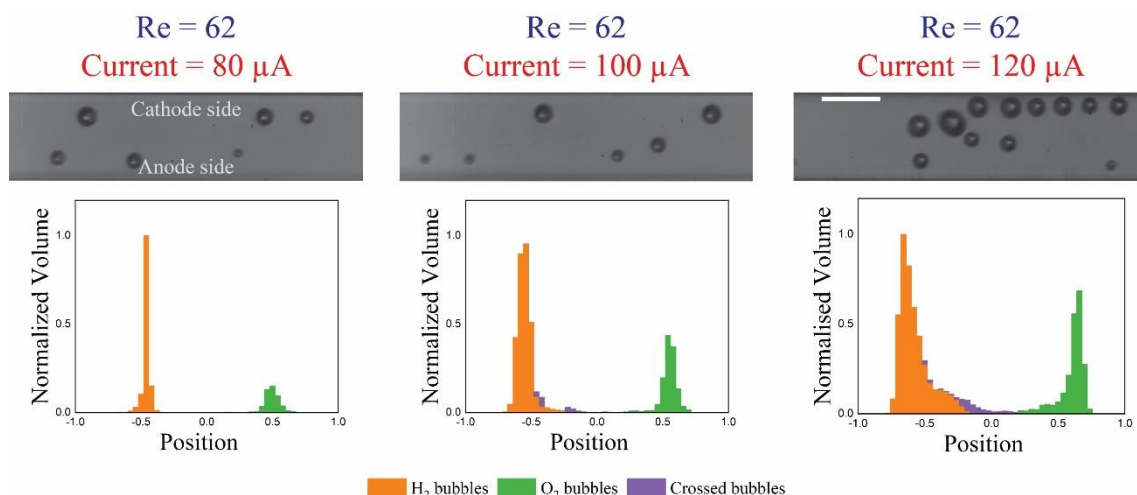


Figure 24. Bubbles generation and flow in 0.5 M sulfuric acid at $Re=62$ and currents from $80 \mu A$ to $120 \mu A$. Top images show instances of bubble motion at the end of the channel and bottom histograms show the corresponding volume distribution of bubbles. The cross contamination starts at the current equal to $100 \mu A$. The scale bar is $100 \mu m$.

Based on calculations of section B.5 of Appendix B, the power needed to increase Re from 10 to 62 rises from $7 \mu W$ to $248 \mu W$. This non-linear dependence indicates the significance of the flow rate optimization in the cell. There is no need to increase the velocity if the bubbles stay small in the channel, and the flow can separate the products efficiently at smaller Re . The bubble detachment frequency and the coalescence are two phenomena that determine the bubble size at the end of the channel. The detachment process depends on the surface tension of the liquid-gas interface [92, 105, 116-118]. The addition of a surfactant to the electrolyte reduces the surface tension [119] that leads to the bubble detachment at a smaller size. In addition, the bubble coalescence can be hindered by increasing the surfactant concentration as a result of full coverage of the bubble interface by the surfactant molecules [113].

We use different concentrations of Triton X-100 as the surfactant in 0.5 M sulfuric acid to investigate the effect of the surfactant concentration on the size of bubbles and product separation. Figure 25 shows the position of bubbles at the end of the microchannel and the corresponding histograms are shown in Figure 26. The radius of the bubbles at different concentrations of the surfactant is shown in Figure 27. This figure shows the average radius of hydrogen and oxygen bubbles together. Figure 65 in Appendix B shows the radius of hydrogen and oxygen bubbles separately. At a low concentration of surfactant ($C^* = 6$) the radius of bubbles is about one-fifth of the channel width. At this diameter, the equilibrium position of bubbles in the electrolyte with surfactant in a rectangular channel is at the center of the wider sidewall [58, 68, 69]. Therefore, at low concentrations, most of the gaseous products cross over even at Re of 62.

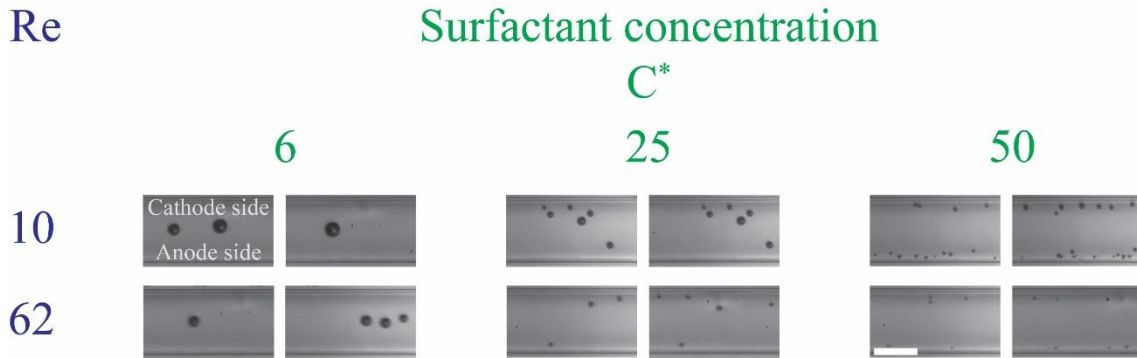


Figure 25. Images of bubbles motion at the end of microchannel using 0.5 M sulfuric acid at three different concentrations of Triton X-100. At $C^* = 6$, most bubbles are flowing in the center of the channel and increasing the Re to 62 cannot push the bubbles to the sidewalls. At higher concentrations of surfactant, the bubbles become smaller and move close to the wall. At $C^* = 50$, the two bubbles streams are completely separated from each other. The applied current is $5 \mu A$. The scale bar is $100 \mu m$.

The diameter of bubbles is smaller at higher concentrations of surfactant as shown in Figure 27, even though the surface tension does not change by increasing the concentration of surfactant from $C^* = 6$ to $C^* = 50$ as shown in Table 5. In an electrolyte with surfactant, a finite time is required for the micelles of the surfactant to cover the bubble interface and reduce the surface tension when a new bubble is generated. The time that is needed for micelles to cover the bubble interface is shorter at higher concentrations of the surfactant [120]. Thus, the diameter of bubbles is smaller at higher concentrations of surfactants [121] as shown in Figure 27. Furthermore, the radius of the flowing bubbles stays small and constant by using the surfactant due to bubble coalescence inhibition. Figure 28a shows the effect of surfactant on the bubble radius at different positions of the channel. This figure shows that the bubbles are smaller by using the electrolyte with surfactant at $C^* = 50$ and their radius stays constant while they are flowing in the channel.

C^*

Re

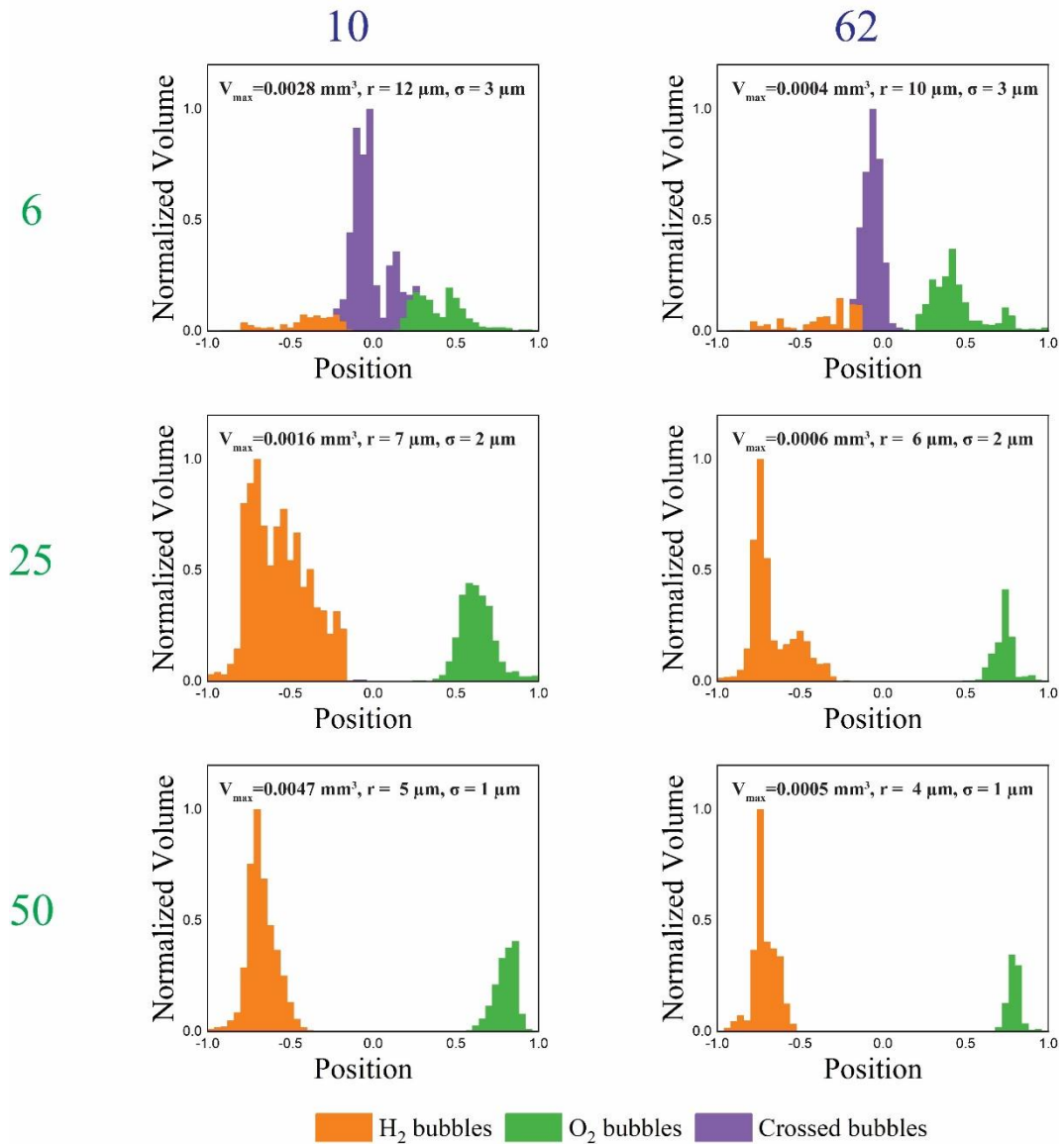


Figure 26. Bubbles volume distribution at the end of the channel at three different concentration of surfactant in 0.5 M sulfuric acid. At $C^* = 6$, the bubbles detach at large radii. The equilibrium position of these bubbles is at the center of the channel which is not desired. The histograms of $C^* = 25$ and $C^* = 50$ show that increasing the surfactant concentration leads to the flow of smaller bubbles in the channel. The flow can efficiently separate these small oxygen and hydrogen bubbles.

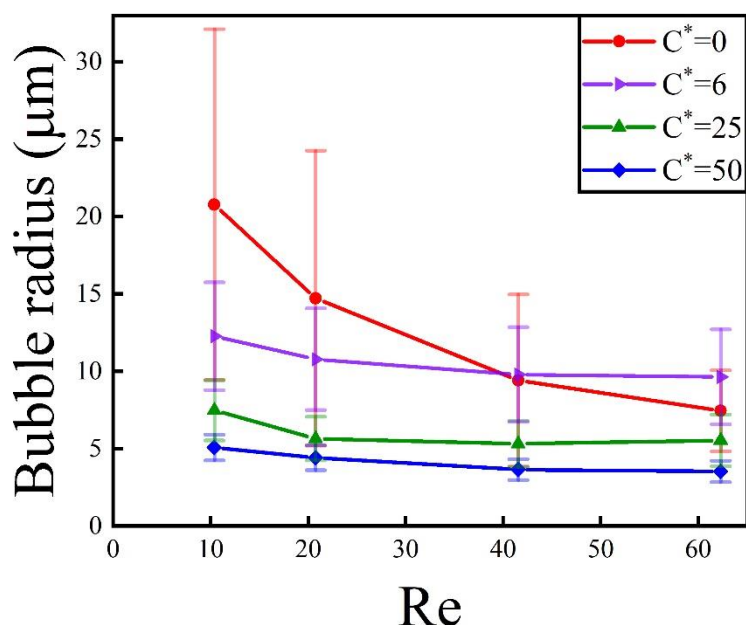


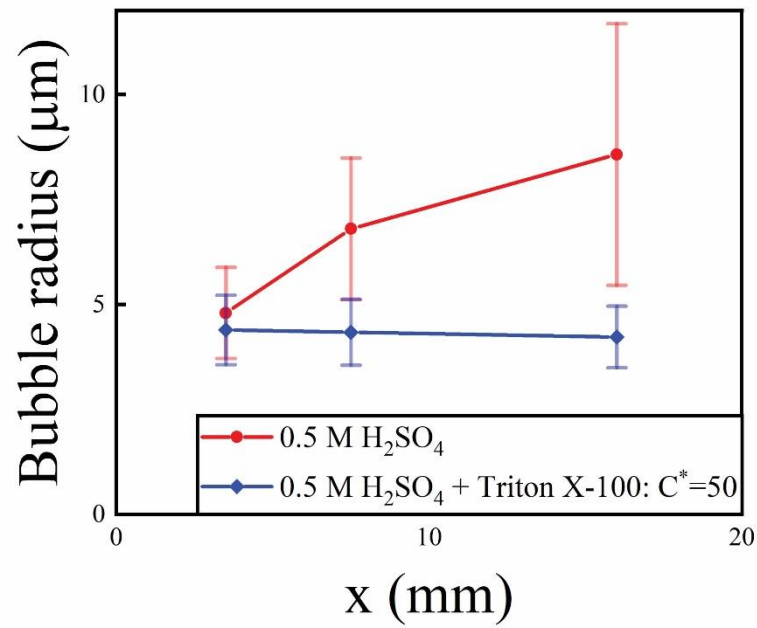
Figure 27. The diagram shows the change in the bubble radius in the clean electrolyte and the electrolyte with three different concentrations of surfactant. The applied current is 5 μA .

Figure 28b shows the volume distribution of bubbles at different positions of the channel in the surfactant-free electrolyte and the electrolyte with surfactant. At $C^* = 50$, the bubbles are closer to the shallower sidewall at the end of the channel since the equilibrium position of bubbles is closer to the wall when they are smaller. Therefore, as shown in Figure 29a it is possible to separate the products at smaller Re in comparison with surfactant-free electrolyte when we add a sufficient amount of surfactant to the electrolyte. These bubbles are moving further from the wall at the end of the channel due to the wall induced lift force but the shear gradient lift force keeps these bubbles away from the center of the channel. Furthermore, by adding surfactant to the electrolyte, the throughput of the electrolyzer increases because the bubbles are small enough to stay far from the centerline even at higher currents. Figure 29b shows the separation quality when the applied current increases to 200 μA at Re of 62. A comparison of Figure 29 with Figure 24 shows that a higher production rate can be achieved when the bubbles are smaller using the electrolyte at $C^* = 50$.

Figure 30 depicts the cross over percentage in the 0.5 M sulfuric acid without the surfactant and with the surfactant at $C^* = 50$ in a range of Re ($10 < Re < 62$) and currents ($5 \mu\text{A} < \text{current} < 120 \mu\text{A}$). The cross over percentage is calculated by dividing the volume of the total crossed bubbles by the total volume of the bubbles. This figure clearly shows the decrease in the cross over by adding a sufficient amount of the surfactant to the electrolyte. Figure 66 in Appendix B shows the hydrogen and oxygen cross over separately.

In a membrane-less electrolyzer, the number of bubbles flowing in the channel is large and the coalescence frequently happens which leads to the large bubble creation. The length of these electrolyzers is limited to a length where large bubbles start to appear. The coalescence can be hindered by using the surfactant in the electrolyte. Therefore, the length of the electrolyzer can be extended which is desirable for increasing the production rate.

a.



b.

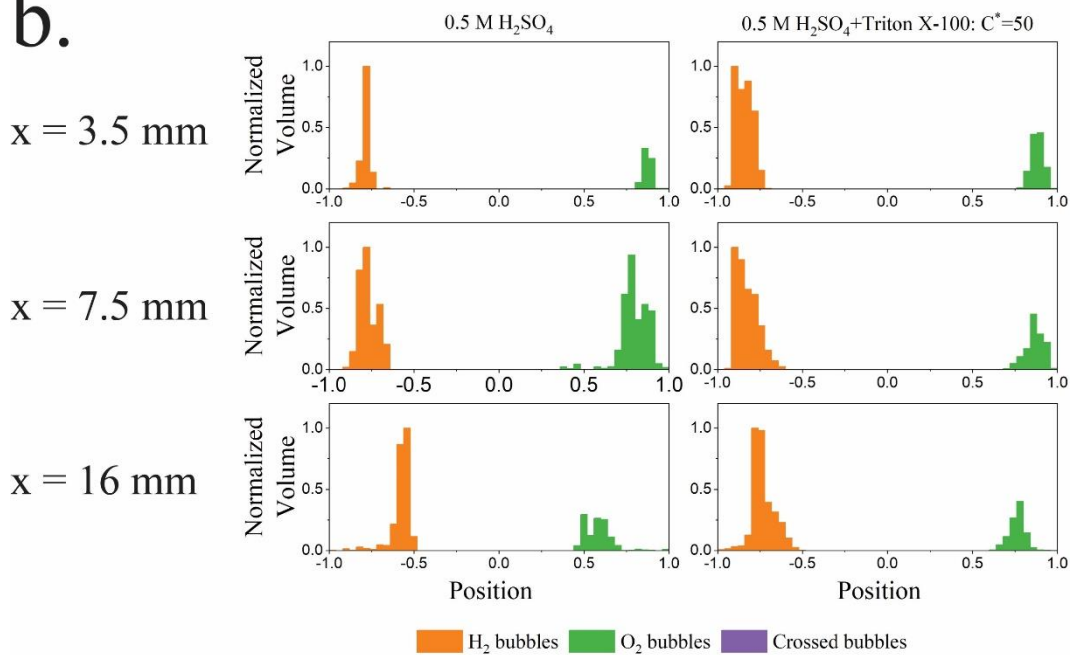


Figure 28. a. The radius of bubbles is plotted against the position in the channel (x) for an electrolyte with and without the surfactant. The bubble radius stays constant in an electrolyte with the surfactant since the bubble coalescence is inhibited in the presence of surfactants. b. The diagrams show the volume distribution of bubbles at different positions of the channel in an electrolyte with and without surfactant. x determines the position in the channel where $x = 3.5 \text{ mm}$ is the position of the first set of electrodes, $x = 7.5 \text{ mm}$ is the position of the second set of electrodes, and $x = 16 \text{ mm}$ is the end of the channel.

The Re is 62 and the applied current is $10 \mu A$.

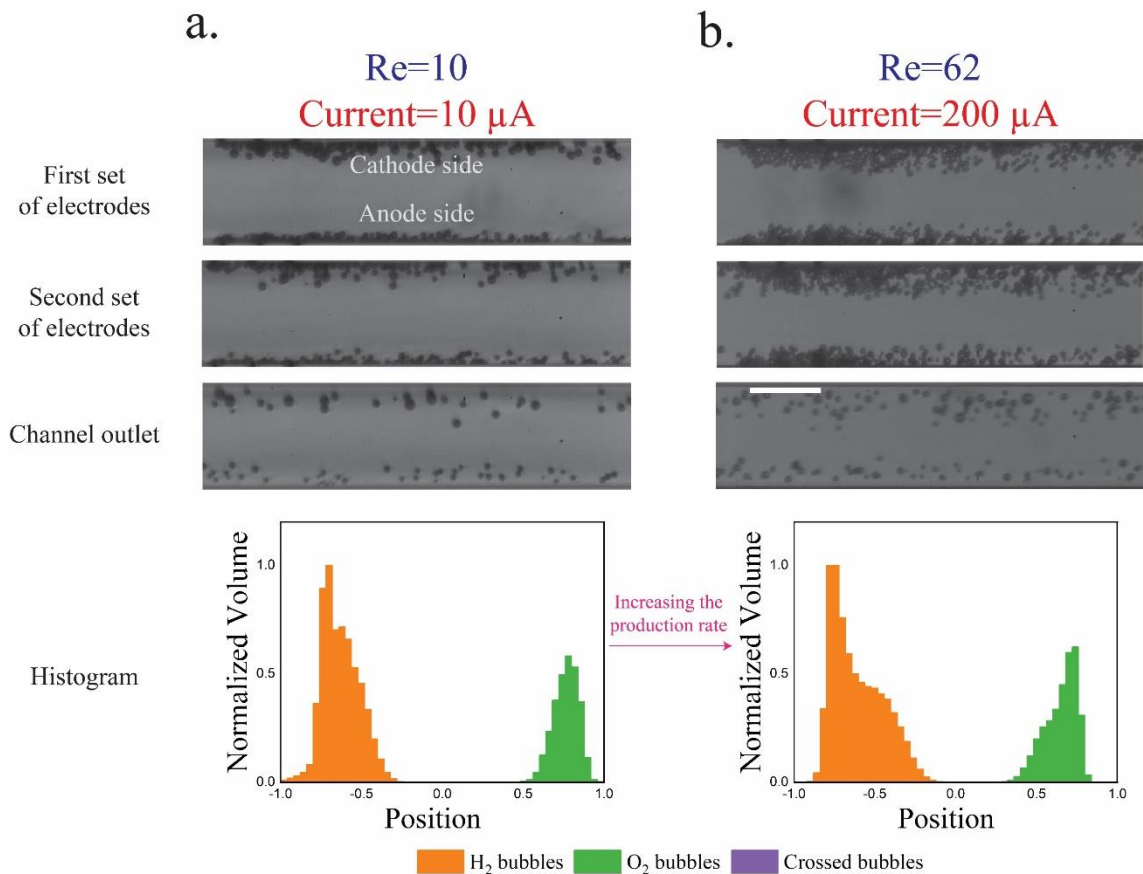


Figure 29. Bubbles generation and motion in the microchannel in 0.5 M sulfuric acid with triton X-100 at $C^* = 50$. Part a. shows the complete product separation in an electrolyte with surfactant that is achieved at smaller Re compared to the surfactant-free electrolyte. Part b. shows that the production rate can be increased with effective product separation using the electrolyte with the surfactant. There are more bubbles at a higher production rate and they spread in a wider area in the channel. Therefore, the distribution of hydrogen and oxygen bubbles is wider in the right histograms. The scale bar is $100 \mu\text{m}$.

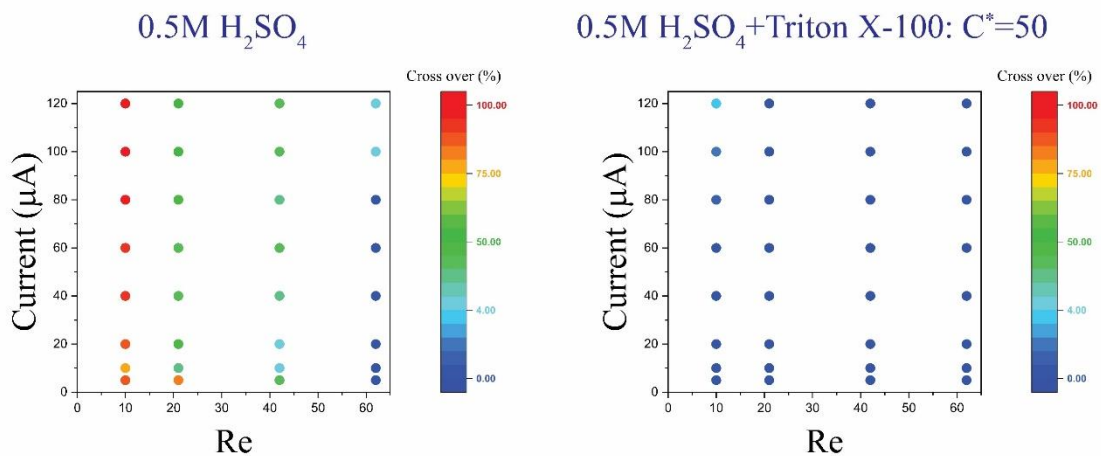


Figure 30. The diagrams show the cross over percentage in the 0.5 M sulfuric acid and the 0.5 M sulfuric acid with Triton X-100 at $C^* = 50$ at different Re and currents. In the 0.5 M sulfuric acid, the cross over is small only at high Re and small currents. In the 0.5 M sulfuric acid with Triton X-100 at $C^* = 50$, the cross over is small (below 4%) over the range of Re and currents shown in the diagram. This diagram indicates the importance of adding surfactant to the electrolyte for effective product separation.

Figure 31 demonstrates the bubble generation in the 0.5 M sulfuric acid without and with surfactant at Re equal to 62 and the current at 800 nA. The bubble grows on the electrode until an equilibrium is achieved between the gas production and the gas dissolution in the surfactant-

free electrolyte. This bubble covers partially the surface of the electrode which reduces its active area. On the other hand, in the presence of surfactants, the residence time of bubbles on the surface of the electrode is shorter compared to the surfactant-free electrolytes since these bubbles detach faster and at smaller radii. This short residence time provides more active areas for the electrochemical reaction and reduces the ohmic resistance between the electrodes induced by the presence of bubbles.

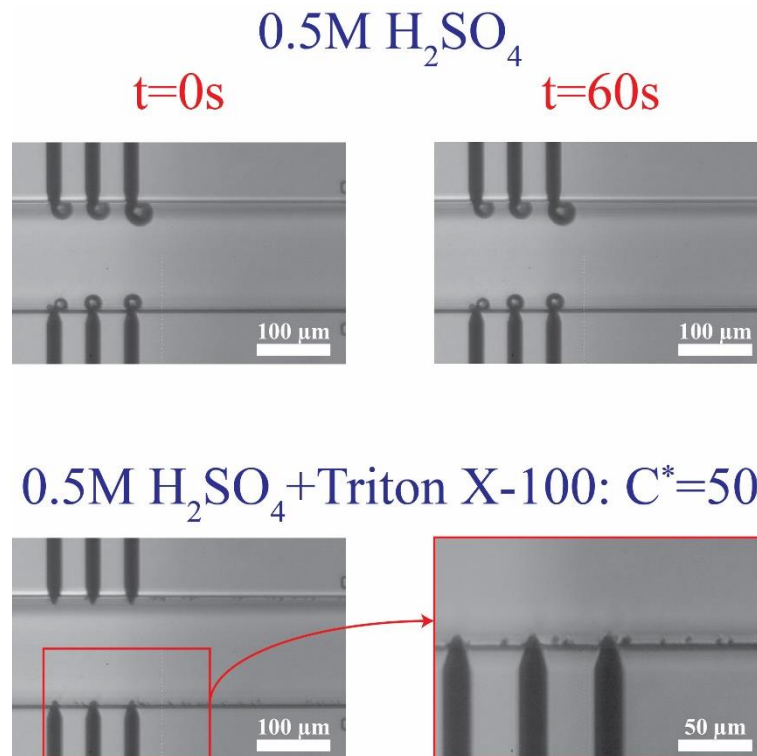


Figure 31. The images of the bubble nucleation at the current of 800 nA in the 0.5 M sulfuric acid without and with surfactant. The Re is 62 . In the clean electrolyte, initially, the bubble grows and then reaches an equilibrium where the amount of gas that is being produced and introduced to the bubble becomes equal to the amount of the gas that is being dissolved in the electrolyte. In this case, the bubble covers the surface of the electrode which increases the ohmic resistance between the electrodes. In the electrolyte with the surfactant, bubbles detach faster and at small sizes. Therefore, the electrode surface remains free for the reaction.

Figure 32.a depicts the current-potential curve of 0.5 M sulfuric acid with and without surfactant at Re of 62 . This diagram indicates that Triton X-100 does not change the onset potential. The Potentio Electrochemical Impedance Spectroscopy (PEIS) measurement shown in Figure 32.b quantifies the resistance of the electrolyte using two platinum wires. The solution resistance of 0.5 M sulfuric acid is $6.7\ \Omega$ and the solution resistance of 0.5 M sulfuric acid with Triton X-100 at $C^* = 50$ is $6.6\ \Omega$. Therefore, the Triton X-100 surfactant does not affect the conductivity of 0.5M sulfuric acid. Figure 32.a shows that the current-potential curve of the surfactant-free electrolyte has a slightly larger slope than the electrolyte with surfactant. This can be the result of the adsorption of surfactant molecules on the electrode surface [122, 123]. The adsorbed molecules can reduce the access of reacting species to the surface of the electrode [124]. However, the potential that is required at high currents becomes approximately 3V in both electrolytes due to the electrode surface coverage in the surfactant-free electrolyte [91, 125, 126].

The electrochemical reaction performance depends on the catalyst material and the surfactant together [127]. Therefore, the performance of the electrolyzer working with an electrolyte with the surfactant can be improved further by using a suitable combination of surfactants and catalysts [127]. For instance, hexadecyltrimethylammonium bromide (HTMAB) surfactant with carbon electrodes can improve oxygen evolution reaction [127] or potassium perfluorooctanesulfonate (PFOS) modulated platinum can improve the hydrogen evolution reaction performance by reducing the dissolved hydrogen concentration close to the electrodes [128].

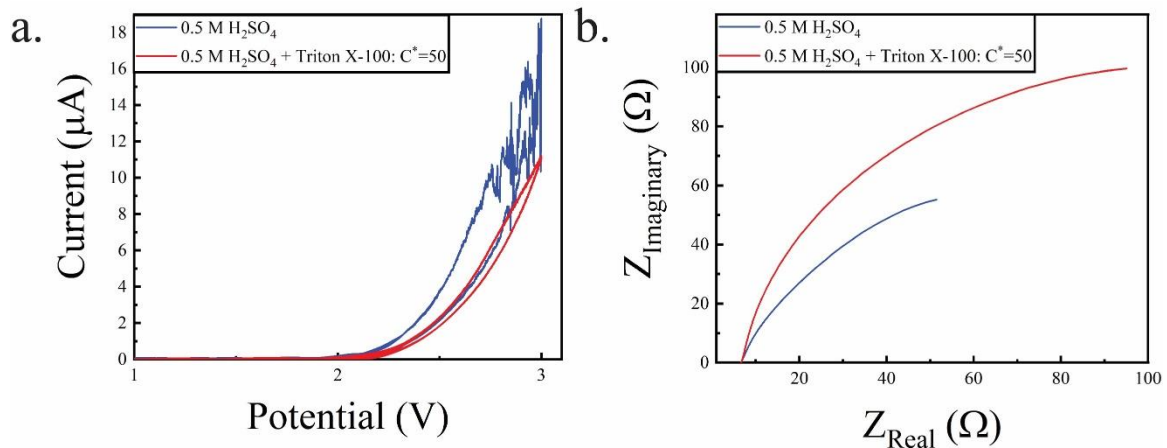


Figure 32. a. The current-potential curve of the water electrolysis in a 0.5 M sulfuric acid with and without the surfactant in the microchannel at $Re=62$. b. PEIS measurement of 0.5 M sulfuric acid and 0.5 M sulfuric acid with surfactant using platinum wires placed at a constant distance from each other. In the PEIS measurement, the applied potential and the sinus amplitude are 2.0 V and 20 mV, respectively. The water splitting starts at the same voltage in both electrolytes and both electrolytes have the same solution resistance. Initially, the current is higher in the surfactant-free electrolyte than the electrolyte with surfactant due to the adsorption of Triton X-100 on the electrode surface. However, by increasing the production rate, the surfactant-free electrolyte diagram becomes noisy due to the long residence time of the bubbles on the electrode. This issue is not present in the electrolyte with the surfactant since the bubbles are detaching fast and their residence time on the electrode is short.

Two-phase flow and the electrochemical performance determine the scale-up strategy of the membrane-less electrolyzers with parallel walls. It is desired to keep the interelectrode distance as small as possible in order to minimize the ionic resistance. The length at which the bubbles start to cross over determines the maximum length of these electrolyzers. This length is longer by using a surfactant in the electrolyte. Furthermore, it is possible to increase the length further by implementing escape points for the bubbles. These escape points are openings in the electrolyzer walls that transfer bubbles to other channels. These escape points prevent the accumulation of bubbles in the channel. The channel depth can be easily scaled up as it has smaller effects on the product separation and the electrochemical performance.

3.5 Conclusion

We investigated the effect of the flow rate and surfactant on the product separation and throughput of the membrane-less electrolyzers. The results show that the inertial forces induced by the liquid flow keep bubbles separated in microchannels, however, a high flow rate ($Re=62$) is required to effectively separate the products due to the coalescence of bubbles in the flow

and large bubbles detachment at the nucleation sites. In such conditions and in the microfluidic channels, the power loss due to the fluidic resistance is comparable to the energy storage in the form of hydrogen. This problem is resolved by adding Triton X-100 as the surfactant to the electrolyte where a lower flow rate ($Re=10$) suppresses the product crossover effectively. This surfactant in the electrolyte assures small bubbles in the flow by inhibiting coalescence and detaching the bubbles faster. Moreover, it is shown that at constant Re of 62, the throughput of the electrolyzer can be increased if the surfactant is added to the electrolyte. A faster detachment of the bubbles from nucleation sites lowers the interelectrode ohmic resistance due to the surface coverage by the bubbles which can compensate for the overpotential caused by the adsorption of the surfactant molecules on the electrode surface. The combination of the catalyst and the surfactant materials determines the electrochemical reaction performance. Combinations such as PFOS surfactant with platinum electrodes or HTMAB surfactant with carbon electrodes can improve the water-electrolysis reaction performance.

Chapter 4

Membrane-less electrolyzer with porous walls for high throughput and pure hydrogen production

Membrane-less electrolyzers utilize fluidic forces instead of solid barriers for the separation of the electrolysis gas products. These electrolyzers have low ionic resistance, simple design, and the ability to work with electrolytes at different pH values. However, the interelectrode distance and the flow velocity should be large at high production rates to prevent gas cross over. This is not energetically favorable as the ionic resistance is higher at larger interelectrode distances and the required pumping power increases with the flow velocity. In this work, a new solution is introduced to increase the throughput of the electrolyzer without the need for increasing these two parameters. The new reactor has three channels separated by porous walls. The electrolyte enters the middle channel and flows into the outer channels through the wall pores. The gas products are being produced in the outer channels. Hydrogen cross over is 0.14 % in this electrolyzer at Reynolds (Re) = 109 and current density (j) = 300 mA/cm². This cross over is 58 times lower than hydrogen cross over in an equivalent membrane-less electrolyzer with parallel electrodes at the same working conditions. Moreover, the addition of passive additives to the electrolyte further reduces the hydrogen cross over by 21 % and the overpotential by 1.9 %. This is due to the positive effects of surfactants on detachment and coalescence dynamics of the bubbles.

4.1 Introduction

Emission-free renewable energies are being harnessed to substitute the energy from polluting sources. However, fluctuations in their availability necessitate innovative solutions to meet energy supply and demand. In this regard, at the times of abundant production, the surplus can be stored in the form of hydrogen using water electrolysis as a sustainable process. [9, 10]. High purity hydrogen produced in this way can be used in fuel cells or engines to produce energy for both mobile and stationary applications. Although the high costs of the necessary infrastructure have slowed down clean H₂'s deployment [6]. Any improvement in the design, efficiency, and throughput of water electrolyzers will positively impact their adoption in the energy sector.

The two main water electrolysis methods are alkaline and polymer electrolyte membrane (PEM) processes that are available commercially. Other systems based on anion exchange membranes (AEM), solid oxide electrolysis (SOE), and membrane-less architecture are in the development and research stage [16, 22, 129]. Alkaline electrolyzers work with basic electrolytes [130] and their inexpensive electrodes are separated by a diaphragm in order to prevent gas cross-contamination [19]. Alkaline electrolyzers are the most mature technologies for hydrogen production due to their simple design and inexpensive catalyst materials [19]. PEM electrolyzers use a membrane coated by catalysts on both sides [14]. This membrane allows the protons migration but prevents the gas from the cross over [131]. PEM electrolyzers can be used at high current densities with very low gas cross over, and in a compact form factor

[14]. AEM electrolyzers work with alkaline electrolytes and use an anion conductive membrane [18]. This technology can reduce the capital cost of electrolyzers due to the usage of non-precious metal electrodes in contrast to PEM systems [132]. The stability of the anion conductive membrane is a barrier against the commercialization of the AEMs [133, 134]. SOEs use a solid electrolyte with two porous electrodes on its two sides [17]. These electrolyzers have higher efficiencies compared to low-temperature electrolyzers since they are operating at elevated temperatures [135]. However, the solid electrolyte and the electrodes should be chemically stable in the harsh operational conditions [17].

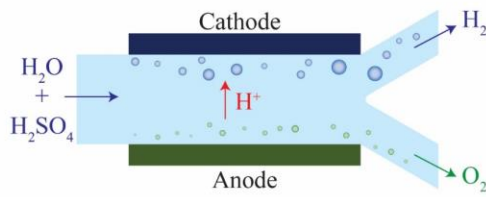
All of the discussed electrolyzers use a membrane or a diaphragm to prevent the gas cross-contamination. However, a diaphragm or a membrane introduces additional resistance between the electrodes, increases the cost of the electrolyzer, and reduces the lifetime of the device [20, 22]. Membrane-less electrolyzers have been introduced to remove the need for the membranes [20]. They rely on the fluidic flow [20, 21, 88, 89, 136, 137], buoyancy forces [138], or surface forces [139] for the product separation. Removing the membrane simplifies the design of the electrolyzer, reduces the electrolyzer cost, and increases the lifetime and durability of the device [22]. Furthermore, a membrane-less electrolyzer is compatible with a wide range of electrolytes at different pH values [20]. Thus, it can be used for various electrochemical reactions such as water electrolysis for hydrogen production or brine electrolysis for chlorine production without significant modifications in its design [21, 140].

The membrane-less electrolyzers geometry can be classified based on the electrodes configuration into parallel [20, 21] and mesh electrodes [88, 89, 136]. In the parallel electrodes (PE) electrolyzer shown in Figure 33a, the electrodes are at the two opposite sides of a rectangular channel where the liquid electrolyte is flowing. In addition to the electrolyte, evolved gaseous products are also flowing in between the electrodes towards the end of the channel. The liquid flow keeps the bubbles at the channel sides to prevent cross over. As the volume fraction of bubbles increases by moving downstream, the channel length and flow rate should be decided carefully to prevent the formation of excessively large bubbles.

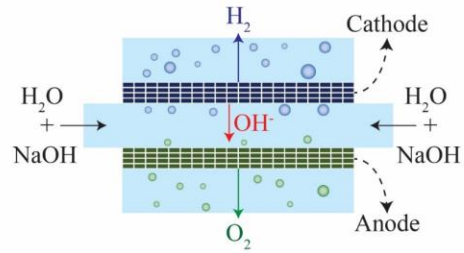
The mesh electrodes geometry as shown in Figure 33b is made of two plane meshes that act as catalysts. The liquid flow enters the area between the meshes and flows through the pores of the mesh. The bubbles are formed at the surface of the mesh and are carried to the outer side of the mesh by the flow. At equal interelectrode distances, the mesh electrodes electrolyzer can achieve a higher production rate compared to the PE electrolyzer as the bubbles go through the mesh pores and leave the interelectrode region faster. However, velocities inside all pores of the mesh should be ideally equal for the efficient removal of the growing bubbles. Furthermore, the bubbles forming in the inner side of the mesh should remain smaller than the mesh pore size in order to be transported to the outer side.

The product separation is a challenge for the membrane-less electrolyzers due to the absence of the membrane or separator. The bubble growth at the electrode and movement in the channel are investigated in order to overcome this challenge [23, 24, 115-117, 141]. The bubble coalescence and large bubble detachment from the electrodes can lead to the formation of bubbles larger than half of the channel width which leads to gas cross over. As the large bubbles form more frequently at high production rates the gas cross over is higher at higher production rates.

a. Parallel electrodes electrolyzer



b. Mesh electrodes electrolyzer



c. Porous walls electrolyzer

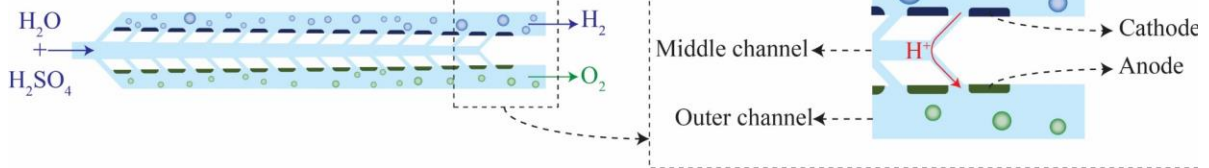


Figure 33. Schematics of membrane-less electrolyzers geometries: a. Parallel electrodes electrolyzer: This electrolyzer has two solid parallel catalysts. The bubbles evolve and flow between the parallel electrodes. b. Mesh electrodes electrolyzer: The electrolyte enters the space between two mesh catalysts. The electrolyte flows through the meshes and removes the generated bubbles in the meshes. c. Porous walls electrolyzer: Bubbles are being generated at the electrodes in the outer channels. The porous wall and the liquid flow prevent the bubble cross over. The bubbles are not flowing between the electrodes in this design. Therefore, it has a smaller overpotential due to the movement of bubbles compared to mesh electrodes and parallel electrodes electrolyzers.

The addition of a surfactant to the electrolyte decreases the surface tension that leads to the smaller bubble detachment. Furthermore, the surfactant molecules adsorbed on the interface of the bubble prevent the bubble coalescence. Therefore, the surfactant can improve the throughput while still having pure streams of products [142]. However, the production rate cannot be increased further when the space between the electrodes is filled with bubbles. Enlarging the space between the electrodes leads to a higher maximum production rate, but it imposes additional ohmic losses due to the larger gap. Moreover, bubbles moving between electrodes block ionic pathways that add to the overpotential losses [25]. Our design is based on the idea that the production rate can be improved by adding pores to the wall of PE electrolyzers for removing bubbles from the interelectrode region faster. However, bubbles larger than the pores cannot go through the pores easily and they flow between the electrodes towards the end of the channel which limits the production rate. To address this limitation and as the second element of our design, we have engineered the nucleation sites to be only present outside of the interelectrode region. By doing so, the overpotential due to the bubble movement between electrodes decreases, and the electrodes distance can be decreased as well.

In what follows, we describe the porous wall (PW) electrolyzer of Figure 33c in order to achieve a higher production rate and lower gas cross over. The liquid electrolyte enters the middle channel and goes to the outer channels through the inclined wall pores. The electrodes are on the outer sides of the porous walls which leads to the generation of bubbles only in the outer channels. The inclined walls and pores ensure sufficient flow in each electrodes pore. The flow through the wall pores prevents the migration of bubbles to the opposite side. In this design, the volume fraction of gas in the interelectrode area is low since there is no flow of bubbles in the middle channel. Therefore, the ohmic loss due to the presence of flowing bubbles between the electrodes is smaller compared to the parallel electrodes design. The performance

of a PW electrolyzer can be improved further by using a surfactant in the electrolyte [142]. We compare the product purity and the performance of the PW electrolyzer with a PE electrolyzer. This comparison demonstrates the effectiveness of the porous walls. As a result, the PW electrolyzer utilizes smaller Re compared to other membrane-less electrolyzers to achieve the cross over comparable to them. This study provides guidelines for the design of membrane-less electrolyzers for achieving high throughput production of hydrogen with high purity.

4.2 Procedures

4.2.1 Device fabrication

The fabrication of the PW electrolyzer starts by depositing 200 nm titanium on a silicon wafer. The electrical connections are made by doing photolithography and metal ion beam etching on the titanium layer. Afterwards, the porous walls supporting vertical electrodes are made using the SU8 process with a height of $70\ \mu m$. Platinum is sputtered on the device followed by ion beam etching [143]. The ion beam etching removes Platinum from the horizontal surfaces but platinum remains on the vertical walls of SU8. The platinum on the vertical walls is in contact with titanium on the horizontal walls. Subsequently, the fluidic channels are fabricated in SU8. The height of the fluidic channels is $80\ \mu m$. The inner sides of the porous walls are covered with SU8 in this step. Therefore, platinum is in contact with electrolyte only in the outer channels. The inlet and outlets are punched in a PDMS piece. A thin layer of SU8 is coated on this piece. Next, this PDMS piece is bonded to the device to seal the channel [98]. Figure 69 of Appendix C shows the detailed process flow. The minimum interelectrode distance is $550\ \mu m$ at the end of electrodes. The maximum interelectrode distance is $690\ \mu m$ at the beginning of electrodes. The electrodes active area of the PW electrolyzer is $0.347\ mm^2$. The PE electrolyzer is fabricated with the same process. The interelectrode distance and electrodes active area of the PE electrolyzer are $620\ \mu m$ and $0.347\ mm^2$.

4.2.2 Experiments

A Cronus Sigma 1000 Series syringe pump is used for flowing electrolytes in the channel. The applied current to the device is controlled by a Bio-Logic SP-300 potentiostat. The images of the bubbles generation and flow is captured using a Photron FASTCAM Mini UX100 camera at the 4000 fps and $1/10000\ s$ shutter speed. Two test tubes are filled with liquid electrolyte. These test tubes are held inversely in a larger container of the liquid electrolyte. The generated hydrogen and oxygen are collected in these test tubes. The diluted gas with air is injected to the SRI 8610C gas chromatogram with a thermal conductive detector. The current is applied to the device for 15 minutes in each experiment. The experiments are repeated three times at each current density and Re .

The Re is calculated using the following equation:

$$Re = \frac{\rho V D}{\mu} \quad (1)$$

where ρ , V , D , and μ are the density of the electrolyte, average velocity at the inlet of the device, hydraulic diameter of the inlet, and viscosity of the electrolyte, respectively. The density and viscosity of 1 M sulfuric acid are $1060\ kg/m^3$ and $0.00114\ kg/m/s$. The dimension of inlet is $300\ \mu m \times 80\ \mu m$.

4.3 Results and discussion

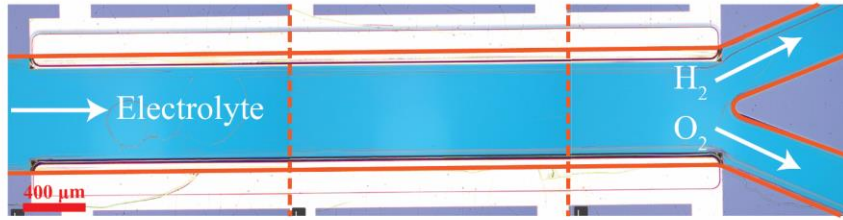
Both the PE and the PW electrolyzers shown in Figure 33a and c are used for hydrogen generation and compared in this study. They have equal electrode surface areas and the interelectrode distance of the PE electrolyzer (620 μm) is equal to the average interelectrode distance of the PW electrolyzer. Initially, we discuss the performance and product purity of the PE electrolyzer, and then present the results of the PW electrolyzer for comparison with the PE electrolyzer.

4.3.1 PE electrolyzer

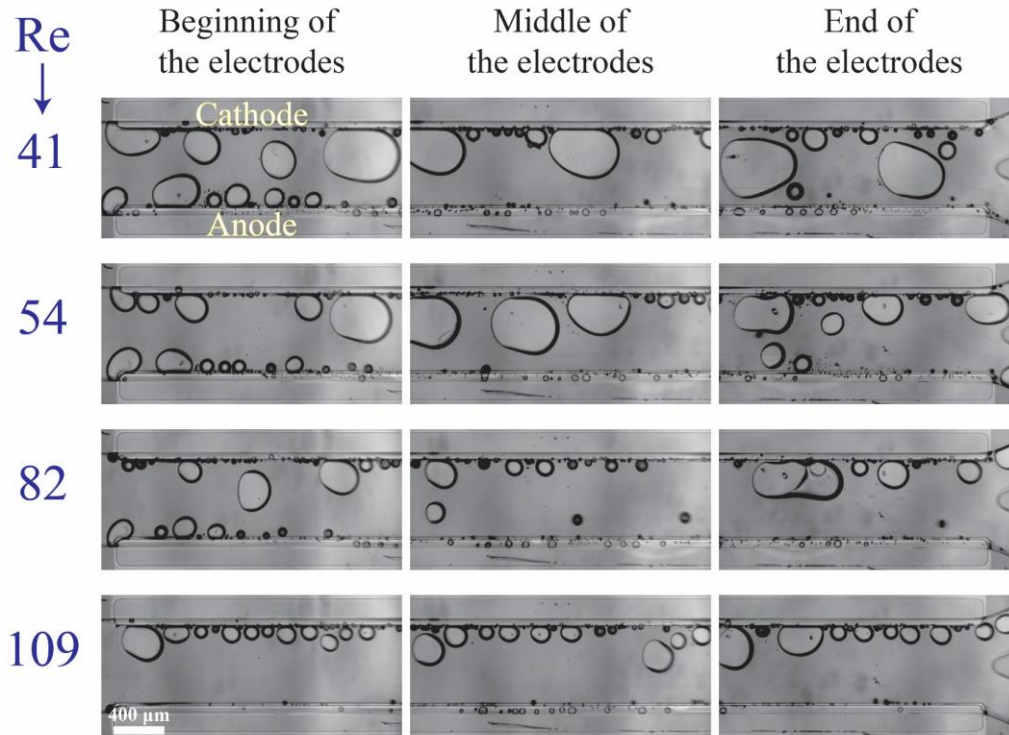
The fabricated PE electrolyzer is shown in Figure 34a. Figure 34b shows the bubble generation in the PE electrolyzer at the current density of $j = 300 \text{ mA/cm}^2$ at different Reynolds numbers. The electrolyte is 1 M sulfuric acid. This figure indicates that the liquid flow detaches bubbles at smaller sizes as the Re increases. However, the small bubble detachment is not enough to prevent large bubble formation in the channel. The bubble coalescence leads to the formation of large bubbles whose equilibrium positions are at the center of the channel [23]. Bubbles moving at the centerline are a mixture of hydrogen and oxygen as they coalesce with bubbles originating from both sides. As a result, large bubbles should be avoided.

Decreasing the production rate is one approach to reduce the bubbles' size and cross over. Figure 34c presents the bubbles flow at $\text{Re}=109$ and $j = 75 \text{ mA/cm}^2$. This figure depicts the reduction in the bubbles' size when the current density is decreased from 300 mA/cm^2 to 75 mA/cm^2 . The number of bubbles in the channel decreases with decreasing the current density. The bubble coalescence becomes less frequent at lower current densities, leading to the formation of smaller bubbles and lower cross overs.

a. Parallel walls electrolyzer



b. $j=300 \text{ mA/cm}^2$, $1 \text{ M H}_2\text{SO}_4$



c. $j=75 \text{ mA/cm}^2$, $1 \text{ M H}_2\text{SO}_4$

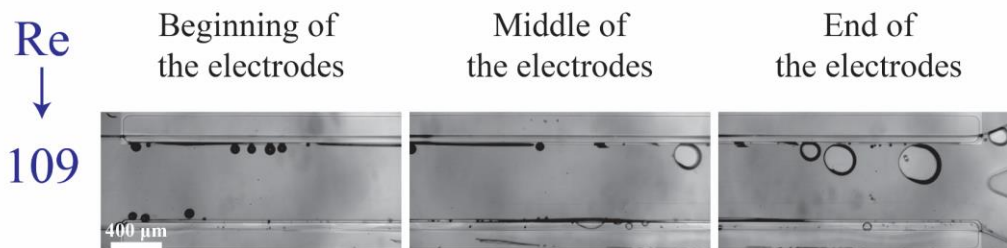


Figure 34. Bubbles generation and flow at different locations in the PE electrolyzer working with $1 \text{ M H}_2\text{SO}_4$: a. The image shows the fabricated PE electrolyzer. Solid lines indicate the walls of the PE electrolyzer. This image is constructed by placing images of three different positions of the device next to each other. b. The applied current density is 300 mA/cm^2 . The large bubbles are the primary cause of gas cross over since they are moving to the channel centerline. The bubbles become smaller by increasing the Re as the flow removes the bubbles faster from the channel. c. The bubbles are smaller at a lower current density of $j = 75 \text{ mA/cm}^2$. Thus, the gas cross-over is smaller at lower current densities.

Adding a surfactant to the electrolyte is another solution for reducing the bubbles' size. Heptadecafluorooctanesulfonic acid potassium (PFOS) is used as the surfactant in this study

since it does not participate in the electrochemical reaction and can reduce the overpotential by lowering the hydrogen dissolution in the electrolyte [128]. Figure 35 shows the bubble generation at $j = 300 \text{ mA/cm}^2$ and different Re . This figure shows many bubbles evolving close to each other. But the surfactant in the electrolyte prevents the coalescence of these bubbles. Therefore, the bubbles at the end of the electrodes are smaller compared to the surfactant-free electrolyte (Figure 34b).

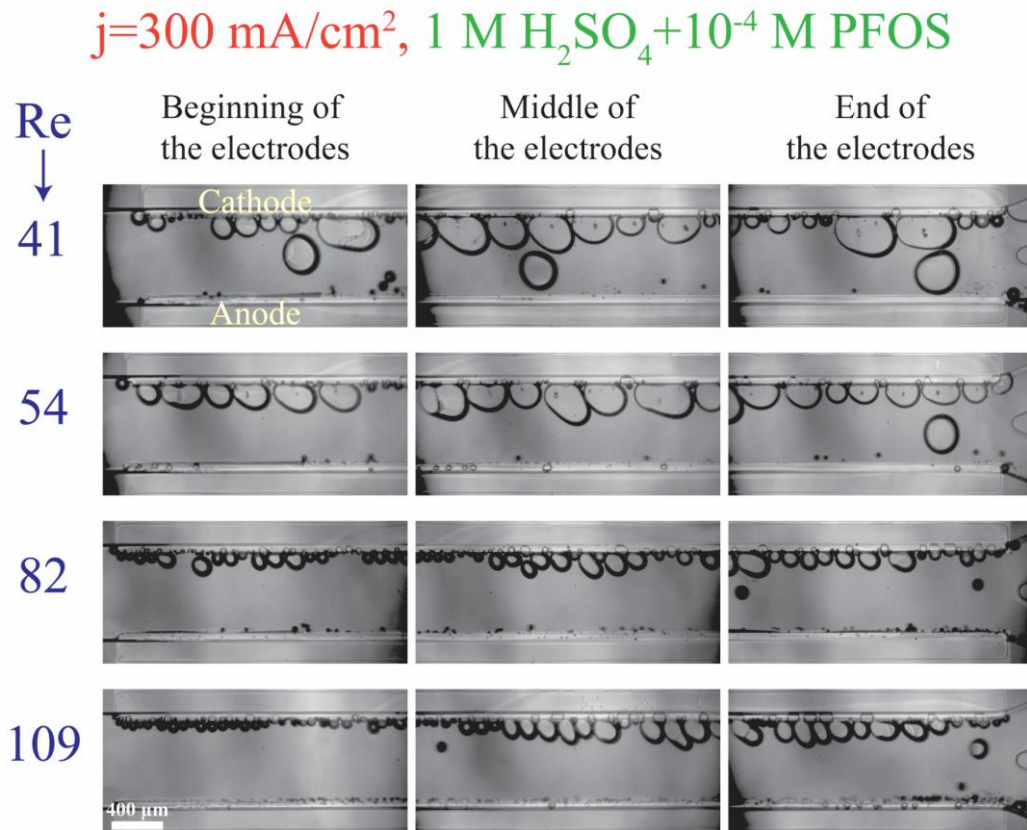


Figure 35. Pictures of different regions of the PE electrolyzer working with $1 \text{ M H}_2\text{SO}_4 + 10^{-4} \text{ M PFOS}$ surfactant: The bubbles detach at smaller sizes at higher Re . The surfactant reduces the bubble detachment size by reducing the surface tension. Moreover, the surfactant inhibits the bubble coalescence. For this reason, the flowing bubbles are smaller in the electrolyte with the surfactant compared to the surfactant-free electrolyte. Thus, product separation is more effective by using a surfactant. The applied current density is 300 mA/cm^2 .

Figure 36a shows the polarization curve of the PE electrolyzer. The slope of the polarization curve is steeper when using the electrolyte with the surfactant. This can be attributed to the faster bubble detachment from the electrodes and smaller bubbles flowing in between the electrodes. Furthermore, PFOS reduces the dissolved hydrogen concentration close to the electrode [128]. This leads to a lower concentration overpotential due to the hydrogen supersaturation at the electrode surface [144]. As a result, the required potential for the reactions decreases at constant current densities as shown in Figure 36a.

Figure 36b presents the hydrogen cross over to the oxygen side for the experiments shown in Figure 34 and Figure 35. The lower flammability limit of the hydrogen-oxygen mixture is 4% [145] and is highlighted by the dashed line in Figure 36b. The cross over is measured using a gas chromatograph (GC SRI 8610C). The cross over is low at high Re because, at higher Re , the gas volume fraction is smaller for a constant production rate. However, the cross over is higher than the flammability limit when the surfactant-free electrolyte is used even at high

Re=109. The bubble coalescence at Re=41 and Re=54 creates large bubbles in the hydrogen outlet. Subsequently, these bubbles merge in the downstream and they block the hydrogen outlet. Consequently, the liquid and all the bubbles flow through the oxygen outlet. The hydrogen channel remains blocked until the end of the experiment which creates an enormous hydrogen cross over. Thereby, the hydrogen cross over is not shown in Figure 36b at Re=41 and Re=54 in the surfactant-free electrolyte. This problem can be resolved by using larger outlet channels but the cross over does not fall below the flammability limit due to large bubble formation inside the electrolyzer. The cross over reduces to below the flammability limit at Re=109 either by adding the surfactant to the electrolyte or decreasing the production rate.

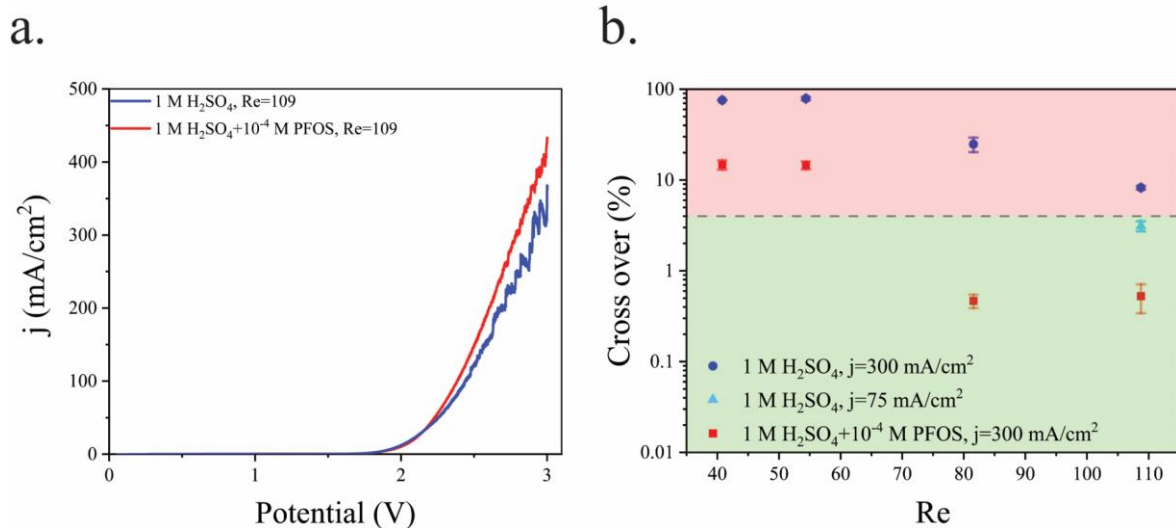


Figure 36. a. Polarization curve of the PE electrolyzer working with $1\text{ M H}_2\text{SO}_4$ with and without the PFOS surfactant: The surfactant reduces the electrode surface coverage by bubbles. Besides, the hydrogen evolution reaction has lower overpotential due to the decrease in the hydrogen solubility in the electrolyte with PFOS. Thus, the PFOS surfactant improves the electrochemical performance of the PE electrolyzer. b. Hydrogen cross over to the oxygen side at different Re: The flammability limit is shown by a dashed line. The cross over is inversely proportional to the Re. The cross over is less than the flammability limit in the surfactant-free electrolyte at Re=109 and $j = 75\text{ mA/cm}^2$. However, the cross over of the PE electrolyzer is not safe by increasing the current density to 300 mA/cm^2 in the surfactant-free electrolyte. The PE electrolyzer can operate with a secure cross over by adding the PFOS surfactant to the electrolyte.

4.3.2 Design of the porous walls electrolyzer

The PW electrolyzer utilizes two porous walls between nucleation sites that help with product separation. The bubbles cannot go through the wall pores due to the opposite flow direction from the middle channel. Furthermore, the pores require the large bubbles to deform in order to pass through them; a phenomenon that is not energetically favorable. A confined bubble travels in the outer channel rather than the wall pores as it experiences smaller deformation. As a result, this design can efficiently deal with large bubbles, forming at high current densities. However, smaller bubbles can flow through the wall pores and move to the middle channel. This often happens at the presence of reverse flows in the wall pores. Moreover, the ionic resistance between the electrodes is directly proportional to the size and density of the wall pores. Therefore, this design should be optimized to achieve effective product separation while minimizing the ionic resistance.

The distance between the electrodes is assumed to be constant and the geometry of porous walls is optimized to achieve a high production rate without any cross over. Two design criteria of the PW electrolyzer are the equal distribution of liquid flow in the wall pores and a negligible

gas cross over. Numerical simulations are carried out using ANSYS Fluent software from ANSYS Inc for design optimization. Figure 37a shows four steps of this process. For each geometry, two types of 2-dimensional simulations are carried out. Initially, the conservation of mass and momentum are solved to determine the flow distribution in the wall pores for single-phase flow. In this simulation, the working fluid is water. Water enters the middle channel at the velocity of 0.4 m/s and exits through outlets of the outer channels.

Secondly, mixture equations are solved to estimate the gas cross over in each geometry. The primary phase is water and the secondary phases are hydrogen and oxygen. The water enters from the bottom port at the velocity of 0.4 m/s and exits through the outer channels' outlets. Hydrogen and oxygen enter the channel through small inlets on the outer sides of posts at the velocities of 0.02 m/s and 0.01 m/s, respectively corresponding to a current density of 1.6 A/cm². It is assumed that the facing sides of the opposite posts are not active production sites. The boundary conditions are shown in Figure 37a. The surface tension for the hydrogen-water and oxygen-water pairs is considered to be equal to the air-water surface tension which is 0.072 N/m [23]. The surface tension between hydrogen and oxygen is neglected. The average diameter of hydrogen and oxygen bubbles is assumed to be 10 μm. Table 6 presents the density and viscosity of the fluids used in these simulations.

Table 6. Properties of the fluids used in the simulations

Fluid	Density (kg. m ⁻³)	Viscosity (kg. m ⁻¹ . s ⁻¹)
Water	998.2	0.001003
Hydrogen	0.08189	1.919 × 10 ⁻⁵
Oxygen	1.2999	8.411 × 10 ⁻⁶

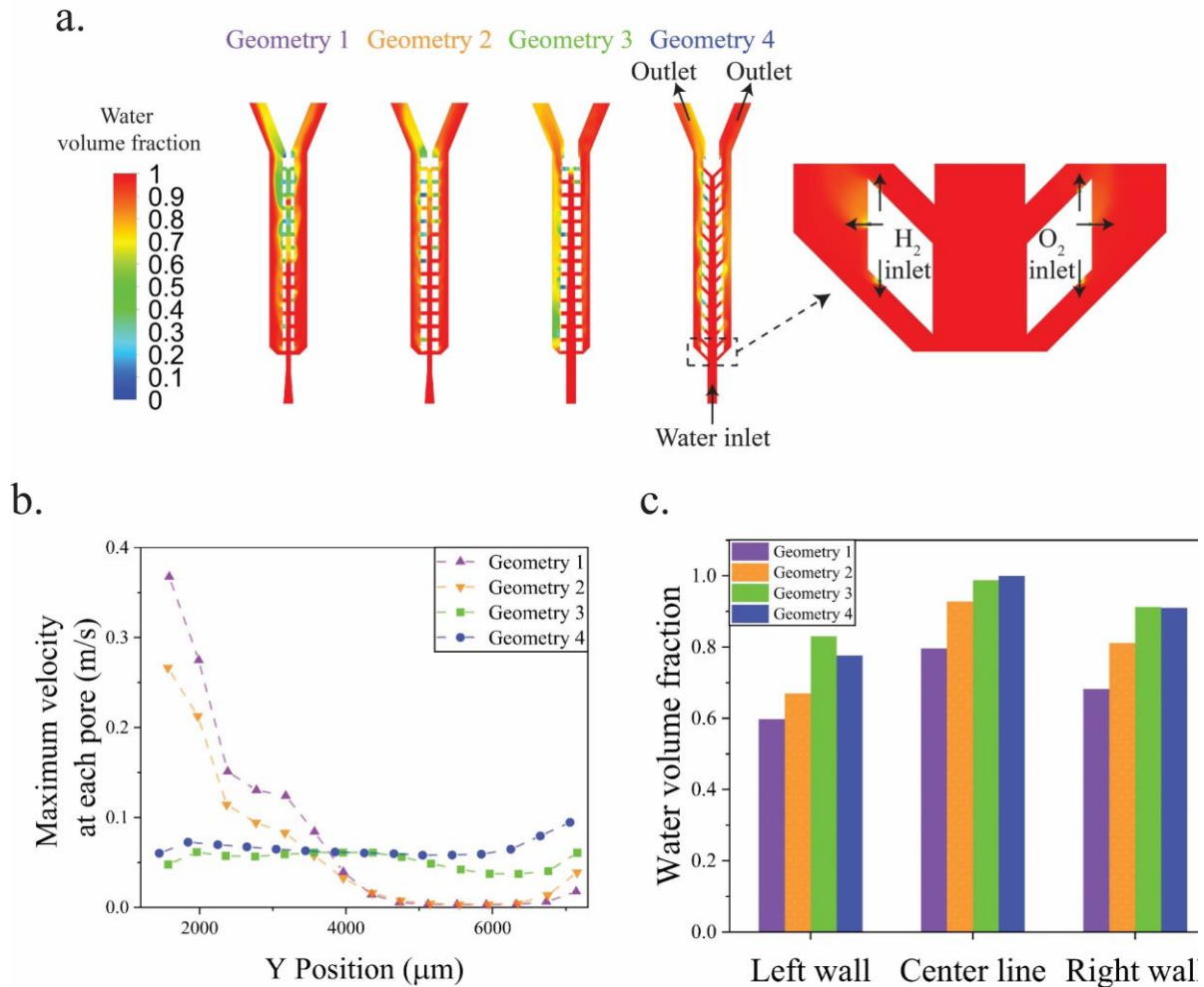


Figure 37. Geometry optimization of the PW electrolyzer: a. The design and boundary conditions are shown at four steps of geometry optimization. The length of wall pores is $100\ \mu\text{m}$ in geometry 1. The length of wall pores is increased to $200\ \mu\text{m}$ in geometry 2 to reduce the gas cross over. Afterwards, the porous walls are rotated by 0.75° in geometry 3 to have equal velocities in the wall pores. The wall pores angle with the horizontal line is 45° in geometry 4 to suppress the gas cross over completely. The contours are the water volume fraction at $t = 0.2\ \text{s}$. Hydrogen and oxygen bubbles enter the left and right channels, respectively. b. The velocity distribution at wall pores: The velocity distribution is uniform in geometries 3 and 4 thanks to the inclined porous walls. c. Average water volume fraction at porous walls and channel centerline: Water volume fraction below one at the centerline indicates gas cross over.

The maximum velocity along the wall pores are presented in Figure 37b based on the single-phase simulations. The water volume fraction contours shown in Figure 37a are the results of the three-phase simulations at $0.2\ \text{s}$. In this figure, hydrogen and oxygen are entering the left and right outer channels, respectively. Figure 37c shows the water volume fraction along lines drawn in the middle of the channel and porous walls based on multi-phase simulations. The water volume fraction is one at the centerline if there is no cross over. The water volume fraction below one in the left and right walls determines that some pores are filled with gas.

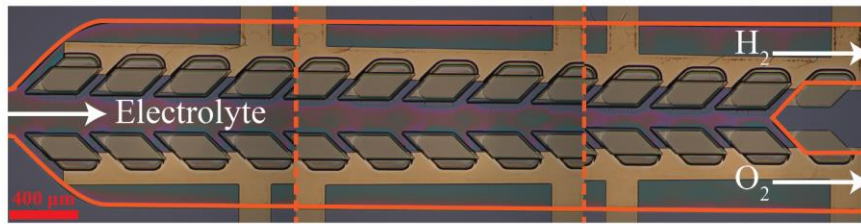
Geometry 1 has $100\ \mu\text{m}$ wide pores. The liquid flow velocity is not equal in the pores of this design and the water volume fraction is less than 0.8 in the centerline. The width of the pores is increased to $200\ \mu\text{m}$ in Geometry 2. This change increases the water volume fraction to 0.93 at the centerline. However, the flow distribution is not uniform in the pores. To address this issue, the porous walls are rotated by 0.75° in opposite directions to construct Geometry 3. In this new geometry, the flow distribution is uniform and the water volume fraction is 0.99. Figure 37a shows the gas cross over at the end of the middle channel of Geometry 3. In the

final step, Geometry 4 is considered by tilting the wall pores by 45° . The water volume fraction becomes 1.0 at the centerline after this change. This modification completely suppresses the gas cross over and keeps the uniform flow distribution in the wall pores. Figure 67 of Appendix C shows the simulations that are carried out to investigate the effect of the wall pores angles and sizes. The water volume fraction is 1.0 and the velocity is equally distributed when the wall pores angle is between 30° and 60° or the wall pores size is between $80 \mu m$ and $160 \mu m$. The PW electrolyzer is designed and fabricated based on Geometry 4 with the wall pores angle = 45° and wall pore size = $80 \mu m$. The fabricated PW electrolyzer is shown in Figure 38a.

4.3.3 Results of the porous walls electrolyzer

Figure 38b shows bubbles generation and flow in the PW electrolyzer at $j = 300 \text{ mA/cm}^2$ at different Re values. In addition to the liquid flow, the porous walls and the controlled bubble production sites (on the outer walls) are contributing to product separation. The bubbles' size is inversely proportional to the Re which means that the large bubbles are more frequent at smaller Re. The large bubbles flowing in the outer channels do not traverse the wall pores towards the main channel in order to keep their surface energy as low as possible. However, these large bubbles contribute to creating a pressure imbalance between the two outer channels. As a consequence of this imbalance, some smaller bubbles from the outer channels move to the middle channel and even to the opposite outer channel, increasing product cross-contamination. Some of these bubbles can even coalesce in the middle channel and create larger bubbles as observed at the end of the middle channel in Figure 38b. Such large bubbles are trapped in the middle channel and their size decreases from Re = 41 until it completely disappears at Re = 109. At Re < 109, some small bubbles migrate to the middle channel and create a large bubble until the steady-state condition is reached in terms of the size of this bubble. At this point, bubbles in the outer channels do not cross over anymore.

a. Porous walls electrolyzer



b. $j=300 \text{ mA/cm}^2$, $1 \text{ M H}_2\text{SO}_4$

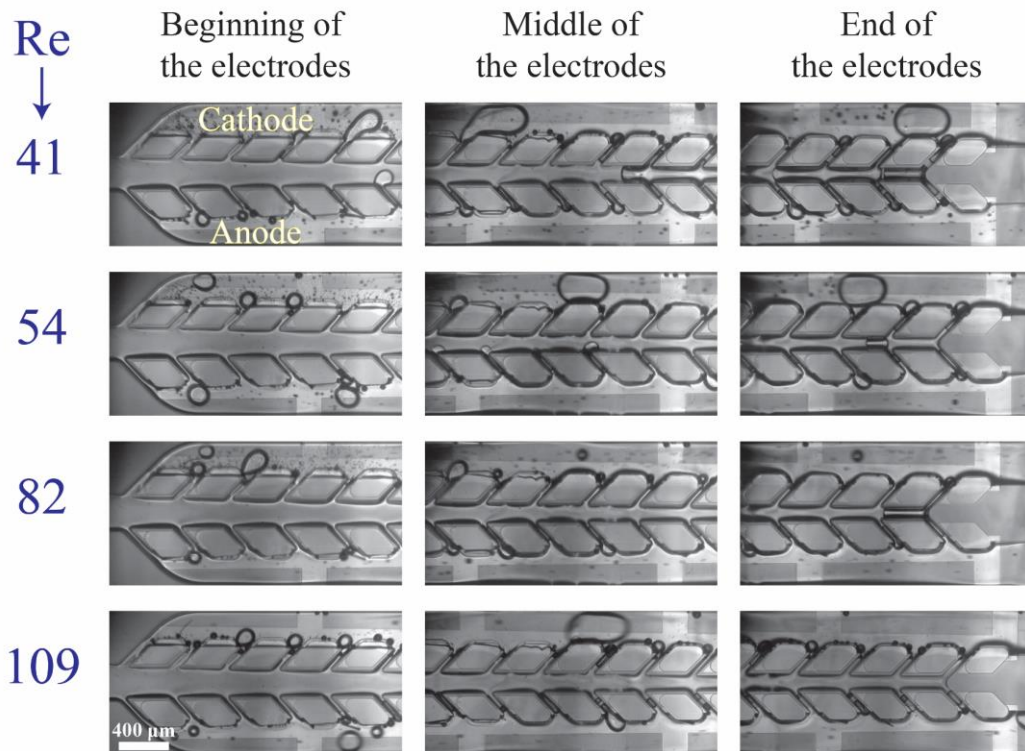
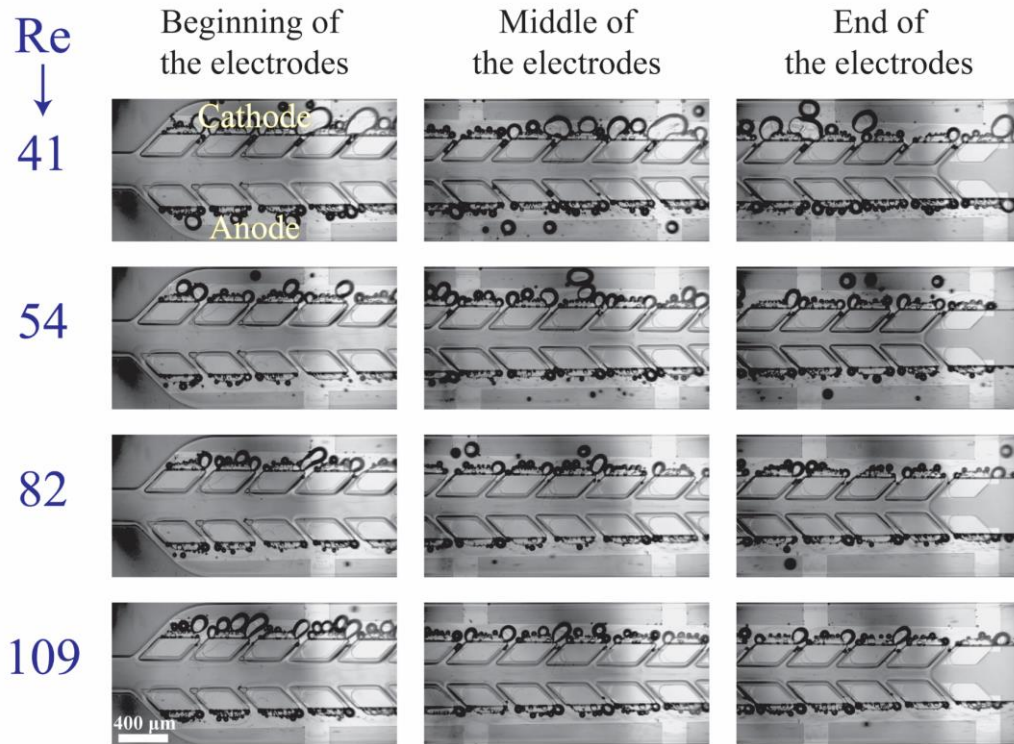


Figure 38. a. Picture of the fabricated PW electrolyzer: This picture is constructed by capturing images from different parts of the device. b. Pictures of the bubble generation and flow in the PW electrolyzer at $j = 300 \text{ mA/cm}^2$ and various Re : The porous walls keep the hydrogen and oxygen bubbles separated. This device is less vulnerable to the large bubble formation since these bubbles cannot go through the wall pores. Some small bubbles move to the middle channel and coalesce. They form a large bubble in the middle channel that cannot go through the pores. This bubble grows until the device reaches the steady-state. The final size of this bubble decreases by increasing the Re . There is no bubble in the middle channel at $Re=109$ since the flow does not allow bubbles migration to the middle channel.

Bubbles should detach at small sizes from the electrode and their coalescence must be inhibited in order to resolve the large bubble formation in the middle channel. Adding surfactants to the electrolyte provides these benefits. The surfactant decreases the bubble size as discussed in the PE electrolyzer section. The bubble generation after adding the PFOS surfactant to the electrolyte is shown in Figure 39. The above-mentioned pressure imbalance due to the formation of large bubbles decreases and, therefore, bubbles do not migrate to the middle channel and no bubble appears in the middle channel even at low $Re=41$. An added benefit of having smaller bubbles is higher production rates. A comparison of Figure 38b and Figure 39 shows that the bubbles are not blocking the wall pores in the electrolyte with surfactant. Therefore, the available area for the transfer of ions is not reduced. The resulting reduction of

the ohmic resistance compared to the PE electrolyzer leads to the higher efficiency of the PW electrolyzer as shown in Figure 40a. Interestingly, the effect of bubble-free ionic pathlength is strong enough to compensate for the lack of generation sites in the sides facing each other in the PW electrolyzer (Figure 40a) versus the PE electrolyzer (Figure 36a).

a. $j=300 \text{ mA/cm}^2$, $1 \text{ M H}_2\text{SO}_4+10^{-4} \text{ M PFOS}$



b. $j=450 \text{ mA/cm}^2$, $1 \text{ M H}_2\text{SO}_4+10^{-4} \text{ M PFOS}$

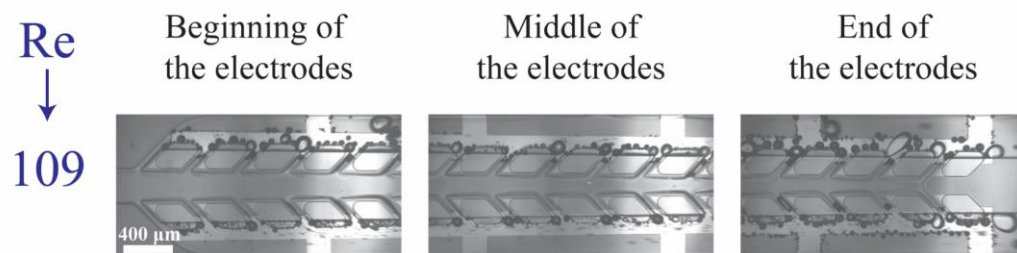


Figure 39. Effect of PFOS surfactant on the bubble generation and flow in the PW electrolyzer working with $1 \text{ M H}_2\text{SO}_4 + 10^{-4} \text{ M PFOS}$. a. Images show the bubble generation and flow at different Re and $j = 300 \text{ mA/cm}^2$. The addition of PFOS to the electrolyte reduces the size of bubbles. There is no bubble in the middle channel in the electrolyte with surfactant at low Re. Moreover, energy losses are smaller since the wall pores as ion-conducting pathways are free from the bubbles. b. Current density of 450 mA/cm^2 is achieved without cross over using PFOS surfactant and the PW electrolyzer design.

The crossover of hydrogen to the oxygen side in the PW electrolyzer is shown in Figure 40b. In the surfactant-free electrolyte, the cross over is higher than the flammability limit only when $\text{Re} = 41$. The liquid velocity is not high enough at this Re to remove the bubbles from the device before the bubbles become large. The cross over falls below the flammability limit by increasing the Re. In the surfactant-free electrolyte, there are bubbles in the middle channel at $\text{Re}=54$ and 82 as shown in Figure 38b, but these bubbles do not contribute to cross-

contamination as they are trapped in the middle channel and cannot go through the wall pores. The addition of PFOS to the electrolyte decreases the cross over further due to the coalescence inhibition and faster bubble detachment which allows for an increase in the current density from 300 mA/cm^2 to 450 mA/cm^2 while operating in the safe crossover range.

A comparison of Figure 36b and Figure 40b indicates a clear improvement in the cross over by changing the design from the PE electrolyzer to the PW electrolyzer design. The PE electrolyzer can produce products with safe cross overs only at Re as high as 109 and using the surfactant. However, the PW electrolyzer achieves a better product separation at smaller Re without using the surfactant. As an example, the mean value of the hydrogen cross over in the PE electrolyzer is $8.2 \pm 0.4 \%$ while it is $0.14 \pm 0.06 \%$ in the PW electrolyzer when $1 \text{ M H}_2\text{SO}_4$ is used at $Re=109$ and $j = 300 \text{ mA/cm}^2$. The cross over reduces in both electrolyzers in the electrolyte with the PFOS surfactant. The product separation is still more effective in the PW electrolyzer compared to the PE electrolyzer when PFOS is added to the electrolyte. The cross over in the PE electrolyzer and PW electrolyzer is $0.5 \pm 0.3 \%$ and $0.11 \pm 0.05 \%$, respectively in $1 \text{ M H}_2\text{SO}_4 + 10^{-4} \text{ M PFOS}$ at $Re = 109$ and $j = 300 \text{ mA/cm}^2$.

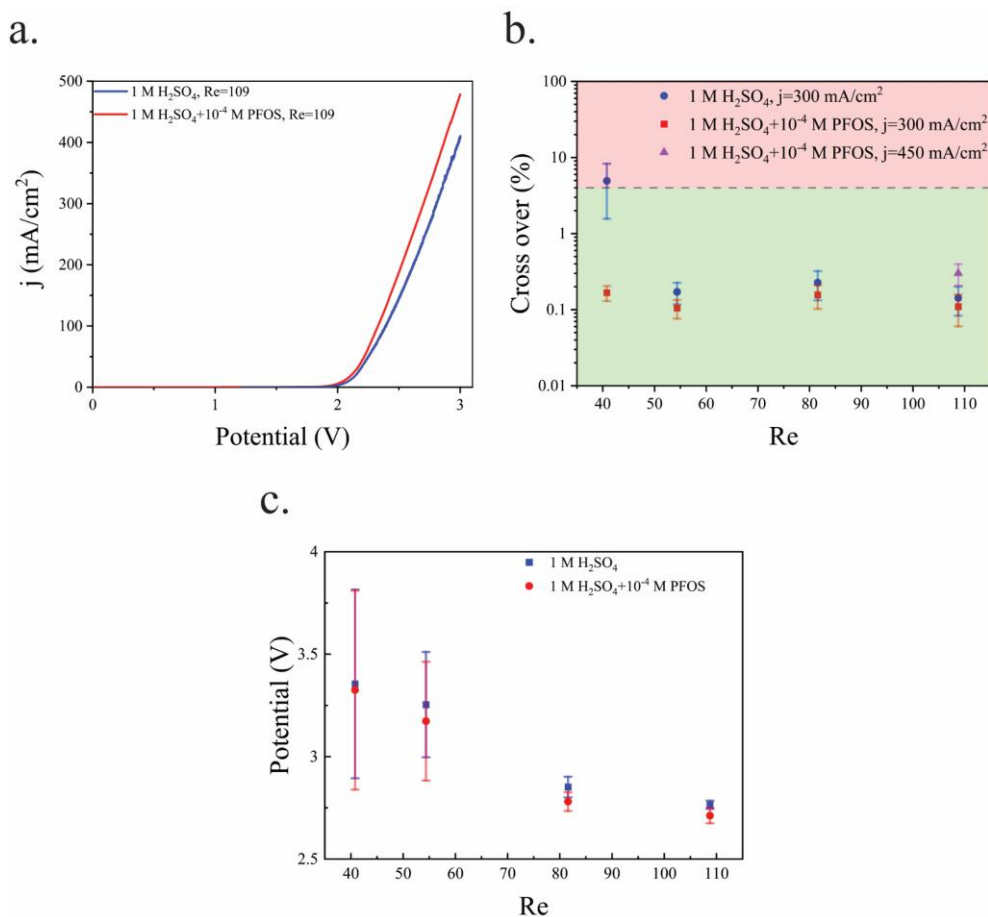


Figure 40. a. Polarization curve of the PW electrolyzer: The electrode surface coverage by bubbles is smaller and the wall pores are not blocked by the bubbles in the presence of PFOS. As a result, the electrochemical performance improves by adding PFOS to the electrolyte. b. The gas cross over is less than the flammability limit in the surfactant-free electrolyte at $Re \geq 54$. The cross over decreases further by adding the PFOS surfactant to the electrolyte. A comparison of this figure with

Figure 36b shows that the cross over is significantly smaller in the PW electrolyzer than the cross over in the PE electrolyzer. c. The working potential at a constant current density of 300 mA/cm^2 : The bars indicate the standard deviation of the potential. More active area is available at higher Re due to the smaller surface coverage by the bubbles. Therefore, the overpotentials and the potential oscillations decrease by increasing the Re . Furthermore, the PFOS surfactant reduces the residence time of bubbles on the electrode surface which reduces overpotential.

Figure 40c illustrates the average and standard deviation of the applied potential to the PW electrolyzer at different Re and constant current density of 300 mA/cm². The bubble residence time on the surface of the electrode decreases as the Re increases. There is more available active area if the bubbles leave the electrode's surface faster. Consequently, the overpotential due to the electrode surface coverage by bubbles is smaller. Therefore, the applied potential and the potential oscillation decrease by increasing the Re.

The performance of the PW electrolyzer is compared with reported membrane-less electrolyzers in Figure 41. The hydrogen cross over in the PW electrolyzer is equal to the smallest reported value but the PW electrolyzer achieves this cross over at smaller Re thanks to its design. Lowering the Re reduces the liquid pumping power and increases the energy conversion efficiency [39]. PE electrolyzers require high Re in order to prevent large gas volume fraction between the electrodes which leads to bubble cross over. Mesh electrodes electrolyzers can operate at smaller Re since the bubbles leave the channel via the closest mesh pore. However, it is difficult to have equal velocity in the mesh pores since they use a uniform mesh size with normal angles. Furthermore, the generation of bubbles between the mesh leads to larger velocity inequality between the mesh pores as the bubbles go through the pores. Therefore, the Re should be increased in the mesh electrodes to compensate for the unequal velocity distribution. The generation of bubbles in the outer channels and tilting the porous walls and pores in the PW electrolyzer ensures the equal velocity in the wall pores. As a result, the PW electrolyzer requires smaller Re for product separation compared to PE and mesh electrodes electrolyzers.

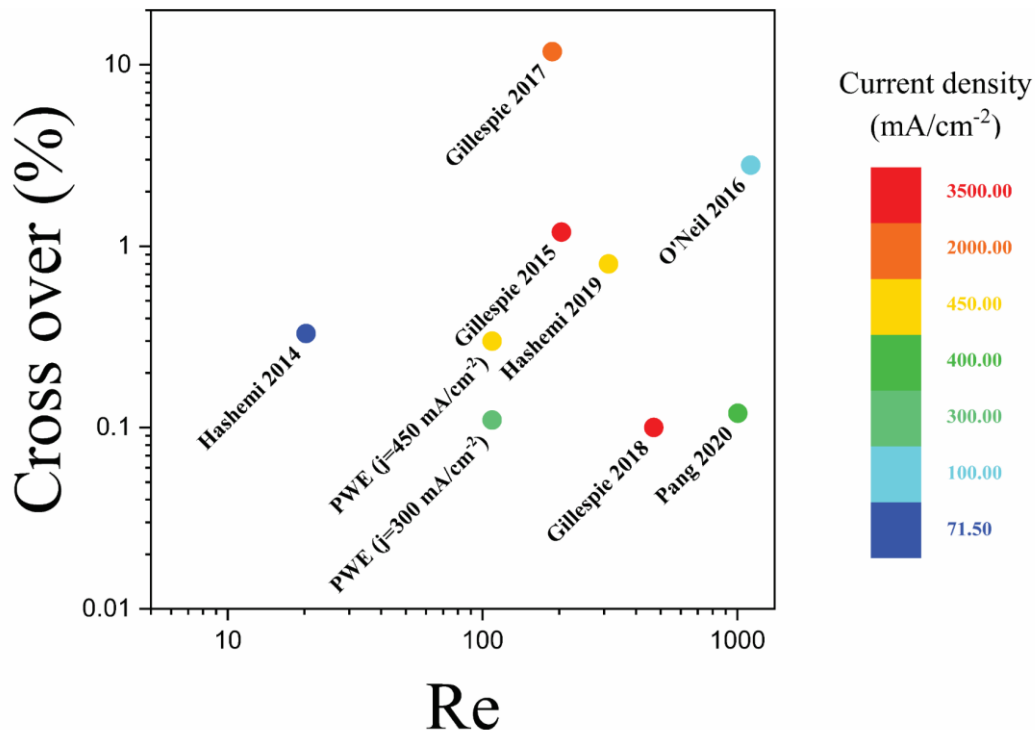


Figure 41. The cross over, Re, and current density of membrane-less electrolyzers [20, 21, 77, 88, 89, 136, 141]: The PW electrolyzer requires smaller Re to achieve hydrogen cross over as small as the other membrane-less electrolyzers. The color bar depicts the maximum current density at which the membrane-less electrolyzers are performing water electrolysis. The PW electrolyzer is represented by PWE. The data of the points are presented in Figure 68 of Appendix C.

4.4 Conclusion

Product separation is a challenging task in the membrane-less electrolyzers at high current densities. This chapter investigates the effects of geometry modification and the addition of surfactant to the electrolyte as two strategies in facilitating product separation. The PE electrolyzer achieves good product separation at a low current density of 75 mA/cm^2 . However, the hydrogen cross over becomes more than the flammability limit at a higher current density of 300 mA/cm^2 . The bubble coalescence and large bubble detachment are the main reasons for the formation of large bubbles in the channel that leads to unsafe cross-contamination. The addition of PFOS surfactant to the electrolyte reduces the cross over to the values below the flammability limit as a result of smaller bubble generation and bubble coalescence prevention. Moreover, the PFOS surfactant decreases the surface screening of the electrodes by the bubbles resulting in lower overpotentials.

In addition to the surfactant, the design of the membrane-less electrolyzer has a significant role in product separation. The PW electrolyzer is presented to improve the production rate without increasing the cross over. The hydrogen cross over is 58 times smaller in the PW electrolyzer compared to the equivalent PE electrolyzer at the current density of 300 mA/cm^2 . Furthermore, the PW electrolyzer can operate at 50 % higher current density compared to the PE electrolyzer with good product separation.

The large-scale membrane-less electrolyzers have a larger interelectrode distance than the microfluidic electrolyzers due to the flow of larger bubbles in the scaled-up electrolyzers. The PW electrolyzer design can be scaled-up without increasing the interelectrode distance since there is no bubble flowing between the electrodes. Large scale fabrication of inclined pores and deposition of catalysts only on one side of the pores might be challenging. However, additive manufacturing technologies that have been developed in recent years can be used to facilitate the fabrication of large-scale PW electrolyzers with custom pore designs. [146].

Chapter 5

Learning from droplet flows in microfluidic channels using deep neural networks

This chapter is the postprint version of the following article published in *Scientific reports*.

Learning from droplet flows in microfluidic channels using deep neural networks

Pooria Hadikhani¹, Navid Borhani¹, S. Mohammad H. Hashemi^{1,2}, and Demetri Psaltis¹

¹ Optics Laboratory, School of Engineering, Swiss Federal Institute of Technology Lausanne (EPFL), Lausanne, Switzerland

² Computational Science & Engineering Laboratory, ETH Zurich, Zurich, Switzerland

Scientific reports 9, no. 1 (2019): 1-7

<https://doi.org/10.1038/s41598-019-44556-x>

A non-intrusive method is presented for measuring different fluidic properties on a microfluidic chip by optically monitoring the flow of droplets. A neural network is used to extract the desired information from the images of the droplets. We demonstrate the method in two applications: measurement of the concentration of each component of a water/alcohol mixture, and measurement of the flow rate of the same mixture. A large number of droplet images are recorded and used to train deep neural networks (DNN) to predict the flow rate or the concentration. It is shown that this method can be used to identify the concentrations of each species with a 0.5% accuracy and the flow rate with 0.05 ml/h. The proposed method can in principle be used to measure other properties of the fluid such as surface tension and viscosity.

5.1 Introduction

Machine learning is a framework that learns from the data without being programmed. Deep learning is a specific approach of machine learning [147] which has emerged in recent years as a powerful technique for a broad range of applications. Deep learning consists of several representation layers where each layer is obtained by the non-linear transformation of the previous layer [148]. Deep neural networks use the combination of these transformations to learn complex functions. In fluid mechanics, neural networks have been reported recently [149-151] as tools that can help computational fluid mechanics simulations by mapping the estimates of low-resolution simulations to those with higher fidelity. In microfluidics, neural networks have been used to estimate various quantities relating to their applications [152-155]. Mahdi and Daoud [156] used neural networks to predict the size of the droplets in an emulsion while Khor et al. [157] used them to predict the stability of droplets in an emulsion. In our work, we employ neural networks to estimate fluid and flow parameters by observing the droplet formation process in a passive microfluidic chip. We extract this information by monitoring the flow of droplets with an optical microscope and training a neural network to obtain useful

information from the recorded images. In one experiment, we trained a network to accurately measure the flow velocity at the inlet of the channel from droplet images. In a separate demonstration, a network was trained to identify the concentration of isopropanol in water in the droplet-forming solution. Our experiments demonstrate that DNNs can capture the complex nonlinear phenomena that result in the flow patterns and droplet shapes.

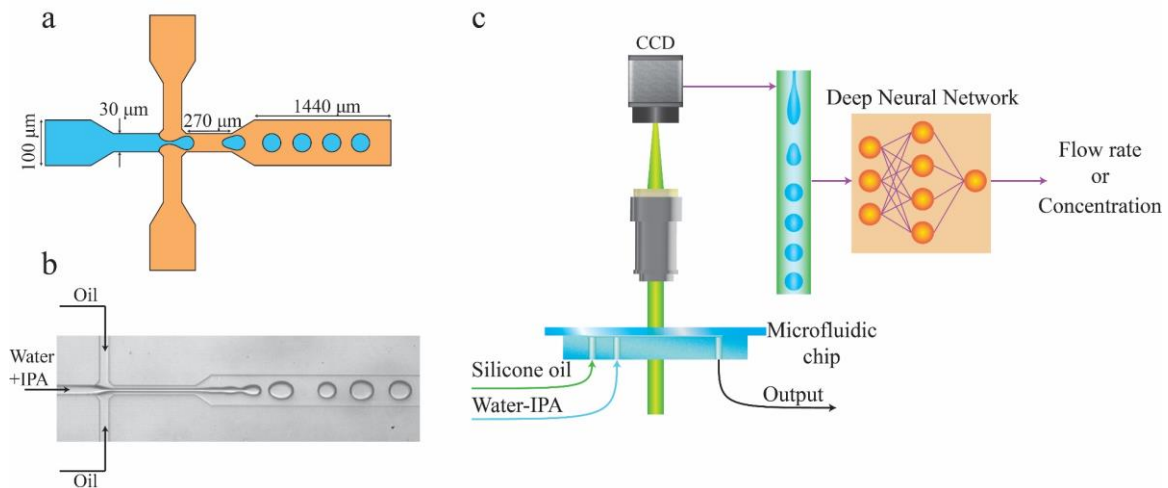


Figure 42. Using neural networks to measure fluidic properties from droplet flow patterns: (a) Schematic of the microfluidic channels (depth is $30\mu\text{m}$), (b) Image of droplet generation. Oil flows from the side channels and the water-IPA flows from the middle channel. (c) The two-phase pattern of the droplet generation in a microfluidic device contains information about the fluid and the flow properties. Neural networks are used to extract these properties while the main process stays intact.

The flow rate is a parameter that affects droplet formation [158] and can change the size, generation frequency, and pattern of droplets [159]. Similarly, the dilution ratio of isopropanol (IPA) in water affects the generation frequency and flow pattern of the droplets; this can also be recognized by the DNN to measure the concentration. There are alternative methods for measuring the flow rate [160-163] or the dilution ratio [164-167] in a microfluidic chip. The two prominent methods for on-chip flow measurements are the Coriolis method [163], based on mechanical oscillations that depend on the flow rate, and thermal measurement [162], in which a heater and thermometer are used to measure temperature changes in the flow. Commercial Coriolis devices are available with 0.05 ml/h accuracy while thermal devices typically have an accuracy of 0.012 in the range 0 to 0.12 ml/h. A thermal flow rate sensor with accuracy as low as 0.0001 ml/h has been reported but for a very small range (0 to 0.09 ml/h). All these alternative methods require integration of additional complex devices on the microfluidic chip whereas the method we describe requires only an optically transparent window and an external camera. In addition, measuring the flow rate of two-phase flows is a challenging task. A correction technique is needed to be applied to the measured values of the flow rate sensor in order to achieve a good accuracy measurement [168-170]. Deep neural networks can be used to measure the flow rate of the desired phase in a two-phase flow. For the measurement of concentration, the Coriolis device can also be used [163] with 0.25% accuracy for commercial devices. Optical methods (refractometry) [167] have been demonstrated to have excellent accuracy (as low as 0.01% concentration of IPA versus 0.5% for our demonstration); however, fine resolution optical refractometers generally rely on resonant mechanisms which are difficult to integrate into microfluidic chips. Optical probes

and DNNs can be implemented to measure compounds concentrations and it finds application in oceanography for ammonium concentration measurement [171], reacting flows for hydrocarbon concentration measurement [172], concentration measurement in microfluidic mixers [173, 174], and measurement of contaminant concentrations in water [175]. From a practical point of view, an interesting feature of the method is that a single mechanism can in principle be used for the measurement of a variety of different quantities, such as surface tension or viscosity, in addition to the ones demonstrated here. The challenge is to design the system and the training process such that the effects due to an individual parameter of the system dominate the pattern of the droplets.

5.2 Methods

A flow-focusing geometry is used to create droplets of water-IPA (Fisher Scientific UK) solution in silicone oil (viscosity 10 cSt, SIGMA-ALDRICH). The water-IPA mixture enters the main channel from the middle and the oil flows from the sides, as illustrated in Figure 42. The microfluidic chip containing this geometry is fabricated from polydimethylsiloxane (PDMS) using standard photolithography. The PDMS is plasma bonded to a glass slide to seal the microfluidic channels and subsequently heated at 80°C for 48 hours to retrieve its hydrophobic properties.

For the concentration measurements, the IPA volume concentration in water is varied in 0.5% steps from 4% to 7%. For the flow rate measurements, the dispersed phase is a solution of 5.5% IPA in water. The flow rate of the water-IPA solutions is varied in 0.05 ml/h steps from 0.1 ml/h to 1.5 ml/h. Considering the precision of the pipettes and syringes used, the accuracy of the IPA volume concentration in water is 0.08%. During the experiment, the inlet and the outlet temperatures were monitored and the mean temperature was 22.5°C. The temperature variations were less than 1 degree during data acquisition, a negligible fluctuation which did not have a noticeable effect on the performance of DNNs.

There is one inlet for each liquid and one output for the two phases. The flow rates of the liquids are regulated using syringe pumps (Cronus Sigma 1000 Series). The images are captured by a high-speed camera (Photron FASTCAM Mini UX100) and the image resolution is 1.8 $\mu\text{m}/\text{pixel}$. Images are recorded from the channel in a regions downstream of the flow focusing geometry in which the channel dimensions are 100 μm by 1440 μm by 30 μm depth. The smallest droplet in experiments has 12 μm diameter and is therefore fully resolved in the images. For each experiment, 4000 images are recorded at 50 frames per second. An image denoising algorithm from the OpenCV library [176] and an edge detection algorithm from Python's scikit-image library (the standard deviation of the Gaussian filter is set to 1.2) are applied to the images to detect the droplet boundaries and remove the effect of the background and the light profile in the images. Image processing is explained in more detail in Appendix D. This procedure is important to make sure that the DNN does not learn something related to the geometry of the channel or the light intensity. The processed images are used to train the DNNs. The structure of the DNNs is shown in Appendix D (Figure 71).

5.3 Results

Figure 42 depicts the microfluidic device with input flows of silicone oil and water-IPA solutions. Droplets of the water-IPA solution are generated at the cross junction. Images of the droplets are captured using a wide-field microscope. Figure 43 shows examples of such images for an IPA concentration in water of 5.5% for different flow rates. A network with the structure shown in Figure 71b of Appendix D is trained with 6000 images of the droplets (400 images for each flow rate) at flow rates ranging from 0.1 ml/h to 1.5 ml/h with 0.1 ml/h steps. The silicone oil flow rate is kept constant at 2 ml/h. The output of the network is a single unit whose analog value is trained to be the flow rate of the corresponding image. The trained network is tested with 2900 new images (100 images for each flow rate) recorded at flow rates ranging from 0.1 ml/h to 1.5 ml/h with 0.05 ml/h increments (Figure 43). Therefore, the ability of the network in determining new flow rates is evaluated in addition to its ability to recognize flow rates from the training set. Figure 44a shows the results of the DNN for all concentrations. The mean error of the prediction is calculated by averaging the absolute relative difference between the predicted value and the true value. The mean error of the prediction for the trained and new flow rates are 2.9% and 5.7%, respectively. For non-trained flow rates, there are some cases in which the predicted flow rate is significantly different from the true value. This happens because a flow regime transition takes place as the flow rate is changed. Two examples of such transitions are shown in Figure 44b. For example, the flow rate at 1.45 ml/h is not predicted correctly by the neural network because the flow pattern switches from individual droplets at a flow rate below 1.45 ml/h into a jet regime above this flow rate. The results of droplet flow rate measurement at another silicone oil flow rate (1.5 ml/h) are shown in Figure 73 of Appendix D which confirms the ability of the DNN in the flow rate measurement. We can improve the performance of the neural network by acquiring multiple recordings under different conditions that undergo the flow regime transitions at different flow rates. For example, we could include multiple channels on a single chip with different dimensions. We discuss this idea further in the following discussion on concentration measurement.

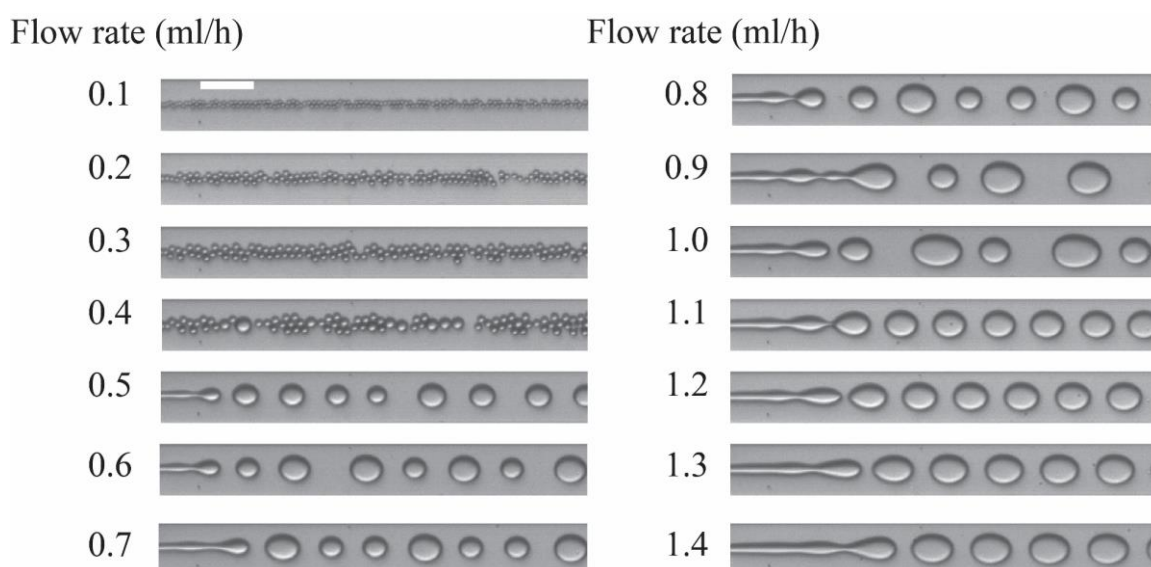


Figure 43. Images of droplet generation at different flow rates of the dispersed phase. The dispersed phase is water-IPA at a concentration of 5.5% and the continuous phase is silicone oil. The flow rate of the droplets are shown in the image and the silicone oil flow rate is 2 ml/h. Scale bar is 100 μm .

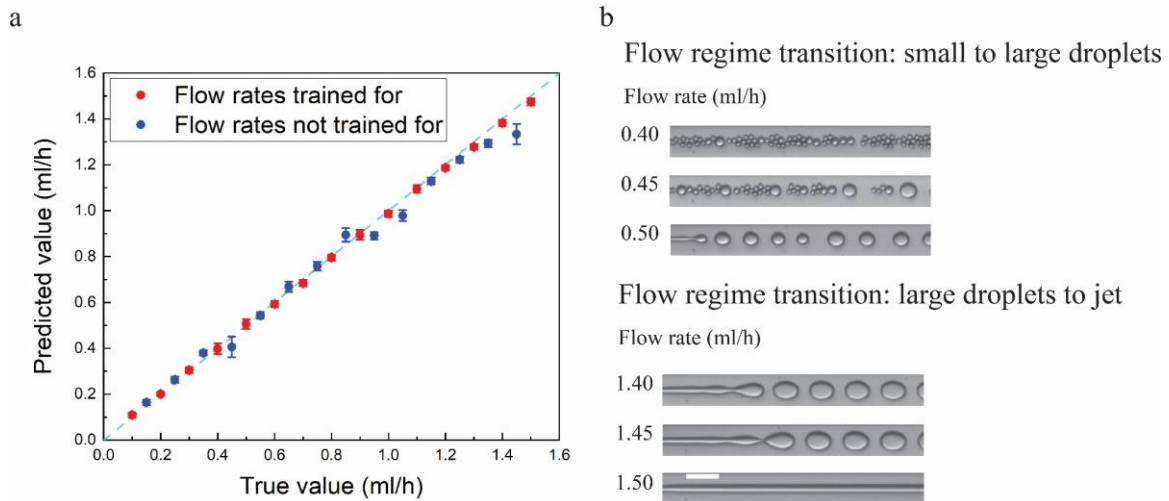


Figure 44. (a) Flow rate measurement: the measured results are compared with the true values for a water-IPA concentration of 5.5%. The red points are the flow rates for which the network is trained and the blue points are the new flow rates. Error bars show the standard deviation of the predicted values. (b) Examples of the flow regime transitions that occur at 0.45 ml/h and 1.45 ml/h flow rate of water-IPA. Silicone oil flow rate is 2 ml/h. The scale bar is 100 μ m.

Figure 45 shows droplet flows at different concentrations of the water-IPA solution where the water-IPA flow rate and the oil flow rate are fixed at 0.2 ml/h and 1.0 ml/h, respectively. The DNN shown in Figure 71b of Appendix D is trained with 3600 images of each of the four concentrations ranging from 4% to 7% with 1% increments. The trained network is tested with 400 images of each of the seven concentrations ranging from 4% to 7% with 0.5% resolution to evaluate the ability of network in predicting new concentrations (4.5%, 5.5%, and 6.5%). The diagram shown in Figure 46a compares the predicted values with the ground truth. The mean error of the network for the trained and non-trained concentrations is 1.5% and 9.3%, respectively.

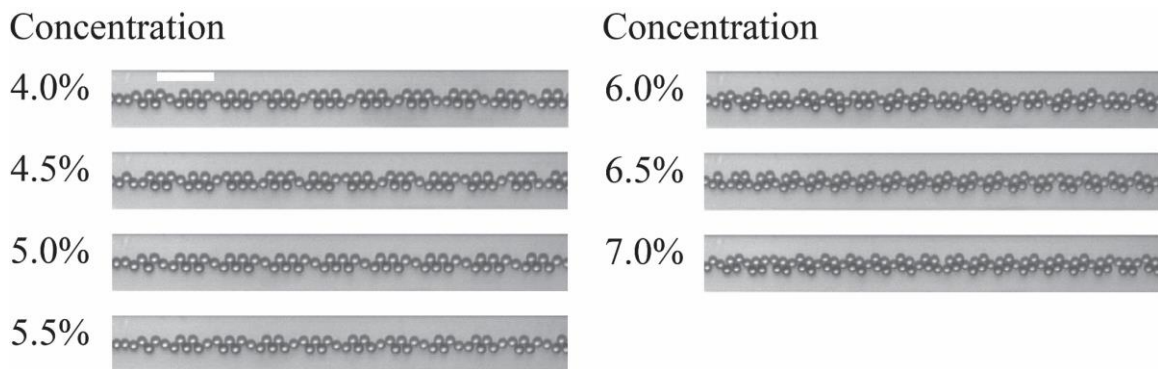


Figure 45. Images of droplet generation at different concentrations of the water-IPA solution where the concentration of the water-IPA solution is changing from 4.0% to 7.0% with 0.5% increment. The water-IPA and the oil flow rates are 0.2 ml/h and 1.0 ml/h, respectively. The scale bar is 100 μ m.

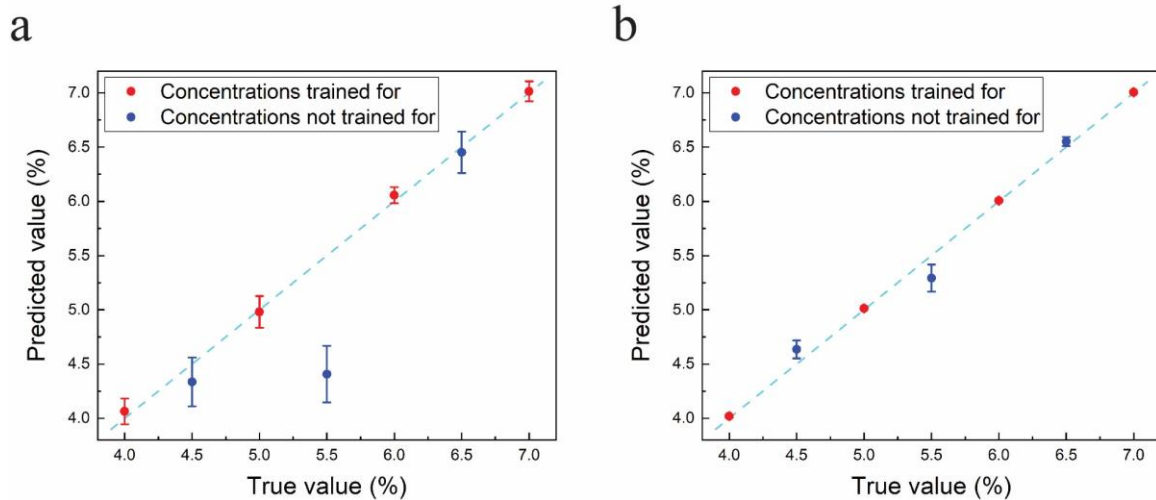


Figure 46. Predicted concentration by the DNN is compared to the true values. (a) Concentration prediction results using one DNN, and (b) concentration prediction results using six DNNs. The red points are the concentrations that the network is trained with and the blue points are the new concentrations. Bars show the standard deviation for each case.

As we can see in Figure 46a, the network correctly estimates the 4.5% and 6.5% concentrations but it cannot correctly identify the 5.5% concentration. This shows that the change in the pattern from 5.0% to 6.0% is not monotonic. This non-monotonic behavior is the result of the transition between different regimes of the droplet flow pattern due to the change in the concentration of IPA in the solution. This flow regime transition is described in more detail in Appendix D (Figure 72).

Since the flow regime transition is a sudden change in the flow pattern for a small change in concentration, the DNN cannot predict values that fall in at or close to this point. However, the concentration at which the transition occurs can be relocated by changing the flow rate of the fluid. In this way the outlier points originating from these transitions can be corrected. We tested this idea by recording images of the flow patterns for six different flow rates and using them to train six DNNs independently. We tested the system by feeding six images of the droplet flows from the six flow rate sets to the corresponding DNNs to generate six concentration estimates. Maximum three outliers are removed to reduce the standard deviation of the predicted values. The closest value to the average of the remaining values is taken as the predicted value for the concentration. Figure 74 in Appendix D shows the result of this procedure. The performance of the system can be enhanced further by recording multiple instances of the droplet patterns for each flow rate. We estimate the concentration by averaging the estimates obtained from the individual samples. This procedure reduces the variance of the estimates but it does not change the mean value. Using ten samples as an input, the mean error for concentrations that were included in the training set is reduced to 0.259% and for the concentrations outside the training set it is 2.583%. Figure 46b compares the predicted values with the true values.

As a final evaluation, we tested the sensitivity of the DNN results to the individual microfluidic chip. The experiment for the concentration measurement was repeated with a new microfluidic chip. Unfortunately, the DNNs that were trained to estimate the IPA concentration using data from the first chip did not give accurate readings for the new chip. When new DNNs were trained with data from the new chip only, the performance obtained was practically the same

as for the first chip (Figure 75 in Appendix D) even though the flow regime transitions occurred at different concentration levels. This indicates that the polydimethylsiloxane (PDMS) fabrication process of the microfluidic channels does not replicate the devices with sufficient fidelity for the DNNs to be used across different iterations. We believe this is mainly due to variations in the PDMS wall properties after O₂ plasma treatment and possibly small dimensional variations. A possible solution to this problem is to train the DNN using data from multiple PDMS devices to make the measurement insensitive to the statistical variations in individual microfluidic devices.

5.4 Conclusion

In this chapter, we discuss how to measure fluidic properties using microfluidics and deep neural networks. We show that the classification of fluid properties using traditional image processing methods of the fluid flow patterns does not lead to a satisfactory result (section D.7 in Appendix D). Using DNNs, the accuracy of the classification is drastically increased. Although image processing can be used to measure droplets size, eccentricity, and velocity [177-179], it is challenging to measure fluid properties such as concentration where the function that relates the effective parameters to the fluid properties is not known. DNNs are shown to be capable of learning the effective factors in two-phase droplet flow for the classification, thus highlighting the potential of deep learning in the microfluidics domain. We use a network with a single analog value output which corresponds to the value of a fluid property. We show that many fluidic properties and parameters can be inferred “on the fly” from this type of DNN, which receives its inputs from a simple imaging system. High accuracy prediction of the composition of the dispersed phase and flow rates are presented as two examples in our work.

The method described in this chapter can be used to measure the flow rate even when the flow rate is changing within the device. This change in flow rate happens for instance in the micro-reactors where gaseous products are generated or consumed in fluidic channels [20, 38, 40, 180]. In these devices, it is important to measure the flow rate of the gas phase in order to determine their throughput and efficiency. Using DNNs is a suitable approach to measure online the gas flow rate. Moreover, DNNs measure the flow rate in the cases where the exact flow rate inside the microfluidic chip is unknown [181, 182]. Furthermore, this method can be used to measure other fluid parameters. For instance, droplets in microfluidic channels are being used as reaction media [183, 184]. This application of droplet microfluidics requires the assessment of the droplet contents [185-187]. DNNs can be utilized for this purpose as chemical reactions change the properties of the droplets. Surface tension and viscosity measurements are other parameters that can be measured using DNNs and optical probes. Many studies have investigated the effect of surface tension and viscosity on the droplet flow pattern [188-190]. In another approach, the changes in the patterns can be used in neural networks to obtain these influential properties.

One of the limitations of our method is the sensitivity of the result to channel dimensions, pressure, and temperature fluctuations. These parameters should be the same during the measurement and during training to achieve highly accurate results. Intelligent control of fluid parameters using machine learning [191] is a recently developed approach that improves the repeatability of an experiment in a microfluidic device. By combining our approach with the control method of [191], we can potentially maintain the same conditions of the training experiment and perform the measurement. In addition to this approach, we can train a DNN

with inputs from a range of channel dimensions, temperatures, and pressures. A network trained with these inputs will predict more accurately because it has learned a range of parameter values. However, if the range of fluctuations increases, more complex design of the microfluidic device is needed to provide more information from the fluid to the network during the training.

This network, in conjunction with a microfluidic chip, can be potentially used for the measurement of multiple fluid/flow properties at the same time. However, it should be taken into consideration that it is possible to reach the same result by changing two parameters separately. In this case, the information in the pictures is not enough to distinguish these parameters. The voting system used for the concentration measurement is an approach to prevent incorrect measurement when two or more combinations of flow parameters can lead to a similar flow pattern. This system considers outputs from multiple networks and determines the correct concentration of the liquid by neglecting outlier output(s). In another approach, the addition of obstacles in the microfluidic channel and changing the geometries of the channels can force droplets to undergo different deformations, which would increase the information present in the images and especially be useful for surface tension and viscosity measurement. Fast and reliable readout of such parameters is important in many microfluidic applications such as chemical synthesis in multiphase flow systems [192, 193], cell culture [194], and electrochemical microreactors [40, 195].

We remark that although much of this same information can be measured using traditional sensors which are physically connected to the chip, their integration adds to the cost, size, and complexity of a microfluidic-based system. The presence of such cumbersome peripheral hardware is in fact what makes most of today's microfluidic devices best described as "Chip-in-a-lab" instead of a "Lab-on-a-chip" [196, 197]. We believe that many functionalities of these physical systems can be integrated into a compact on-chip imaging system [198, 199] that benefits from a pretrained learning algorithm to decode the rich information encoded in the images.

Chapter 6

Conclusion

In this thesis, we studied two-phase flows in order to improve the performance of membrane-less electrolyzers. These electrolyzers utilize fluidic flows instead of membranes for the gas product separation. Therefore, precise control of two-phase flows is important for pure hydrogen production.

In chapter 2, we studied the bubble motion in a rectangular channel. The bubble lateral equilibrium position is determined by the forces acting on the bubble in the liquid flow. These forces are dependent on the Reynolds number, Capillary number, bubble diameter, and the channel cross section. The experimental and numerical results show that a bubble equilibrates close to the channel corners by increasing the Reynolds number to values higher than one. On the other hand, the bubble moves to the channel centerline at Capillary number higher than 0.8 and bubbles diameter larger than half of the channel width. Moreover, the bubbles stay further from the channel centerline in the channels with aspect ratios higher than one. The equilibrium position of bubbles is also dependent on the impurities of the liquid. Impurities such as surfactant can be adsorbed at the interface of the bubble and change the liquid-gas interaction. This phenomenon changes the bubble equilibrium position in the channel. Bubbles should stay far from the centerline in order to prevent cross over in membrane-less electrolyzers. This can be achieved when the Reynolds number is higher than one and the bubbles are smaller than half of the channel width. Furthermore, product separation is more effective in channels with aspect ratios higher than one since the bubbles' equilibrium position is close to the shallower sidewall in these channels.

We investigated the bubble detachment and coalescence in an electrolyzer in chapter 3 in the next step. We designed an electrolyzer with small nucleation sites based on our findings in chapter 2. We found that the large bubble detachment and bubble coalescence are the main reasons for the bubble cross over. These two processes create large bubbles in the channel. The equilibrium position of these large bubbles is at the centerline where they can mix with bubbles from the opposite electrodes. Increasing the Reynolds number leads to smaller bubble generation which improves product separation. However, the fluidic loss increases super-linearly with the Reynolds number. This fluidic loss is 6% of the stored energy in a membrane-less electrolyzer working at Reynolds number of 62 and current density of 300 mA/cm² with 150 μm × 100 μm cross section. This fluidic loss can be decreased by using a larger interelectrode distance, but the ohmic loss increases. We added Triton X-100 surfactant to the electrolyte in order to resolve this problem. The surfactant reduces the surface tension between liquid and gas. The bubble detachment size is smaller at lower surface tensions. Furthermore, the surfactant molecules adsorbed at the interface of bubbles prevent the bubble coalescence. In addition to the surface tension, the rate of surfactant adsorption at the bubble interface determines the bubble detachment size. This rate is faster at higher concentrations that lead to smaller bubble detachment. We found that product separation is successful when Triton X-100 concentration is 50 times higher than critical micelle concentration. An electrolyzer operates

at a higher production rate and constant Reynolds number or at lower Reynolds number and constant production rate by adding a surfactant to the electrolyte.

We presented the porous walls (PW) electrolyzer for pure hydrogen production at high production rates in chapter 4. This electrolyzer has two porous walls. The electrolyte enters the region between the porous walls and flows through the wall pores to reach to the outer channels. The electrodes are on the outer sides of porous walls. Consequently, the electrochemical reactions and bubble nucleation happen only in the outer channels. The porous walls and liquid flow in the wall pores prevent the bubble cross over to the opposite side. We compared the performance of the PW electrolyzer with an equivalent parallel electrodes (PE) electrolyzer. The PE electrolyzer can produce hydrogen with cross overs below the flammability limits at high Reynolds numbers and low current densities. However, the hydrogen cross over of the PE electrolyzer is $8.2 \pm 0.4 \%$ at a high production rate of 300 mA/cm^2 and Reynolds number of 109. The PW electrolyzer has cross over of $0.14 \pm 0.06 \%$ at the same operating conditions. This shows a significant decrease in the cross over thanks to the design of the PW electrolyzer. As discussed above, it is possible to improve the product separation of the device by adding a surfactant to the electrolyte. We showed that the hydrogen cross over of the PW electrolyzer decreases to $0.11 \pm 0.05 \%$ by using heptadecafluorooctanesulfonic acid potassium (PFOS) surfactant in the electrolyte at the same conditions. This surfactant not only improves product separation, but also improves the electrochemical performance of the PW electrolyzer. Furthermore, the overpotential losses are smaller in the PW electrolyzer compared to the PE electrolyzer as the bubbles are not flowing between the electrodes in the PW electrolyzer.

The large-scale membrane-less electrolyzers have a larger interelectrode distance than the microfluidic electrolyzers. This is mainly due to the flow of larger bubbles in the scaled-up electrolyzers. The bubbles become smaller by adding a surfactant to the working electrolyte as we discussed in chapter 3. Therefore, the interelectrode distance of the scaled-up electrolyzer can be decreased which leads to energy conversion at higher efficiencies. In addition to the usage of surfactant, the PW electrolyzer design presented in chapter 4 can be scaled-up without increasing the interelectrode distance. However, the fabrication of inclined pores and deposition of catalysts only on one side of the porous walls might be challenging.

Additive manufacturing technologies have been developed in recent years. The minimum resolution of additive manufacturing technologies has been reached the microscale [146]. Furthermore, these technologies can print different materials such as metal catalysts and plastics at different resolutions as shown in Figure 47. Therefore, they can be used to facilitate the fabrication of large-scale PW electrolyzers. Additive manufacturing can also be used to fabricate electrolyzers with different catalyst materials for hydrogen and oxygen evolution reactions. By doing this, the catalysts with the smallest overpotentials can be used in order to improve the electrochemical performance of the membrane-less electrolyzer [200].

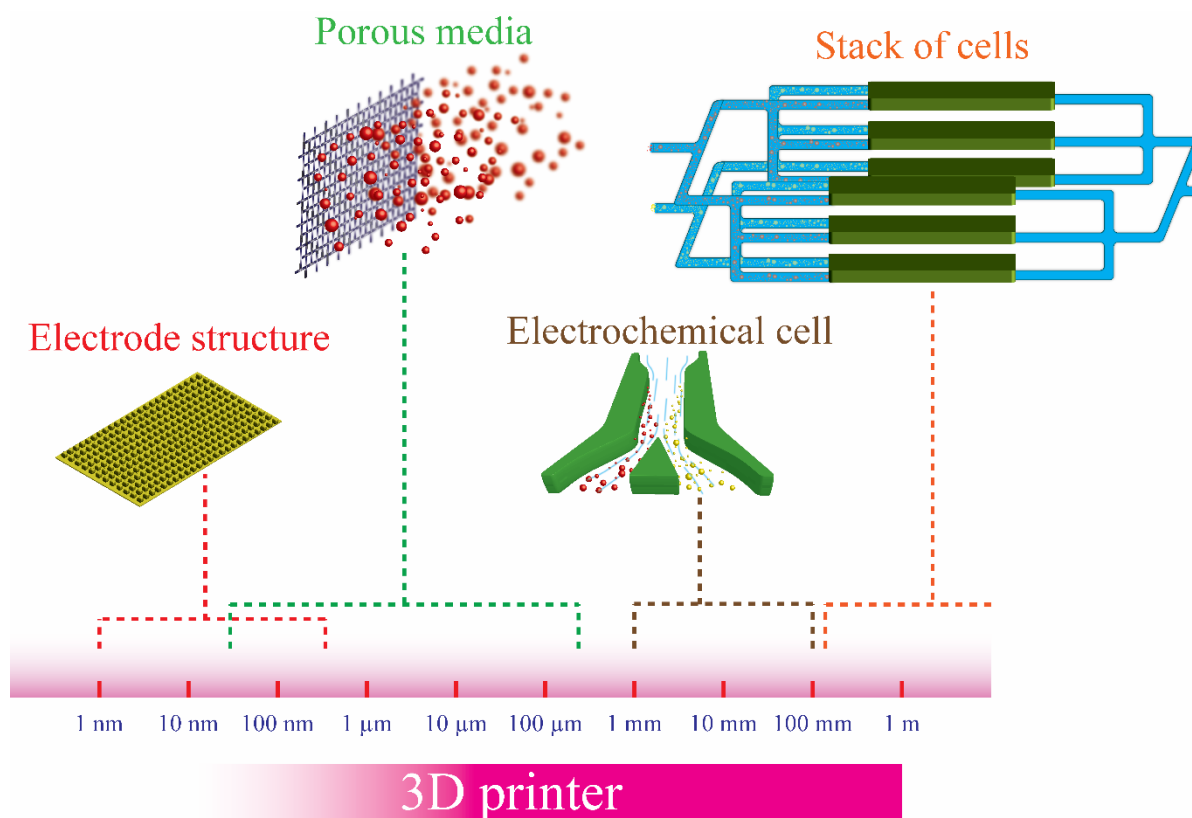


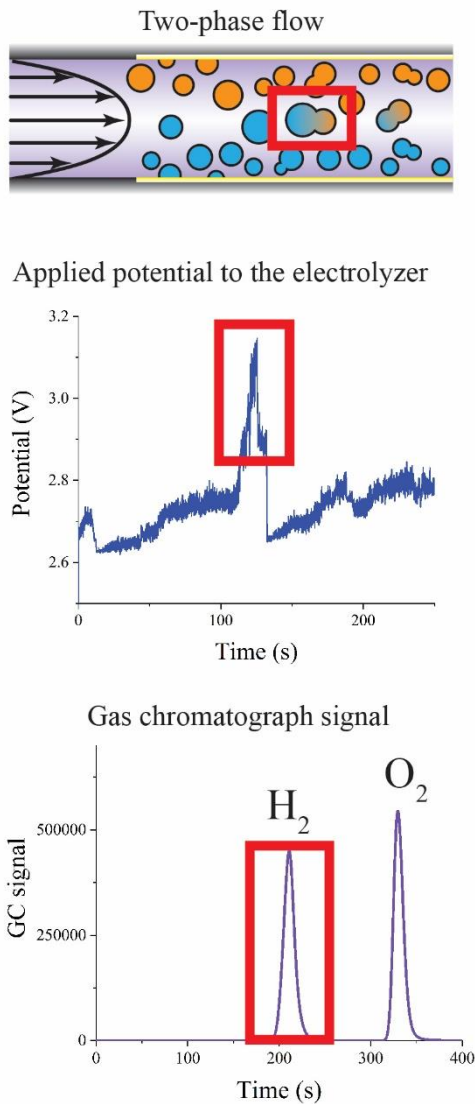
Figure 47. Additive manufacturing can be used to fabricate different parts of membrane-less electrolyzers at different scales [146].

We developed a non-intrusive method for the measurement of the liquid/flow properties in chapter 5. This method uses neural networks and images of the droplet generation in a flow-focusing microchannel for this measurement. We trained neural networks to measure the alcohol concentration in the dispersed phase or the flow rate of the dispersed phase. The liquid properties and flow conditions affect droplet generation patterns. The neural networks see different droplet generation patterns at different conditions. Therefore, they learn the relation between droplet generation patterns and the changing variable. The network can predict alcohol concentrations between 4.0% and 7.0% with 0.5 % accuracy. The network trained for the flow rate measurement can determine the flow rates between 0.1 to 1.4 ml/h with 0.05 ml/h resolution. These networks are capable to determine concentrations or flow rates that have not been used for the training. This measurement method can be extended to control two-phase flows in the membrane-less electrolyzers.

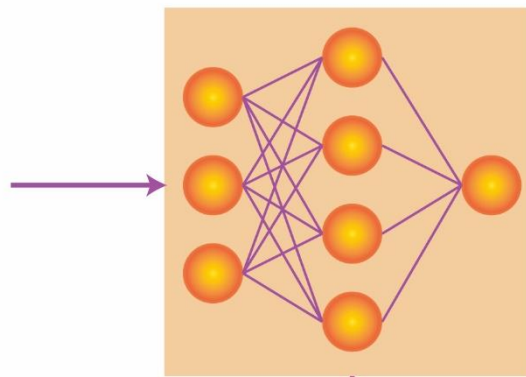
The membrane-less electrolyzers operate at constant liquid flow rates and current densities. It is possible that a large bubble forms in the channel due to a disturbance in the fluidic flow or the applied current. This bubble can lead to significant cross-contamination. Therefore, active control of the two-phase flow is necessary for a secure operation of the electrolyzer. The formation of large bubbles is visually detectable by cameras or the gas cross over can be measured using a gas chromatograph (GC). Besides, the input electrical power increases when a large bubble forms in the channel. The measurement method developed in chapter 5 can be utilized to measure the product cross over in real-time by looking at the bubble motion in the electrolyzer, GC measurement, or electrical power oscillations as shown in Figure 48. Afterwards, a trained neural network can modify the operating conditions such as current

density or flow rate based on this measurement. This network should be optimized in order to achieve the maximum throughput with the minimum bubble cross over.

Monitored parameters



Deep Neural Network



Controlled parameters

Flow rate
Applied current

Figure 48. The neural network can monitor different measurement and control the electrochemical performance and product separation. The red rectangles are the regions that the neural network can monitor: the bubble coalescence in the fluidic channel, the sudden increase in the applied potential, and detection of hydrogen in the oxygen stream in the gas chromatograph (GC) measurement. The network can prevent the gas cross over or the increase in the input power by changing the applied current and liquid flow rate.

Appendix A

Inertial manipulation of bubbles in rectangular microfluidic channels

A.1 Microfabrication

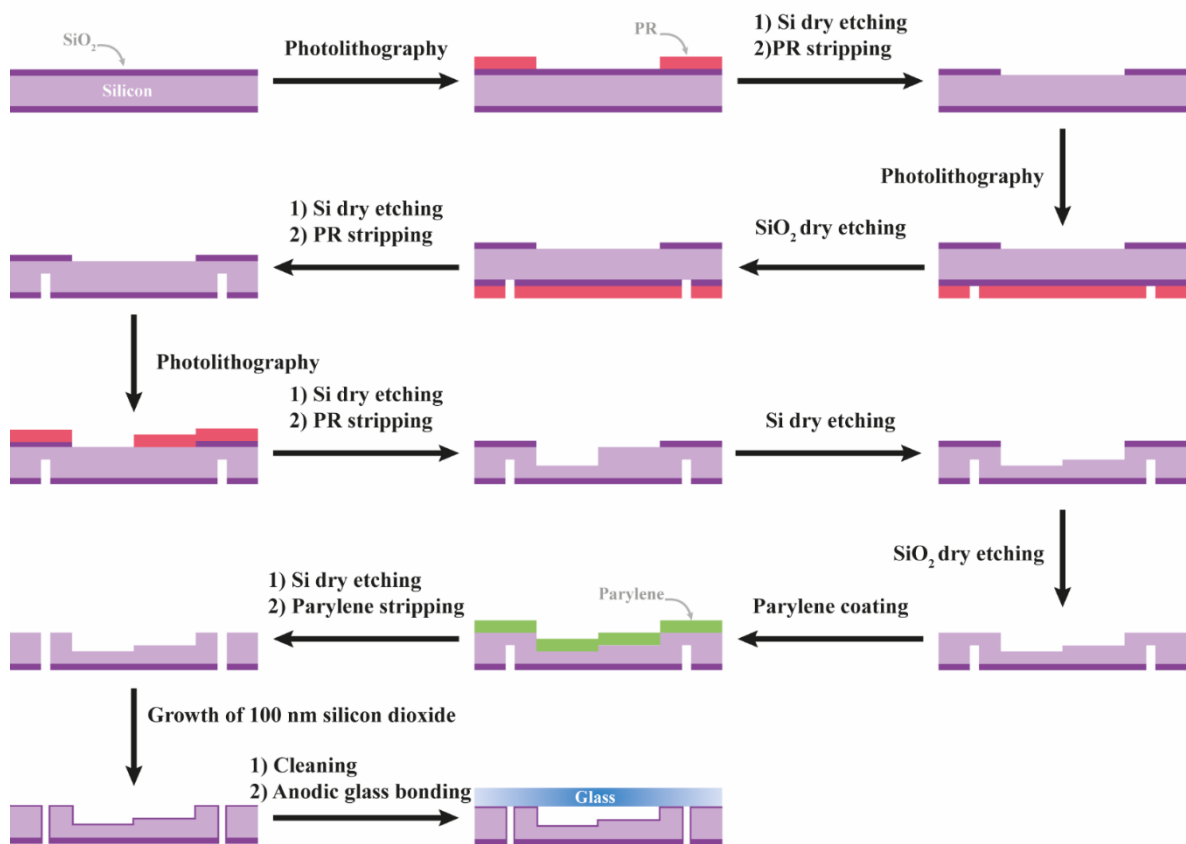


Figure 49. Microfabrication process flow

A.2 Numerical simulations for different grid sizes

Table 7. Numerical simulation results for different grid sizes

$Re = 9.48$ $Ca = 0.162$ $\bar{D} = 0.61$		
Grid points	Equilibrium position	U_{bubble}/U_{cl}
105407	$\bar{Y} = 0.52$ $\bar{Z} = 0.52$	0.860
220639	$\bar{Y} = 0.50$ $\bar{Z} = 0.51$	0.855
425697	$\bar{Y} = 0.50$ $\bar{Z} = 0.50$	0.853
650855	$\bar{Y} = 0.50$ $\bar{Z} = 0.49$	0.852

A.3 Equilibrium position of the bubble in the rectangular channel

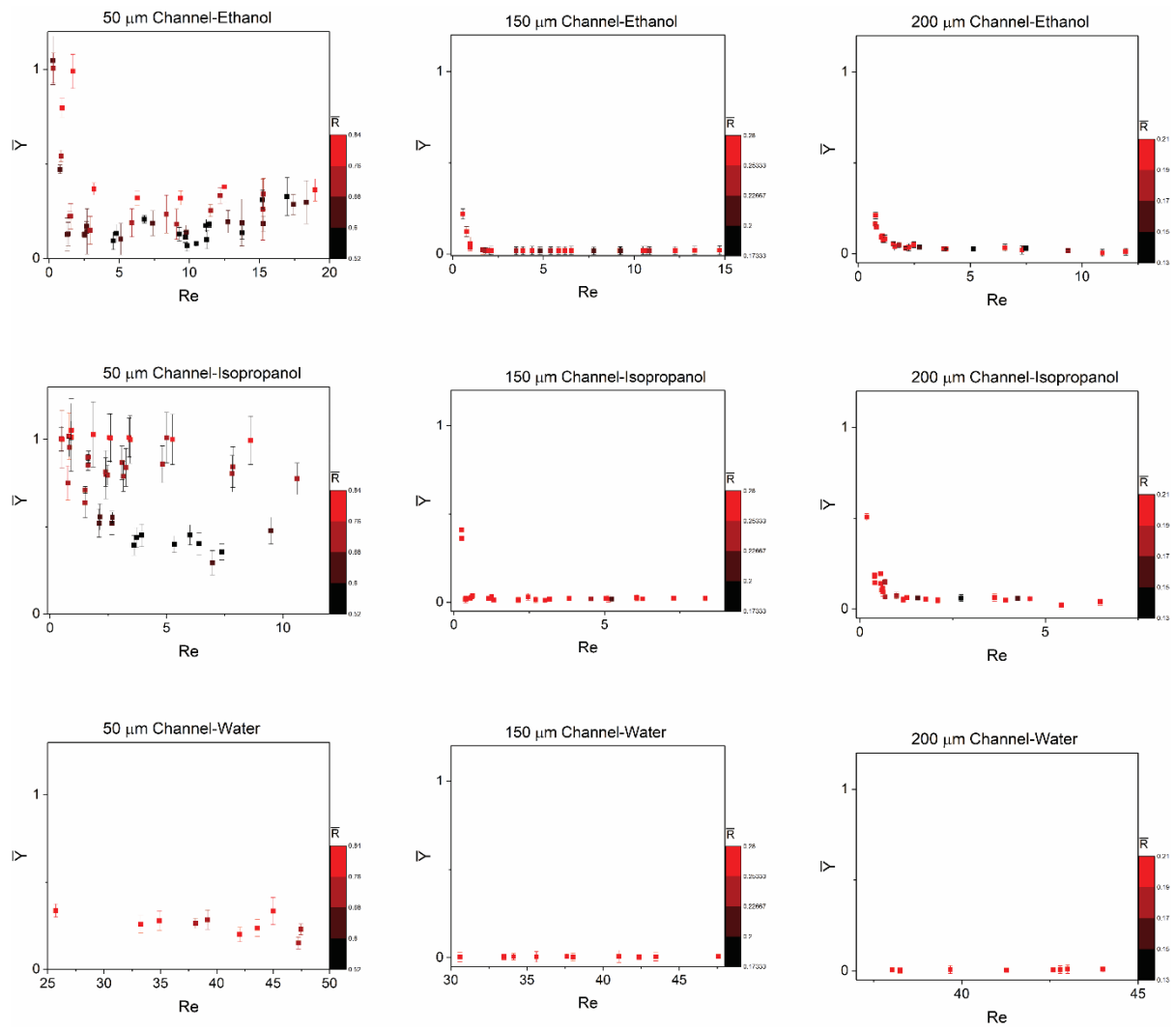


Figure 50. Diagrams of the bubble position with the error bars representing the standard deviation from the average value

A.4 Equilibrium position of the bubble in the rectangular channel

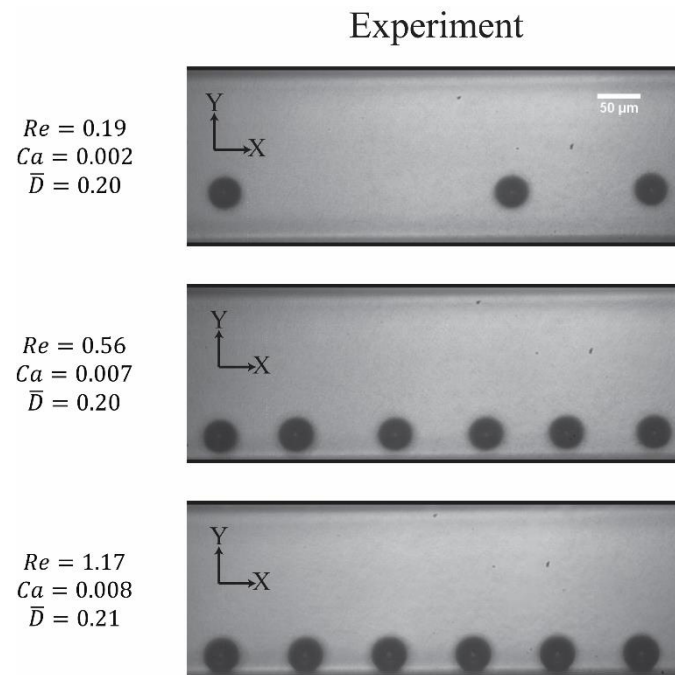


Figure 51. Diagrams of the bubble position with the error bars representing the standard deviation from the average value

A.5 Experimental results for the effect of Reynolds number on the bubble position

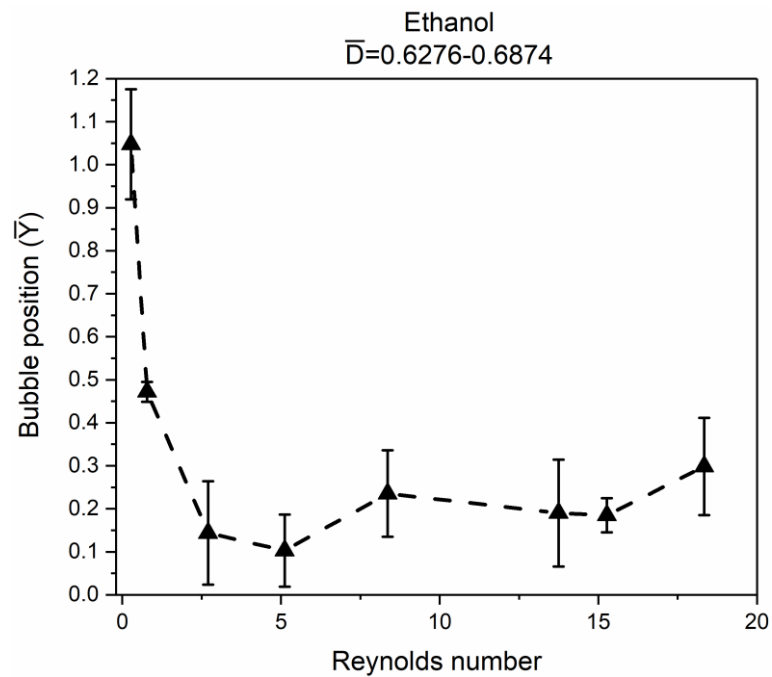


Figure 52. Effect of the Reynolds number on the bubble position in the square channel ($50 \mu\text{m}$ width and depth). The continuous phase is ethanol and the error bars represent the standard deviation from the average value. $\bar{Y} = 1$ corresponds to the bubble position at the centerline and $\bar{Y} = 0$ corresponds to the bubble position at the wall. The diameter of the bubbles \bar{D} are between 0.6276 and 0.6874.

A.6 Shear rate at the channel cross section

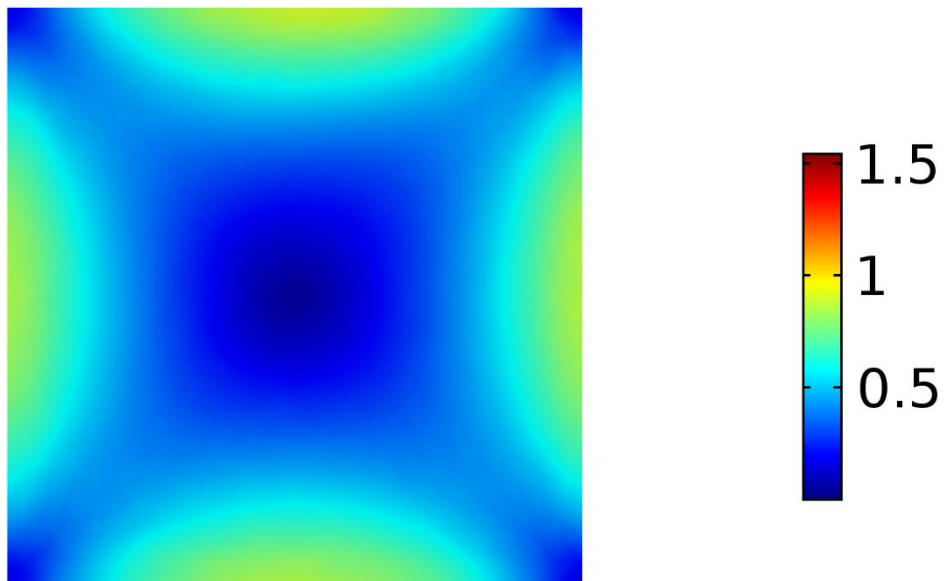


Figure 53. Shear rate at the channel cross section: Center of the channel has the smallest value of the shear rate. Also, diagonals have a smaller shear rate in comparison with the center of sidewalls. The simulation is done for $Re = 10$ in a square channel. The boundary conditions at the inlet and outlet are inlet velocity and outlet pressure, respectively.

A.7 Effect of the surfactant

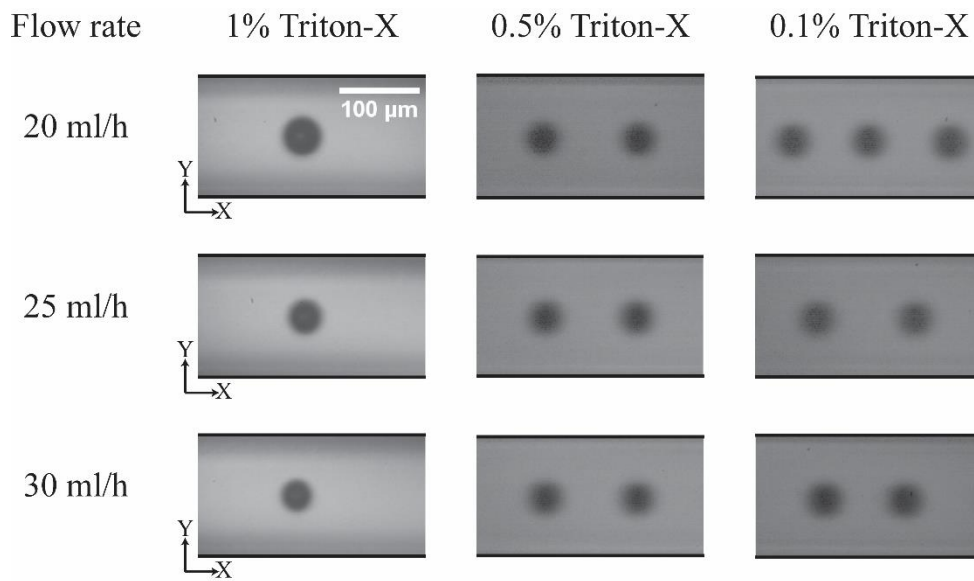


Figure 54. Effect of different Triton-X concentration on the bubble position in a channel with $150 \mu\text{m}$ width and $50 \mu\text{m}$ depth. Since the concentration of the surfactant is enough to cover the interface of the bubble and the liquid, there is no difference between the different concentrations.

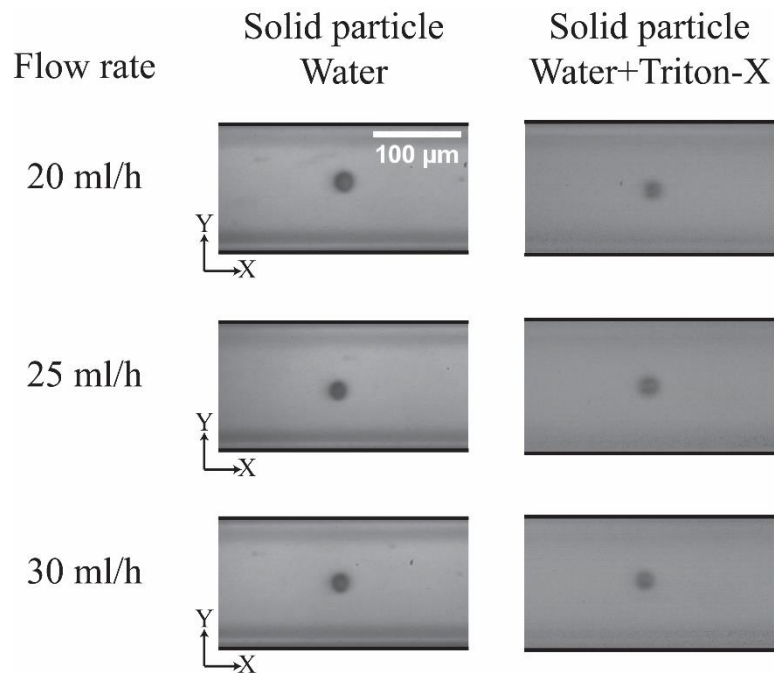


Figure 55. Effect of surfactant on the equilibrium position of a solid particle in a rectangular channel ($150 \mu\text{m}$ width and $50 \mu\text{m}$ depth). The equilibrium position of the solid particle does not change by adding the surfactant to the carrier phase. Water+Triton=X liquid is 1% volumetric aqueous solution of Triton-X.

Appendix B

The impact of surfactants on the inertial separation of bubbles in microfluidic electrolyzers

B.1 Microfabrication

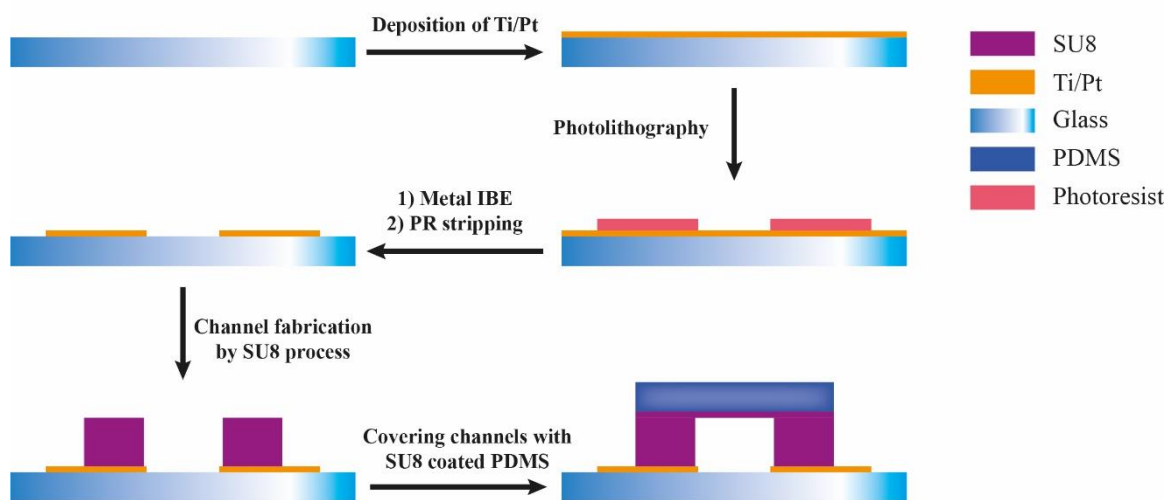


Figure 56. Fabrication process of the microchannels with small nucleation sites

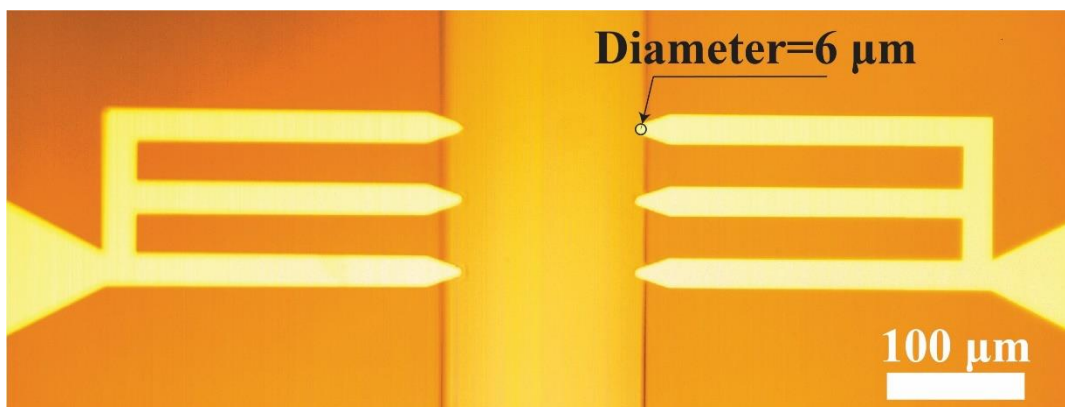


Figure 57. Picture of the fabricated electrodes at the bottom of the fluidic channel: the tip of the electrodes has a $6\ \mu\text{m}$ diameter.

B.2 Image processing and bubble detection

Figure 58 shows the schematic of the channel. The videos of bubbles motion in the flow is captured at red squares specified in this image. The region at the end of the channel is 8.5 mm far from bubble nucleation sites in order to capture the equilibrium position of the bubbles. Figure 59 compares the histograms captured at two different sampling times of 20 s and 12 s. The videos with 20 s duration are captured at 50 frame per second (fps) and 1/10000 s shutter speed. The videos with 12 s duration are captured at 500 fps and 1/10000 s shutter speed. The bubbles volume distribution is approximately the same in both sampling times. The histograms of the main text are drawn by analyzing videos with the length of 20s.

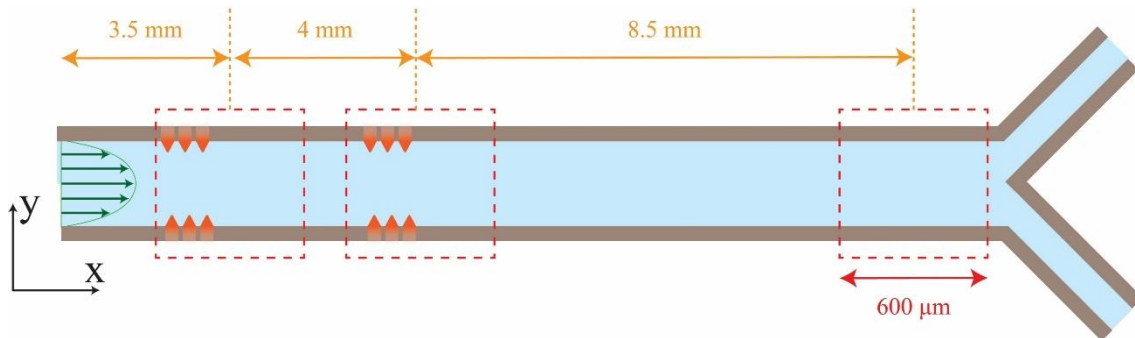


Figure 58. Schematic of the channel design: The red squares determine the regions used to capture videos of bubbles motion. The aspect ratios are not to scale.

Duration of sampling

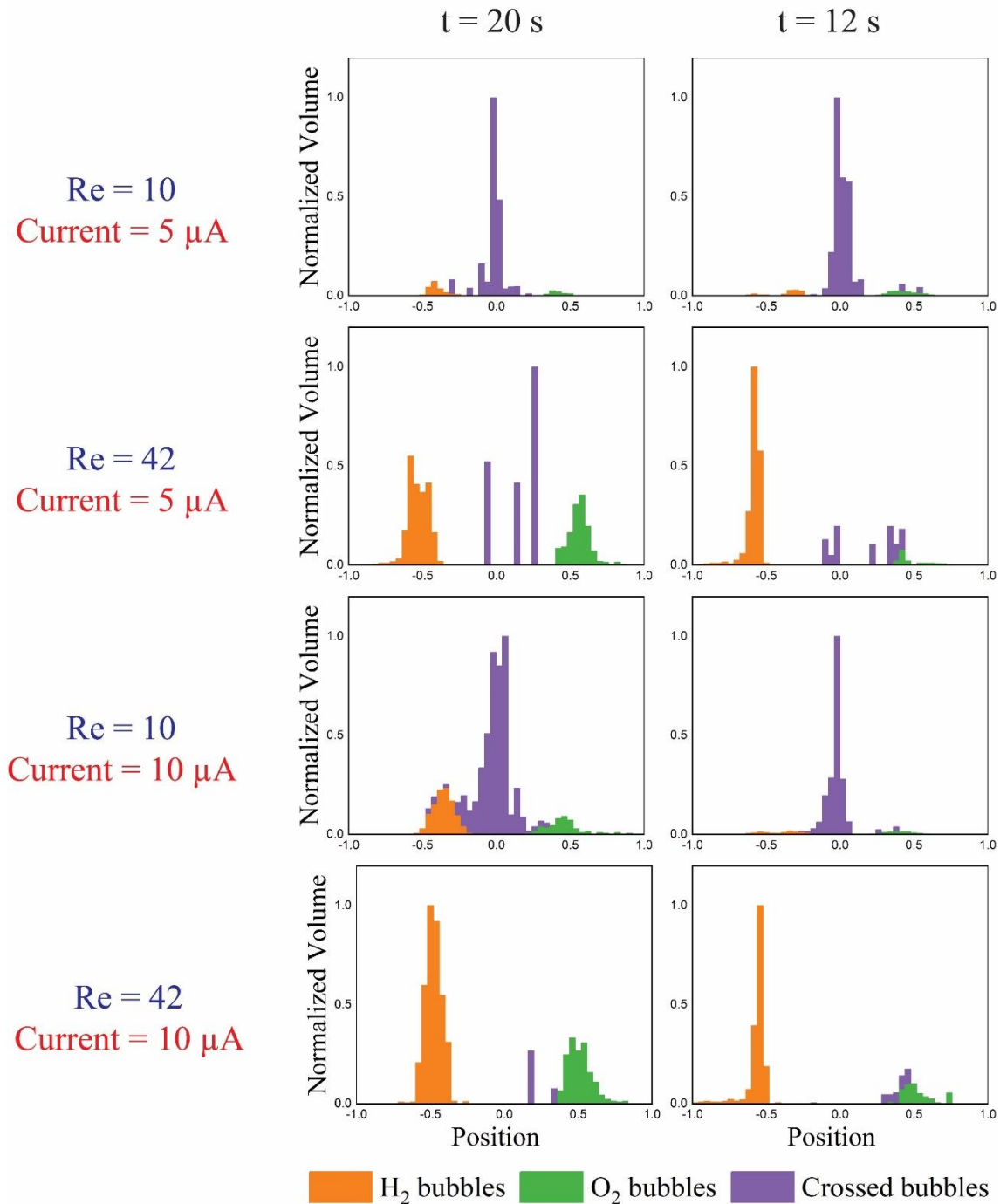


Figure 59. The histograms of bubbles volume distribution at two different sampling time and same conditions in 0.5 M H₂SO₄: 20 s videos are captured at 50 fps and 1/10000 s shutter speed. 12 s videos are captured at 500 fps and 1/10000 s shutter speed.

The images of the last 600 μ m of the channel are taken and analyzed using OpenCV library in python [201]. Initially, by using the fastNIMeansDenoisingColored command, noises of the images are reduced. The filter strength, template window size, and the search window size for this command are set to 10, 3, and 15, respectively. Afterwards, the images are converted to grayscale. A median blur filter with the kernel size between 7 to 15 is used to increase the circles contrast. Finally, the circles are detected using the Hough transform. The method,

accumulator ratio, minimum distance between the centers, higher threshold, accumulator threshold, and the maximum radius of the circles are set to HOUGH_GRADIENT, 1, 10, 38, 18, and 80. Table 8 presents the python code for bubble detection. Figure 60 shows the images after each process of image processing.

Table 8. The python code for detecting bubbles

```
import cv2
src = cv2.imread('image.jpg')
src = cv2.fastNlMeansDenoisingColored(src,None,10,10,3,15)
gray = cv2.cvtColor(src, cv2.COLOR_BGR2GRAY)
gray = cv2.medianBlur(gray, 9)
circles = cv2.HoughCircles(gray,cv2.HOUGH_GRADIENT,1,10,
param1=38,param2=18,minRadius=0,maxRadius=80)
```

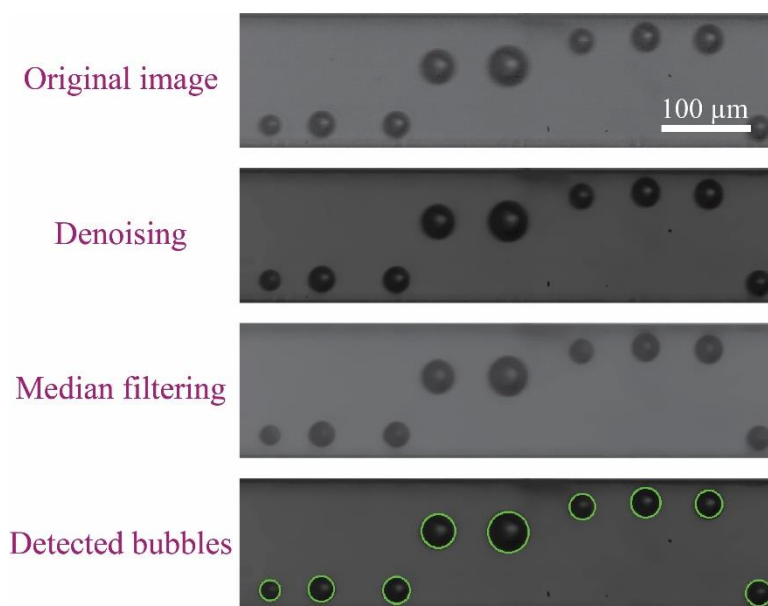


Figure 60. Bubbles detection process: initially the noises of the images are removed using fastNlMeansDenoisingColored command. Afterwards, the images are converted to gray scale and a median blur filter is applied in order to highlight the circles. Finally, the bubbles are detected using HoughCircles command.

Table 9 shows the percentage of the detected bubble by the image processing. We used the videos of the bubble generation at the electrodes for this measurement. The videos are captured at 10000 fps for a duration of 0.1s. The percentage is below 100% due to the gas dissolution in the liquid and also the errors of image processing. The image processing method sometimes overlooks very small bubbles or bubbles very close together.

Table 9. The percentage of detected hydrogen and oxygen bubbles in 0.5 M H_2SO_4 : The total amount of hydrogen and oxygen is calculated by Faraday's laws of electrolysis.

Re	current (μA)	% of detected hydrogen bubbles	% of detected oxygen bubbles
62	80	98.5	87.4
62	100	95.5	89
62	120	99	89.2

Triton X-100 can be oxidized at the cathode and therefore it can reduce the Faradaic efficiency of oxygen evolution reaction. The decrease in faradaic efficiency has been reported to be 3-4%

[99]. Table 10 shows the measured ratio of the volume of oxygen bubbles to the volume of the hydrogen bubbles at $Re=62$ and different currents. The ratio approximately remains constant after adding Triton X-100 to the electrolyte. The image processing is more challenging when there is a surfactant in the electrolyte since the bubbles are smaller. Furthermore, the bubbles move on top of the other bubbles and there are overlaps between the bubbles in the electrolyte with surfactant. This causes an error in the detection of all bubbles in the electrolyte with the surfactant. However, Table 10 presents an estimate of the effect of surfactant on the volume ratio of the oxygen bubbles to the hydrogen bubbles. This table leads to the same result of Allen et al. [99] considering the errors in image processing.

Table 10. The volume ratio of the generated oxygen to the generated hydrogen in the 0.5 M H_2SO_4 with and without Triton X-100.

Re	current (μA)	Volume ratio of O_2 to H_2	
		0.5 M H_2SO_4	0.5 M H_2SO_4 + Triton X-100: $C^* = 50$
62	80	0.45	0.42
62	100	0.47	0.52
62	120	0.45	0.46

The radius of generated bubbles in the membrane-less microfluidic electrolyzer of [20] at 10 ml/h is measured in order to compare with the radius of generated bubbles in the finger electrode device. We used the SI movies of [20] for this measurement. This measurement considers hydrogen and oxygen bubbles together. The average bubble radius of [20] is $19 \pm 11 \mu m$. The average bubble radius of the finger electrodes device used in this study is $10.2 \pm 3.9 \mu m$ at the flow rate of 10 ml/h ($Re=21$) and the current= $10 \mu A$. This difference is due to the difference in the electrode geometry, the channel design, and the production rate.

B.3 Forces acting on the bubble at the detachment

For a bubble growing at the electrode the force balance is as follows[105, 106, 108, 109]:

$$\begin{aligned}\sum F_y &= F_{\sigma,y} + F_{G,y} + F_{SL} + F_{CP} \\ \sum F_x &= F_{\sigma,x} + F_{G,x} + F_{G,bulk} + F_D\end{aligned}\quad (1)$$

In the Eq. (1), F_{σ} , F_G , F_{SL} , F_{CP} , $F_{G,bulk}$, and F_D are the surface tension force, the force due to the bubble growth, the shear lift force, the contact pressure forces, the bubble growth force in a bulk liquid velocity, and the drag force, respectively. x determines the direction parallel to the wall and y determines the direction perpendicular to the wall.

The surface tension force, F_{σ} can be expressed as [107, 108]

$$\begin{aligned}F_{\sigma} &= - \int_0^{2\pi} \frac{d_w}{2} \sigma \cos(\gamma(\phi)) \cos(\phi) d\phi \vec{e}_x \\ &\quad - \int_0^{2\pi} \frac{d_w}{2} \sigma \sin(\gamma(\phi)) d\phi \vec{e}_y\end{aligned}\quad (2)$$

where σ is the surface tension, d_w is the contact diameter, ϕ is the circumferential angle, and γ is the bubble contact angle. The closed form approximation of this force can be written as[108]

$$\begin{aligned}F_{\sigma} &= -1.25d_w\sigma \frac{\pi(\alpha - \beta)}{\pi^2 - (\alpha - \beta)^2} (\sin \alpha + \sin \beta) \vec{e}_x \\ &\quad - d_w\sigma \frac{\pi}{\alpha - \beta} (\cos \beta - \cos \alpha) \vec{e}_y\end{aligned}\quad (3)$$

where α and β are the advancing and receding contact angles. An estimation of the growth force, F_G is [109]

$$F_G = -\pi\rho r^2 \left(\frac{3}{2} \dot{r}^2 + r\ddot{r} \right) (\sin \theta \vec{e}_x + \cos \theta \vec{e}_y) \quad (4)$$

where ρ is the liquid density, r is the bubble radius, θ is the bubble tilt angle. \dot{r} and \ddot{r} are the first and the second time derivatives of the bubble radius. The bubble growth at high current densities can be expressed as [202]

$$r(t) = \left[\frac{3RTI}{4\pi zFP} \right]^{0.33} t^{0.33} \quad (5)$$

Where R is the universal gas constant, T is the temperature, I is the current, z is the number of transferred electrons per ion, F is the Faraday constant, P is the pressure, and t is the time.

The shear lift force, F_{SL} can be calculated using the following equation [203]

$$F_{SL} = \frac{1}{2} C_{L1} \frac{1}{2} \frac{d_w}{r} A \rho U^2 \vec{e}_y + C_{L2} \rho V_b (U\omega) \vec{e}_y \quad (6)$$

In Eq. (6), A is the area of the bubble normal to the flow, V_b is the bubble volume, ω is the vorticity, U is the velocity of the liquid. C_{L1} for a hemispherical bubble is 11/8. C_{L2} is

approximately equal to 0.53 in an unbounded liquid. The contact pressure can be written as [107, 108]

$$F_{CP} = \frac{\pi d_w^2}{4} \times \frac{2\sigma}{r_c} \vec{e}_y \quad (7)$$

where r_c is the radius of the curvature of the bubble at the contact with the wall. The bubble growth force in a bulk liquid velocity, $F_{G,bulk}$ is [109]

$$F_{G,bulk} = 2\pi\rho r^2 U \vec{e}_x \quad (8)$$

The drag force, F_D can be calculated using the following equation [106]

$$F_D = 6\pi\mu U r \left\{ \frac{2}{3} + \left[\frac{12}{Re_b} + 0.75 \left[1 + \frac{3.315}{Re_b^{\frac{1}{2}}} \right] \right]^{-1} \right\} \vec{e}_x \quad (9)$$

μ is the viscosity of the liquid. Re_b can be calculated using the following equation:

$$Re_b = \frac{2rU\rho}{\mu} \quad (10)$$

where μ is the viscosity of the liquid. The contact angle is measured using the image of the bubble generation at $Re=62$ and current=800 nA as shown in Figure 61. Table 11 presents the contact angle of bubbles in the middle of the detachment process at different Re . It should be noted that the contact angle is changing as the bubble grows. In addition, the contact angle is dependent on the flow rate. For the simplicity, the contact angle is assumed constant in Eq. (3). The contact angle measured at $Re=62$ is used for solving the force balance. Furthermore, the effect of dissolved gases and temperature are not considered in these equations. The bubble generation frequency is plotted at different currents and at different Re and shear rates in Figure 62. The generation frequency increases linearly by the current and increases non-linearly by the Re and the shear rate.

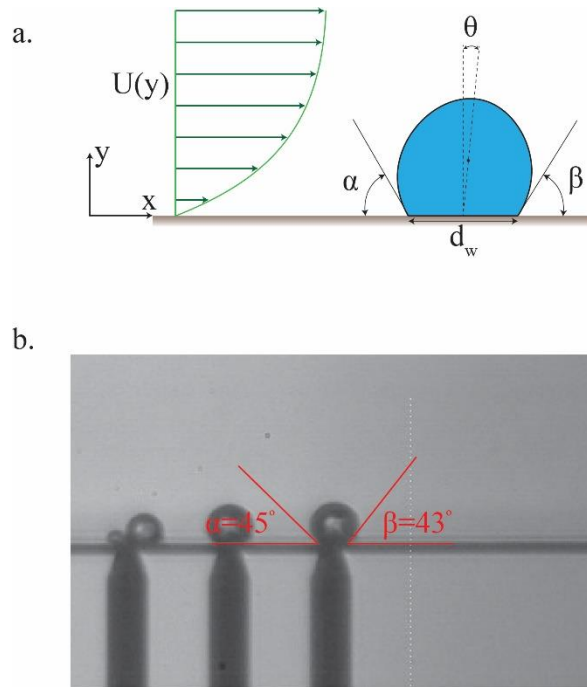


Figure 61. a. The advancing and receding contact angles are shown in the picture. b. The contact angle of the bubbles is measured using the image of bubble generation at $Re=62$ and current=800 nA.

Table 11. Approximate contact angle at different Re

Current (μA)	Re	α ($^\circ$)	β ($^\circ$)
5	10	48	41
5	21	48	43
5	42	45	43

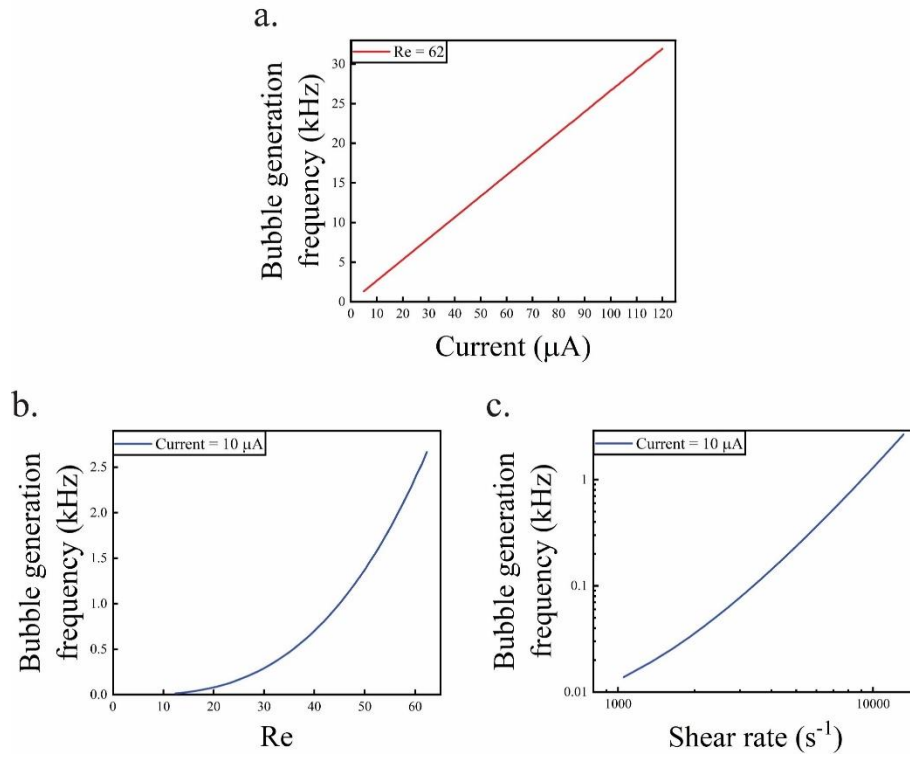


Figure 62. a. The diagram shows the bubble generation frequency against current at $\text{Re}=62$. b. and c. show the bubble generation frequency at different Re and shear rates at current= $10 \mu\text{A}$. The bubble generation frequency increases linearly by the current but it increases non-linearly by the Re and the shear rate.

B.4 Electrolyte properties and the flow rates

The viscosity and density of 0.5M sulfuric acid are 0.001102 Pa.s and 1030 kg/m³, respectively. The flow rates used in this study and the corresponding Re are presented in Table 12.

Table 12. Flow rates used in this study and the corresponding Re

Flow rate (ml/h)	Re
5	10
10	21
20	42
30	62

B.5 Power loss due to fluidic resistance

In laminar flow, the pressure loss (ΔP) inside a channel can be calculated using the following equation [204]:

$$\Delta P = \left(\frac{64}{Re}\right) \rho \frac{L V^2}{D} \quad (11)$$

where the Reynolds number (Re) is calculated based on the following equation.

$$Re = \frac{\rho V D}{\mu} \quad (12)$$

In the above equations, ρ is the density, L is the length of the channel, D is the (hydraulic) diameter of the channel, V is the mean velocity in the channel, and μ is the viscosity. We can substitute the velocity (V) by the flow rate (Q). The flow rate equation is:

$$Q = VA \quad (13)$$

where A is the cross-sectional area of the channel. The power loss due to the fluidic flow can be calculated by the following equation:

$$\text{Power} = \Delta P Q \quad (14)$$

Therefore, the power that is required to flow liquid across tubes and microchannels is calculated based on the following equation:

$$\text{Power} = \frac{32\mu L}{AD^2} Q^2 \quad (15)$$

where μ is the viscosity, L is the length of the channel, A is the area of the channel, D is the (hydraulic) diameter of the channel, and Q is the flow rate.

Following table shows the dimensions of the fluidic channels:

Table 13. The dimensions of the fluidic tubes and the microchannel

	Fluidic tubes	Microchannel
L (mm)	400	21
D (μm)	600	120
A (μm^2)	282743	15000

The viscosity and density of 0.5M sulfuric acid are 0.001102 Pa.s and 1030 kg/m³, respectively. Figure 63 shows the power loss at different Re . At $Re=10$, the power loss is 7 μW and at $Re=62$ the power loss is 248 μW .

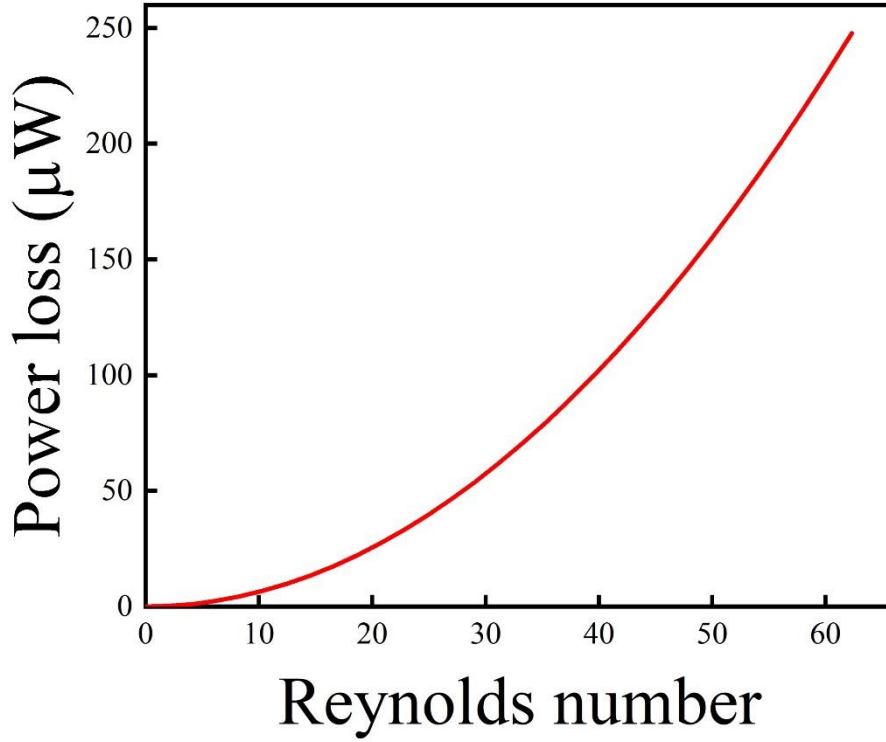


Figure 63. The power loss due to the fluidic resistance as a function of Reynolds number: The power loss increases non-linearly as the Re increases.

The electrodes of a microfluidic electrolyzer cover two parallel channel walls. The electrode area can be $12000 \times 100 \mu\text{m}^2$ if the channel geometry is the same as the device used in this study. The chemical energy stored in the form of hydrogen per unit time is

$$P_{\text{storage}} = jA_{\text{electrode}}E_0 \quad (16)$$

where j is the current density, $A_{\text{electrode}}$ is the electrode area, and $E_0 = 1.23 \text{ V}$ is the thermodynamic equilibrium potential of water electrolysis. $P_{\text{storage}} = 4428 \mu\text{W}$ if the current density is 300 mA/cm^2 . The energy used for the pumping at $\text{Re}=62$ is 5.6% of this stored energy. A higher percentage of this stored energy is required for the pumping if higher Re is required for effective product separation. The power loss due to the fluidic flow is dependent on the channel cross-section. This power loss can be reduced by increasing the cross-sectional area of the channel. However, the interelectrode distance is larger if the channel cross-section increases, and power loss due to the ohmic loss increases. Therefore, the channel dimensions should be optimized in order to minimize power losses due to the fluidic flow and ohmic resistance [39].

B.6 Hydrogen and oxygen bubbles radius at different Reynolds numbers

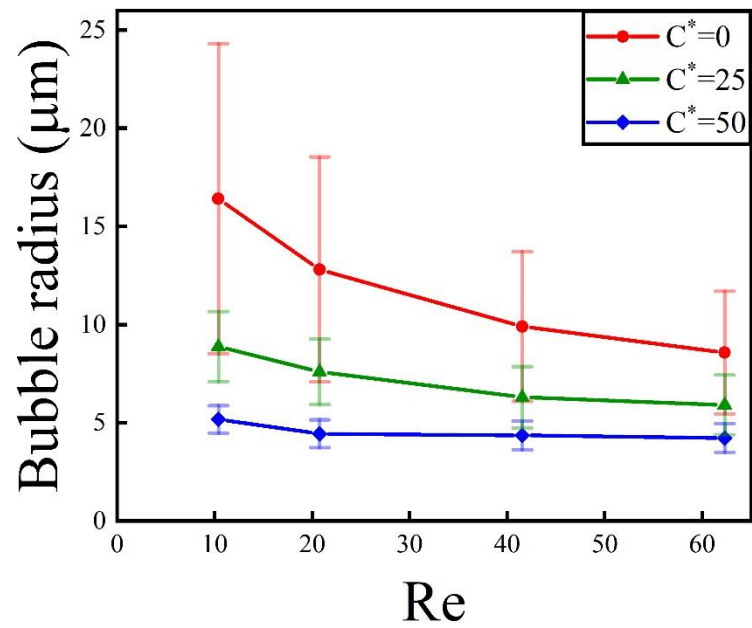


Figure 64. The average radius of the oxygen and hydrogen bubbles in the electrolyte with different concentration of surfactant at the applied current of $10\mu A$. The bubbles radii decrease as the surfactant concentration increases. Furthermore, the bubbles detach at smaller sizes by increasing the Re.

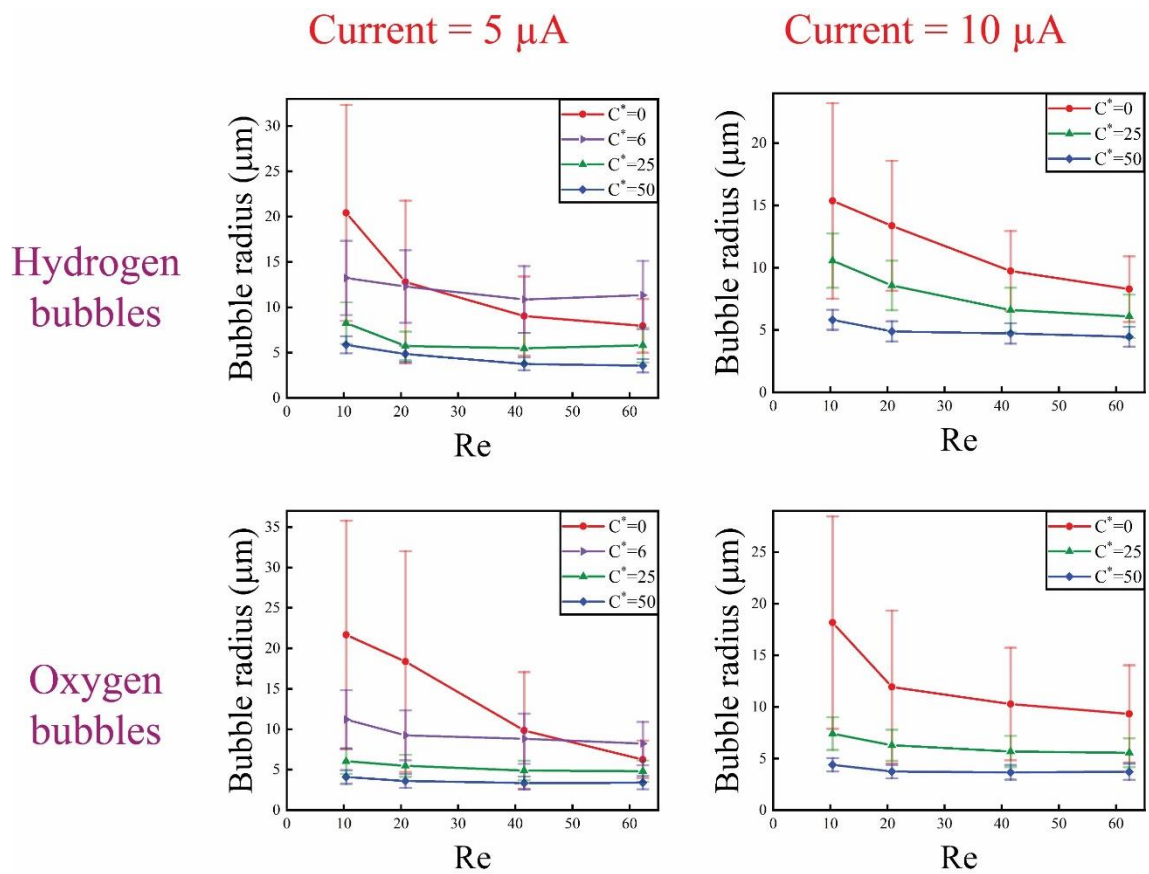


Figure 65. The radius of oxygen and hydrogen bubbles at different surfactant concentrations, currents, and Reynolds numbers. Only separated bubbles are considered in these diagrams and the bubbles that are in the channel centerline are not used in the measurements. The bubbles radii decrease as the concentration of the surfactant increases and/or the Re increases.

B.7 The origin of crossed bubbles

Figure 66 shows the hydrogen and oxygen bubbles cross over individually. The percentage of cross over is calculated by dividing the volume of crossed over gas by the total volume of generated bubbles. The mixture of bubbles or the bubbles moving at the centerline are presented with a separate cross over percentage. The hydrogen bubbles cross over is more than oxygen bubbles cross over since hydrogen is being generated twice the oxygen. The hydrogen cross over is smaller than oxygen cross over at some currents at $Re=10$ because many hydrogen bubbles coalesce and move to the centerline.

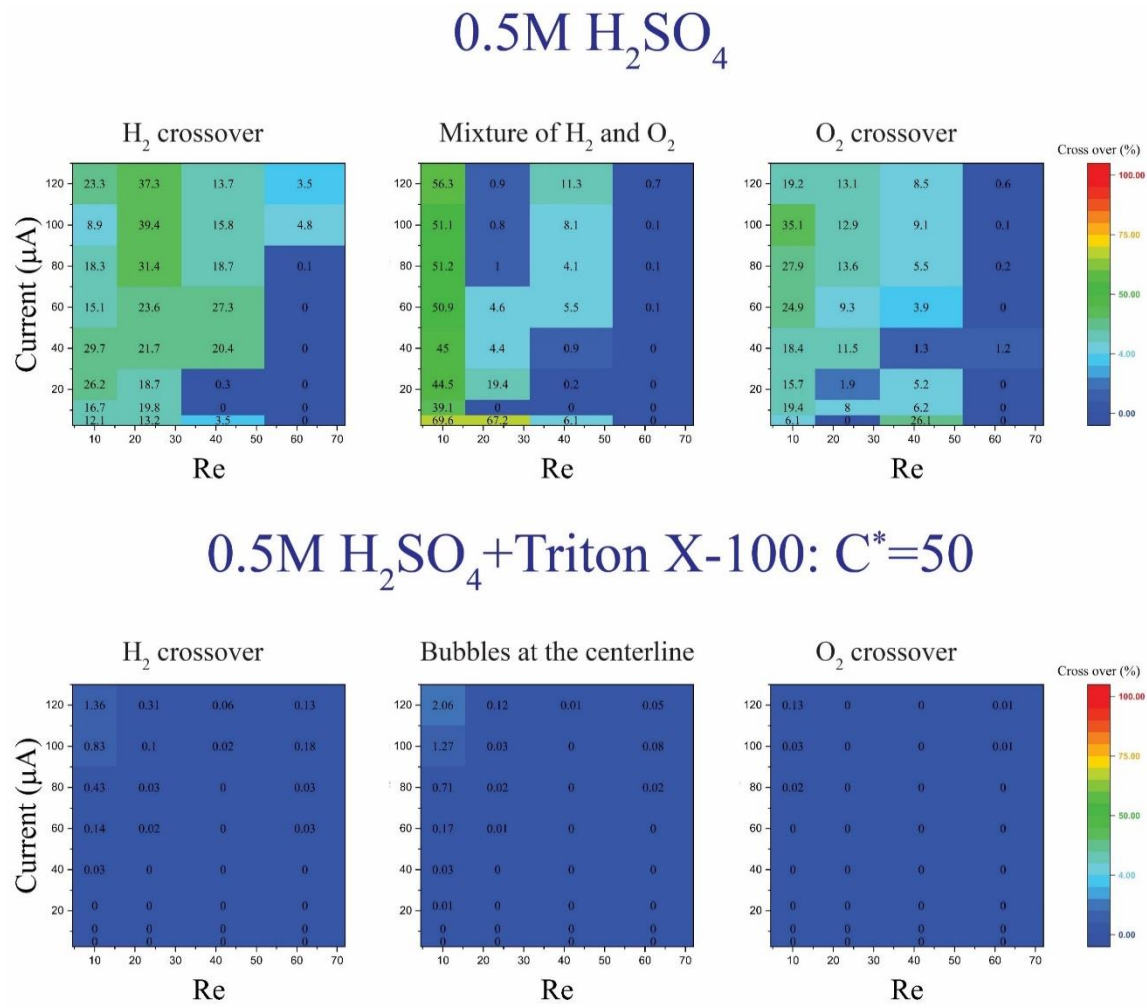


Figure 66. The origin of crossed bubbles at different Re and currents: the percentage is calculated by dividing the volume of bubbles based on their origin by the total volume of generated bubbles. The coalesced bubbles in the $0.5 M H_2SO_4$ are the mixture of hydrogen and oxygen bubbles. These bubbles are reported with a separate percentage since it is not possible to determine accurately the exact percentage of hydrogen and oxygen. Furthermore, the bubbles that are moving at the channel center in the $0.5 M H_2SO_4$ at $C^* = 50$ are reported separately as their origin cannot be determined. The summation of the three percentages at each Re and current is the value reported in Figure 29 in the main text.

Appendix C

Membrane-less electrolyzer with porous walls for high throughput and pure hydrogen production

C1. Effect of wall pores angle and size

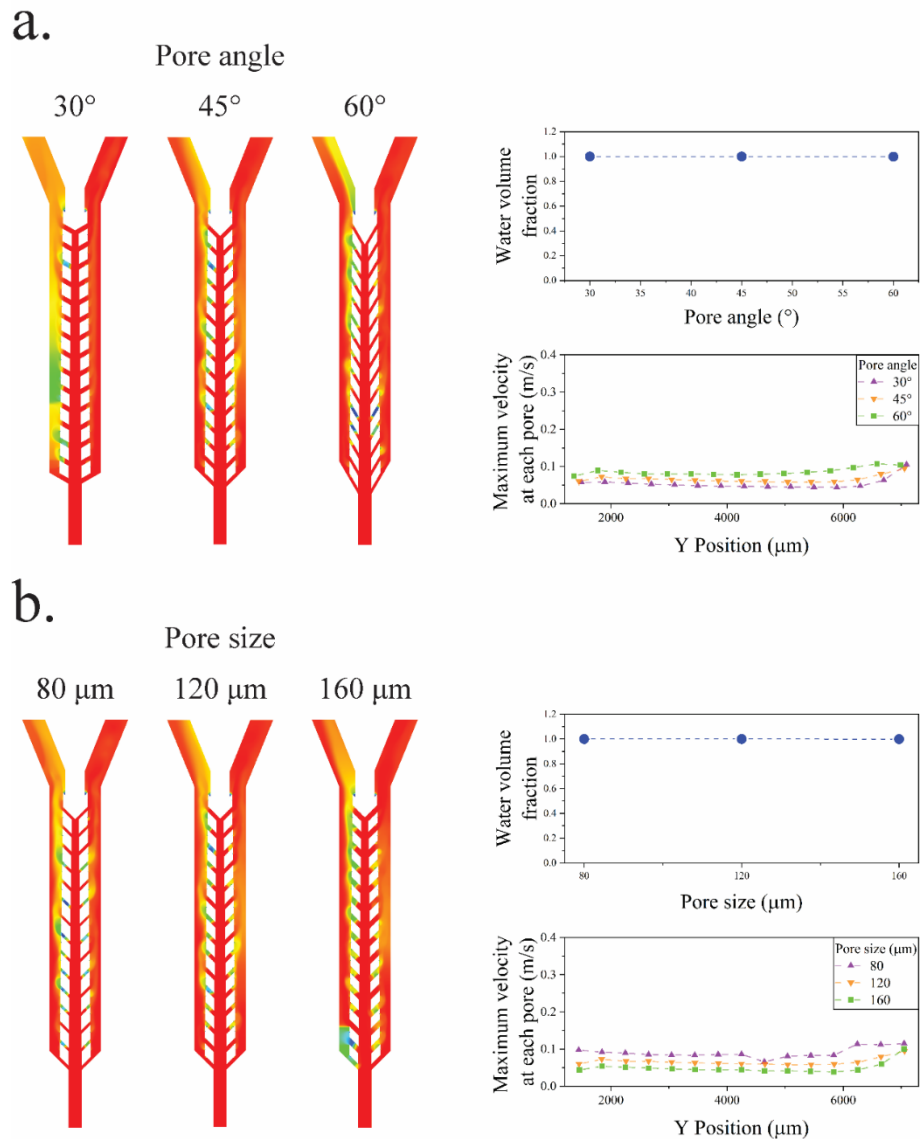


Figure 67. a. Changing the wall pores angle from 30° to 60° does not affect the velocity distribution in the pores or the water volume fraction in the middle channel. b. The velocity distribution in the pores remains uniform across the pores and the water volume fraction in the middle channel does not decrease when the pore size increases from 80 μm to 160 μm.

C2. Membrane-less electrolyzers

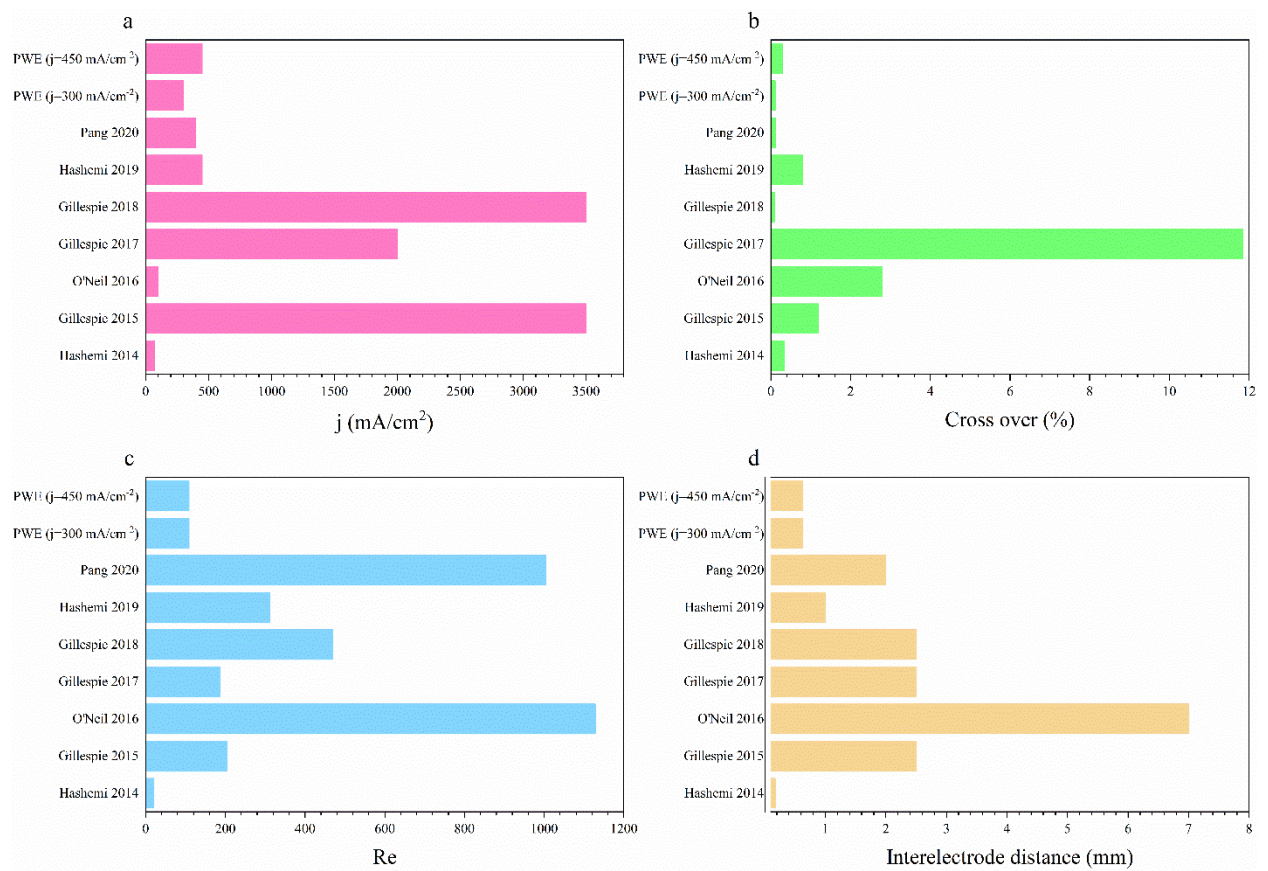


Figure 68. The current density (a), cross over (b), Re (c), and interelectrode distance (d) of membrane-less electrolyzers shown in Figure 41.

C3. Microfabrication

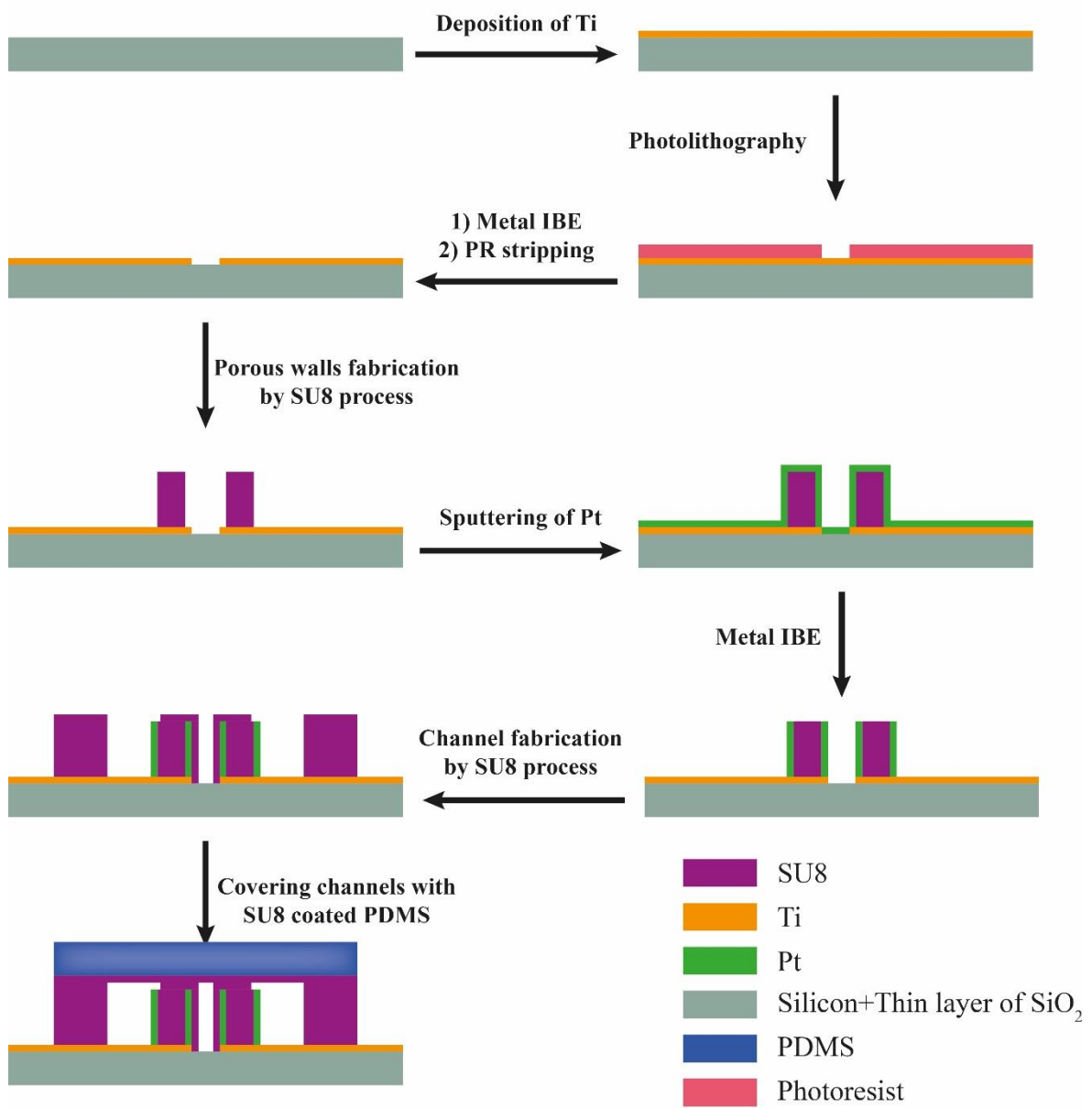


Figure 69. Fabrication process of the porous walls electrolyzer

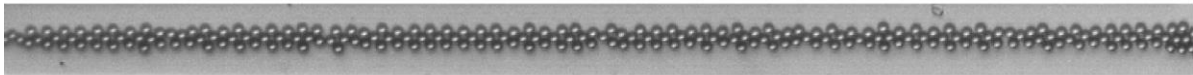
Appendix D

Learning from droplet flows in microfluidic channels using deep neural networks

D.1 Image preparation for the neural network

OpenCV and Python's scikit-image libraries are used in python to prepare the input images of the neural network. The image from the experiment is cropped to achieve an image without the channel walls (Figure 70.1). From OpenCV, fastNlMeansDenoising is applied to reduce noises in the image as shown in Figure 70.2. In this procedure, the template window size and search window size are set to 7 and 21, respectively. Finally, the Canny edge detector filter is used to detect droplets boundaries as shown in Figure 70.3. The standard deviation of the Gaussian filter used in the Canny edge detector is set to 1.2.

1. Image from experiment



2. Denoising



3. Edge detection

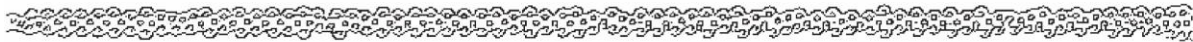


Figure 70. Image processing procedure: 1. cropped image from the experiment, 2. Applying denoising algorithm to remove the noise in the image, 3. Result of edge detection algorithm in detecting droplets boundaries.

D.2 Neural Network Structure

The Tensorflow library is used to implement the neural networks [205]. For the classification of the images based on the concentration, a convolutional neural network (CNN) with two convolutional layers followed by two fully connected layers is used [206]. The rectified linear activation function is applied to all layers. Each convolutional layer is accompanied by a max pooling layer that reduces the spatial size by half. The structure of this network is depicted in Figure 71a. A dropout layer (40% rate) is added after the fully connected layer to prevent the overfitting by setting the randomly chosen neurons to zero [207]. The learning rate and the batch size are set to 0.001 and 40. A gradient descent optimizer is applied to minimize the cross-entropy cost function. 90% of the images are used for the training and the validation of the network and 10% of them are used for the testing. The accuracy of this network is the proportion that classified correctly.

Another CNN, shown in Figure 71b, is used to predict the concentration of the solutions that the network has not seen. This CNN contains three convolutional and two fully connected layers, where the rectified linear activation function is applied to the output of each layer. There are three max-pooling layers for three convolutional layers and there is a dropout layer (50% rate) after the fully connected layer to reduce the overfitting. The output of this network has one neuron that gives the concentration value. An Adam optimizer is used to minimize the mean squared error cost function. Initially, the learning rate is 0.001 and decreased by half every 50 epochs.

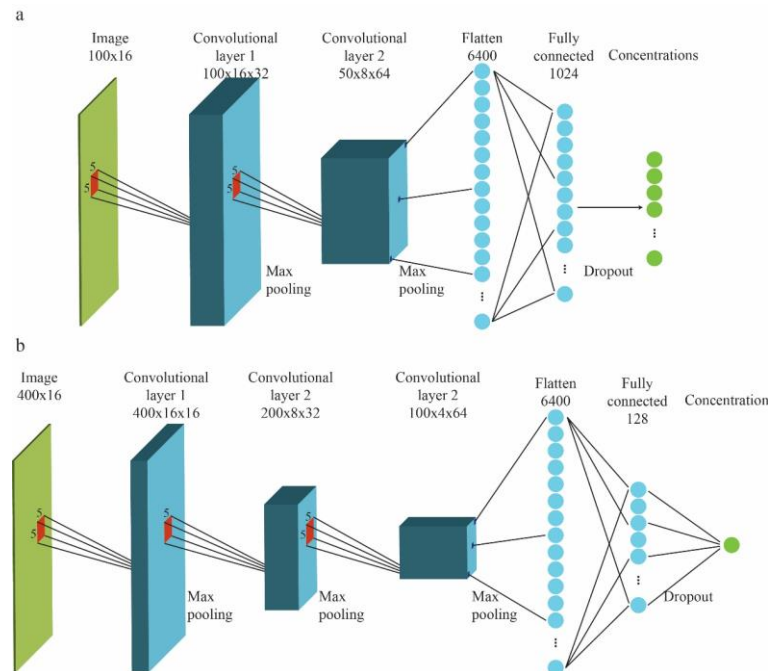


Figure 71. The structure of the convolutional neural networks: (a) A classifier network with two convolutional layers and two fully connected layers is used to classify the images based on their concentrations. The convolutional filters are 5×5 and there is a max pooling layer after each convolutional layer. A dropout layer is used before the last layer. (b) A regression neural network is implemented to predict the concentration of the inputs. This network consists of three convolutional layers followed by a fully connected layer. There is a max pooling layer after each convolutional layer and a dropout layer after the fully connected layer.

D.3 Flow pattern

Figure 72 shows the two-phase flow pattern at two different flow rates and for two different concentrations. As we can see in this figure, droplet generation patterns are changing by the flow rate or the concentration. The five symbols in Figure 72 correspond to droplet flow patterns that represent the five flow regimes that were observed in this case. The pictures in Figure 72c are examples for each of the phases.

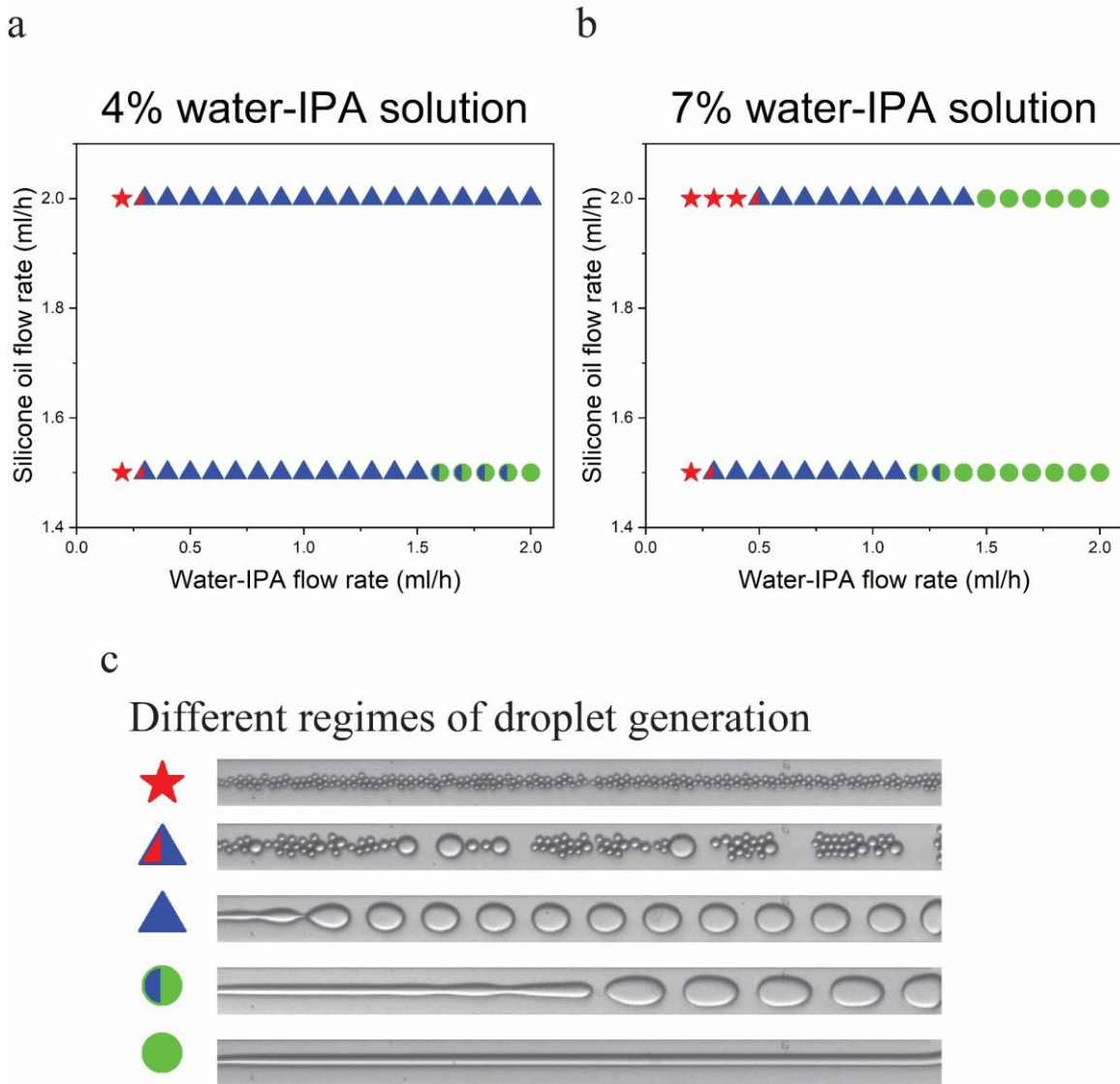


Figure 72. Flow pattern of droplet flows: (a) 4.0% water-IPA concentration. (b) 7.0% water-IPA concentration. (c) for two different concentrations: The phase transition happens by changing the flow rate or the concentration.

D.4 Concentration prediction using six networks and one image input

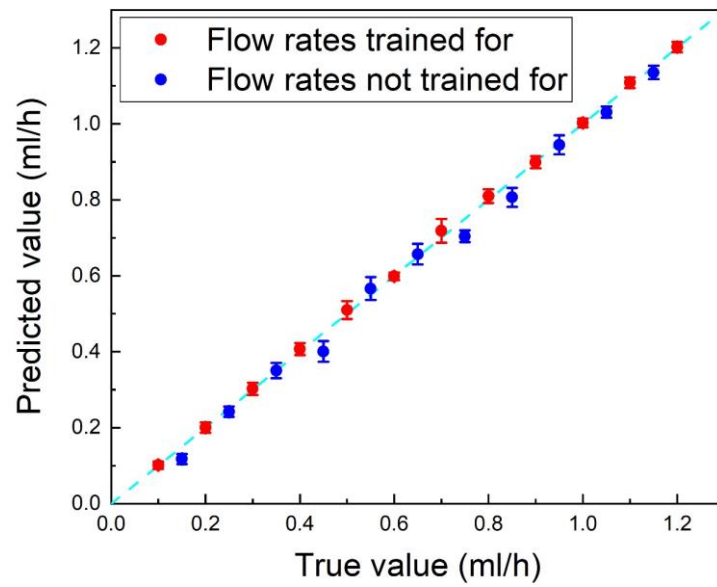


Figure 73. Water-IPA flow rate measurement at silicone oil flow rate of 1.5ml/h.

D.5 Concentration prediction using six networks and one image input

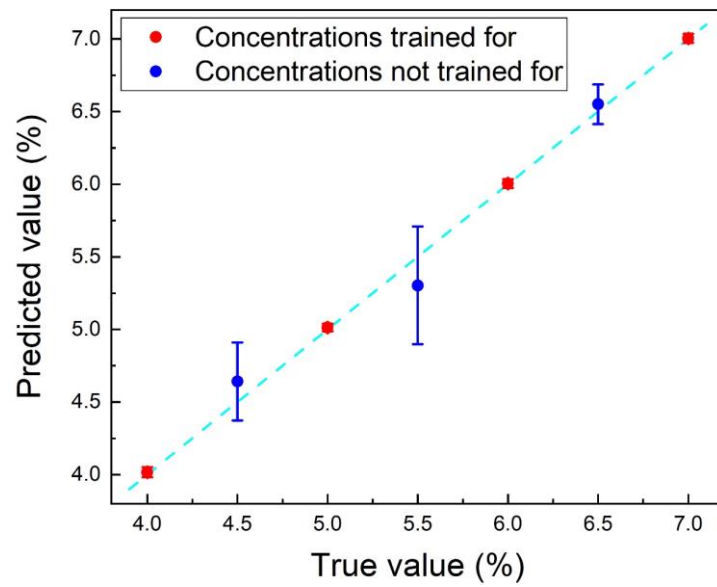


Figure 74. Concentration prediction results using six DNNs and one image input. The red points are the concentrations that the network is trained with and the blue points are the new concentrations. Bars show the standard deviation for each case.

D.6 Results of the repeated experiment for the concentration measurement

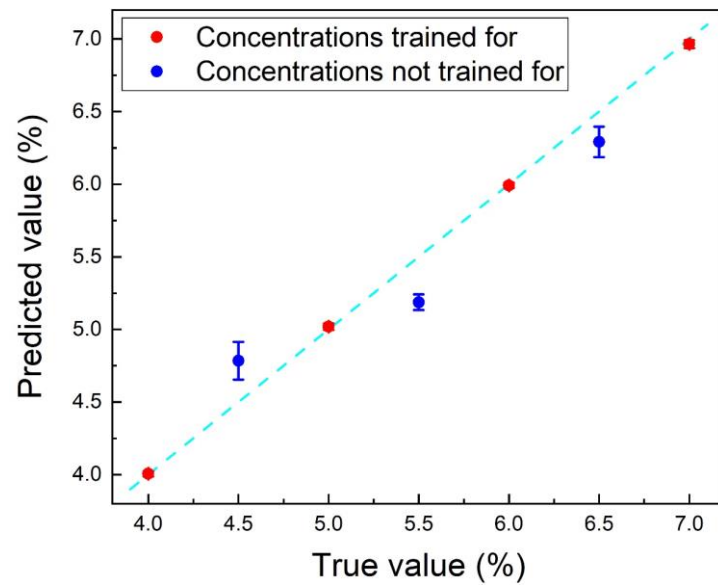


Figure 75. The diagram shows the results of applying the proposed method to the repeated experiment for the concentration measurement.

D.7 Comparison between a clustering algorithm (nearest neighbor) classification and neural network classification

In this section, we extract two features of the droplet generation regimes and use them for determining the water-IPA concentration ranging from 4.0% to 7.0%. The extracted features are the number of the generated droplets (area is $100\mu\text{m}$ by $1440\mu\text{m}$) in one snapshot and their radius. A simple clustering method is applied to these features to classify each image. The circle Hough Transform (CHT) is applied to each image to detect the circles. Based on the outcome, each image is labeled by the number of the droplets and the mean value of their radii.

A collection of points in radius-number space is presented in Figure 76 by extracting the data from 25200 images. The new image is classified in the class of the closest point clusters. 2800 new images are classified in this way and the obtained accuracy is 54%. The reason for such a low accuracy is the overlap between the data of the different classes. In addition, we remark that the classification is more challenging for droplet generation regimes where the droplets are not circular.

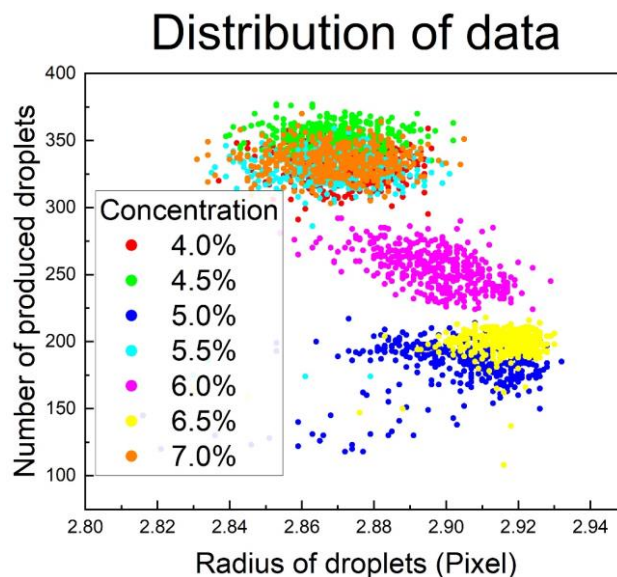


Figure 76. Distribution of the dataset where the number and the radii of the droplets are presented for different concentrations.

Classification based on only the radius and the number of droplets is unreliable. More features must be extracted from the images for a better accuracy. DNN is an alternative approach for feature-based classification. Figure 77 shows some of the features that are detected by the convolutional layers of a DNN. In the first part of this figure, images of two different concentrations are shown in the experiment row. The second part shows the images after applying the edge detection algorithm to these experimental images. In the third part, each image shows the difference between the convolutional layer outputs of the two different concentrations shown in the first part. Figure 77a shows that the DNN detects the width of the droplets cluster as one of the features for the small droplets. The local number density of droplets is another feature that the DNN discovers as shown in Figure 77b. In this image, the brighter spots show that the number density of droplets in one image is higher than the other image in those positions. For the big droplets, two features detected by DNN are the droplets (Figure 77c), and the liquid jet (Figure 77d). Figure 77c shows that the DNN removes the liquid

jet and only detects the boundaries of the droplets where features like periodicity, droplet size, and the droplet deformation can be extracted. On the other hand, in Figure 77d, the DNN highlights the liquid jet and extracts the length and the width of the jet as features.

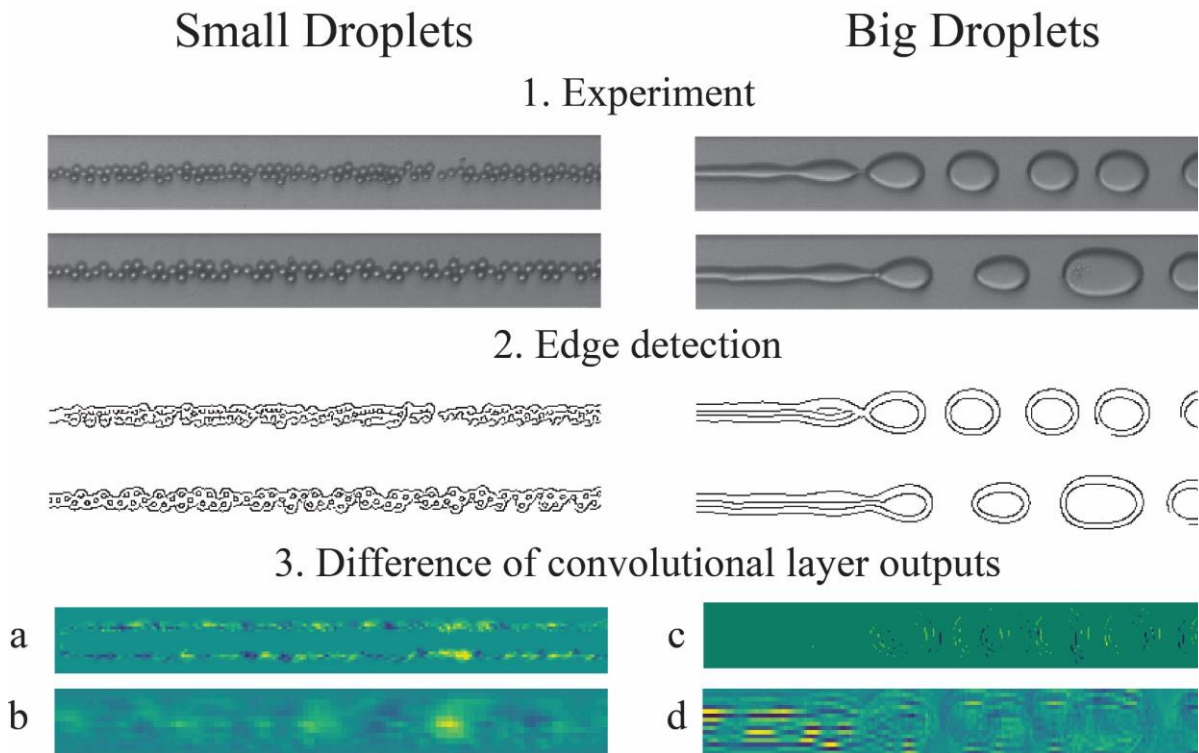


Figure 77. Droplet images and the features detected by the DNN: 1. The images of the droplet generation from the experiment for small and big droplets at two different concentrations. 2. The results of the edge detection algorithm applied to the images from the experiment. 3. Difference of convolutional layer outputs for two different concentrations: (a) the DNN detects the width of the droplet clusters, (b) the local number density of the droplets are identified as the brighter regions indicate higher number of droplets in one image than the other, (c) the DNN extracts the leading edges of the droplets that represent the number of droplets and their periodicity, (d) the enhanced edges of the boundaries with an emphasis on the liquid jet which is detected by brighter color.

The DNN classifier [207] (illustrated in Figure D1a) is employed to classify the images of droplet generation at concentrations ranging from 4.0% to 7.0%. The DNN accuracies is 97.4%. The convergence and the loss diagrams of both cases are drawn in Figure 78. The DNN achieves a higher accuracy compared to the classification based on two features.

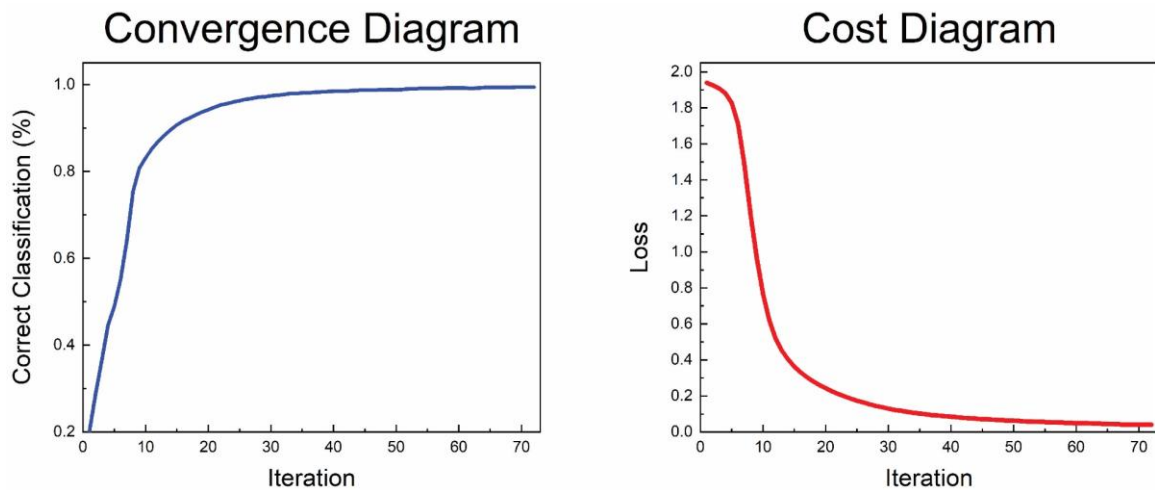


Figure 78. The convergence plot and the cost diagram. The cost function is calculated using cross entropy loss.

References

1. Nazir, Muhammad Shahzad, Ali Jafer Mahdi, Muhammad Bilal, Hafiz M Sohail, Nisar Ali, and Hafiz MN Iqbal, *Environmental impact and pollution-related challenges of renewable wind energy paradigm—A review*. *Science of the Total Environment*, 2019. **683**: p. 436-444.
2. Zoundi, Zakaria, *CO2 emissions, renewable energy and the Environmental Kuznets Curve, a panel cointegration approach*. *Renewable and Sustainable Energy Reviews*, 2017. **72**: p. 1067-1075.
3. Comello, Stephen, Stefan Reichelstein, and Anshuman Sahoo, *The road ahead for solar PV power*. *Renewable and Sustainable Energy Reviews*, 2018. **92**: p. 744-756.
4. Wiser, Ryan, Karen Jenni, Joachim Seel, Erin Baker, Maureen Hand, Eric Lantz, and Aaron Smith, *Expert elicitation survey on future wind energy costs*. *Nature Energy*, 2016. **1**(10): p. 1-8.
5. Dudley, Dominic. *Renewable Energy Costs Take Another Tumble, Making Fossil Fuels Look More Expensive Than Ever*. 2019 2019/05/29 [cited 2020 07/28]; Available from: <https://www.forbes.com/sites/dominicdudley/2019/05/29/renewable-energy-costs-tumble/#27aa749de8ce>.
6. Glenk, Gunther and Stefan Reichelstein, *Economics of converting renewable power to hydrogen*. *Nature Energy*, 2019. **4**(3): p. 216-222.
7. Pan, Yong, *Theoretical discovery of high capacity hydrogen storage metal tetrahydrides*. *International Journal of Hydrogen Energy*, 2019. **44**(33): p. 18153-18158.
8. Edwards, Peter P, Vladimir L Kuznetsov, William IF David, and Nigel P Brandon, *Hydrogen and fuel cells: towards a sustainable energy future*. *Energy policy*, 2008. **36**(12): p. 4356-4362.
9. Balat, Mustafa, *Potential importance of hydrogen as a future solution to environmental and transportation problems*. *International journal of hydrogen energy*, 2008. **33**(15): p. 4013-4029.
10. Cano, Zachary P, Dustin Banham, Siyu Ye, Andreas Hintennach, Jun Lu, Michael Fowler, and Zhongwei Chen, *Batteries and fuel cells for emerging electric vehicle markets*. *Nature Energy*, 2018. **3**(4): p. 279-289.
11. Goswami, D Yogi, Samantha T Mirabal, Nitin Goel, and HA Ingley. *A review of hydrogen production technologies*. in *International Conference on Fuel Cell Science, Engineering and Technology*. 2003.
12. Chi, Jun and Hongmei Yu, *Water electrolysis based on renewable energy for hydrogen production*. *Chinese Journal of Catalysis*, 2018. **39**(3): p. 390-394.
13. Schmidt, Oliver, Ajay Gambhir, Iain Staffell, Adam Hawkes, Jenny Nelson, and Shreiban Few, *Future cost and performance of water electrolysis: An expert elicitation study*. *International Journal of Hydrogen Energy*, 2017. **42**(52): p. 30470-30492.
14. Carmo, Marcelo, David L Fritz, Jürgen Mergel, and Detlef Stolten, *A comprehensive review on PEM water electrolysis*. *International journal of hydrogen energy*, 2013. **38**(12): p. 4901-4934.
15. Zeng, Kai and Dongke Zhang, *Recent progress in alkaline water electrolysis for hydrogen production and applications*. *Progress in energy and combustion science*, 2010. **36**(3): p. 307-326.

16. Ursua, Alfredo, Luis M Gandia, and Pablo Sanchis, *Hydrogen production from water electrolysis: current status and future trends*. Proceedings of the IEEE, 2011. **100**(2): p. 410-426.
17. Ni, Meng, Michael KH Leung, and Dennis YC Leung, *Technological development of hydrogen production by solid oxide electrolyzer cell (SOEC)*. International Journal of Hydrogen Energy, 2008. **33**(9): p. 2337-2354.
18. Vincent, Immanuel and Dmitri Bessarabov, *Low cost hydrogen production by anion exchange membrane electrolysis: A review*. Renewable and Sustainable Energy Reviews, 2018. **81**: p. 1690-1704.
19. David, Martín, Carlos Ocampo-Martínez, and Ricardo Sánchez-Peña, *Advances in alkaline water electrolyzers: A review*. Journal of Energy Storage, 2019. **23**: p. 392-403.
20. Hashemi, S Mohammad H, Miguel A Modestino, and Demetri Psaltis, *A membrane-less electrolyzer for hydrogen production across the pH scale*. Energy & Environmental Science, 2015. **8**(7): p. 2003-2009.
21. Hashemi, S Mohammad H, Petr Karnakov, Pooria Hadikhani, Enrico Chinello, Sergey Litvinov, Christophe Moser, Petros Koumoutsakos, and Demetri Psaltis, *A versatile and membrane-less electrochemical reactor for the electrolysis of water and brine*. Energy & Environmental Science, 2019. **12**(5): p. 1592-1604.
22. Esposito, Daniel V, *Membraneless electrolyzers for low-cost hydrogen production in a renewable energy future*. Joule, 2017. **1**(4): p. 651-658.
23. Hadikhani, Pooria, S Mohammad H Hashemi, Gioele Balestra, Lailai Zhu, Miguel A Modestino, François Gallaire, and Demetri Psaltis, *Inertial manipulation of bubbles in rectangular microfluidic channels*. Lab on a Chip, 2018. **18**(7): p. 1035-1046.
24. Li, Yifan, Gaoqiang Yang, Shule Yu, Zhenye Kang, Jingke Mo, Bo Han, Derrick A Talley, and Feng-Yuan Zhang, *In-situ investigation and modeling of electrochemical reactions with simultaneous oxygen and hydrogen microbubble evolutions in water electrolysis*. International Journal of Hydrogen Energy, 2019. **44**(52): p. 28283-28293.
25. Angulo, Andrea, Peter van der Linde, Han Gardeniers, Miguel Modestino, and David Fernández Rivas, *Influence of bubbles on the energy conversion efficiency of electrochemical reactors*. Joule, 2020. **4**(3): p. 555-579.
26. Lee, Jaeseon and Issam Mudawar, *Two-phase flow in high-heat-flux micro-channel heat sink for refrigeration cooling applications: Part II—heat transfer characteristics*. International Journal of Heat and Mass Transfer, 2005. **48**(5): p. 941-955.
27. Green, Craig, Peter Kottke, Xuefei Han, Casey Woodrum, Thomas Sarvey, Pouya Asrar, Xuchen Zhang, Yogendra Joshi, Andrei Fedorov, and Suresh Sitaraman, *A Review of Two-Phase Forced Cooling in Three-Dimensional Stacked Electronics: Technology Integration*. Journal of Electronic Packaging, 2015. **137**(4): p. 040802.
28. Kandlikar, Satish G, *History, advances, and challenges in liquid flow and flow boiling heat transfer in microchannels: a critical review*. Journal of heat transfer, 2012. **134**(3): p. 034001.
29. Pijnenburg, RHW, R Dekker, CCS Nicole, A Aubry, and EHEC Eummelen. *Integrated micro-channel cooling in silicon*. in *Solid-State Device Research conference, 2004. ESSDERC 2004. Proceeding of the 34th European*. 2004. IEEE.
30. Wang, Evelyn N, Lian Zhang, Linan Jiang, Jae-Mo Koo, James G Maveety, Eduardo A Sanchez, Kenneth E Goodson, and Thomas W Kenny, *Micromachined jets for liquid impingement cooling of VLSI chips*. Journal of Microelectromechanical systems, 2004. **13**(5): p. 833-842.
31. Ranade, Vivek V, Raghunath Chaudhari, and Prashant R Gunjal, *Trickle bed reactors: reactor engineering & applications*. 2011: Elsevier.

32. Werther, Joachim, *Fluidized-Bed Reactors*. 1992: Wiley Online Library.
33. Leonard, C, J-H Ferrasse, O Boutin, S Lefevre, and A Viand, *Bubble column reactors for high pressures and high temperatures operation*. Chemical Engineering Research and Design, 2015. **100**: p. 391-421.
34. Crook, Jedidiah and Aliyar Mousavi, *The chlor-alkali process: A review of history and pollution*. Environmental Forensics, 2016. **17**(3): p. 211-217.
35. Severo, Dagoberto S, André F Schneider, Elton CV Pinto, Vanderlei Gusberti, and Vinko Potocnik, *Modeling magnetohydrodynamics of aluminum electrolysis cells with ANSYS and CFX*. Light Metals, 2005. **2005**: p. 475-480.
36. Modestino, Miguel A, S Mohammad H Hashemi, and Sophia Haussener, *Mass transport aspects of electrochemical solar-hydrogen generation*. Energy & Environmental Science, 2016. **9**(5): p. 1533-1551.
37. Esposito, Daniel V, *Membraneless Electrolyzers for Low-Cost Hydrogen Production in a Renewable Energy Future*. Joule, 2017.
38. O'Neil, Glen D, Corey D Christian, David E Brown, and Daniel V Esposito, *Hydrogen production with a simple and scalable membraneless electrolyzer*. Journal of The Electrochemical Society, 2016. **163**(11): p. F3012-F3019.
39. Modestino, Miquel A, D Fernandez Rivas, Seyyed Mohammad Hosseini Hashemi, Johannes GE Gardeniers, and Demetri Psaltis, *The potential for microfluidics in electrochemical energy systems*. Energy & environmental science, 2016. **9**(11): p. 3381-3391.
40. Hashemi, SMH, M Neuenschwander, P Hadikhani, MA Modestino, and Demetri Psaltis, *Membrane-less micro fuel cell based on two-phase flow*. Journal of Power Sources, 2017. **348**: p. 212-218.
41. Segre, G, *Radial particle displacements in Poiseuille flow of suspensions*. Nature, 1961. **189**: p. 209-210.
42. Segre, G and A Silberberg, *Behaviour of macroscopic rigid spheres in Poiseuille flow Part 2. Experimental results and interpretation*. Journal of Fluid Mechanics, 1962. **14**(01): p. 136-157.
43. Di Carlo, Dino, Daniel Irimia, Ronald G Tompkins, and Mehmet Toner, *Continuous inertial focusing, ordering, and separation of particles in microchannels*. Proceedings of the National Academy of Sciences, 2007. **104**(48): p. 18892-18897.
44. Bhagat, Ali Asgar S, Sathyakumar S Kuntaegowdanahalli, and Ian Papautsky, *Enhanced particle filtration in straight microchannels using shear-modulated inertial migration*. Physics of Fluids (1994-present), 2008. **20**(10): p. 101702.
45. Xuan, Xiangchun, Junjie Zhu, and Christopher Church, *Particle focusing in microfluidic devices*. Microfluidics and nanofluidics, 2010. **9**(1): p. 1-16.
46. Lu, Xinyu and Xiangchun Xuan, *Continuous microfluidic particle separation via elasto-inertial pinched flow fractionation*. Analytical chemistry, 2015. **87**(12): p. 6389-6396.
47. Jimenez, M and H Bridle, *Microfluidics for effective concentration and sorting of waterborne protozoan pathogens*. Journal of microbiological methods, 2016. **126**: p. 8-11.
48. Xue, ChunDong, XiaoDong Chen, Chao Liu, and GuoQing Hu, *Lateral migration of dual droplet trains in a double spiral microchannel*. Science China Physics, Mechanics & Astronomy, 2016. **59**(7): p. 1-10.
49. Choi, Yong-Seok and Sang-Joon Lee, *Holographic analysis of three-dimensional inertial migration of spherical particles in micro-scale pipe flow*. Microfluidics and nanofluidics, 2010. **9**(4-5): p. 819-829.

50. Bhagat, Ali Asgar S, Sathyakumar S Kuntaegowdanahalli, Necati Kaval, Carl J Seliskar, and Ian Papautsky, *Inertial microfluidics for sheath-less high-throughput flow cytometry*. Biomedical microdevices, 2010. **12**(2): p. 187-195.
51. Karimi, A, S Yazdi, and AM Ardekani, *Hydrodynamic mechanisms of cell and particle trapping in microfluidics*. Biomicrofluidics, 2013. **7**(2): p. 021501.
52. Chung, Aram J, Daniel R Gossett, and Dino Di Carlo, *Three dimensional, sheathless, and high-throughput microparticle inertial focusing through geometry-induced secondary flows*. Small, 2013. **9**(5): p. 685-690.
53. Kayani, Aminuddin A, Khashayar Khoshmanesh, Stephanie A Ward, Arnan Mitchell, and Kourosh Kalantar-Zadeh, *Optofluidics incorporating actively controlled micro-and nano-particles*. Biomicrofluidics, 2012. **6**(3): p. 031501.
54. Mortazavi, SAEED and Grétar Tryggvason, *A numerical study of the motion of drops in Poiseuille flow. Part I. Lateral migration of one drop*. Journal of Fluid Mechanics, 2000. **411**: p. 325-350.
55. Stan, Claudiu A, Laura Guglielmini, Audrey K Ellerbee, Daniel Caviezel, Howard A Stone, and George M Whitesides, *Sheathless hydrodynamic positioning of buoyant drops and bubbles inside microchannels*. Physical Review E, 2011. **84**(3): p. 036302.
56. Chen, Xiaodong, Chundong Xue, Li Zhang, Guoqing Hu, Xingyu Jiang, and Jiashu Sun, *Inertial migration of deformable droplets in a microchannel*. Physics of Fluids (1994-present), 2014. **26**(11): p. 112003.
57. Hur, Soojung Claire, Nicole K Henderson-MacLennan, Edward RB McCabe, and Dino Di Carlo, *Deformability-based cell classification and enrichment using inertial microfluidics*. Lab on a Chip, 2011. **11**(5): p. 912-920.
58. Zhang, Jun, Sheng Yan, Dan Yuan, Gursel Alici, Nam-Trung Nguyen, Majid Ebrahimi Warkiani, and Weihua Li, *Fundamentals and applications of inertial microfluidics: a review*. Lab on a Chip, 2016. **16**(1): p. 10-34.
59. Ho, BP and LG Leal, *Inertial migration of rigid spheres in two-dimensional unidirectional flows*. Journal of Fluid Mechanics, 1974. **65**(02): p. 365-400.
60. Martel, Joseph M and Mehmet Toner, *Inertial focusing in microfluidics*. Annual review of biomedical engineering, 2014. **16**: p. 371.
61. Goldsmith, HL and SG Mason, *The flow of suspensions through tubes. I. Single spheres, rods, and discs*. Journal of Colloid Science, 1962. **17**(5): p. 448-476.
62. Schaaf, Christian and Holger Stark, *Inertial migration and axial control of deformable capsules*. Soft Matter, 2017.
63. Rivero-Rodriguez, Javier and Benoit Scheid, *Bubbles dynamics in microchannels: inertial and capillary migration forces*. arXiv preprint arXiv:1708.01114, 2017.
64. Daerr, Adrian and Adrien Mogné, *Pendent_drop: an imagej plugin to measure the surface tension from an image of a pendent drop*. Journal of Open Research Software, 2016. **4**(1).
65. Balestra, G., L. Zhu, and F. Gallaire, *A viscous droplet in a capillary tube: from Bretherton's theory to empirical models*. arXiv preprint arXiv:1711.10447, 2017.
66. Wang, Yechun and Panagiotis Dimitrakopoulos, *Low-Reynolds-number droplet motion in a square microfluidic channel*. Theoretical and Computational Fluid Dynamics, 2012. **26**(1): p. 361-379.
67. Bhagat, Ali Asgar S, Sathyakumar S Kuntaegowdanahalli, and Ian Papautsky, *Enhanced particle filtration in straight microchannels using shear-modulated inertial migration*. Physics of Fluids, 2008. **20**(10): p. 101702.
68. Prohm, Christopher and Holger Stark, *Feedback control of inertial microfluidics using axial control forces*. Lab on a Chip, 2014. **14**(12): p. 2115-2123.

69. Amini, Hamed, Wonhee Lee, and Dino Di Carlo, *Inertial microfluidic physics*. Lab on a Chip, 2014. **14**(15): p. 2739-2761.
70. Paiè, Petra, Francesca Bragheri, Dino Di Carlo, and Roberto Osellame, *Particle focusing by 3D inertial microfluidics*. Microsystems & Nanoengineering, 2017. **3**: p. 17027.
71. Takagi, Shu and Yoichiro Matsumoto, *Surfactant effects on bubble motion and bubbly flows*. Annual Review of Fluid Mechanics, 2011. **43**: p. 615-636.
72. Clift, R, JR Grace, and ME Webber, *Bubbles, drop, and particles*. 1978, New York: Academic Press.
73. Acar, Canan and Ibrahim Dincer, *Review and evaluation of hydrogen production options for better environment*. Journal of cleaner production, 2019.
74. Kumar, S Shiva and V Himabindu, *Hydrogen production by PEM water electrolysis—A review*. Materials Science for Energy Technologies, 2019.
75. Ardo, Shane, David Fernandez Rivas, Miguel A Modestino, Verena Schulze Greiving, Fatwa F Abdi, Esther Alarcon Llado, Vincent Artero, Katherine Ayers, Corsin Battaglia, and Jan-Philipp Becker, *Pathways to electrochemical solar-hydrogen technologies*. Energy & environmental science, 2018. **11**(10): p. 2768-2783.
76. Kothari, Richa, D Buddhi, and RL Sawhney, *Comparison of environmental and economic aspects of various hydrogen production methods*. Renewable and Sustainable Energy Reviews, 2008. **12**(2): p. 553-563.
77. Gillespie, MI, F Van Der Merwe, and RJ Kriek, *Performance evaluation of a membraneless divergent electrode-flow-through (DEFT) alkaline electrolyser based on optimisation of electrolytic flow and electrode gap*. Journal of Power Sources, 2015. **293**: p. 228-235.
78. Ferrigno, Rosaria, Abraham D Stroock, Thomas D Clark, Michael Mayer, and George M Whitesides, *Membraneless vanadium redox fuel cell using laminar flow*. Journal of the American Chemical Society, 2002. **124**(44): p. 12930-12931.
79. Choban, Eric R, Larry J Markoski, Andrzej Wieckowski, and Paul JA Kenis, *Microfluidic fuel cell based on laminar flow*. Journal of Power Sources, 2004. **128**(1): p. 54-60.
80. Jayashree, Ranga S, Lajos Gancs, Eric R Choban, Alex Primak, Dilip Natarajan, Larry J Markoski, and Paul JA Kenis, *Air-breathing laminar flow-based microfluidic fuel cell*. Journal of the American Chemical Society, 2005. **127**(48): p. 16758-16759.
81. Mota, Nicolas Da, David A Finkelstein, Joseph D Kirtland, Claudia A Rodriguez, Abraham D Stroock, and Héctor D Abruña, *Membraneless, room-temperature, direct borohydride/cerium fuel cell with power density of over 0.25 W/cm²*. Journal of the American Chemical Society, 2012. **134**(14): p. 6076-6079.
82. Kjeang, Erik, Raphaëlle Michel, David A Harrington, Ned Djilali, and David Sinton, *A microfluidic fuel cell with flow-through porous electrodes*. Journal of the American Chemical Society, 2008. **130**(12): p. 4000-4006.
83. Jayashree, Ranga S, Michael Mitchell, Dilip Natarajan, Larry J Markoski, and Paul JA Kenis, *Microfluidic hydrogen fuel cell with a liquid electrolyte*. Langmuir, 2007. **23**(13): p. 6871-6874.
84. Braff, William A, Martin Z Bazant, and Cullen R Buie, *Membrane-less hydrogen bromine flow battery*. Nature communications, 2013. **4**: p. 2346.
85. Yang, Yuan, James Loomis, Hadi Ghasemi, Seok Woo Lee, Yi Jenny Wang, Yi Cui, and Gang Chen, *Membrane-free battery for harvesting low-grade thermal energy*. Nano letters, 2014. **14**(11): p. 6578-6583.

86. Leung, PK, T Martin, AA Shah, MR Mohamed, MA Anderson, and J Palma, *Membrane-less hybrid flow battery based on low-cost elements*. Journal of Power Sources, 2017. **341**: p. 36-45.
87. Leung, PK, T Martin, AA Shah, MA Anderson, and J Palma, *Membrane-less organic–inorganic aqueous flow batteries with improved cell potential*. Chemical Communications, 2016. **52**(99): p. 14270-14273.
88. Gillespie, MI and RJ Kriek, *Scalable hydrogen production from a mono-circular filter press Divergent Electrode-Flow-Through alkaline electrolysis stack*. Journal of Power Sources, 2018. **397**: p. 204-213.
89. Gillespie, MI and RJ Kriek, *Hydrogen production from a rectangular horizontal filter press Divergent Electrode-Flow-Through (DEFT™) alkaline electrolysis stack*. Journal of Power Sources, 2017. **372**: p. 252-259.
90. Davis, JT, DE Brown, X Pang, and DV Esposito, *High Speed Video Investigation of Bubble Dynamics and Current Density Distributions in Membraneless Electrolyzers*. Journal of The Electrochemical Society, 2019. **166**(4): p. F312-F321.
91. Eigeldinger, J and H Vogt, *The bubble coverage of gas-evolving electrodes in a flowing electrolyte*. Electrochimica Acta, 2000. **45**(27): p. 4449-4456.
92. Li, Yifan, Gaoqiang Yang, Shule Yu, Zhenye Kang, Jingke Mo, Bo Han, Derrick A Talley, and Feng-Yuan Zhang, *In-situ investigation and modeling of electrochemical reactions with simultaneous oxygen and hydrogen microbubble evolutions in water electrolysis*. International Journal of Hydrogen Energy, 2019.
93. Fernandez, Damaris, Paco Maurer, Milena Martine, JMD Coey, and Matthias E Möbius, *Bubble formation at a gas-evolving microelectrode*. Langmuir, 2014. **30**(43): p. 13065-13074.
94. Folgueiras-Amador, Ana A, Katie E Jolley, Peter R Birkin, Richard CD Brown, Derek Pletcher, Stephen Pickering, Medhat Sharabi, Oscar De Frutos, Carlos Mateos, and Juan A Rincón, *The influence of non-ionic surfactants on electrosynthesis in extended channel, narrow gap electrolysis cells*. Electrochemistry Communications, 2019. **100**: p. 6-10.
95. Craig, VSJ, BW Ninham, and RM Pashley, *Effect of electrolytes on bubble coalescence*. Nature, 1993. **364**(6435): p. 317.
96. Henry, Christine L, Casuarina N Dalton, Lehoa Scruton, and Vincent SJ Craig, *Ion-specific coalescence of bubbles in mixed electrolyte solutions*. The Journal of Physical Chemistry C, 2007. **111**(2): p. 1015-1023.
97. Jungwirth, Pavel and Douglas J Tobias, *Specific ion effects at the air/water interface*. Chemical reviews, 2006. **106**(4): p. 1259-1281.
98. Wang, Lisen, Lisa Flanagan, and Abraham P Lee, *Side-wall vertical electrodes for lateral field microfluidic applications*. Journal of microelectromechanical systems, 2007. **16**(2): p. 454-461.
99. Allen, Robert A and Todd G Deutsch, *Photoelectrochemical Water-splitting Ancillary Components*. 2014.
100. Lee, Hwi Yong, Cedrick Barber, and Adrienne R Minerick, *Improving electrokinetic microdevice stability by controlling electrolysis bubbles*. Electrophoresis, 2014. **35**(12-13): p. 1782-1789.
101. Dow, Chemical Company. *What is the viscosity for TRITON™ X-100 surfactant?* 2018 11/13/2018 [cited 2020 18/02].
102. Dow, Chemical Company. *TRITON™ X-Series Surfactants - Viscosity of Aqueous Solutions*. 2018 11/13/2018 [cited 2020 18/02].
103. Hussain, Ejaz, Niu Niu, Huipeng Zhou, Sohail Anjum Shahzad, and Cong Yu, *Aggregation enhanced excimer emission (AEEE) of benzo [ghi] perylene and*

- coronene: multimode probes for facile monitoring and direct visualization of micelle transition*. Analyst, 2018. **143**(18): p. 4283-4289.
104. Bradski, Gary, *The opencv library*. Dr Dobb's J. Software Tools, 2000. **25**: p. 120-125.
 105. Taqieddin, Amir, Roya Nazari, Ljiljana Rajic, and Akram Alshawabkeh, *Physicochemical hydrodynamics of gas bubbles in two phase electrochemical systems*. Journal of The Electrochemical Society, 2017. **164**(13): p. E448-E459.
 106. Chen, Deqi, Liang-ming Pan, and Song Ren, *Prediction of bubble detachment diameter in flow boiling based on force analysis*. Nuclear Engineering and Design, 2012. **243**: p. 263-271.
 107. Duhar, Géraldine and Catherine Colin, *Dynamics of bubble growth and detachment in a viscous shear flow*. Physics of fluids, 2006. **18**(7): p. 077101.
 108. Klausner, JF, R Mei, DM Bernhard, and LZ Zeng, *Vapor bubble departure in forced convection boiling*. International journal of heat and mass transfer, 1993. **36**(3): p. 651-662.
 109. Thorncroft, GE and James F Klausner, *Bubble forces and detachment models*. Multiphase Science and Technology, 2001. **13**(3&4).
 110. Bazaz, Sajad Razavi, Ali Mashhadian, Abbas Ehsani, Suvash Saha, Timm Krueger, and Majid Ebrahimi Warkiani, *Computational Inertial Microfluidics: A Review*. Lab on a Chip, 2020.
 111. Ho, BP and LG Leal, *Inertial migration of rigid spheres in two-dimensional unidirectional flows*. Journal of fluid mechanics, 1974. **65**(2): p. 365-400.
 112. Rivero-Rodriguez, Javier and Benoit Scheid, *Bubble dynamics in microchannels: inertial and capillary migration forces*. Journal of fluid mechanics, 2018. **842**: p. 215-247.
 113. Rastello, Marie, Jean-Louis Marié, and Michel Lance, *Clean versus contaminated bubbles in a solid-body rotating flow*. Journal of Fluid Mechanics, 2017. **831**: p. 592-617.
 114. Rastello, Marie, Jean-Louis Marié, Nathalie Grosjean, and Michel Lance, *Drag and lift forces on interface-contaminated bubbles spinning in a rotating flow*. Journal of fluid mechanics, 2009. **624**: p. 159-178.
 115. Groß, TF, J Bauer, G Ludwig, D Fernandez Rivas, and PF Pelz, *Bubble nucleation from micro-crevices in a shear flow*. Experiments in fluids, 2018. **59**(1): p. 12.
 116. Zhao, Xu, Hang Ren, and Long Luo, *Gas bubbles in electrochemical gas evolution reactions*. Langmuir, 2019. **35**(16): p. 5392-5408.
 117. van der Linde, Peter, Pablo Peñas-López, Álvaro Moreno Soto, Devaraj van der Meer, Detlef Lohse, Han Gardeniers, and David Fernández Rivas, *Gas bubble evolution on microstructured silicon substrates*. Energy & environmental science, 2018. **11**(12): p. 3452-3462.
 118. Taqieddin, Amir, Michael R Allshouse, and Akram N Alshawabkeh, *Critical Review—Mathematical Formulations of Electrochemically Gas-Evolving Systems*. Journal of The Electrochemical Society, 2018. **165**(13): p. E694-E711.
 119. Robinson, JE, CM Sutton, and GF Reid, *Dilute Triton X-100 in water as a reference liquid for hydrometer calibration using Cuckow's method*. Measurement, 2014. **57**: p. 132-137.
 120. Babu, R and Malay K Das, *Effects of surface-active agents on bubble growth and detachment from submerged orifice*. Chemical Engineering Science, 2018. **179**: p. 172-184.
 121. Parhizkar, M, M Edirisinghe, and E Stride, *The effect of surfactant type and concentration on the size and stability of microbubbles produced in a capillary embedded T-junction device*. Rsc Advances, 2015. **5**(14): p. 10751-10762.

122. Romero-Cano, MS, A Martín-Rodríguez, and FJ De las Nieves, *Adsorption and desorption of triton X-100 in polystyrene particles with different functionality: I. Adsorption study*. Journal of colloid and interface science, 2000. **227**(2): p. 322-328.
123. Devaraj, S and N Munichandraiah, *The effect of nonionic surfactant triton X-100 during electrochemical deposition of MnO₂ on its capacitance properties*. Journal of The Electrochemical Society, 2007. **154**(10): p. A901-A909.
124. Li, Dongguo, Chao Wang, Dusan Tripkovic, Shouheng Sun, Nenad M Markovic, and Vojislav R Stamenkovic, *Surfactant removal for colloidal nanoparticles from solution synthesis: the effect on catalytic performance*. ACS Catalysis, 2012. **2**(7): p. 1358-1362.
125. Matsushima, Hisayoshi, Takami Iida, and Yasuhiro Fukunaka, *Gas bubble evolution on transparent electrode during water electrolysis in a magnetic field*. Electrochimica Acta, 2013. **100**: p. 261-264.
126. Angulo, Andrea, Peter van der Linde, Han Gardeniers, Miguel Modestino, and David Fernández Rivas, *Influence of Bubbles on the Energy Conversion Efficiency of Electrochemical Reactors*. Joule, 2020.
127. Wei, ZD, MB Ji, SG Chen, Y Liu, CX Sun, GZ Yin, PK Shen, and SH Chan, *Water electrolysis on carbon electrodes enhanced by surfactant*. Electrochimica Acta, 2007. **52**(9): p. 3323-3329.
128. Zhao, Xu, Ruchiranga Ranaweera, and Long Luo, *Highly efficient hydrogen evolution of platinum via tuning the interfacial dissolved-gas concentration*. Chemical communications, 2019. **55**(10): p. 1378-1381.
129. Bessarabov, Dmitri and Pierre Millet, *PEM water electrolysis*. Vol. 1. 2018: Academic Press.
130. Bodner, Merit, Astrid Hofer, and Viktor Hacker, *H₂ generation from alkaline electrolyzer*. Wiley Interdisciplinary Reviews: Energy and Environment, 2015. **4**(4): p. 365-381.
131. Xiang, Chengxiang, Kimberly M Papadantonakis, and Nathan S Lewis, *Principles and implementations of electrolysis systems for water splitting*. Materials Horizons, 2016. **3**(3): p. 169-173.
132. Ayers, Katherine E, Everett B Anderson, Christopher B Capuano, Michael Niedzwiecki, Michael A Hickner, Chao-Yang Wang, Yongjun Leng, and Wei Zhao, *Characterization of anion exchange membrane technology for low cost electrolysis*. ECS Transactions, 2013. **45**(23): p. 121.
133. Gottesfeld, Shimshon, Dario R Dekel, Miles Page, Chulsung Bae, Yushan Yan, Piotr Zelenay, and Yu Seung Kim, *Anion exchange membrane fuel cells: Current status and remaining challenges*. Journal of Power Sources, 2018. **375**: p. 170-184.
134. Hagesteijn, Kimberly FL, Shanxue Jiang, and Bradley P Ladewig, *A review of the synthesis and characterization of anion exchange membranes*. Journal of materials science, 2018. **53**(16): p. 11131-11150.
135. Mohammadi, Amin and Mehdi Mehrpooya, *Techno-economic analysis of hydrogen production by solid oxide electrolyzer coupled with dish collector*. Energy Conversion and Management, 2018. **173**: p. 167-178.
136. O'Neil, Glen D, Corey D Christian, David E Brown, and Daniel V Esposito, *Hydrogen production with a simple and scalable membraneless electrolyzer*. Journal of The Electrochemical Society, 2016. **163**(11): p. F3012.
137. Pang, Xueqi, Jonathan T Davis, Albert D Harvey III, and Daniel V Esposito, *Framework for evaluating the performance limits of membraneless electrolyzers*. Energy & Environmental Science, 2020.

138. Davis, Jonathan T, Ji Qi, Xinran Fan, Justin C Bui, and Daniel V Esposito, *Floating membraneless PV-electrolyzer based on buoyancy-driven product separation*. International Journal of Hydrogen Energy, 2018. **43**(3): p. 1224-1238.
139. Long, Zhiyun, Yuyan Zhao, Chunhui Zhang, Yuheng Zhang, Cunming Yu, Yuchen Wu, Jun Ma, Moyuan Cao, and Lei Jiang, *A Multi-Bioinspired Dual-Gradient Electrode for Microbubble Manipulation toward Controllable Water Splitting*. Advanced Materials, 2020. **32**(17): p. 1908099.
140. Talabi, Oyinkansola O, Anna E Dorfi, Glen D O'Neil, and Daniel V Esposito, *Membraneless electrolyzers for the simultaneous production of acid and base*. Chemical Communications, 2017. **53**(57): p. 8006-8009.
141. Davis, JT, DE Brown, X Pang, and DV Esposito, *High Speed Video Investigation of Bubble Dynamics and Current Density Distributions in Membraneless Electrolyzers*. Journal of The Electrochemical Society, 2019. **166**(4): p. F312.
142. Hadikhani, Pooria, S Mohammad H Hashemi, and Demetri Psaltis, *The Impact of Surfactants on the Inertial Separation of Bubbles in Microfluidic Electrolyzers*. Journal of the Electrochemical Society, 2020.
143. Kilchenmann, Samuel C, Enrica Rollo, Pietro Maoddi, and Carlotta Guiducci, *Metal-coated SU-8 structures for high-density 3-D microelectrode arrays*. Journal of Microelectromechanical Systems, 2016. **25**(3): p. 425-431.
144. Dukovic, John and Charles W Tobias, *The influence of attached bubbles on potential drop and current distribution at gas-evolving electrodes*. Journal of the Electrochemical Society, 1987. **134**(2): p. 331.
145. Miao, Haiyan, Lin Lu, and Zuohua Huang, *Flammability limits of hydrogen-enriched natural gas*. international journal of hydrogen energy, 2011. **36**(11): p. 6937-6947.
146. Hashemi, S Mohammad H, Ugljesa Babic, Pooria Hadikhani, and Demetri Psaltis, *The potentials of additive manufacturing for mass production of electrochemical energy systems*. Current Opinion in Electrochemistry, 2020.
147. Zappone, Alessio, Marco Di Renzo, and M erouane Debbah, *Wireless Networks Design in the Era of Deep Learning: Model-Based, AI-Based, or Both?* arXiv preprint arXiv:1902.02647, 2019.
148. LeCun, Yann, Yoshua Bengio, and Geoffrey Hinton, *Deep learning*. nature, 2015. **521**(7553): p. 436.
149. Wan, Zhong Yi and Themistoklis P Sapsis, *Machine learning the kinematics of spherical particles in fluid flows*. Journal of Fluid Mechanics, 2018. **857**.
150. Verma, Siddhartha, Guido Novati, and Petros Koumoutsakos, *Efficient collective swimming by harnessing vortices through deep reinforcement learning*. Proceedings of the National Academy of Sciences, 2018: p. 201800923.
151. Beck, Andrea D, David G Flad, and Claus-Dieter Munz, *Neural Networks for Data-Based Turbulence Models*. arXiv preprint arXiv:1804.04482, 2018.
152. Chen, Claire Lifan, Ata Mahjoubfar, Li-Chia Tai, Ian K Blaby, Allen Huang, Kayvan Reza Niazi, and Bahram Jalali, *Deep learning in label-free cell classification*. Scientific reports, 2016. **6**: p. 21471.
153. Van Valen, David A, Takamasa Kudo, Keara M Lane, Derek N Macklin, Nicolas T Quach, Mialy M DeFelice, Inbal Maayan, Yu Tanouchi, Euan A Ashley, and Markus W Covert, *Deep learning automates the quantitative analysis of individual cells in live-cell imaging experiments*. PLoS computational biology, 2016. **12**(11): p. e1005177.
154. Gopakumar, G, K Hari Babu, Deepak Mishra, Sai Siva Gorthi, and Gorthi RK Sai Subrahmanyam, *Cytopathological image analysis using deep-learning networks in microfluidic microscopy*. JOSA A, 2017. **34**(1): p. 111-121.

155. Stoecklein, Daniel, Kin Gwn Lore, Michael Davies, Soumik Sarkar, and Baskar Ganapathysubramanian, *Deep learning for flow sculpting: Insights into efficient learning using scientific simulation data*. Scientific reports, 2017. **7**: p. 46368.
156. Mahdi, Yassine and Kamel Daoud, *Microdroplet size prediction in microfluidic systems via artificial neural network modeling for water-in-oil emulsion formulation*. Journal of Dispersion Science Technology, 2017. **38**(10): p. 1501-1508.
157. Khor, Jian Wei, Neal Jean, Eric S Luxenberg, Stefano Ermon, and Sindy KY Tang, *Using machine learning to discover shape descriptors for predicting emulsion stability in a microfluidic channel*. Soft matter, 2019.
158. Hong, Yiping and Fujun Wang, *Flow rate effect on droplet control in a co-flowing microfluidic device*. Microfluidics Nanofluidics, 2007. **3**(3): p. 341-346.
159. Anna, Shelley Lynn, *Droplets and bubbles in microfluidic devices*. Annual Review of Fluid Mechanics, 2016. **48**: p. 285-309.
160. Wu, Chun-Hui, Dongyang Kang, Ping-Hei Chen, and Yu-Chong Tai, *MEMS thermal flow sensors*. Sensors Actuators A: Physical, 2016. **241**: p. 135-144.
161. Li, Ying, Guofeng Yan, Liang Zhang, and Sailing He, *Microfluidic flowmeter based on micro "hot-wire" sandwiched Fabry-Perot interferometer*. Optics Express, 2015. **23**(7): p. 9483-9493.
162. Kuo, Jonathan TW, Lawrence Yu, and Ellis Meng, *Micromachined thermal flow sensors—A review*. Micromachines, 2012. **3**(3): p. 550-573.
163. Wang, Tao and Roger Baker, *Coriolis flowmeters: a review of developments over the past 20 years, and an assessment of the state of the art and likely future directions*. Flow Measurement Instrumentation, 2014. **40**: p. 99-123.
164. Son, HS, YS Hong, WM Park, MA Yu, and CH Lee, *A novel approach for estimating sugar and alcohol concentrations in wines using refractometer and hydrometer*. Journal of food science, 2009. **74**(2): p. C106-C111.
165. Castritius, Stefan, Alexander Kron, Thomas Schäfer, Matthias Rädle, and Diedrich Harms, *Determination of alcohol and extract concentration in beer samples using a combined method of near-infrared (NIR) spectroscopy and refractometry*. Journal of agricultural food chemistry, 2010. **58**(24): p. 12634-12641.
166. Sparks, D, R Smith, M Straayer, J Cripe, R Schneider, A Chimbayo, S Anasari, and N Najafi, *Measurement of density and chemical concentration using a microfluidic chip*. Lab on a Chip, 2003. **3**(1): p. 19-21.
167. Li, Cheng, Gang Bai, Yunxiao Zhang, Min Zhang, and Aoqun Jian, *Optofluidics refractometers*. Micromachines, 2018. **9**(3): p. 136.
168. Liu, RP, MJ Fuent, MP Henry, and MD Duta, *A neural network to correct mass flow errors caused by two-phase flow in a digital coriolis mass flowmeter*. Flow Measurement and Instrumentation, 2001. **12**(1): p. 53-63.
169. Tombs, Michael, Feibiao Zhou, and Manus Henry, *Two-phase coriolis mass flow metering with high viscosity oil*. Flow Measurement and Instrumentation, 2018. **59**: p. 23-27.
170. Zhang, Jian-Guo, Ke-Jun Xu, Shuai Dong, Zheng Liu, Qi-Li Hou, and Zheng-Yu Fang, *Mathematical model of time difference for Coriolis flow sensor output signals under gas-liquid two-phase flow*. Measurement, 2017. **95**: p. 345-354.
171. Hashihama, Fuminori, Jota Kanda, Ami Tauchi, Taketoshi Kodama, Hiroaki Saito, and Ken Furuya, *Liquid waveguide spectrophotometric measurement of nanomolar ammonium in seawater based on the indophenol reaction with o-phenylphenol (OPP)*. Talanta, 2015. **143**: p. 374-380.

172. Do, Hyungrok and Campbell Carter, *Hydrocarbon fuel concentration measurement in reacting flows using short-gated emission spectra of laser induced plasma*. Combustion and Flame, 2013. **160**(3): p. 601-609.
173. Noroozi, Zahra, Horacio Kido, Miodrag Micic, Hansheng Pan, Christian Bartolome, Marko Princevac, Jim Zoval, and Marc Madou, *Reciprocating flow-based centrifugal microfluidics mixer*. Review of Scientific Instruments, 2009. **80**(7): p. 075102.
174. You, Jae Bem, Kyowon Kang, Thanh Tinh Tran, Hongkeun Park, Wook Ryol Hwang, Ju Min Kim, and Sung Gap Im, *PDMS-based turbulent microfluidic mixer*. Lab on a Chip, 2015. **15**(7): p. 1727-1735.
175. Zulkifli, Syahidah Nurani, Herlina Abdul Rahim, and Woei-Jye Lau, *Detection of contaminants in water supply: A review on state-of-the-art monitoring technologies and their applications*. Sensors and Actuators B: Chemical, 2018. **255**: p. 2657-2689.
176. Bradski, Gary and Adrian Kaehler, *OpenCV*. Dr. Dobb's journal of software tools, 2000. **3**.
177. Basu, Amar S, *Droplet morphometry and velocimetry (DMV): a video processing software for time-resolved, label-free tracking of droplet parameters*. Lab on a Chip, 2013. **13**(10): p. 1892-1901.
178. Hadwen, B, GR Broder, D Morganti, A Jacobs, C Brown, JR Hector, Y Kubota, and Hywel Morgan, *Programmable large area digital microfluidic array with integrated droplet sensing for bioassays*. Lab on a Chip, 2012. **12**(18): p. 3305-3313.
179. Chong, Zhuang Zhi, Shu Beng Tor, Alfonso M Gañán-Calvo, Zhuang Jie Chong, Ngiap Hiang Loh, Nam-Trung Nguyen, and Say Hwa Tan, *Automated droplet measurement (ADM): an enhanced video processing software for rapid droplet measurements*. Microfluidics and Nanofluidics, 2016. **20**(4): p. 66.
180. Hashemi, S Mohammad H, Petr Karnakov, Pooria Hadikhani, Enrico Chinello, Sergey Litvinov, Christophe Moser, Petros Koumoutsakos, and Demetri Psaltis, *A versatile and membrane-less electrochemical reactor for the electrolysis of water and brine*. Energy & Environmental Science, 2019.
181. Temiz, Yuksel, Jelena Skorucak, and Emmanuel Delamarche, *Capillary-driven microfluidic chips with evaporation-induced flow control and dielectrophoretic microbead trapping*. Journal of Micro/Nanolithography, MEMS, and MOEMS, 2014. **13**(3): p. 033018.
182. Liu, Bendong, Jianchuang Sun, Desheng Li, Jiang Zhe, and Kwang W Oh, *A high flow rate thermal bubble-driven micropump with induction heating*. Microfluidics and Nanofluidics, 2016. **20**(11): p. 155.
183. Shang, Luoran, Yao Cheng, and Yuanjin Zhao, *Emerging droplet microfluidics*. Chemical reviews, 2017. **117**(12): p. 7964-8040.
184. Song, Helen, Delai L Chen, and Rustem F Ismagilov, *Reactions in droplets in microfluidic channels*. Angewandte chemie international edition, 2006. **45**(44): p. 7336-7356.
185. Kelly, Ryan T, Jason S Page, Ioan Marginean, Keqi Tang, and Richard D Smith, *Dilution-free analysis from picoliter droplets by nano-electrospray ionization mass spectrometry*. Angewandte Chemie International Edition, 2009. **48**(37): p. 6832-6835.
186. Fidalgo, Luis M, Graeme Whyte, Brandon T Ruotolo, Justin LP Benesch, Florian Stengel, Chris Abell, Carol V Robinson, and Wilhelm TS Huck, *Coupling microdroplet microreactors with mass spectrometry: reading the contents of single droplets online*. Angewandte Chemie International Edition, 2009. **48**(20): p. 3665-3668.
187. Jeffries, Gavin DM, Robert M Lorenz, and Daniel T Chiu, *Ultrasensitive and high-throughput fluorescence analysis of droplet contents with orthogonal line confocal excitation*. Analytical chemistry, 2010. **82**(23): p. 9948-9954.

188. Utada, Andrew S, Alberto Fernandez-Nieves, Howard A Stone, and David A Weitz, *Dripping to jetting transitions in coflowing liquid streams*. Physical review letters, 2007. **99**(9): p. 094502.
189. Cubaud, Thomas and Thomas G Mason, *Capillary threads and viscous droplets in square microchannels*. Physics of Fluids, 2008. **20**(5): p. 053302.
190. Montessori, Andrea, Marco Lauricella, Elad Stolovicki, David A Weitz, and Sauro Succi, *Jetting to dripping transition: Critical aspect ratio in step emulsifiers*. Physics of Fluids, 2019. **31**(2): p. 021703.
191. Dressler, Oliver J, Philip D Howes, Jaebum Choo, and Andrew J deMello, *Reinforcement Learning for Dynamic Microfluidic Control*. ACS Omega, 2018. **3**(8): p. 10084-10091.
192. Nightingale, Adrian M and John C de Mello, *Microscale synthesis of quantum dots*. Journal of Materials Chemistry, 2010. **20**(39): p. 8454-8463.
193. Zhao, Yuanjin, Yao Cheng, Luoran Shang, Jie Wang, Zhuoying Xie, and Zhongze Gu, *Microfluidic synthesis of barcode particles for multiplex assays*. Small, 2015. **11**(2): p. 151-174.
194. Utech, Stefanie, Radivoje Prodanovic, Angelo S Mao, Raluca Ostafe, David J Mooney, and David A Weitz, *Microfluidic generation of monodisperse, structurally homogeneous alginate microgels for cell encapsulation and 3D cell culture*. Advanced healthcare materials, 2015. **4**(11): p. 1628-1633.
195. Hashemi, S Mohammad H, Miguel A Modestino, and Demetri Psaltis, *A membrane-less electrolyzer for hydrogen production across the pH scale*. Energy Environmental Science, 2015. **8**(7): p. 2003-2009.
196. Mohammed, Mazher Iqbal, Steven Haswell, and Ian Gibson, *Lab-on-a-chip or Chip-in-a-lab: Challenges of Commercialization Lost in Translation*. Procedia Technology, 2015. **20**: p. 54-59.
197. Neuzil, P, CDM Campos, CC Wong, JBW Soon, J Reboud, and A Manz, *From chip-in-a-lab to lab-on-a-chip: towards a single handheld electronic system for multiple application-specific lab-on-a-chip (ASLOC)*. Lab on a Chip, 2014. **14**(13): p. 2168-2176.
198. Erickson, David, Dakota O'Dell, Li Jiang, Vlad Oncescu, Abdurrahman Gumus, Seoho Lee, Matthew Mancuso, and Saurabh Mehta, *Smartphone technology can be transformative to the deployment of lab-on-chip diagnostics*. Lab on a Chip, 2014. **14**(17): p. 3159-3164.
199. Lee, Seung Ah and Changhuei Yang, *A smartphone-based chip-scale microscope using ambient illumination*. Lab on a Chip, 2014. **14**(16): p. 3056-3063.
200. McCrory, Charles CL, Suho Jung, Ivonne M Ferrer, Shawn M Chatman, Jonas C Peters, and Thomas F Jaramillo, *Benchmarking hydrogen evolving reaction and oxygen evolving reaction electrocatalysts for solar water splitting devices*. Journal of the American Chemical Society, 2015. **137**(13): p. 4347-4357.
201. Bradski, G., *The OpenCV Library*. Dr. Dobb's Journal of Software Tools, 2000.
202. Donose, Bogdan C, Falk Harnisch, and Elena Taran, *Electrochemically produced hydrogen bubble probes for gas evolution kinetics and force spectroscopy*. Electrochemistry communications, 2012. **24**: p. 21-24.
203. Van Helden, WGJ, CWM Van Der Geld, and PGM Boot, *Forces on bubbles growing and detaching in flow along a vertical wall*. International journal of heat and mass transfer, 1995. **38**(11): p. 2075-2088.
204. Pritchard, Philip J and John W Mitchell, *Fox and McDonald's introduction to fluid mechanics*. 2016: John Wiley & Sons.

205. Abadi, Martín, Paul Barham, Jianmin Chen, Zhifeng Chen, Andy Davis, Jeffrey Dean, Matthieu Devin, Sanjay Ghemawat, Geoffrey Irving, and Michael Isard. *Tensorflow: a system for large-scale machine learning*. in *OSDI*. 2016.
206. Krizhevsky, Alex, Ilya Sutskever, and Geoffrey E Hinton. *Imagenet classification with deep convolutional neural networks*. in *Advances in neural information processing systems*. 2012.
207. Simonyan, Karen and Andrew Zisserman, *Very deep convolutional networks for large-scale image recognition*. arXiv preprint arXiv:1409.0482, 2014.

Pooria Hadikhani

Email: pooria.hadikhani@epfl.ch

PhD candidate in Mechanics

March 2016 - 2020

Optics Laboratory, École polytechnique fédérale de Lausanne (EPFL)

Thesis title: Multiphase flows in microfluidic reactors

Publications (directly related to the thesis)

Membrane-less electrolyzer with porous walls for high throughput and pure hydrogen production

Hadikhani P, Hashemi SMH, Schenk SA, Psaltis D, Under preparation

The impact of surfactants on the inertial separation of bubbles in microfluidic electrolyzers

Hadikhani P, Hashemi SMH, Psaltis D, Journal of Electrochemical Society, 2020.

Learning from droplet flows in microfluidic channels using deep neural networks

Hadikhani P, Borhani N, Hashemi SMH, Psaltis D, Scientific reports, 2019.

Inertial manipulation of bubbles in rectangular microfluidic channels

Hadikhani P, Hashemi SMH, Balestra G, Zhu L, Modestino MA, Gallaire F, Psaltis D, Lab on a Chip, 2018.

Publications (related to the thesis)

The potentials of additive manufacturing for mass production of electrochemical energy systems

Hashemi SMH, Babic U, Hadikhani P, Psaltis D, Current Opinion in Electrochemistry, 2020.

A versatile and membrane-less electrochemical reactor for the electrolysis of water and brine

Hashemi SMH, Karnakov P, Hadikhani P, Chinello E, Litvinov S, Moser C, Koumoutsakos P, Psaltis D, Energy & Environmental Science, 2019.

Membrane-less micro fuel cell based on two-phase flow

Hashemi SMH, Neuenschwander M, Hadikhani P, Modestino MA, Psaltis D, Journal of Power Sources, 2017.

Conference contributions

Learning the fluid/flow properties using microfluidics (Oral presentation)

Hadikhani P, Hashemi SMH, Psaltis D, EOS Optical Technologies: Optofluidics and Manufacturing, Tolerancing, and Testing of Optical Systems, 5th conference on Optofluidics, Munich, Germany, 24-27 June 2019.

Inertial manipulation of bubbles in rectangular microfluidic channels (Oral presentation)

Hadikhani P, Hashemi SMH, Balestra G, Zhu L, Modestino MA, Gallaire F, Psaltis D, COMSOL conference, Lausanne, Switzerland, 22-24 October 2018.

Inertial manipulation of bubbles in rectangular microfluidic channels (Oral presentation)

Hadikhani P, Hashemi SMH, Balestra G, Zhu L, Modestino MA, Gallaire F, Psaltis D, ICMFLOC 2018, Beijing, China, 8-10 June 2018